Design, synthesis, and characterization of linear and branched semifluorinated polymers for therapeutic and diagnostic drug delivery applications

by

Montira Tangsangasaksri

A dissertation submitted in partial fulfillment of

the requirements for the degree of

Doctor of Philosophy

(Pharmaceutical Sciences)

at the

UNIVERSITY OF WISCONSIN-MADISON

2020

Date of final oral examination: August 17, 2020

The dissertation is approved by the following members of the Final Oral Committee:

Sandro Mecozzi, Professor, Department of Chemistry and School of Pharmacy
Glen S. Kwon, Professor, School of Pharmacy
Paul C. Marker, Professor, School of Pharmacy
Jamey Weichert, Associate Professor, Department of Radiology

Design, synthesis, and characterization of linear and branched semifluorinated polymers for therapeutic and diagnostic drug delivery applications

Montira Tangsangasaksri

Under the supervision of Professor Sandro Mecozzi

At the University of Wisconsin-Madison

ABSTRACT

The unique dual hydrophobicity and lipophobicity of perfluorocarbons have attracted a lot of attention due to their advantages in biomedical applications. Semifluorinated polymers are one example of the fluorinated materials that have been extensively studied for their use as carriers in drug delivery systems. Different semifluorinated polymer design and architecture can lead to the formation of nanoparticles with different morphologies and properties. Thus, self-assembly of a semifluorinated polymer in aqueous solution can lead to the formation of ordered, thermodynamically stable water-soluble aggregates. On the other hand, the stabilization of two immiscible liquids through a semifluorinated polymer may lead to kinetically stable nanoemulsions. Finally, the insertion of a fluorocarbon block in multi-block copolymers can lead to an increase in overall stability of the resulting nanoparticles.

In this thesis, therapeutic and diagnostic nanoparticles have been developed using semifluorinated polymers, which provided an entry into improved particle stability, therapeutic efficacy, and diagnostic sensitivity. A semifluorinated polymer with a targeting ligand was synthesized to increase the therapeutic efficacy of the corresponding micelles. The prepared micelles showed an improved accumulation and penetration in 2D and 3D cultured cancer cells *in*

vitro which resulted in an enhanced therapeutic efficacy of encapsulated paclitaxel, a model hydrophobic anticancer drug. In addition, the effect of different polymer architectures on the micelle properties was explored. Dibranched semifluorinated triblock copolymers were designed, synthesized, and characterized. The physicochemical and the micelle properties of the dibranched semifluorinated triblock copolymers were compared to the linear triblock copolymer and the linear and the dibranched diblock copolymers. All polymers were able to encapsulate paclitaxel. The encapsulation efficiency solely depended on the hydrophobic moiety of the corresponding micelles. Prolonged release was observed in the micelles prepared with the dibranched semifluorinated copolymers. This was mostly due to a superior sealing of the drug in the micelle hydrophobic core through the intermediate fluorous shell. In addition, the introduction of the fluorocarbon block surprisingly considerably reduced the cellular toxicity of the polymers, showcasing the potential of semifluorinated polymers in clinical translation. Semifluorinated polymers also offer advantages in diagnostic applications, especially in magnetic resonance imaging (MRI). A semifluorinated triblock copolymer was used to prepare a nanoemulsion that was able to stabilize a large volume of ^{19}F MRI agent. The nanoemulsion exhibited a long-term stability under different storage conditions. *In vivo* ^{19}F MRI revealed an improved signal sensitivity as observed from a high ^{19}F signal intensity in the tumors. This was due to the high concentration of the fluorinated agent in the nanoemulsion as well as to passive accumulation of nanoemulsion particles in the tumor by the enhanced permeability and retention (EPR) effect. Finally, we also investigated the combination of fluorinated materials with paramagnetic metal ions, Fe^{3+}, in the form of extremely small iron oxide nanoparticles (ESIONs) and magnetic ionic liquids (MILs) for improving ^{19}F signal sensitivity. The use of the ESIONs and the MILs led to a decrease in T_1 relaxation, suggesting that the sensitivity of ^{19}F MRI can be enhanced by the appropriate choice of iron(III)-containing materials.

ACKNOWLEDGMENTS

I would first like to thank my advisor, Professor Sandro Mecozzi, for his kind guidance and continual support throughout my time in his research group. Thank you for always finding the time for our meeting no matter how busy you were. Thank you for encouraging me to do something that I never thought I would and never doubted my abilities. Sandro's passion for science always inspires me and it has fostered me to become the curious scientist I am today.

I would also like to thank the members of my thesis committee: Professor Glen Kwon, Professor Paul Marker, Professor Jamey Weichert, and my previous committee Professor Ron Burnette, for their time and support in this process. Thank you for your valuable feedback and advice during my graduate career.

I would like to acknowledge the faculty and staff at the School of Pharmacy. Specifically, I would like to thank the Analytical Instrumentation Center (AIC) and the Medicinal Chemistry Center (MCC), especially Dr. Tom Stringfellow and Dr. John Feltenberger. I would like to thank Dr. Gary Girdaukas for his invaluable help throughout my graduate career. I would like to thank the Zeeh Pharmaceutical Experiment Station team, especially Dr. Mark Sacchetti for the opportunities to work as a project assistant. I have gained a lot of valuable knowledge and skills outside of my research focus. A special thanks to Mr. Ken Niemeyer who took a really good care of all graduate students. Thank you for your invaluable help with everything, seriously everything! I would also like to thank Bonnie Fingerhut and Dr. Melgardt De Villiers for having me as their TA. I really enjoyed working for both of them. It gave me an excuse to be out of the lab. I am thankful for their support during the hard time. I will definitely miss our TA meeting with all the good foods! I would like to thank Anna Reinhart, Julie Steinle, Dr. Eric Buxton, Kate Collins, Sally Griffith-Oh, Shelley Calhoun, and Jasmyn Booker for their help and support for putting together

the 51st PGSRM conference. I would also like to thank Dr. Chuck Lauhon, Josh Cutler and Debbie King for their help, support, and encouragement during my graduate career.

I am thankful for my wonderful labmates, current and former, who supported me, provided me with insightful suggestions, proofread my writing materials, and listened to me practice presentations. Thank you to Stephanie, Alexa, Michelle, and Moira for a warm welcome during my first year. Thank you to Michelle for letting me play with Flynn. Thank you to Moira for running tons of MALDI samples. Thank you to Stephanie for her chemistry and biology skills, generous help in the lab, wonderful discussion, and laughs. Thank you to Alexa for our food adventures. Thank you to Marshall for his NMR skills and all year-round Christmas music in the lab. I will never forget the time we spent shredding all the paper.

Thank you to all the PGSRM committee and volunteers, especially Ashita and Yuna, for making the 51st PGSRM happened here in Madison. I could not do it without everyone. Thank you to my cohort (Geetika, Brynn, and Kelly), my friends in the School of Pharmacy, and my Thai friends inside and outside of Madison, for keeping me away from the lab and helping me enjoy the graduate school life. Thank you to Thai American Association of Madison for keeping my Sunday morning busy with Thai language tutoring session for the kids and giving me a distraction from all the stress I have during my graduate school.

Finally, I am extremely thankful to my family. Your love and support have always driven me to be a better self. None of these would have been possible without you! Thank you to my brother who always comes up with new cooking ideas for me to try. A special thank you to Rak for being the greatest supporter and partner. I am incredibly lucky to meet you here at UW-Madison. You always brighten my day with your smile – thank you!

TABLE OF CONTENTS

LIST OF FIGURES

LIST OF TABLES

LIST OF SCHEMES

LIST OF ABBREVIATIONS

4T1-Luc	Luciferase-expressing murine breast cancer cell line
ACN	Acetonitrile
Ar	Argon
BTF	α,α,α-trifluorotoluene (benzotrifluoride)
C153	Coumarin 153
CMC	Critical Micelle Concentration
DBU	1,8-diazabicyclo[5.4.0]undec-7-ene
DCM	Dichloromethane
DLS	Dynamic light scattering
DMF	Dimethylformamide
DMSO	Dimethylsulfoxide
DOPET	3-Hydroxytyrosol
DSG	Distearoyl-rac-glycerol
DSG	1,2-distearoyl-rac-glycerol
EPR	Enhanced permeability and retention effect
ESI	Electrospray ionization
EtOAc	Ethyl acetate
HPLC	High performance liquid chromatography
IC_{50}	the half maximal inhibitory concentration
IV	Intravenous
KI	Potassium iodide

LogP	Partition coefficient
MALDI	Matrix-assisted laser desorption/ionization
MeOH	Methanol
$MgSO_4$	Magnesium sulfate
MsCl	Methanesulfonyl chloride
MW	Molecular weight
N_{agg}	Aggregation number
NH_4Cl	Ammonium chloride
NMR	Nuclear magnetic resonance
P3P	1,3-bis(1'-pyrenyl)propane
PBS	Phosphate buffered saline
PEG	Poly(ethylene glycol)
$mPEG_{2K}$-DSG	1,2-distearoyl-rac-glycero-3-(methylpolyoxyethylene)-2000
PFCE	Perfluoro-15-crown-5-ether
PFPE	Perfluoropolyether
$POCl_3$	Phosphoryl chloride
PTX	Paclitaxel
R_f	Retention factor
T_1	Longitudinal relaxation time
T_2	Transverse relaxation time
TBA	Tert-butanol
TEA	Triethylamine
THF	Tetrahydrofuran
TLC	Thin-layer chromatography

USP	United States Pharmacopeia
WHO	World Health Organization

CHAPTER 1 – BIOMEDICAL APPLICATIONS OF FLUORINATED NANOPARTICLES

1.1 Fluorinated molecules

1.1.1 History of fluorine

Fluorine is one of the abundant elements on earth. It is normally found in various mineral forms. Fluorspar (CaF_2), a mineral form of fluorine, was first described by George Bauer in 1592 initiating the trajectory of fluorine's various applications (**Figure 1.1**). Although the composition of fluorspar was still unknown, it was mostly used in the ceramic and glass industry to lower the melting points of metal ores which results in an increased fluidity. Thus, the name fluorspar was given, as the Latin word "fluo" means "to flow".[1] In 1771, Carl W. Scheele, a Swedish chemist, discovered hydrogen fluoride from mixing fluorspar with concentrated sulfuric acid. Proposed by Andre-Marie Ampere, the French scientist, in 1809, this hydrogen fluoride consists of a hydrogen atom and a new element which was later named "Fluorine" by Humphry Davy in 1813.[2] The first synthesized organofluorine molecule was reported in 1835 by Dumas and Péligot where they reacted potassium fluoride and dimethyl sulfate to yield fluoromethane.[3] In 1886, Henri Moissan successfully isolated the element fluorine and later in 1890 reported that the product isolated from the reaction between carbon and fluorine was carbon tetrafluoride.[1, 4] Since then fluorocarbons have found numerous applications toward several industries. For example, the use of chlorofluorocarbons (CFCs) as refrigerants was introduced by Midgley and Henne in 1930 and the use of Teflon as a nonstick coating or electrical insulation was discovered by DuPont in 1938.[4] This era was noted as an establishment of the organofluorine chemistry foundation. Additionally, fluorine also discovered itself in pharmaceutical applications. Fluorocarbons were found to have anesthetic properties, marking the first step towards the use of fluorinated anesthetics in 1946.[5] Moreover, during the 1980s, an increase in the number of active pharmaceutical ingredients (APIs) containing fluorine was observed, suggesting a significant usage of fluorine containing molecules.[6] The trend of fluorinated drugs keeps increasing, in fact, the fluorinated drugs accounted for almost one-fourth of the FDA approved drugs in 2019.[7]

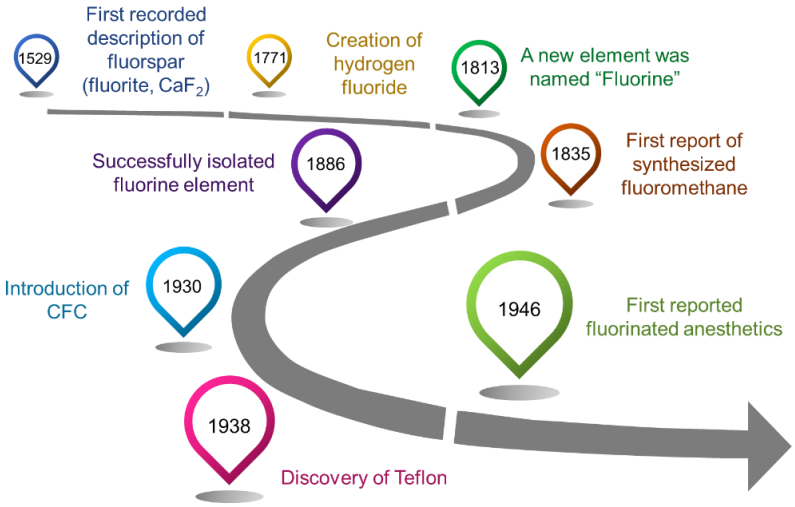

Figure 1.1 History of Fluorocarbons.

1.1.2 Fluorocarbon and its physical properties

Fluorocarbon is a molecule that resembles a hydrocarbon but in which hydrogens (H) are substituted with fluorine (F) atoms. Unique characteristics of fluorine atoms have given fluorocarbon special properties. Fluorine is the element that has the highest electronegativity of 4.0 according to Pauling's scale. The high electronegativity of fluorine results in a low polarization and a small size of the fluorine atom (van der Waal radius, 1.47 Å).[8] A substitution of hydrogen with fluorine leads to a formation of the strongest bond in organic chemistry, the C-F bond, where the bond dissociation energy (BDE) can be as high as 130 kcal/mol.[4, 9-11] A significant difference of electronegativity between fluorine and carbon (4.0 vs 2.5 according to Pauling’s scale, respectively) leads to a high polarity of the C-F bond which hugely contributes to its bond strength.[4] This high BDE offers fluorocarbons their high thermal stability. Moreover, the larger size of fluorine compared to proton results in a longer C-F bond length (1.35 Å) compared to a C-H bond length (1.09 Å).[9] This leads to a larger volume of perfluorocarbon molecules compared to their hydrocarbon counterparts; for example, a volume of 92 $Å^3$ for a CF_3 group versus 54 $Å^3$ for a CH_3 group, thus, providing bulkiness and rigidity to fluorocarbon molecules (**Figure 1.2**).[12]

Finally, a low polarizability of fluorine leads to low surface energy and, thus, results in low van der Waals forces of fluorocarbons. As a consequence, the fluorous molecule becomes chemically inert.[10] All

of these physical properties of fluorine contribute to the unique characteristics of fluorocarbons which has been exploited in various applications.

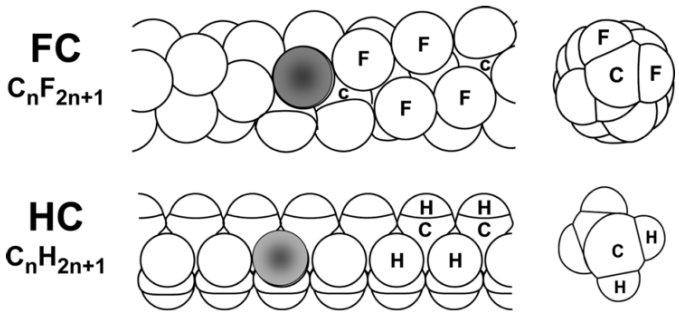

Figure 1.2 Schematic diagram of fluorocarbon and hydrocarbon structures and their cross-sections. Figure from Riess, J. G.[13]

1.1.3 Fluorous phase

The term "superhydrophobicity" has been used to describe fluorocarbons, a.k.a. perfluorocarbons (PFCs), due to their immiscibility with water. Such characteristic comes from their low polarizability, low surface energy, and low intermolecular interactions.[10] As shown in **Figure 1.3**, the mixture of water, hexane, and perfluorohexane separates into three immiscible phases after equilibrium, suggesting that PFCs are poorly miscible with both water and hydrocarbons. In fact, fluorocarbons are excluded from the other phases rather than just preferentially interacting with themselves due to their low van der Waal interactions. The segregation of perfluorohexane gives rise to a new phase formation, termed the fluorous phase.[9-10] This phenomenon bestows the perfluorocarbon with unique dual hydrophobicity and lipophobicity properties.

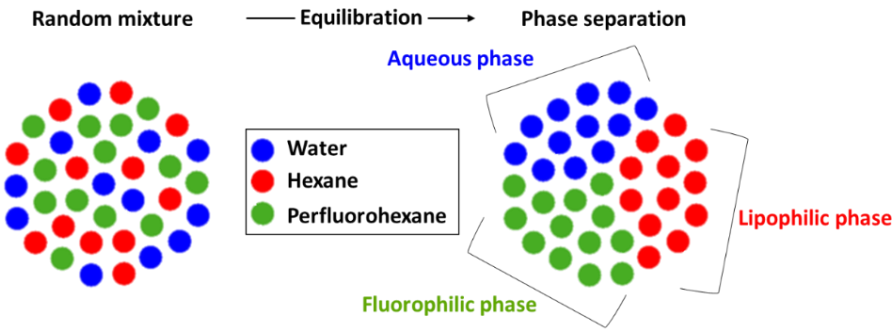

Figure 1.3 Fluorous phase formation diagram. After equilibrium, the random mixture of water, hexane and perfluorohexane undergoes phase separation, resulting in three immiscible phases: aqueous phase (water), lipophilic phase (hexane), and fluorous phase (perfluorohexane).

1.1.4 Perfluorocarbons (PFCs) and their applications

The physical properties of fluorine provide the fluorocarbons with high thermal stability, resistance to corrosive environments, water and oil repellency, and low chemical reactivity, making them attractive for several applications.[4] For example, polytetrafluoroethylene (PTFE), known as Teflon, is one of the most well-known fluorinated polymers that has been used across a broad range of industries. For instance, it has been used to prepared O-rings used in the automotive industry, electrical insulations in the electronic industry, coating for pumps or reaction vessels in the chemical industry, and non-stick surfaces.[14] Polyvinylidenefluoride (PVDF) is another example of a semifluorinated polymer that has very good chemical resistance which has been widely used in various applications such as coating and solar panels.[14]

Other than the usage in several aforementioned industries, PFCs have also found their ways in biomedical applications (**Figure 1.4**).[10, 12, 15] For example, PFCs have been used as oxygen carriers for blood substitution. Due to PFCs' low intermolecular interactions, the formation of interstitial spaces results in an extremely high gas solubility; *i.e.*, for O_2, it can be approximately 20 – 25 times higher than water or blood plasma.[16] In addition, the use of PFCs in drug delivery systems has gained popularity over the past several years. The development of new synthetic semifluorinated amphiphilic polymers leads to a formation of various PFC-based nanoparticles such as liposomes, emulsions, dendrimers, micelles, etc. Nanoparticles prepared from semifluorinated polymers possess higher stability over conventional hydrocarbon polymers.

This is due to the energetically favorable formation of the fluorous phase which has a less dynamic environment and thus providing its high stability.

Furthermore, due to a 100% natural abundance of ^{19}F and high sensitivity of ^{19}F, 83% to that of ^{1}H, PFCs have been utilized as tracers for ^{19}F magnetic resonance imaging (MRI). ^{19}F signal can be presented as a "hot-spot" or "second color", providing a clearer image interpretation. Moreover, negligible background noises of fluorine in biological tissues make ^{19}F MRI an exceptional imaging option compared to conventional ^{1}H MRI where the images are presented in grey scale with high background noises from water and fats in the tissues.[17-18] These advantages of ^{19}F strongly benefit diagnostic applications, especially in tumor detection and cell labeling/cell tracking applications.[17, 19-20]

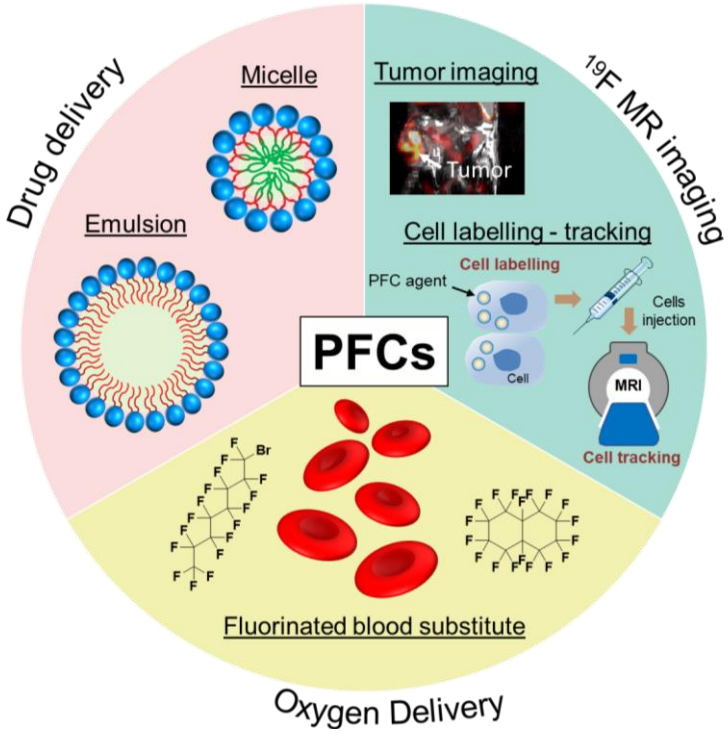

Figure 1.4 Example of perfluorocarbons (PFCs) usage in biomedical applications.

1.1.5 Semifluorinated polymer design and architecture

The high stability of PFC-based nanoparticles has driven the development of various semifluorinated polymers used as carriers in drug delivery system.[10, 12, 21] Different polymer structures have been designed and synthesized based on their intended application. The design and architecture of polymers

are crucial for determining the physicochemical properties of nanoparticles. In drug delivery, water solubility is one of the main criteria for any polymer design. Because of the dual hydrophobicity and lipophobicity of PFCs, the semifluorinated polymer design necessitates the inclusion of a hydrophilic portion in the polymers, leading to a block copolymer design. The commonly used hydrophilic portion in semifluorinated block copolymers is poly(ethylene glycol) or PEG which provides not only water solubility but also stealth properties to the corresponding nanoparticles.[22] Typical semifluorinated block copolymers arrangements are diblock and triblock copolymers with linear or branched architectures (**Figure 1.5**).

The combination of hydrophilic and fluorophilic components in semifluorinated diblock copolymers allows the formation of self-assembled nanoaggregates in water which result from strong hydrophobic interactions and low van der Waal forces of the fluorous block.[12] Given the fluorous phase separation, the self-aggregated nanoparticles in an aqueous environment possess a highly stable fluorophilic core and hydrophilic corona, so-called a core-shell structure, allowing the encapsulation of highly fluorinated molecules inside the core while maintaining water solubility of the particles through the hydrophilic corona. Different architectures of the fluorous block have been developed to be exploited in various biomedical applications. For example, self-assemblies of the linear semifluorinated diblock copolymers shown in **Figure 1.5**, form micelles that have been shown to successfully encapsulate sevoflurane, a highly fluorinated anesthetic drug, suggesting the possible intravenous delivery of gaseous anesthetics.[23-24] Linear semifluorinated diblock copolymers can also serve as fluorinated surfactant stabilizing large fluorinated oil droplets. A study done in our group by Fast *et al*. has shown that the nanoemulsions prepared from semifluorinated diblock copolymers significantly increased the solubility of sevoflurane in the formulation compared with Intralipid® which is a hydrocarbon-based emulsion.[25] Another example of alternate semifluorinated diblock copolymers is the branched architecture design of fluorous block which was designed to possess dual therapeutic and diagnostic, *i.e.* theranostic, properties, for drug delivery and imaging *via* ^{19}F MRI. This specific branched design (shown in **Figure 1.5**) exhibits one strong ^{19}F signal, allowing its usage as a potential ^{19}F MRI tracer.[26]

Semifluorinated triblock copolymers have also received a lot of attention and have been developed in various architectures to be used in biomedical applications. Different architectures are, for example, linear, branched, dibranched, grafted, and miktoarm (mixed arm) copolymers (**Figure 1.5**). Similar to diblock copolymers, the triblock copolymers can also self-assemble in aqueous environments, resulting in water-soluble nanoparticles with specific morphologies. Unlike diblock copolymers, the order and arrangement of the blocks in the semifluorinated triblock copolymers, can affect the properties and morphologies of self-assembled nanoparticles.[27] Herein, the block sequence with a hydrophilic portion as a terminal position will be the focus. Consequently, this leads to two different orientations: **ABC** and **ACB** where **A** is a hydrophilic block, **B** is a lipophilic block, and **C** is a fluorophilic block. The self-assembly of these semifluorinated triblock copolymers in water tends to form multicompartment morphology due to dual hydrophobicity and lipophobicity of the fluorous block. The **ABC** arrangement with the fluorophilic block at the terminal forms a fluorous core, enclosed by a hydrophobic shell which is once again protected by hydrophilic corona when self-assemble in water. This formation is called a corona-shell-core morphology.[28] Similarly, **ACB** arrangement also results in the corona-shell-core structure but with a hydrophobic segment forming the inner core covered by a fluorophilic segment. However, the same semifluorinated block sequence does not result in similar self-assembled nanoparticle morphology. Interestingly, the self-assembled morphology can also be influenced by the length of each block which can lead to different compartmentalization morphologies of the nanoparticles.[28-29] The advantage of multicompartment nanoparticles is that it allows the solubilization of two distinct types of molecules: hydrophobic and highly fluorinated molecules, in two separate nanodomains inside one particle, making the simultaneous transportation of two incompatible active ingredients possible. A study from Lodge *et al*. has demonstrated a successful encapsulation of pyrene (a hydrophobic molecule) and 1-naphthyl perfluoroheptanyl ketone (a fluorinated molecule) in different compartments formed by semifluoriated miktoarm copolymers where the multicompartment morphology was confirmed by cryo-TEM.[30]

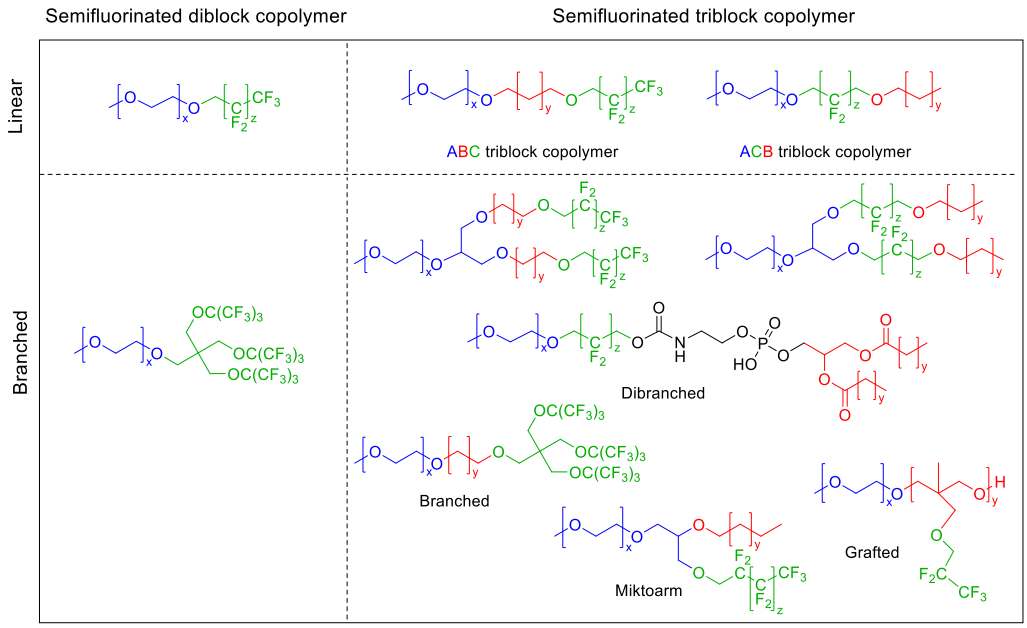

Figure 1.5 Different architectures of semifluorinated polymers synthesized in the Mecozzi lab. Within the polymer nomenclature, x, y, and z represent the repeating units for hydrophilic, lipophilic, and fluorophilic blocks, respectively.

In addition to the nanoscopic domains formed by different types of triblock copolymers, the other properties concerning drug delivery application still have not been fully explored, for example, drug encapsulation properties, drug release profiles, and nanoparticle stabilities. These effects will be further discussed in *Chapter 3*.

1.2 Nanoparticles for drug delivery: Micelles and Nanoemulsions

The concept of nanoparticles in drug delivery started more than 50 years ago by Paul Ehrlich through the idea of "Magic Bullets" which refers to a method that can specifically deliver drugs to the target.[31] Nanoparticles are the main tool for drug delivery and, according to IUPAC, are defined as particles of any shape having a size ranging from 1 – 500 nm (the extended upper limit).[32] Various types of nanoparticles have been developed for treatments and diagnostics of diseases as delivery carriers to deliver active pharmaceutical ingredients (APIs) to the target. These nanoparticles can be either organic or inorganic materials, including but not limited to micelles, nanoemulsions, liposomes, dendrimers, superparamagnetic iron oxide nanoparticles (SPIONs), gold nanoparticle, and quantum dots (QDs).[33] Based

on the design and type of materials, each type of nanoparticle offers unique characteristics which suit different delivery purposes. Herein, two different types of nanoparticles will be discussed: micelles and nanoemulsions.

1.2.1 What are micelles?

Micelles are colloidal nano-sized particles prepared from amphiphilic block copolymers. The polymers, consisting of hydrophobic and hydrophilic segments, self-assemble forming spherical aggregates, so-called polymeric micelles, with a size ranging from 5 – 100 nm (**Figure 1.6**).[34] The formation of cylindrical and worm-like micelles are also possible under specific conditions, but these aggregates do not have many applications and they will not be discussed here. Spherical micelle self-assembly allows a formation of a core-shell architecture where the aggregation of the hydrophobic segments assembles the core structure through hydrophobic interactions, leaving the hydrophilic segment to form a protective hydrophilic corona, thus, rendering the particles' water solubility.[35-36] Polymeric micelles are thermodynamically stable aggregates. The formation of polymeric micelles depends on the concentration of polymers in which at low concentration, the polymers remain as monomers. When polymer concentration increases to a certain point, those unimers start to aggregate and self-assemble to form particles. The concentration at which these unimers start to form micelles is called the critical micelle concentration (CMC). The CMC is a parameter that determines the thermodynamic stability of polymeric micelles.[34-35] Additionally, polymeric micelles can increase the solubility of poorly water-soluble drugs through the hydrophobic interaction of hydrophobic drugs with the hydrophobic micellar core. As a result, a higher therapeutic concentration can be achieved, and, at the same time, the pharmacokinetics properties of the molecules can also be improved. Polymeric micelles can be used to not only encapsulate hydrophobic molecules but also other therapeutic agents such as small interfering RNA (siRNA)[37-39] and DNA[40-41]. The encapsulation properties of micelles rely heavily on the structure of the hydrophobic segment. These structures can be tailored based on the desired payloads, allowing a specific encapsulation with high loading efficiency.

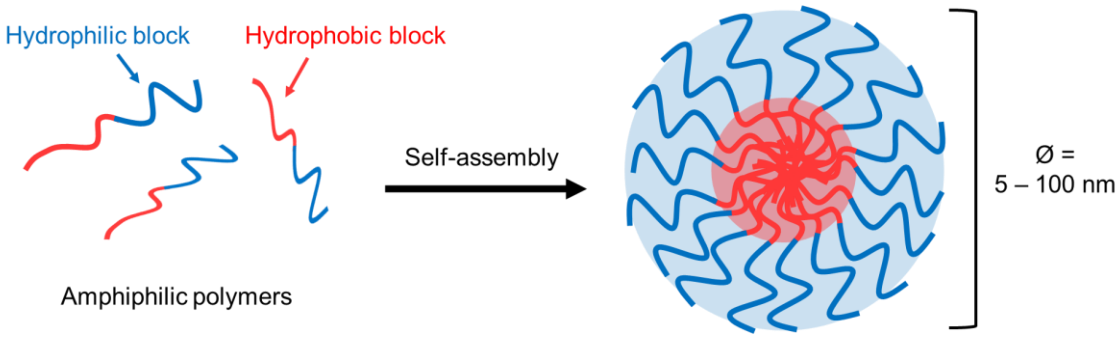

Figure 1.6 Schematic self-assembly of micelles. Amphiphilic polymers self-assemble in aqueous environment to form micelles with a hydrophobic core and a hydrophilic corona, representing a core-shell architecture.

1.2.2What are nanoemulsions?

Nanoemulsions are colloidal particles prepared from two immiscible liquids stabilized by surfactants, forming small droplets with a broad size range from 50 – 1000 nm.[42] Typically, there are two major types of nanoemulsions; i) oil in water (o/w) emulsion where oil droplets are dispersed in a water continuous phase and ii) water in oil (w/o) emulsion where water droplets are dispersed in an oil continuous phase. In pharmaceutical industries, nanoemulsions can be found in various pharmaceutical dosage forms, such as gel, cream, and liquid, to deliver APIs through different routes of administration, such as oral, topical, nasal and intravenous (I.V.).[43] For intravenous applications, the focus of this work, o/w nanoemulsion are preferable due to its water-based formulation. The average droplet size of nanoemulsions should be in sub-500 nm range[42-43] according to USP <729> which states that the size cutoff for intravenous delivery of any lipid-based nanoparticles is 500 nm in order to avoid pulmonary embolism.[44] Preparation of o/w nanoemulsions, unlike micelles, is usually non-spontaneous and energy is required to form these particles. The energy input is needed to break apart the oil phase into small droplets which are then stabilized by surfactants, thus, dispersing those droplets in the aqueous phase (**Figure 1.7**). As a result, the nanoemulsions can be kinetically stable rather than thermodynamically stable.[45] The large oil droplet core of nanoemulsions allows for the solubilization of large quantity of hydrophobic molecules which is an advantage of nanoemulsions over other types of nanoparticles. In addition, the oil phase can also act as the

active ingredient itself, for example, the use of fluorinated anesthetic oil phase, e.g. sevoflurane or perfluorooctyl bromide (PFOB), for preparation of fluorinated anesthetic nanoemulsions.[46-47]

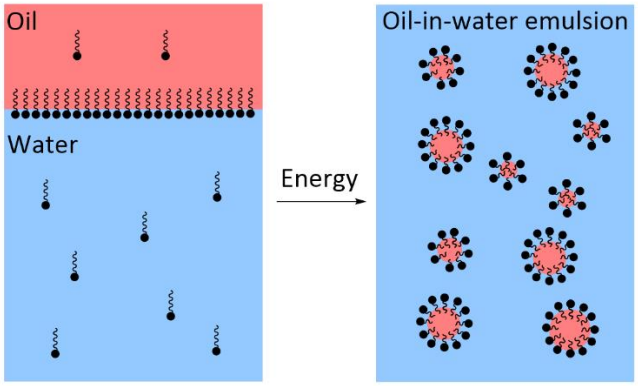

Figure 1.7 Diagram of oil in water (o/w) nanoemulsion formation. The system consists of oil phase (red), water phase (blue) and polymers/surfactants. The high energy is exerted into the system, resulting in the formation of nanoemulsions.

1.2.3 In vivo stability of nanoparticles

In our body, there are several barriers that limit the effective delivery of nanoparticles to the targeted area, for example, a poor stability of nanoparticles in biological conditions, a difficult transportation of nanoparticles through cell membranes, and a release of drug from the nanoparticles (**Figure 1.8**).[48-49] The stability of nanoparticles is one of the important factors that determines the fate of nanoparticles *in vivo*. Unlike nanoemulsions, whose kinetic stability can make them highly stable *in vivo*, micelles are susceptible to dissociate upon dilution. As such, the following sections elaborate on the *in vivo* stability of micelle and how to overcome their tendency to dissociate.

As noted, the thermodynamic stability of micelles is typically determined from the CMC. Following an I.V. injection, micelles undergo an extreme dilution in the bloodstream, the body's first line of defense. This can result in a dilution of the polymer solution below its CMC, leading to a dissociation of micelles. In addition, due to the dynamic properties of micelles, the binding of blood components to the micelles' unimers can result in a disruption of the micelle structure, allowing an early release of the hydrophobic payload from the micelles. Savić *et al*.[50] reported a rapid dissociation of the micelles prepared

from poly(ethylene oxide)-*b*-poly(caprolactone) (PEG-*b*-PCL), a hydrophilic-hydrocarbon diblock copolymer, from the blood circulation and a fast elimination from the body after the I.V. injection in mice. Burt *et al*.[51] and Chen *et al*.[52] also reported the instability of poly(ethylene glycol)-poly(D,L-lactic acid) (PEG-PDLLA) micelles. Burt *et al*. observed a rapid dissociation of the paclitaxel from the micelles within minutes after the I.V. injection in rats. The instability of the PEG-PDLLA diblock copolymer was also reported as the cleavage of the polymer into two components was observed during the systemic circulation.[51] Chen *et al*. used the FRET technique to monitor the stability of the PEG-PDLLA micelles. Significant reduction of FRET ratio was observed within 15 minutes after an I.V. injection, suggesting the rapid released of the FRET dyes. The authors further demonstrated that the destabilization of micelles which led to a rapid release of the hydrophobic cargo, was mainly caused by α- and β-globulins rather than γ-globulin, albumin, or red blood cells.

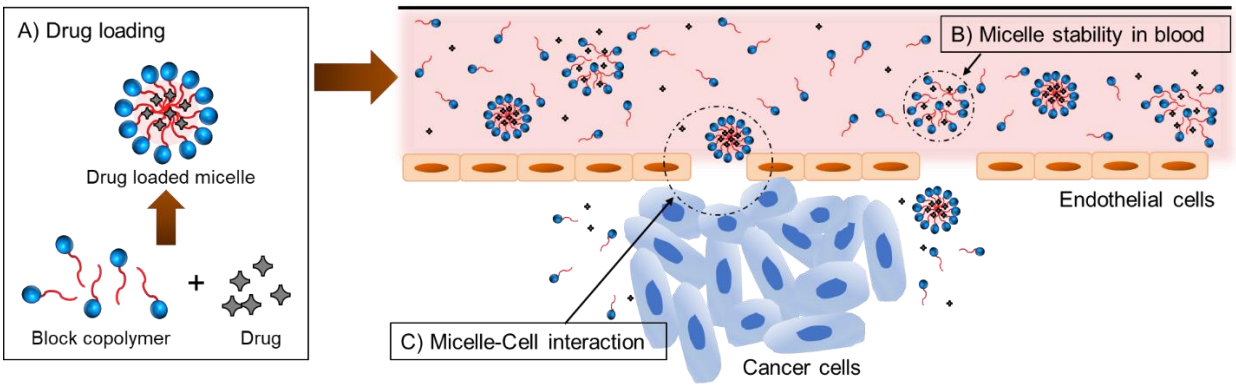

Figure 1.8 Barriers in developing an effective micelle formulation for drug delivery. A) Low drug loading, B) Dissociation of micelle in bloodstream after intravenous injection, and C) Cell membrane barrier for extravasation of micelles.

Several strategies have been developed to overcome the micelle instability. Improving physicochemical properties of the polymers is one of the strategies that has been employed to enhance physical stability of micelles. For example, the introduction of cross-linking functionalities to the polymers leads to the formation of cross-linked micelles. The cross-linking improves the micelle's core stability by reducing its dynamic environment which results in a prolonged blood circulation time.[53-54] The introduction

of the fluorocarbon block to the polymers is another strategy for improving physicochemical properties of polymers. The use of semifluorinated triblock copolymers, consisting of hydrophilic, fluorophilic, and lipophilic segments, provides a higher stability to the corresponding micelles. The dual hydrophobicity and lipophobicity of the fluorocarbons lead to the formation of an energetically favorable fluorous phase. This results in a less dynamic environment, thus improving micelle stability. Jee *et al*.[55] reported the improved thermodynamic stability of fluorocarbon-containing micelles as demonstrated by a lower CMC compared to the micelles without fluorocarbon. In addition, the fluorocarbon-containing micelles showed a high *in vitro* stability in the presence of human serum as well as a sustained release of hydrophobic molecules. Decato *et al*.[56] also reported the enhanced thermodynamic and kinetic stability of the micelles prepared from the semifluorinated triblock copolymer both *in vitro* and *in vivo*. The high stability of semifluorinated micelles resulted in a prolonged blood circulation time *in vivo*. These results suggested the use of fluorocarbon to enhanced thermodynamic and kinetic stability of the self-assembling aggregates.

1.3 Tumor targeting: Passive vs Active

1.3.1 Passive targeting

The selective tumor accumulation of nanoparticles was first discovered in 1986 by Y. Matsumura and H. Maeda where they observed a progressive accumulation and prolonged retention of polymer conjugated neocarzinostatin complex (smancs) in the tumor tissue.[57] These two phenomena were attributed to the fenestration of the tumor endothelial cells and the poor lymphatic drainage of the tumor tissue and were called the enhanced permeability and retention (EPR) effect (**Figure 1.9a**). Tumor angiogenesis in fast-growing solid tumors leads to the formation of leaky vasculature with a gap size ranging from 100 nm to several μm, depending on the location and type of tumors.[58] It should be noted that the gap size between two normal endothelial cells is 2 nm.[58-59] The large gap size of the tumor endothelial cells allows the extravasation of nanoparticles from the bloodstream into the tumor which attributes to the enhanced accumulation. In addition, the lack of lymphatic drainage at the tumor site together with a larger size of

nanoparticles prevents the particles from being excreted ascribing to the retention of nanoparticles inside the tumor.[60-61]

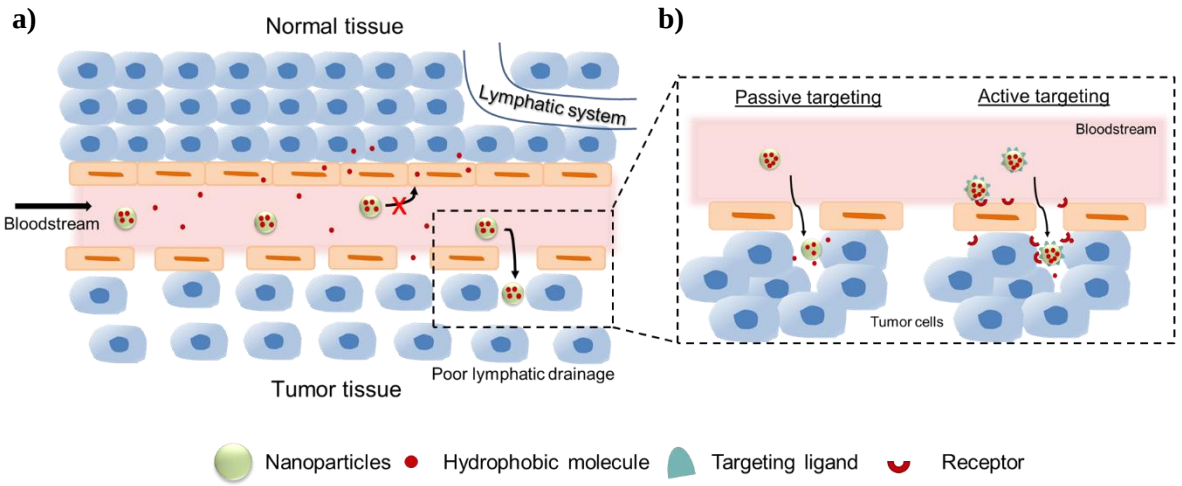

Figure 1.9 Illustration of tumor targeting. a) Enhanced permeability and retention (EPR) effect: The leaky vasculature formation from tumor angiogenesis allows the extravasation of nanoparticles from the blood vessel to the tumor tissue. With poor lymphatic drainage of the tumor, the nanoparticles can be retained at the tumor site and b) comparison of passive and active targeting.

Even though, this EPR effect, a.k.a. passive targeting, allows a preferential accumulation of nanoparticles at tumor tissues, there are several limitations that hamper its high therapeutic efficacy. It should be noted that tumors are heterogeneous in nature. The degree of tumor angiogenesis can directly affect the permeability of tumor vasculatures which determines the extravasation ability of nanoparticles. The heterogeneity of a tumor depends on various factors, for example, tumor size and location, type of tumors, and tumor necrosis.[58, 60-62] Additionally, the rate of extravasation of nanoparticles also relies on the particle's plasma concentration. The longer the half-life of nanoparticles, the more the particles can accumulate at the tumor.[61, 63] Another factor that prevents nanoparticles from accumulating at the tumor is the high interstitial fluid pressure (IFP). The tumor's high IFP not only prohibits the flow of fluid from the capillaries into the surrounding tissue but, once the nanoparticles accumulate in the tumor, it also impedes the nanoparticles' distribution.[64] Therefore, a new strategy that can improve nanoparticles' affinity to the

tumor should be employed to increase the accumulation and improve the nanoparticle's fate inside the tumor.

1.3.2 Active targeting

Active targeting or ligand-mediated targeting is a targeting method that utilizes various ligands having specific affinities to the receptors presented on the targeted cell surface (**Figure 1.9b**).[60-61] In cancer therapy, the targeting ligands are designed to bind the receptors that are scarcely presented on normal cells but are overexpressed in tumor cells. There are several targetable receptors overexpressed on tumor endothelial cells and tumor cells. For example, the $\alpha_v\beta_3$ integrins are receptors that are responsible for tumor angiogenesis and are overexpressed in tumor endothelial cells and some tumor cells.[65-66] This integrin receptor can be recognized by the arginine-glycine-aspartic acid (RGD) sequence which was first discovered by E. Ruoslahti in the early 1970s and became a golden sequence for tumor active targeting.[67] The binding of RGD functionalized nanoparticles to $\alpha_v\beta_3$ integrins allows for the internalization of the nanoparticles through receptor-mediated endocytosis, thus, improving the nanoparticle accumulation at the tumor.[61, 68] The vascular endothelial growth factor receptors (VEGFR-1 and VEGFR-2) are another two receptors that also play an important role in tumor angiogenesis, especially VEGFR-2 in which its signal cascades involve cell survival, cell migration and differentiation, and vessel permeability and dilation, displaying the ideal target for tumor treatment.[69] The upregulation of these receptors in the tumor endothelial cells allows the active targeting of nanoparticles by, for example, the anti-VEGFR2 monoclonal antibodies[70] and the human recombinant $VEGF_{121}$ molecule.[71] This binding improves the localization and internalization of nanoparticles and also inhibits its signaling cascades, thus, providing therapeutic effects.[72]

Varieties of ligand have been used for tumor targeting. These ligands differ in size and charges, ranging from small molecule to monoclonal antibodies and from highly negative to highly positive charges, respectively. The functionalization of these ligands to nanoparticles leads to different physicochemical properties of the nanoparticle systems and therefore affects the pharmacokinetic properties and internalization ability of nanoparticles (**Figure 1.10**).[60] Typically, ligands can be covalently or non-

covalently attached to the nanoparticles and the number of ligands on the nanoparticles' surfaces can be controlled during the formulation process. The quantity of ligands conjugated on the nanoparticle's surface or the ligand density has to be carefully monitored based on the types and functions of the ligands to effectively exploit their properties and thus maximizing the internalization. In addition, sizes, charges, and orientations of the ligands and nanoparticles also determine the particles' fate after intravenous injection, i.e. circulation half-life and biodistribution. Therefore, these factors must be thoroughly considered when designing functionalized nanoparticles.[60-61, 72]

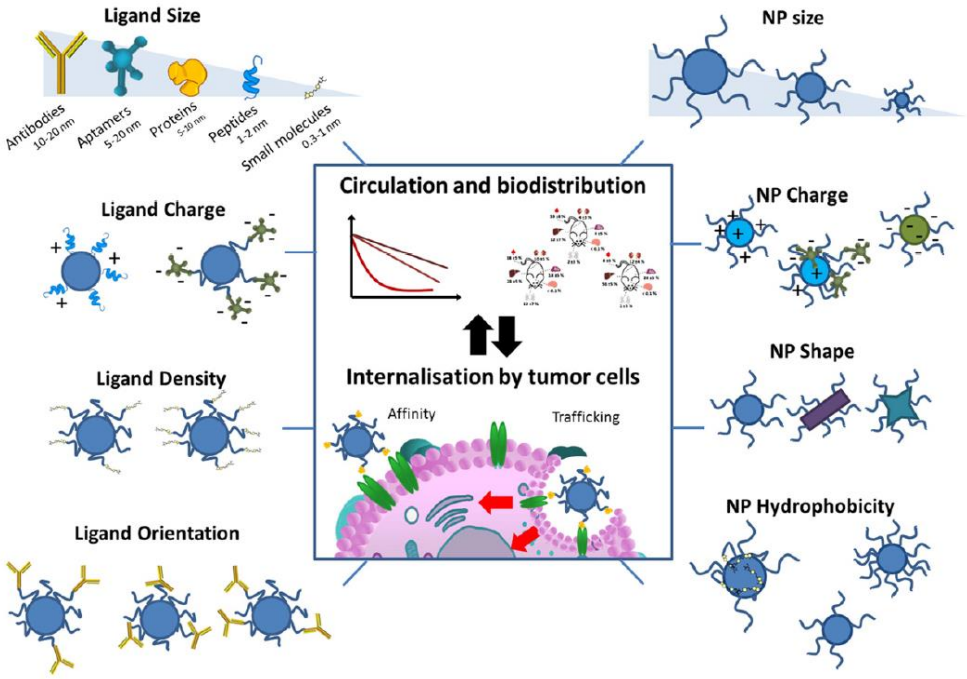

Figure 1.10 Architectures/properties of ligands and nanoparticles and their effects on tumor targetability. Figure from Bertrand *et al.*[60]

1.4 Magnetic resonance imaging (MRI) and the use of fluorinated materials for MRI application

1.4.1 MRI and contrast agents (CAs)

Magnetic resonance imaging or MRI is a non-invasive imaging technique that can provide three-dimensional and high-resolution images. MRI uses strong external magnetic fields, magnetic field gradients, and radio frequency (RF) waves, instead of radioactive materials or radiations, to affect the precession of protons in anatomical water and fats. The detection of different RF signal emissions followed by data

conversion and image processing leads to a generation of MR images. Different intrinsic relaxation times and local concentrations of proton nuclei in water and lipid provide the contrast in the MR images and, therefore, the information on the anatomical structure of tissues and organs. Contrasts in MR images are mainly governed by two parameters: longitudinal (T_1) relaxation and transverse (T_2) relaxation. Longitudinal or T_1 relaxation is a process where the net magnetization restores to its original maximum value (**Figure 1.11a**). T_1 relaxation time refers to the time required to gain the signal sensitivity which can clinically be translated as the time between each scan cycle. In the clinic, since total MRI scanning time is limited, minimum T_1 time is desirable to achieve a high image sensitivity which can be recognized as bright spots/regions on the images. Transverse or T_2 relaxation, on the other hand, is a process where the transverse component of the signal decays (**Figure 1.11b**). T_2 relaxation time is, therefore, translated as the time at which the signal decays. The shorter T_2 time indicates that the signal decays faster which results in dark spots/regions on the images. Therefore, in order to obtain high contrast images, T_1 and T_2 relaxations should be optimized so that the desired information can be gathered.

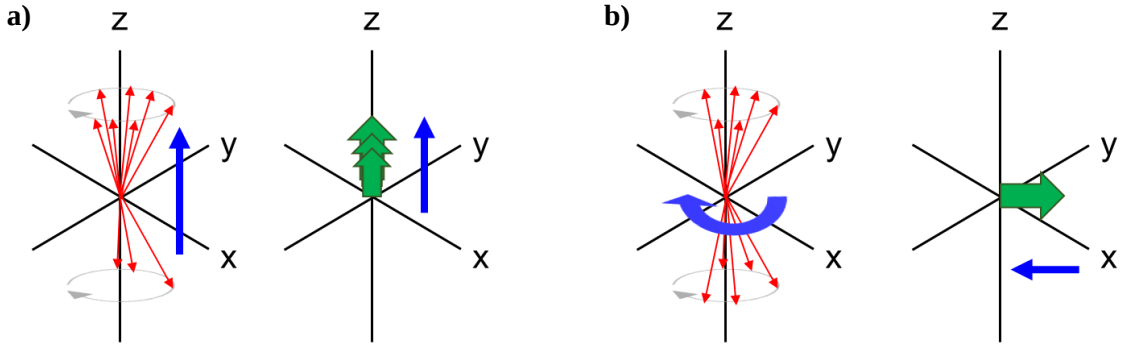

Figure 1.11 Schematic illustration of a) Longitudinal (T_1) and b) Transverse (T_2) relaxations.

Even though contrast images can be achieved from normal MRI scans due to different intrinsic relaxation times of protons in the body, there is still a need to develop contrast agents (CAs) to better differentiate each region which could provide higher accuracy for image interpretation. CAs, depending on their properties, can be used to lower T_1 and T_2 relaxation times, so-called T_1 or T_2 agents, resulting in brighter or darker spots/regions in the images. Commonly used CAs are paramagnetic metal ions, such as

the lanthanide metal, gadolinium (Gd^{3+}), and the transition metal, manganese (Mn^{2+}), which are T_1 agents and superparamagnetic iron oxide nanoparticles (SPIONs), a T_2 agent.

Paramagnetic metal ions possess unpaired electrons (7 unpaired electrons for Gd^{3+} and 5 unpaired electrons for Mn^{2+}), resulting in paramagnetic properties of these ions which can generate local fluctuation of magnetic fields.[73-74] The effect of paramagnetic metal ions leads to the improved signal intensity of neighboring water protons by shortening T_1 relaxation time which results in bright images. The relaxation enhancement is mainly contributed by a direct binding of water protons to metal ions (inner-sphere mechanism, **Figure 1.12a**) rather than the bulk water protons (outer-sphere mechanism). The important parameters governing the relaxation are the rotational correlation time (τ_r) of the contrast agent, the exchange correlation time (τ_m) of water molecules with the surrounding, and the diffusion correlation time (τ_d).[74-76] Despite decreasing T_1 relaxation, the fluctuated magnetic fields caused by paramagnetic metal ions also affect the transverse or T_2 relaxation. This can be observed by a line broadening effect which results in a reduction of T_2. This T_2 effect is highly concentration-dependent which is of limited use due to the toxicity of metal ions.[73-74] Therefore, used at low concentration, these CAs focus on shortening T_1 and they are normally called T_1 or positive contrast agents. Due to the toxicity of these metal ions, they are normally formulated as metal ion-chelates, e.g., Gd-DTPA (Magnevist®) and Mn-DPDP (Teslascan™) or metal ion-containing nanoparticles to reduce toxicity and improve pharmacokinetics properties of the CAs.[77] The most commonly used paramagnetic metal ion is Gd^{3+} of which several Gd(III)-based contrast agents (GBCAs) have been approved by FDA for clinical use.

Superparamagnetic iron oxide nanoparticles (SPIONs) are particles containing a magnetite (Fe_3O_4) or maghemite (γ-Fe_2O_3) core with a diameter less than 50 nm.[74, 78] The cluster of iron ions in the nanoparticle generates a strong local magnetic moment in the presence of an external magnetic field from an MRI scanner, leading to a rapid dephasing of surrounding protons and, therefore, decreasing T_2 relaxation time.[74, 76-77, 79] This phenomenon is assumed to be caused by a bulk susceptibility of protons in the outer-sphere

effect (**Figure 1.12b**).[74-75, 80] This T_2 shortening effect accelerates the signal decay, resulting in dark spots on MR images. These CAs are, therefore, called T_2 or negative contrast agents.

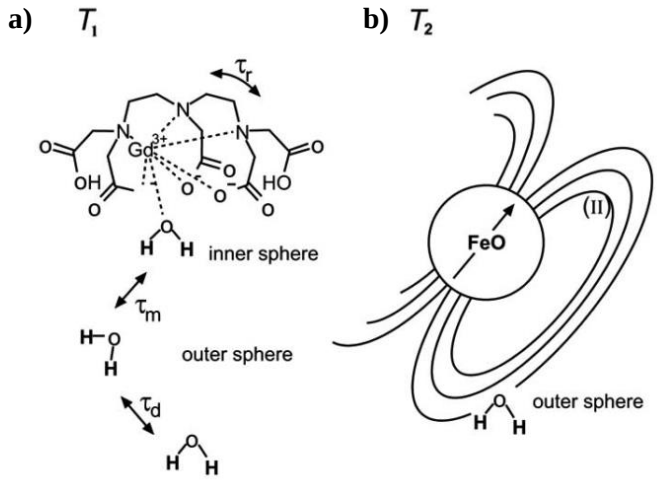

Figure 1.12 Schematic Illustration of MRI contrast agents. a) T_1 contrast agent: Gd-DTPA. The effect involves the inner-sphere mechanism where water molecule directly binds to Gd^{3+}. The relaxation depends upon the exchange correlation time (τ_m), rotational correlation time (τ_r), and diffusion correlation time (τ_d). b) T_2 contrast agent: superparamagnetic iron oxide nanoparticles (SPIONs). Bulk susceptibility from the outer-sphere effect, a dynamic and diffusion of nearby water molecules, induces dephasing and causes rapid loss of transverse magnetization. Figure from Strijkers *et al*.[74]

Even though the use of CAs in MRI application provides a higher accuracy and less ambiguous image interpretation due to their contrast enhancement properties, the presence of high background noises attributable to the endogenous protons within the human body is still a major hurdle for the acquisition of clear images. In addition, the commonly used GBCAs have been shown to cause some toxicities such as nephrogenic systemic fibrosis (NSF) in patients with impaired renal function.[81-82] The U.S. food and drug administration (FDA) has also raised a concern for the retention of GBCAs in the body. Gd^{3+} deposition has been found in the brain and other tissues including skin, liver, and bone even in healthy patients with normal renal function.[81-84] These patients have experienced acute and chronic symptoms after receiving GBCAs which were coined to gadolinium deposition disease (GDD).[81, 85] Although no direct pathophysiologic mechanism has been proven, U.S. FDA has modified and approved a new Patient Medication Guides for all GBCAs to raise patients' awareness prior to administration[86] while the European

Medicines Agency restricted the use of some linear GBCAs to prevent any risks associated with the gadolinium deposition.[87]

1.4.2 ^{19}F MRI

An alternative method, bypassing the use of CAs and avoiding high background signals, is to utilize multinuclear MRI such as ^{13}C, ^{23}Na, ^{31}P, ^{35}Cl, and ^{19}F.[88-89] The identification of the second nuclei species by MRI allows a presentation of those nuclei as "hot spot" or "second color", which allows a presentation of additional information apart from an anatomical grayscale ^{1}H images.[17, 88, 90] Among those nuclei, ^{19}F is the most prominent candidate due to its similar imaging properties to ^{1}H (**Table 1.1**).[91] ^{19}F has a 100% natural abundance and 83% sensitivity of that of proton. A low physiological abundance of ^{19}F in the body provides another advantage over protons. In the human body, the main sources of fluorine are in bones and teeth. The signals from these immobilized fluorine atoms are undetectable by MRI due to the fast signal decay (very short T_2 relaxation time), thus, resulting in negligible background noises. In addition, due to its similar Larmor frequency, ^{19}F MRI can be used with clinical scanners by the addition of a tunable radiofrequency (RF) coil for ^{19}F frequency, suggesting its clinical translatability.[17-18, 92]

Table 1.1 Properties of ^{1}H and ^{19}F.

Isotope	Spin	Natural abundance Isotope (%)	Gyromagnetic ratio γ [10^7·rad·s^{-1}·T^{-1}]	NMR frequency at 9.4 Tesla [MHz]	Physiological abundance
^{1}H	½	99.98	26.75	400.13	100.0000
^{19}F	½	100.00	25.16	376.50	0.0001

With low endogenous ^{19}F in the human body (< 10^{-6} M),[90, 93] the sensitivity of ^{19}F MRI solely relies on exogenous fluorine sources where the signal intensity is concentration-dependent.[94-95] These fluorine sources are introduced as fluorinated probes and should be designed to i) provide high fluorine content with chemically equivalent fluorine atoms to achieve immense signal intensity and ii) be water-soluble to enable the *in vivo* applications. Herein, the development of different types of fluorinated probes for MRI

application, including the use of various delivery carriers and the synthesis of new fluorinated compounds, will be discussed.

1.4.3 Fluorinated probes and their applications

1.4.3.1 Fluorinated nanoemulsions

The use of fluorinated nanoemulsions in biomedical applications as oxygen-carrying blood substitutes started in the 1960s where the perfluorocarbons (PFCs) were emulsified with lipids and surfactants to enable parenteral administration.[96] PFCs are recognized as a good source of fluorine for ^{19}F MRI, especially in the liquid form where it has a minimal toxicity and higher fluorine concentration than gaseous PFCs.[97-98] The dual hydrophobicity and lipophobicity properties of PFCs prevent a direct injection of a large quantity of liquid PFCs into the body. Therefore, to introduce PFCs into the body, a drug delivery system is needed. Nanoemulsions are one of the delivery carriers used for delivering liquid payloads. Formulating liquid PFCs into nanoemulsions is, therefore, a crucial key that allows an introduction of a high concentration of exogenous fluorine into living systems. Several commercially available liquid PFCs, such as perfluorooctyl bromide (PFOB), perfluorodecalin (PFD), perfluoro-15-crown-5-ether (PFCE), and perfluoropolyether (PFPE) (**Figure 1.13**), have been used in the development of diagnostic fluorinated nanoemulsions. The early development of fluorinated nanoemulsions as ^{19}F MRI tracers focused on PFD and PFOB because of their application as blood substitutes and their nontoxic properties. These nanoemulsions are commonly prepared from commercially available phospholipids and/or non-ionic surfactants, depending on the properties of the PFCs. PFD is a cyclic perfluorocarbon that was first commercialized as PFD emulsions known as Fluosol® which was used as an oxygen-carrying blood substitute. This PFD emulsion was prepared from a mixture of egg lecithin (a phospholipid) and Pluronic® F68 (a non-ionic surfactant poly(ethylene oxide)-poly(propylene oxide)-poly(ethylene oxide) triblock copolymer).[96, 99] Another nanoemulsion formulation of PFD was reported by Jacoby *et al*.[100] where PFD was formulated with egg lecithin. This formulation was used as a fluorinated probe for diagnostic application through ^{19}F MRI. However, the *in vivo* study in a mouse inflammation model revealed a weak

^{19}F MR signal after intravenous injection of the PFD nanoemulsions which was attributed to the fast excretion of PFD. This makes PFD a poor candidate as a fluorinated probe for ^{19}F MRI application.

In the case of PFOB (also known as Perflubron), this linear PFC possesses an extremely high hydrophobicity, compared to PFD, due to an addition of Br at the end of the structure.[13, 101] Pure non-ionic surfactants, i.e., poloxamers (Pluronic®), were unable to stabilize PFOB droplets, as evidenced by a slow droplet growth overtime.[102] PFOB nanoemulsions are, therefore, normally stabilized by phospholipids such as egg or soy lecithin rather than the non-ionic surfactants.[100, 103-106] Lim *et al*.[105] reported a preparation of PFOB nanoemulsions stabilized by egg lecithin, cholesterol, and PEG-DSPE through a two-step high energy input method; a homogenization followed by a microfluidization at high pressure. Further functionalization of the PFOB nanoemulsion with IRDye800 enabled the nanoemulsion's dual imaging modality. The authors also demonstrated the successful labelling of dendritic cells (DCs) and the *in vivo* cell tracking using subcutaneously injected labelled DCs with IRDye800-coated PFOB nanoemulsions. The Flögel group in Germany fabricated the PFOB nanoemulsions using egg lecithin with an addition of a semifluorinated alkane ($C_6F_{13}C_{10}H_{21}$, a.k.a. F6H10) for stabilizing purposes.[100, 106] The prepared nanoemulsions were administered intravenously *in vivo* and the results revealed a high signal-to-noise ratio (SNR) of ^{19}F in the inflamed region.[100] They further demonstrated that the PFOB nanoemulsions were mainly uptaken by monocytes through the actin-dependent phagocytosis pathway and the migration of these monocytes to the inflamed region led to the site-specific ^{19}F MR imaging.[100, 106]

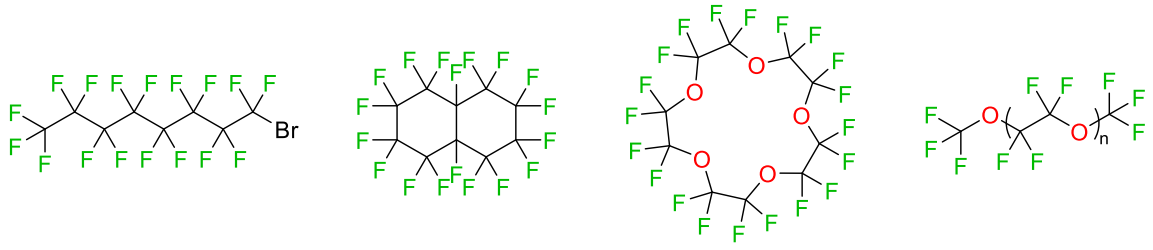

Figure 1.13 Example of commercially available liquid PFCs for ^{19}F MRI applications.

Another type of liquid PFCs used for fluorinated nanoemulsion preparation are perfluoropolyethers. Perfluoropolyethers have gained their popularity in nanoemulsion preparation due to its lower hydrophobicity and fluorophilicity compared to pure PFCs which can impede the creaming or phase separation of fluorocarbon in the nanoemulsions, allowing higher formulation stability.[107-108] PFPE and PFCE are the two perfluoropolyethers in a linear and a macrocyclic form (**Figure 1.13**), respectively, that have been extensively studied as ^{19}F MRI agents because they provide high density fluorine atoms with equivalent chemical shifts from the repeating -(CF_2CF_2O)- unit which results in high signal intensity. In 2008, Janjic *et al*. reported a preparation of fluorescent PFPE nanoemulsions as dual fluorescent and ^{19}F MRI probes for cell tracking applications using Pluronic® F68. The nanoemulsions prepared by microfluidization method had a size of 160 – 190 nm with a polydispersity index (PDI) < 0.15 and demonstrated long-term stability (at least 5 months) at different storage temperature (4, 25 and 37 °C). The uptake of nanoemulsions was confirmed by both phagocytic (e.g. DCs) and non-phagocytic (e.g. T cells) cells *in vitro*. The *in vivo* intraperitoneal (I.P.) injection of labeled naïve T cells revealed the observed ^{19}F signal (at 11.4 T) in lymph nodes with an undetectable signal in other tissues and circulation.[94] In 2012, a PFPE theranostic platform, a combination of therapeutic and diagnostic properties, was developed by O'Hanlon *et al*.[109] The authors reported a modification of PFPE oil with tyramine as a hydrophobic moiety to induce self-aggregation of fluorocarbon-hydrocarbon which was used for a preparation of triphasic (PFC/hydrocarbon/aqueous) PFPE nanoemulsions with hydrophobic oil solubilizing celecoxib (a hydrophobic anti-inflammatory drug) and NIR815 (a hydrophobic near-infrared (NIR) fluorescent dye). Similar PFPE triphasic formulations were prepared from the same group with a higher concentration of PFPE of up to 18.75% wt/v.[110-111] The triphasic PFPE nanoemulsions stabilized by Cremophor EL® and Pluronic® P105 demonstrated high stability under storage (4 °C) and stress conditions (pH 5) for at least 100 and 5 days, respectively. *In vivo* studies in mouse inflammation model demonstrated the accumulation of theranostic PFPE nanoemulsion at the inflammation site through fluorescence imaging and ^{19}F MRI after a tail vain administration.[110] Furthermore, functionalization of PFPE nanoemulsions with cell-penetrating

peptides (CPPs) led to an improved cellular uptake in weakly phagocytic cells, enhancing ^{19}F MRI sensitivity as demonstrated by Hingorani *et al*.[112] In addition to a new development of PFPE probes, there are commercially available PFPE nanoemulsion products; Cell Sense and V-Sense (Celsense, Inc., Pittsburgh, PA) for ^{19}F MRI cell tracking application for pre-clinical and clinical uses, suggesting that there is an increasing trend of ^{19}F MRI usage.

Another perfluoropolyether that has received a lot of attention due to its 20 chemically equivalent fluorine atoms is a macrocyclic PFCE (**Figure 1.13**). Several nanoemulsion platforms have been developed for PFCE delivery. In 2008, Flögel *et al*.[113] reported a dual fluorescent and PFCE (10% wt/wt) nanoemulsion probe prepared from egg lecithin through high pressure (70 Mpa) homogenization with an average size of 130 nm. High ^{19}F MR signal (at 9.4 T) was observed at the inflammation site after an I.V. injection, suggesting the use of fluorinated probe for monitoring the inflammation process. Pluronic®, a non-ionic surfactant, also serves as a good PFCE stabilizer. The average diameter of around 160 nm of PFCE nanoemulsions prepared with Pluronic® F68 using sonication methods were reported by Wang *et al*.[114] and Shin *et al*.[115] 60% wt/v PFCE loading was achieved with this preparation and the nanoemulsion demonstrated stability in a 4 °C storage condition up to 3 weeks.[115] In addition to commercially available phospholipids and non-ionic surfactants, specially designed and synthesized polymers also provide an unprecedented encapsulation and stability of PFCE. Barres *et al*.[95] reported the preparation of PFCE nanoemulsion with 35% v/v or 62.3% wt/v PFCE loading using a novel semifluorinated polymer, M2F8H18 (**Figure 1.14a**), as a non-ionic surfactant. The average diameter of PFCE nanoemulsions prepared by a two-step high energy input method was 210 ± 38 nm with long-term stability in a 4 °C storage condition for at least 100 days. *In vivo* ^{19}F MR images revealed high signal intensities (at 4.7 T) in the tumor after an I.V. injection which resulted from a passive tumor targeting of the nanoemulsion through the EPR effect, suggesting the tumor diagnostic application of the formulation.

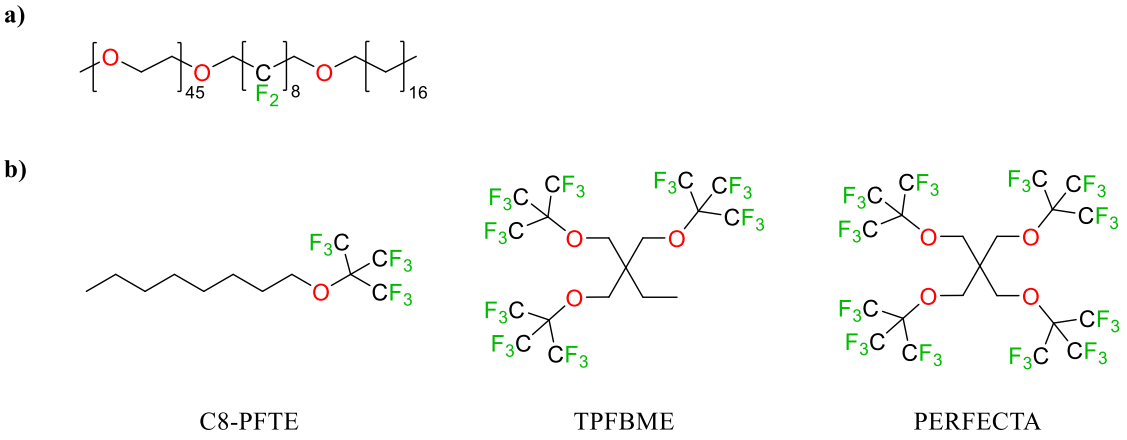

Figure 1.14 Structure of synthesized fluorinated molecules. a) Structure of synthesized semifluorinated polymer M2F8H18 used for stabilizing PFCE nanoemulsions and b) Example of synthesized liquid PFCs as ^{19}F agents.

Furthermore, the synthesized fluorinated molecules especially with the introduction of the trifluoromethyl group (CF_3) which provides chemically equivalent fluorine signals have also been utilized for the preparation of fluorinated nanoemulsions. Patel *et al.*[116] reported a synthesis of 1-((1,1,1,3,3,3-hexafluoro-2-(trifluoromethyl)propan-2-yl)oxy)octane (C8-PFTE, **Figure 1.14b)**, a hydrocarbon molecule modified with perfluoro-*tert*-butyl ether. C8-PFTE nanoemulsions demonstrated high stability in all storage temperatures (4, 25, and 37 °C) and comparable cell labeling efficiency to PFPE nanoemulsions. Having a lower density than PFPE and PFCE, C8-PFTE provides an advantage for cell labeling applications as the low density facilitated the washing process after the labeling. Another molecule exploiting the advantage of perfluoro-*tert*-butyl group is 1,1,1-tris(perfluoro-*tert*-butoxymethyl)ethane or TPFBME (**Figure 1.14b**) which contains 27 equivalent fluorine atoms. Nanoemulsions formulated with TPFBME in the presence of lecithin and Pluronic® F68 were developed by Peng *et al.*[117] Incorporation of the paramagnetic metal ion, Fe^{3+}, was also reported by the same authors where Fe^{3+} was chelated with the same fluorinated TPFBME structure. The resulting nanoemulsion demonstrated an enhanced ^{19}F signal intensity *in vivo*. PERFECTA (**Figure 1.14b**), a superfluorinated molecular probe, was introduced in 2014 by Tirotta *et al.*[118] PERFECTA, containing 36 equivalent fluorine atoms, was formulated with egg lecithin and safflower oil as nanoemulsions to achieve the probe concentration as high as 74.4 mM with an average diameter in Milli-

Q water of 214 nm. A high cellular compatibility and efficient cell labelling with intense and persistent signal were achieved with PERFECTA nanoemulsions. The *in vivo* ^{19}F MR imaging of subcutaneously injected labelled cells revealed detectable ^{19}F signal 48 h post-injection.

These fluorinated nanoemulsion formulations enable the *in vivo* ^{19}F MR imaging applications because of the delivery of a large quantity of exogenous PFC into the body. It should be noted that due to the size of the fluorinated nanoemulsions, they were mainly captured by the reticuloendothelial systems (RES).[94-95, 100, 106, 113] The uptake of the nanoemulsion is independent of PFC types but depends on the physicochemical properties of the emulsions such as size and surface charges. Various studies have proven that most biocompatible liquid PFCs are highly stable, non-toxic, and are not metabolized in the body.[90, 93, 100, 119] In fact, the captured PFCs by RES are released back to the circulation through blood lipids, such as lipoproteins, and subsequently eliminated through exhalation. The PFCs reintroduction to the bloodstream depends on the physicochemical properties of PFCs, e.g. lipophobicity and molecular weight, which determine how well PFC molecules can diffuse back across the cell membrane, be taken up by lipids and eventually be excreted through the lung alveoli.[97, 99-100, 120] The biological half-lives of PFCs, which have been reported to rage from 3 – 250 days depending on the PFCs and the administered concentrations, also play an important role for the probe selection.[93, 99-100]

1.4.3.2 Fluorinated dendrimers

Dendrimers are spherical molecules with a tree-like nanostructure that can be specifically designed to contain a tremendous amount of chemically equivalent fluorine atoms, providing advantages for ^{19}F MRI applications. In 2009, Criscione *et al*.[121] reported a preparation of fluorinated dendrimers through a terminal branch functionalization of poly(amidoamine) starburst dendrimers generation 3 (PAMAM(G3)) with heptafluorobutyric acid anhydride (**Figure 1.15a**). This fluorination led to self-assembled micron-sized spherical particulates as a result of the fluorophobic effect. Another fluorinated dendrimer is based on a bispherical fluorocarbon molecule developed by the Yu research group. This bispherical molecule, so-called ^{19}FIT-27, contains F- and H-dendrons (**Figure 1.15c**) where the F-dendron has 27 chemically

equivalent fluorine atoms which was designed to serve as a fluorine source for MR imaging, while the H-dendron was designed to provide water-solubility. ^{19}FIT-27 demonstrated a single sharp ^{19}F signal *in vitro* and *in vivo* with a high water-solubility. *In vivo* ^{19}F MR images revealed that, unlike fluorinated nanoemulsions, no ^{19}F signal was observed in the liver nor the spleen after 2 h but a strong signal was detected in the bladder, suggesting a rapid excretion of ^{19}FIT-27 through the kidneys.[122-123] In 2015, Yu *et al*.[124] developed a proof-of-concept fluorinated dendrimer (**Figure 1.15b**) consisting of 540 pseudosymmetrical fluorine atoms that provide one strong ^{19}F signal. *In vitro* MR phantom images confirmed a clear signal even at a low dendrimer concentration. However, further development is still needed to improve the water-solubility of this dendrimer. Later in 2016, self-assembled fluorinated "Janus" dendrimers (**Figure 1.15d**) were developed by Xiao *et al*.[125] The Janus dendrimers consist of a fluorinated dendron and a hydrophilic part which can self-assemble to form onion-like nanoscale vesicular dendrimersomes in which the thickness of the bilayer was similar to a biological membrane. In addition, the design of the particle enables both fluorescence and ^{19}F MRI imaging applications which can be used as an important tool for synthetic biology. In 2017, Liu *et al*.[126] reported the synthesis of a fluorinated amphiphile containing four trifluoromethyl groups as a fluorine source for ^{19}F MRI. Different hydrophilic structures in the fluorinated amphiphiles (**Figure 1.15e**) led to different sizes of self-assembled dendrimers and distinctive interactions with small molecule payloads which can be used for monitoring self-assembly and the drug loading process through ^{19}F MRI. Recently, the same group developed a fluorinated dendrimer with 108 symmetrical ^{19}F and used it as an "add-on" for enabling a theranostic application to the liposomal drug delivery system through ^{19}F MRI.[127]

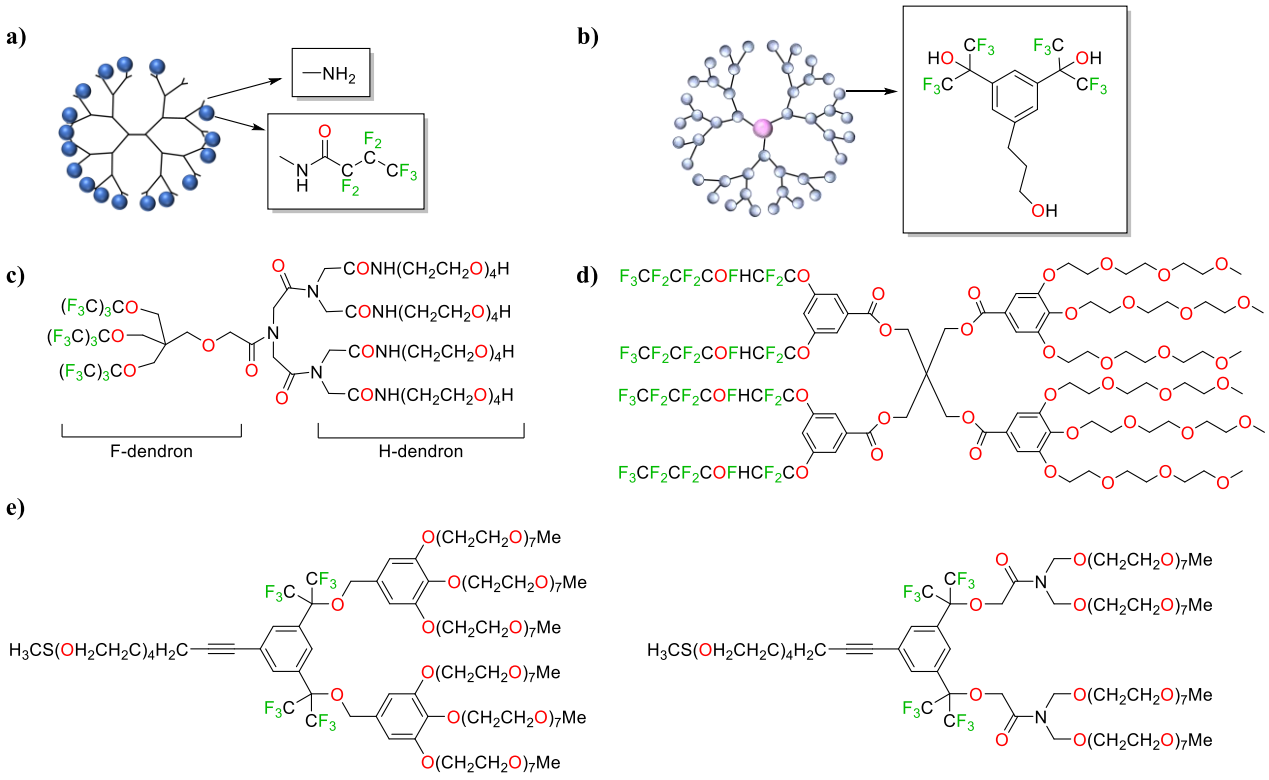

Figure 1.15 Structure of fluorinated dendrimers. a) heptafluoroacylated PAMAM(G3) (Ref [121]), b) Fluorinated dendrimer and its building block (Ref [124]), c) ^{19}F imaging tracer with 27 fluorine atoms (^{19}FIT-27) (Ref [122]), d) fluorinated (R_F) Janus dendrimer (Ref [125]), and e) fluorinated amphiphiles (Ref [126]).

1.4.3.3 Fluorinated polymers

Fluorinated polymers have been widely developed and used as fluorinated probes. The design of a long-fluorinated polymer chain allows an introduction of a high fluorine density to the molecule. Perfluoropolyether is one of the fluorinated polymers that found its application in ^{19}F MRI. Due to its high hydrophobicity and low water-solubility, it has been mainly developed as nanoemulsions. Interestingly, these fluorinated polymers can also be designed as amphiphiles by introducing a hydrophilic segment to improve its water-solubility. One strategy is to functionalize commercially available PFCs as reported by Zhang *et al.*[128] The authors developed the (poly(OEGA)$_m$-PFPE) where a hydrophilic segment, an oligo(ethylene glycol) methyl ether acrylate (OEGA), was conjugated to PFPE. The introduction of hydrophilic OEGA led to either a folding of poly(OEGA)$_m$-PFPE molecules or a formation of aggregates, depending on the length of the attached hydrophilic OEGA. The high fluorine content (up to 29% wt)

resulted in high resolution ^{19}F MR images *in vivo*. Another strategy for preparing fluorinated polymers is through a polymerization of monomers containing fluorine. The most widely used fluorinated monomers are 2,2,2-trifluoroethyl acrylate (TFEA) and 2,2,2-trifluoroethyl methyl acrylate (TFEMA). As shown in **Figure 1.16a** and **b**, the monomer contains three equivalent fluorine atoms which give rise to one strong ^{19}F signal, benefiting ^{19}F MRI. In 2010, Nurmi *et al*.[129] reported a polymerization of TFEMA, a fluorinated monomer, and 2-(dimethylamino)ethyl methacrylate (DMAEMA), the electrostatically charged monomers, for a preparation of block and statistical, an even distribution of monomer units, copolymers. Aqueous solutions of these copolymers provided different conformations which resulted in different ^{19}F mobility and T_2 relaxation. A similar approach was reported by Wang *et al*.[130] where the segmented highly branched polymers (SHBPs) were developed from TFEA and poly(ethylene glycol) methyl monoether acrylate (PEGA) monomers. The water-soluble statistical copolymers (fluorine content up to 60 mol%) formed nanoparticles with an average size of 4 – 8 nm and exhibited a single ^{19}F signal. However, the high fluorine contents from the polymers, after forming nanoparticles, led to an increased fluorinated association, leading to a limited chain flexibility and, consequently, lower signal intensity of ^{19}F MR images. This result supported the relationship of chain flexibility and T_2 relaxation which is indicative of ^{19}F imaging performance. In 2018, Fu *et al*.[131] reported a polymerization of TFEA and a highly water-soluble monomer 2-(methylsulfinyl)ethyl acrylate (MSEA), PMSEA-PTEFA, with a fluorine content of 5.8 – 19.3% wt. This fluorinated polymer demonstrated good biocompatibility with tunable properties to achieve different molecular weight sizes. The I.V. injection of fluorinated polymer solution *in vivo* revealed a rapid clearance of polymers due to its small size (diameter ~ 5.5 nm) as observed from a clear signal in the bladder 30 min post injection through ^{19}F MRI.

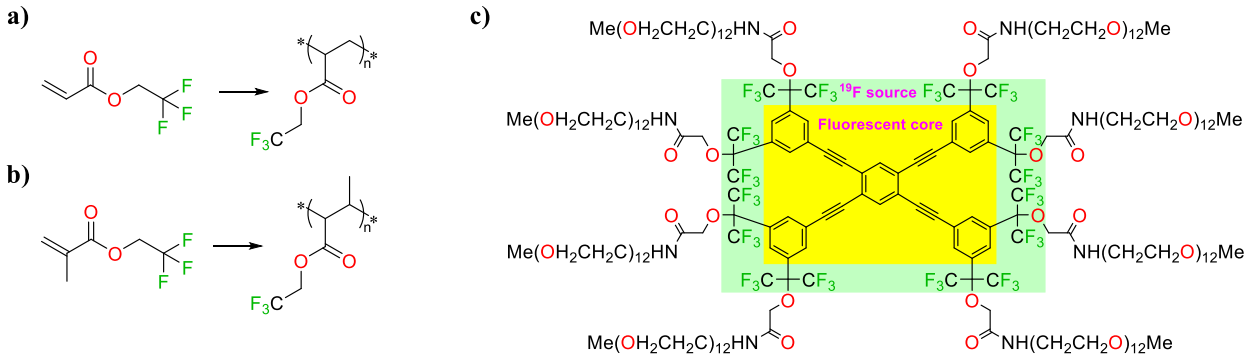

Figure 1.16 Structure of fluorinated polymers. a) structure of 2,2,2-trifluoroethyl acrylate (TFEA) and its corresponding polymer, b) structure of 2,2,2-trifluoroethyl methyl acrylate (TFEMA) and its corresponding polymer, and c) structure of ^{19}F MRI and fluorescence dual-modal fluorinated amphiphile (Ref [132]).

A dual-modal imaging technique has also been applied to fluorinated amphiphiles. Bo *et al.*[132] reported a synthesis of fluorinated amphiphiles containing a fluorescent core, 48 chemically equivalent fluorine atoms as a ^{19}F source, and PEG as a solubility enhancer (**Figure 1.16c**). This freely water-soluble molecule exhibited a weak ^{19}F NMR signal due to the hydrophobic aggregation from π-stacking, limiting its mobility which resulted in a short T_2 and, thus, turned the ^{19}F signal off. Increasing hydrophilicity by introducing additional PEG or breaking coplanarity by hydrogenation of triple bonds in the fluorescent core relieved the self-assembly and, therefore, lengthened T_2, turning the ^{19}F signal on. The molecule with additional PEGs provided a high sensitivity as demonstrated by ^{19}F MR phantom images where the minimum detectable ^{19}F concentration was 24 mM with a short scanning time of 150 s. Another semifluorinated polymer synthesis was reported by Decato *et al.*[26] where a hydrophilic segment, PEG, was coupled to tri-perfluoro-*tert*-butanol, which contains 27 chemically equivalent fluorine atoms (**Figure 1.17a**). The semifluorinated polymers self-assembled in aqueous solution, forming micelles, with an average diameter of 11 nm. ^{19}F MR phantom images of the fluorinated micelles revealed an intense ^{19}F MR signal with a detection limit at 1 mM (**Figure 1.17b**).

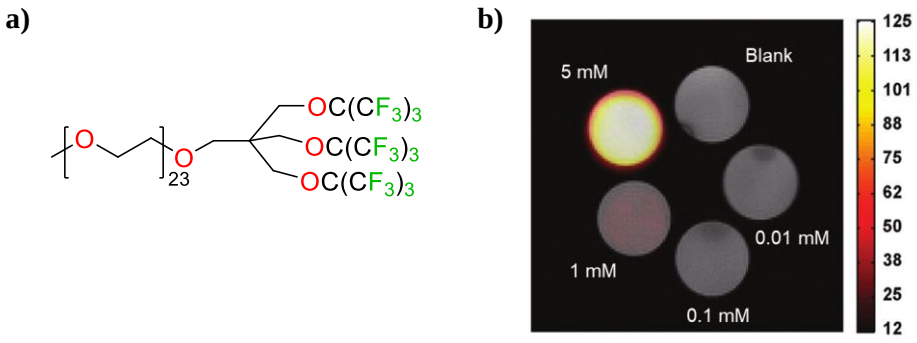

Figure 1.17 a) Structure of M1PFtB$_{TRI}$ and b) ^{19}F MR phantom images superimposed on ^{1}H MR phantom images at 4.7 T. 5 mM concentration shows a high signal intensity with a detection limit at 1 mM. Figure from Decato *et al*.[26]

1.4.3.4 Fluorinated inorganic nanoparticles (gold and silica)

The interest in developing fluorinated probes has also spanned into the field of inorganic nanoparticles. Many researchers have been focusing on utilizing gold and silica nanoparticles as alternative strategies due to their facile synthesis, surface modifiability, biocompatibility, and smaller size compared to nanoemulsions. As fluorinated probes, the use of gold nanoparticles allows for a dual-modal imaging or a combined photodynamic therapy owing to the physiochemical properties of the gold core.[133] A commonly used method for introducing fluorine to gold nanoparticles is through perfluorinated alkane thiols. However, as expected, the introduction of a high density of fluorine compromises the water-solubility property of the particles, providing disadvantages for biomedical applications. Hence, several strategies have been applied to improve their colloidal stability, for example, through the PEGylation of perfluorinated alkane[134] or perfluoroether[135-136] thiols. In 2017, Michelena *et al*.[137] reported the synthesis of gold nanoparticles with fluorinated ligands that contains chemically equivalent ^{19}F based on perfluoro-*tert*-butanol group and the colloidal stability was improved by the insertion of a long PEG chain.

For silica nanoparticles, the biological inert-ness, surface modifiability, and favorable colloidal properties also make them a good candidate as fluorinated probes. In 2014, Matsushita *et al*.[138] reported a good colloidal stability and an easily modifiable surface for targeting purposes of a core-shell fluorine accumulated silica nanoparticle for MRI contrast enhancement (FLAME). Later in 2015, the same group

reported the use of multifunctional mesoporous silica nanoparticles (MSNs) where the PFCE liquid core was covered by fluorescent dye filling a mesoporous silica shell. This specific design provides dual-modal imaging along with the delivery of hydrophobic therapeutic agents allowing its usage as a theranostic tool.[139] Another use of MSNs was reported by Bouchoucha *et al*.[140] where fluorosilane or polyfluorosiloxane was grafted on the surface of MSNs as sources of fluorine, as well as, PEG and chelated Gd^{3+} for improving water-solubility and enhancing their detectability by ^{1}H MRI, serving it purpose as a binuclear (^{1}H and ^{19}F) probe. Recently, Zhu *et al*.[141] reported the development of the first fluorinated ionic liquid-based activatable ^{19}F MRI platform (FILAMP) where the water-soluble fluorinated ionic liquid (IL) was loaded into hollow mesoporous silica (HMS) nanoparticles. The surface of the particles was coated by stimuli-responsive polymers that control the release of fluorinated IL, turning ^{19}F signal off and on. The FILAMP restricted the movement of fluorinated IL inside the particles, resulting in a short T_2 and, thus, turning the ^{19}F MRI signal off. In a stimuli-activated environment such as low pH, FILAMP released fluorinated IL, leading to an increased movement and hence, turning the ^{19}F MRI signal on.

1.5 Improving the sensitivity of ^{19}F MRI

Granting the low physiological abundance of fluorine, the detectable ^{19}F signal solely depends on the fluorine density/concentration. Difficulty in delivering large quantities of PFCs due to their unique properties can, inevitably, lead to low ^{19}F signals. Moreover, most PFCs possess intrinsically long longitudinal (T_1) relaxation times of 1 – 4 s which necessitates long image acquisition times, resulting in limited scan cycles in a given clinical scanning time and, thus, limiting the clinical translation.[18, 142] Increasing sensitivity of ^{19}F MRI can be accomplished through various strategies including the delivery of large amounts of PFCs, designing probes with a high density of equivalent ^{19}F nuclei, and reducing an intrinsically long T_1 relaxation times of fluorine.[18, 142-143]

1.5.1 Improving the ^{19}F sensitivity through high-density of ^{19}F nuclei

This straightforward strategy involves an incorporation of a large number of fluorinated materials at the area of interest. The increased ^{19}F nuclei density results in a greater signal intensity, thus, enhancing

its sensitivity. Commercially available and commonly used liquid PFCs as fluorine sources for ^{19}F MRI are PFOB, PFPE, and PFCE. While the direct injection of these liquid PFCs is inexecutable, they are typically formulated into nanoemulsions, comprising of liquid PFC core stabilized by surfactants or polymers. This allows a delivery of water-soluble nanoemulsions loaded with large PFC volume, resulting in a high ^{19}F signal intensity. For example, Barres *et al*.[95] reported the preparation of PFCE nanoemulsion using semifluorinated polymer at 35% v/v PFCE which is the highest concentration prepared so far. The I.V. injection of PFCE nanoemulsions to tumor-bearing mice showed a local accumulation of PFCE nanoemulsions in the tumor due to a passive targeting through the EPR effect in which the ^{19}F signal could be clearly observed with high SNR in a short image acquisition time.

In addition to delivering a large quantity of commercially available PFCs, introducing a substantial amount of fluorine nuclei to the fluorinated molecules also serves the purpose of increasing nuclei density. However, the high-density of fluorine nuclei usually results in a high fluorophilicity which leads to insolubility of the molecules in water. Therefore, optimization is needed to maximize the nuclei density as well as maintaining water-solubility. Additionally, fluorinated molecules should be designed in such a way that all fluorine nuclei are chemically equivalent to maximize ^{19}F sensitivity and to avoid split ^{19}F signals which can lower the SNR and lead to blurry MR images or artifacts. For example, Yu *et al*.[124] reported a synthesis of fluorinated dendrimer consisting of 540 pseudosymmetrical fluorines from -CF_3 groups. This highly dense fluorinated dendrimer provided a strong ^{19}F signal and demonstrated an enhanced ^{19}F sensitivity with a low detection limit. However, as expected, this fluorinated dendrimer was not soluble in water due to its high fluorine density. This formulation was a proof-of-concept design for improving the sensitivity of ^{19}F MRI. Further PEGylation of the fluorinated dendrimer could be employed to provide water-solubility to the particles.

1.5.2 Improving the ^{19}F sensitivity by using paramagnetic metal ions

Another strategy that is used to improve ^{19}F sensitivity is through the incorporation of paramagnetic metal ions. This method, unlike the one mentioned above, aims to shorten the intrinsically long longitudinal

(T_1) relaxation times of fluorine. As noted before, long T_1 relaxation times require a long imaging session in order to acquire high SNR images which would not be practical for *in vivo* imaging, especially in human clinical imaging. Since the time for imaging is limited, the high T_1 relaxation times lead to a lower number of total scan cycles, resulting in low SNR images. Therefore, by shortening T_1 relaxation times, more scan cycles can be achieved which leads to a higher SNR and, thus, enhances its sensitivity. For instance, a lot of research has been focusing on integrating paramagnetic metal ions to the fluorinated nanoemulsions where the ^{19}F sensitivity could be enhanced by a shortened T_1 relaxation time due to the effect of paramagnetic metal ions. In 2012, Harvey *et al.*[144] reviewed the lanthanide complexes used as fluorinated probes for ^{19}F MRI/MRS applications. The lanthanide ions were chelated by -CF_3 containing chelator molecules to achieve chemically equivalent ^{19}F signals. The lanthanide-based ^{19}F probes provided an improved ^{19}F sensitivity of 15 – 20 times owing to the paramagnetic properties of these metal ions. In 2016, Kislukhin *et al.*[143] reported a comprehensive study on the effect on the relaxations of different paramagnetic metal ions bound to a PFPE payload in fluorinated nanoemulsions. The paramagnetic metal ions in this study include chromium (Cr^{3+}), erbium (Er^{3+}), europium (Eu^{3+}), terbium (Tb^{3+}), neodymium (Nd^{3+}), gadolinium (Gd^{3+}), dysprosium (Dy^{3+}), manganese (Mn^{2+}), and iron (Fe^{3+}). Among these paramagnetic metal ions, a profound effect on T_1 shortening was found when using Mn^{2+}, Gd^{3+}, or Fe^{3+}. However, since the fluctuated magnetic fields caused by paramagnetic metal ions can also affect T_2 relaxation, as observed from a line broadening effect (as mentioned in section **1.4.1**), which can lead to a lower sensitivity, the effect on both T_1 and T_2 relaxations have to be compromised to maximize the sensitivity enhancement. Gd^{3+} and Mn^{2+} are the two most common T_1 agents used in the clinic for ^1H MRI. Even though the T_1 shortening effect was shown for these two metal ions, a severe line broadening effect was also observed. Therefore, compared to Gd^{3+} and Mn^{2+}, Fe^{3+} demonstrated a more modest line broadening with a significantly reduced T_1 relaxation time, suggesting its advantages for enhancing ^{19}F sensitivity. Later in 2018, Jahromi *et al.*[145] from the same research group reported a synthesis of metal chelator (SALTAME), which is soluble in PFCs, and demonstrated that the chelation of Fe^{3+} provided a superior T_1 shortening, a modest line broadening

effect, and a stable chelated form. The paramagnetic nanoemulsions prepared from PFOB and chelated Fe^{3+} yielded a sensitivity enhancement with low T_1 relaxation time and demonstrated its successful usage as an inflammation imaging agent in an *in vivo* inflammation mouse model. Peng *et al*.[117] also reported a sensitivity enhancement of Fe^{3+}-containing paramagnetic nanoemulsion over other types of paramagnetic metal ions, namely Gd^{3+}, Mn^{2+}, Eu^{3+}, Er^{3+}, and Tb^{3+}, as observed from a significant T_1 reduction with a sharp ^{19}F NMR peak which suggested a low line broadening effect. This Fe^{3+} chelator was synthesized to contain the same fluorinated structure as the fluorinated oil, TPFBME (**Figure 1.14b**), used for preparing the nanoemulsions. The paramagnetic nanoemulsions demonstrated a good biocompatibility and an efficient uptake by various cell lines, serving cell labeling purposes. The subcutaneously injected labeled cells with the paramagnetic nanoemulsions *in vivo* revealed the improved signal intensity, suggesting a sensitive fluorinated probe.

1.6 Thesis Objective and Overview

In part, this thesis research serves to continue the promising applications of the $PFtB_{TRI}$-based semifluorinated polymer developed in the Mecozzi group by Dr. Sarah Decato.[26] Dr. Decato developed the polymer, consisting of a hydrophilic PEG block and the fluorophilic $PFtB_{TRI}$, and explored its advantages as a drug delivery carrier and as a fluorinated probe for ^{19}F MRI application. Later modification of this polymer with a middle hydrocarbon block allows for an encapsulation of hydrophobic drugs (unpublished results, Chapter 3, Sarah Decato Ph.D. Thesis, 2015). This special fluorous $PFtB_{TRI}$ design provides not only the improved colloidal stability of the corresponding semifluorinated aggregates but also a benefit for ^{19}F MRI due to its 27 chemically equivalent fluorine atoms that give rise to only one strong ^{19}F NMR signal. However, our preliminary data demonstrated that after the I.V. injection of the $PFtB_{TRI}$-PEG polymer in a tumor-bearing mouse, a negligible ^{19}F signal was observed in the tumor after the *in vivo* MR imaging. In fact, even when observed *ex vivo* with a 5 h scan time, the signal in the tumor had a low SNR. This suggests a limited accumulation of micelles at the tumor as well as a low sensitivity of the fluorine (unpublished

results, Chapter 4, Sarah Decato Ph.D. Thesis, 2015). Therefore, the projects described in *Chapter 2* and *4* of this thesis aimed to improve the accumulation of the micelles at the target site and enhance the sensitivity of the fluorine. With an interest in semifluorinated polymers for micelle preparation, the project in *Chapter 3* focuses on studying the effect of different semifluorinated polymer architectures on micelle formation used as drug delivery carriers.

Chapter 2 focuses on the use of targeting ligands to increase the accumulation of micelles at a tumor which would lead to the delivery of a greater payload. iRGD, or internalizing RGD, was chosen as the targeting ligand due to its ability to readily penetrate a tumor in comparison to RGD and was conjugated to the modified $PFtB_{TRI}$-based polymer through a thiol-maleimide coupling reaction. This chapter also describes the polymer characterization as well as the optimization of the amount of iRGD introduced to the micelles through the investigation of size and *in vitro* cellular uptake in both 2D and 3D cultured cells. The optimized formulation was further studied for its cytotoxic effect compared to non-targetable micelles and free hydrophobic anticancer drug, paclitaxel (*Chapter 2*). In *Chapter 3*, the effect of semifluorinated polymer architectures on micelle preparation was studied. Our interest arose from previous studies that demonstrated the successful preparation of nanoemulsions using our novel linear M2F8H18 polymer with high stability.[146] The use of linear M2F8H18 polymer has been expanded to micelle preparation. In addition, various architectures of semifluorinated polymers were also designed to contain different fluorinated structures, i.e. symmetrical and asymmetrical dibranched structures, based on the F8H18 moiety and compared the architecture effect to the micelle stability. The fluorinated dibranched alcohol structures studied here were first introduced in the Mecozzi group by Dr. Corinna Galli (unpublished results). These dibranched semifluorinated polymers were synthesized and characterized for their physicochemical properties (*Chapter 3*). The encapsulation efficiencies, the *in vitro* time release profiles, and the *in vitro* cytotoxicities were also studied and compared among different architectures (*Chapter 3*). Finally, the advantage of fluorine as fluorinated probes for ^{19}F MRI application was also investigated (*Chapter 4*). The

strategies to improve this sensitivity were explored through the use of high-density fluorine atoms as well as paramagnetic metal ions (*Chapter 4*).

1.7 References

(1) Bond, D.; Guenther, M.; Stimpson, L.; Toth, L.; Young, D. Experience with fluorine and its safe use as a propellant. **1979**.

(2) Davy, H. Some experiments and observations on the substances produced in different chemical processes on fluor spar. *Philosophical Transactions of the Royal Society of London* **1813,** *103*, 263-279.

(3) Prakash, G. K. S.; Zhang, Z. 11 - New Nucleophilic Fluoroalkylations. In *Modern Synthesis Processes and Reactivity of Fluorinated Compounds*, Groult, H.; Leroux, F. R.; Tressaud, A., Eds. Elsevier: 2017; pp 289-337.

(4) Lemal, D. M. Perspective on fluorocarbon chemistry. *The Journal of organic chemistry* **2004,** *69* (1), 1-11.

(5) Terrell, R. Future Development of Volatile Anesthetics. In *ZAK Zürich*, Springer: 1986; pp 87-92.

(6) Braun, M.; Eicher, J. Chapter Two - The Fluorine Atom in Health Care and Agrochemical Applications: A Contribution to Life Science. In *Modern Synthesis Processes and Reactivity of Fluorinated Compounds*, Groult, H.; Leroux, F. R.; Tressaud, A., Eds. Elsevier: 2017; pp 7-25.

(7) de la Torre, B. G.; Albericio, F. The pharmaceutical industry in 2019. An analysis of FDA drug approvals from the perspective of molecules. *Molecules* **2020,** *25* (3), 745.

(8) Tredwell, M.; Gouverneur, V. 1.5 Fluorine in Medicinal Chemistry: Importance of Chirality. In *Comprehensive Chirality*, Carreira, E. M.; Yamamoto, H., Eds. Elsevier: Amsterdam, 2012; pp 70-85.

(9) Neil, E.; Marsh, G. Towards the nonstick egg: designing fluorous proteins. *Chemistry & biology* **2000,** *7* (7), R153-R157.

(10) Krafft, M. P.; Riess, J. G. Perfluorocarbons: Life sciences and biomedical uses Dedicated to the memory of Professor Guy Ourisson, a true RENAISSANCE man. *Journal of Polymer Science Part A: Polymer Chemistry* **2007,** *45* (7), 1185-1198.

(11) Decato, S.; Mecozzi, S. Chapter 16 - Highly fluorinated colloids in drug delivery and imaging. In *Colloid and Interface Science in Pharmaceutical Research and Development*, Ohshima, H.; Makino, K., Eds. Elsevier: Amsterdam, 2014; pp 319-345.

(12) Krafft, M. P. Fluorocarbons and fluorinated amphiphiles in drug delivery and biomedical research. *Advanced drug delivery reviews* **2001,** *47* (2-3), 209-228.

(13) Riess, J. G. Understanding the Fundamentals of Perfluorocarbons and Perfluorocarbon Emulsions Relevant to *In Vivo* Oxygen Delivery. *Artificial Cells, Blood Substitutes, and Biotechnology* **2005,** *33* (1), 47-63.

(14) Teng, H. Overview of the development of the fluoropolymer industry. *Applied Sciences* **2012,** *2* (2), 496-512.

(15) Zhang, T.; Zhang, Q.; Tian, J.-H.; Xing, J.-F.; Guo, W.; Liang, X.-J. Perfluorocarbon-based nanomedicine: emerging strategy for diagnosis and treatment of diseases. *MRS Communications* **2018,** *8* (2), 303-313.

(16) Lowe, K. C. Fluorinated blood substitutes and oxygen carriers. *Journal of Fluorine Chemistry* **2001,** *109* (1), 59-65.

(17) Srinivas, M.; Heerschap, A.; Ahrens, E. T.; Figdor, C. G.; de Vries, I. J. M. ^{19}F MRI for quantitative *in vivo* cell tracking. *Trends in biotechnology* **2010,** *28* (7), 363-370.

(18) Ruiz‐Cabello, J.; Barnett, B. P.; Bottomley, P. A.; Bulte, J. W. Fluorine (^{19}F) MRS and MRI in biomedicine. *NMR in Biomedicine* **2011,** *24* (2), 114-129.

(19) Gonzales, C.; Yoshihara, H. A.; Dilek, N.; Leignadier, J.; Irving, M.; Mieville, P.; Helm, L.; Michielin, O.; Schwitter, J. In-Vivo Detection and Tracking of T Cells in Various Organs in a Melanoma Tumor Model by ^{19}F-Fluorine MRS/MRI. *PLOS one* **2016,** *11* (10), e0164557.

(20) Ahrens, E. T.; Bulte, J. W. Tracking immune cells in vivo using magnetic resonance imaging. *Nature Reviews Immunology* **2013,** *13* (10), 755-763.

(21) Riess, J. G. Highly fluorinated amphiphilic molecules and self-assemblies with biomedical potential. *Current Opinion in Colloid & Interface Science* **2009,** *14* (5), 294-304.

(22) Masayuki, Y.; Mizue, M.; Noriko, Y.; Teruo, O.; Yasuhisa, S.; Kazunori, K.; Shohei, I. Polymer micelles as novel drug carrier: adriamycin-conjugated poly (ethylene glycol)-poly (aspartic acid) block copolymer. *Journal of controlled release* **1990,** *11* (1-3), 269-278.

(23) Hoang, K. C.; Mecozzi, S. Aqueous solubilization of highly fluorinated molecules by semifluorinated surfactants. *Langmuir* **2004,** *20* (18), 7347-7350.

(24) Parks, C. L.; Tucker, W.; Amlong, C. A.; Mecozzi, S.; Pearce, R. A. Lipid-free Fluoropolymer-based Propofol Emulsions and Lipid Reversal of Propofol Anesthesia in Rats. *Anesthesiology: The Journal of the American Society of Anesthesiologists* **2016,** *124* (6), 1328-1337.

(25) Fast, J. P.; Perkins, M. G.; Pearce, R. A.; Mecozzi, S. Fluoropolymer-based emulsions for the intravenous delivery of sevoflurane. *Anesthesiology: The Journal of the American Society of Anesthesiologists* **2008,** *109* (4), 651-656.

(26) Decato, S.; Bemis, T.; Madsen, E.; Mecozzi, S. Synthesis and characterization of perfluoro-tert-butyl semifluorinated amphiphilic polymers and their potential application in hydrophobic drug delivery. *Polymer chemistry* **2014,** *5* (22), 6461-6471.

(27) Tucker, W. B.; McCoy, A. M.; Fix, S. M.; Stagg, M. F.; Murphy, M. M.; Mecozzi, S. Synthesis, physicochemical characterization, and self‐assembly of linear, dibranched, and miktoarm semifluorinated triphilic polymers. *Journal of Polymer Science Part A: Polymer Chemistry* **2014,** *52* (23), 3324-3336.

(28) Skrabania, K.; Berlepsch, H. v.; Böttcher, C.; Laschewsky, A. Synthesis of Ternary, Hydrophilic− Lipophilic− Fluorophilic Block Copolymers by Consecutive RAFT Polymerizations and Their Self-Assembly into Multicompartment Micelles. *Macromolecules* **2010,** *43* (1), 271-281.

(29) Marsat, J.-N.; Heydenreich, M.; Kleinpeter, E.; Berlepsch, H. v.; Böttcher, C.; Laschewsky, A. Self-Assembly into Multicompartment Micelles and Selective Solubilization by Hydrophilic− Lipophilic− Fluorophilic Block Copolymers. *Macromolecules* **2011,** *44* (7), 2092-2105.

(30) Lodge, T. P.; Rasdal, A.; Li, Z.; Hillmyer, M. A. Simultaneous, segregated storage of two agents in a multicompartment micelle. *Journal of the American Chemical Society* **2005,** *127* (50), 17608-17609.

(31) Kreuter, J. Nanoparticles—a historical perspective. *International Journal of Pharmaceutics* **2007,** *331* (1), 1-10.

(32) Vert, M.; Doi, Y.; Hellwich, K.-H.; Hess, M.; Hodge, P.; Kubisa, P.; Rinaudo, M.; Schué, F. Terminology for biorelated polymers and applications (IUPAC Recommendations 2012). *Pure and Applied Chemistry* **2012,** *84* (2), 377-410.

(33) Pelaz, B.; Alexiou, C.; Alvarez-Puebla, R. A.; Alves, F.; Andrews, A. M.; Ashraf, S.; Balogh, L. P.; Ballerini, L.; Bestetti, A.; Brendel, C.; Bosi, S.; Carril, M.; Chan, W. C. W.; Chen, C.; Chen, X.; Chen, X.; Cheng, Z.; Cui, D.; Du, J.; Dullin, C.; Escudero, A.; Feliu, N.; Gao, M.; George, M.; Gogotsi, Y.; Grünweller, A.; Gu, Z.; Halas, N. J.; Hampp, N.; Hartmann, R. K.; Hersam, M. C.; Hunziker, P.; Jian, J.; Jiang, X.; Jungebluth, P.; Kadhiresan, P.; Kataoka, K.; Khademhosseini, A.; Kopeček, J.; Kotov, N. A.; Krug, H. F.; Lee, D. S.; Lehr, C.-M.; Leong, K. W.; Liang, X.-J.; Ling Lim, M.; Liz-Marzán, L. M.; Ma, X.; Macchiarini, P.; Meng, H.; Möhwald, H.; Mulvaney,

P.; Nel, A. E.; Nie, S.; Nordlander, P.; Okano, T.; Oliveira, J.; Park, T. H.; Penner, R. M.; Prato, M.; Puntes, V.; Rotello, V. M.; Samarakoon, A.; Schaak, R. E.; Shen, Y.; Sjöqvist, S.; Skirtach, A. G.; Soliman, M. G.; Stevens, M. M.; Sung, H.-W.; Tang, B. Z.; Tietze, R.; Udugama, B. N.; VanEpps, J. S.; Weil, T.; Weiss, P. S.; Willner, I.; Wu, Y.; Yang, L.; Yue, Z.; Zhang, Q.; Zhang, Q.; Zhang, X.-E.; Zhao, Y.; Zhou, X.; Parak, W. J. Diverse applications of nanomedicine. *ACS Nano* **2017,** *11* (3), 2313-2381.

(34) Oerlemans, C.; Bult, W.; Bos, M.; Storm, G.; Nijsen, J. F. W.; Hennink, W. E. Polymeric micelles in anticancer therapy: targeting, imaging and triggered release. *Pharmaceutical Research* **2010,** *27* (12), 2569-2589.

(35) Kataoka, K.; Harada, A.; Nagasaki, Y. Block copolymer micelles for drug delivery: design, characterization and biological significance. *Advanced Drug Delivery Reviews* **2001,** *47* (1), 113-131.

(36) Blanco, E.; Kessinger, C. W.; Sumer, B. D.; Gao, J. Multifunctional micellar nanomedicine for cancer therapy. *Experimental Biology and Medicine* **2009,** *234* (2), 123-131.

(37) Tangsangasaksri, M.; Takemoto, H.; Naito, M.; Maeda, Y.; Sueyoshi, D.; Kim, H. J.; Miura, Y.; Ahn, J.; Azuma, R.; Nishiyama, N.; Miyata, K.; Kataoka, K. siRNA-Loaded Polyion Complex Micelle Decorated with Charge-Conversional Polymer Tuned to Undergo Stepwise Response to Intra-Tumoral and Intra-Endosomal pHs for Exerting Enhanced RNAi Efficacy. *Biomacromolecules* **2016,** *17* (1), 246-255.

(38) Kim, H. J.; Ishii, T.; Zheng, M.; Watanabe, S.; Toh, K.; Matsumoto, Y.; Nishiyama, N.; Miyata, K.; Kataoka, K. Multifunctional polyion complex micelle featuring enhanced stability, targetability, and endosome escapability for systemic siRNA delivery to subcutaneous model of lung cancer. *Drug Delivery and Translational Research* **2013**, 1-11.

(39) Oe, Y.; Christie, R. J.; Naito, M.; Low, S. A.; Fukushima, S.; Toh, K.; Miura, Y.; Matsumoto, Y.; Nishiyama, N.; Miyata, K.; Kataoka, K. Actively-targeted polyion complex micelles stabilized by cholesterol and disulfide cross-linking for systemic delivery of siRNA to solid tumors. *Biomaterials* **2014,** *35* (27), 7887-7895.

(40) Chang, S.-F.; Chang, H.-Y.; Tong, Y.-C.; Chen, S.-H.; Hsaio, F.-C.; Lu, S.-C.; Liaw, J. Nonionic polymeric micelles for oral gene delivery in vivo. *Human gene therapy* **2004,** *15* (5), 481-493.

(41) Kakizawa, Y.; Kataoka, K. Block copolymer micelles for delivery of gene and related compounds. *Advanced Drug Delivery Reviews* **2002,** *54* (2), 203-222.

(42) Chime, S.; Kenechukwu, F.; Attama, A. Nanoemulsions—advances in formulation, characterization and applications in drug delivery. In *Application of Nanotechnology in Drug Delivery*, Sezer, A. D., Ed. IntechOpen: 2014.

(43) Singh, Y.; Meher, J. G.; Raval, K.; Khan, F. A.; Chaurasia, M.; Jain, N. K.; Chourasia, M. K. Nanoemulsion: Concepts, development and applications in drug delivery. *Journal of Controlled Release* **2017,** *252*, 28-49.

(44) Pharmacopea, U. Globule size distribution in lipid injectable emulsions. *US Pharm. Rockv. MD US Pharm* **2011,** *1*, 297-299.

(45) Tucker, W. B.; Mecozzi, S. Nanoemulsions in Medicine. In *Handbook of Nanobiomedical Research*, 2014; pp 141-167.

(46) Jee, J.-P.; Parlato, Maria C.; Perkins, Mark G.; Mecozzi, S.; Pearce, Robert A. Exceptionally Stable Fluorous Emulsions for the Intravenous Delivery of Volatile General Anesthetics. *Anesthesiology: The Journal of the American Society of Anesthesiologists* **2012,** *116* (3), 580-585.

(47) Parlato, M. C.; Jee, J.-P.; Teshite, M.; Mecozzi, S. Synthesis, characterization, and applications of hemifluorinated dibranched amphiphiles. *The Journal of organic chemistry* **2011,** *76* (16), 6584-6591.

(48) Kim, S.; Shi, Y.; Kim, J. Y.; Park, K.; Cheng, J.-X. Overcoming the barriers in micellar drug delivery: loading efficiency, in vivo stability, and micelle–cell interaction. *Expert Opinion on Drug Delivery* **2010,** *7* (1), 49-62.

(49) Kore, G.; Kolate, A.; Nej, A.; Misra, A. Polymeric Micelle as Multifunctional Pharmaceutical Carriers. *Journal of Nanoscience and Nanotechnology* **2014,** *14* (1), 288-307.

(50) Savić, R.; Azzam, T.; Eisenberg, A.; Maysinger, D. Assessment of the Integrity of Poly(caprolactone)-b-poly(ethylene oxide) Micelles under Biological Conditions: A Fluorogenic-Based Approach. *Langmuir* **2006,** *22* (8), 3570-3578.

(51) Burt, H. M.; Zhang, X.; Toleikis, P.; Embree, L.; Hunter, W. L. Development of copolymers of poly(d,l-lactide) and methoxypolyethylene glycol as micellar carriers of paclitaxel. *Colloids and Surfaces B: Biointerfaces* **1999,** *16* (1), 161-171.

(52) Chen, H.; Kim, S.; He, W.; Wang, H.; Low, P. S.; Park, K.; Cheng, J.-X. Fast Release of Lipophilic Agents from Circulating PEG-PDLLA Micelles Revealed by in Vivo Förster Resonance Energy Transfer Imaging. *Langmuir* **2008,** *24* (10), 5213-5217.

(53) Christie, R. J.; Miyata, K.; Matsumoto, Y.; Nomoto, T.; Menasco, D.; Lai, T. C.; Pennisi, M.; Osada, K.; Fukushima, S.; Nishiyama, N. Effect of polymer structure on micelles formed between

siRNA and cationic block copolymer comprising thiols and amidines. *Biomacromolecules* **2011,** *12* (9), 3174-3185.

(54) Iijima, M.; Nagasaki, Y.; Okada, T.; Kato, M.; Kataoka, K. Core-Polymerized Reactive Micelles from Heterotelechelic Amphiphilic Block Copolymers. *Macromolecules* **1999,** *32* (4), 1140-1146.

(55) Jee, J.-P.; McCoy, A.; Mecozzi, S. Encapsulation and release of Amphotericin B from an ABC triblock fluorous copolymer. *Pharmaceutical Research* **2012,** *29* (1), 69-82.

(56) Decato, S.; Tangsangasaksri, M.; Tucker, W. B.; Madsen, E. J.; Miura, Y.; Matsumoto, Y.; Kataoka, K.; Mecozzi, S. Long-circulating, tumor-targeting drug nanocarriers: in vivo stability of triphilic polymer self-assemblies enhanced by branched semifluorinated cores. *Manuscript submitted for publication.* **2020**.

(57) Matsumura, Y.; Maeda, H. A new concept for macromolecular therapeutics in cancer chemotherapy: mechanism of tumoritropic accumulation of proteins and the antitumor agent smancs. *Cancer research* **1986,** *46* (12 Part 1), 6387-6392.

(58) Prabhakar, U.; Maeda, H.; Jain, R. K.; Sevick-Muraca, E. M.; Zamboni, W.; Farokhzad, O. C.; Barry, S. T.; Gabizon, A.; Grodzinski, P.; Blakey, D. C. Challenges and key considerations of the enhanced permeability and retention effect for nanomedicine drug delivery in oncology. *Cancer Research* **2013,** *73* (8), 2412-2417.

(59) Jun, Y. W.; Lee, J. H.; Cheon, J. Chemical design of nanoparticle probes for high-performance magnetic resonance imaging. *Angewandte Chemie International Edition* **2008,** *47* (28), 5122-5135.

(60) Bertrand, N.; Wu, J.; Xu, X.; Kamaly, N.; Farokhzad, O. C. Cancer nanotechnology: The impact of passive and active targeting in the era of modern cancer biology. *Advanced Drug Delivery Reviews* **2014,** *66*, 2-25.

(61) Danhier, F.; Feron, O.; Préat, V. To exploit the tumor microenvironment: Passive and active tumor targeting of nanocarriers for anti-cancer drug delivery. *Journal of Controlled Release* **2010,** *148* (2), 135-146.

(62) Fang, J.; Nakamura, H.; Maeda, H. The EPR effect: unique features of tumor blood vessels for drug delivery, factors involved, and limitations and augmentation of the effect. *Advanced drug delivery reviews* **2011,** *63* (3), 136-151.

(63) Maeda, H. Toward a full understanding of the EPR effect in primary and metastatic tumors as well as issues related to its heterogeneity. *Advanced drug delivery reviews* **2015,** *91*, 3-6.

(64) Heldin, C.-H.; Rubin, K.; Pietras, K.; Östman, A. High interstitial fluid pressure—an obstacle in cancer therapy. *Nature Reviews Cancer* **2004,** *4* (10), 806-813.

(65) Dubey, P. K.; Mishra, V.; Jain, S.; Mahor, S.; Vyas, S. P. Liposomes Modified with Cyclic RGD Peptide for Tumor Targeting. *Journal of Drug Targeting* **2004,** *12* (5), 257-264.

(66) Wang, K.; Zhang, X.; Liu, Y.; Liu, C.; Jiang, B.; Jiang, Y. Tumor penetrability and anti-angiogenesis using iRGD-mediated delivery of doxorubicin-polymer conjugates. *Biomaterials* **2014,** *35* (30), 8735-8747.

(67) Ruoslahti, E.; Pierschbacher, M. D. New perspectives in cell adhesion: RGD and integrins. *Science* **1987,** *238* (4826), 491-497.

(68) Danhier, F.; Le Breton, A.; Préat, V. RGD-based strategies to target alpha (v) beta (3) integrin in cancer therapy and diagnosis. *Molecular pharmaceutics* **2012,** *9* (11), 2961-2973.

(69) Cebe-Suarez, S.; Zehnder-Fjällman, A.; Ballmer-Hofer, K. The role of VEGF receptors in angiogenesis; complex partnerships. *Cellular and molecular life sciences* **2006,** *63* (5), 601.

(70) Li, L.; Wartchow, C. A.; Danthi, S. N.; Shen, Z.; Dechene, N.; Pease, J.; Choi, H. S.; Doede, T.; Chu, P.; Ning, S.; Lee, D. Y.; Bednarski, M. D.; Knox, S. J. A novel antiangiogenesis therapy using an integrin antagonist or anti–Flk-1 antibody coated 90Y-labeled nanoparticles. *International Journal of Radiation Oncology*Biology*Physics* **2004,** *58* (4), 1215-1227.

(71) Backer, M. V.; Gaynutdinov, T. I.; Patel, V.; Bandyopadhyaya, A. K.; Thirumamagal, B.; Tjarks, W.; Barth, R. F.; Claffey, K.; Backer, J. M. Vascular endothelial growth factor selectively targets boronated dendrimers to tumor vasculature. *Molecular cancer therapeutics* **2005,** *4* (9), 1423-1429.

(72) Byrne, J. D.; Betancourt, T.; Brannon-Peppas, L. Active targeting schemes for nanoparticle systems in cancer therapeutics. *Advanced Drug Delivery Reviews* **2008,** *60* (15), 1615-1626.

(73) Xiao, Y.-D.; Paudel, R.; Liu, J.; Ma, C.; Zhang, Z.-S.; Zhou, S.-K. MRI contrast agents: Classification and application. *International journal of molecular medicine* **2016,** *38* (5), 1319-1326.

(74) Strijkers, G. J.; M. Mulder, W. J.; F. van Tilborg, G. A.; Nicolay, K. MRI Contrast Agents: Current Status and Future Perspectives. *Anti-Cancer Agents in Medicinal Chemistry- Anti-Cancer Agents)* **2007,** *7* (3), 291-305.

(75) Huang, G.; Li, H.; Chen, J.; Zhao, Z.; Yang, L.; Chi, X.; Chen, Z.; Wang, X.; Gao, J. Tunable T_1 and T_2 contrast abilities of manganese-engineered iron oxide nanoparticles through size control. *Nanoscale* **2014,** *6* (17), 10404-10412.

(76) Wahsner, J.; Gale, E. M.; Rodríguez-Rodríguez, A.; Caravan, P. Chemistry of MRI Contrast Agents: Current Challenges and New Frontiers. *Chemical Reviews* **2019,** *119* (2), 957-1057.

(77) Gao, Z.; Ma, T.; Zhao, E.; Docter, D.; Yang, W.; Stauber, R. H.; Gao, M. Small is Smarter: Nano MRI Contrast Agents – Advantages and Recent Achievements. *Small* **2016,** *12* (5), 556-576.

(78) Qiao, R.; Yang, C.; Gao, M. Superparamagnetic iron oxide nanoparticles: from preparations to in vivo MRI applications. *Journal of Materials Chemistry* **2009,** *19* (35), 6274-6293.

(79) Lee, N.; Yoo, D.; Ling, D.; Cho, M. H.; Hyeon, T.; Cheon, J. Iron oxide based nanoparticles for multimodal imaging and magnetoresponsive therapy. *Chemical Reviews* **2015,** *115* (19), 10637-10689.

(80) Zhang, H.; Li, L.; Liu, X. L.; Jiao, J.; Ng, C.-T.; Yi, J. B.; Luo, Y. E.; Bay, B.-H.; Zhao, L. Y.; Peng, M. L. Ultrasmall Ferrite Nanoparticles Synthesized via Dynamic Simultaneous Thermal Decomposition for High-Performance and Multifunctional T 1 Magnetic Resonance Imaging Contrast Agent. *ACS nano* **2017,** *11* (4), 3614-3631.

(81) Ramalho, M.; Ramalho, J.; Burke, L. M.; Semelka, R. C. Gadolinium Retention and Toxicity—An Update. *Advances in Chronic Kidney Disease* **2017,** *24* (3), 138-146.

(82) Rogosnitzky, M.; Branch, S, Gadolinium-based contrast agent toxicity: a review of known and proposed mechanisms. *BioMetals* **2016,** *29* (3), 365-376.

(83) Guo, B. J.; Yang, Z. L.; Zhang, L. J. Gadolinium Deposition in Brain: Current Scientific Evidence and Future Perspectives. *Frontiers in Molecular Neuroscience* **2018,** *11* (335).

(84) Gulani, V.; Calamante, F.; Shellock, F. G.; Kanal, E.; Reeder, S. B. Gadolinium deposition in the brain: summary of evidence and recommendations. *The Lancet Neurology* **2017,** *16* (7), 564-570.

(85) Harvey, H. B.; Gowda, V.; Cheng, G. Gadolinium Deposition Disease: A New Risk Management Threat. *Journal of the American College of Radiology* **2020,** *17* (4), 546-550.

(86) U.S. FDA. FDA Drug Safety Communication: FDA warns that gadolinium-based contrast agents (GBCAs) are retained in the body; requires new class warnings. https://www.fda.gov/drugs/drug-safety-and-availability/fda-drug-safety-communication-fda-warns-gadolinium-based-contrast-agents-gbcas-are-retained-body (accessed June 4, 2020).

(87) European Medicines Agency. EMA's final opinion confirms restrictions on use of linear gadolinium agents in body scans. https://www.ema.europa.eu/en/documents/press-release/emas-final-opinion-confirms-restrictions-use-linear-gadolinium-agents-body-scans_en.pdf (accessed June 4, 2020).

(88) Pirogov, Y. A. Multinuclear Magnetic Resonance Imaging and NMR Spectroscopy in Biomedical Investigations. *Physics Procedia* **2016,** *82*, 3-7.

(89) DeVience, S. J.; Pham, L. M.; Lovchinsky, I.; Sushkov, A. O.; Bar-Gill, N.; Belthangady, C.; Casola, F.; Corbett, M.; Zhang, H.; Lukin, M.; Park, H.; Yacoby, A.; Walsworth, R. L. Nanoscale

NMR spectroscopy and imaging of multiple nuclear species. *Nature Nanotechnology* **2015,** *10* (2), 129-134.

(90) Tirotta, I.; Dichiarante, V.; Pigliacelli, C.; Cavallo, G.; Terraneo, G.; Bombelli, F. B.; Metrangolo, P.; Resnati, G. ^{19}F Magnetic Resonance Imaging (MRI): from design of materials to clinical applications. *Chemical reviews* **2014,** *115* (2), 1106-1129.

(91) Cho, M. H.; Shin, S. H.; Park, S. H.; Kadayakkara, D. K.; Kim, D.; Choi, Y. Targeted, Stimuli-Responsive, and Theranostic ^{19}F Magnetic Resonance Imaging Probes. *Bioconjugate chemistry* **2019,** *30* (10), 2502-2518.

(92) Darçot, E.; Colotti, R.; Pellegrin, M.; Wilson, A.; Siegert, S.; Bouzourene, K.; Yerly, J.; Mazzolai, L.; Stuber, M.; van Heeswijk, R. B. Towards Quantification of Inflammation in Atherosclerotic Plaque in the Clinic - Characterization and Optimization of Fluorine-19 MRI in Mice at 3 T. *Scientific Report* **2019,** *9* (1), 17488.

(93) Hequet, E.; Henoumont, C.; Muller, R. N.; Laurent, S. Fluorinated MRI contrast agents and their versatile applications in the biomedical field. *Future medicinal chemistry* **2019,** *11* (10), 1157-1175.

(94) Janjic, J. M.; Srinivas, M.; Kadayakkara, D. K.; Ahrens, E. T. Self-delivering nanoemulsions for dual fluorine-19 MRI and fluorescence detection. *Journal of the American Chemical Society* **2008,** *130* (9), 2832-2841.

(95) Barres, A. R.; Lechuga, L. M.; Tangsangasaksri, M.; Ludwig, K. D.; Fain, S. B.; Mecozzi, S. A stable, highly concentrated fluorous nanoemulsion formulation for *in vivo* cancer imaging via ^{19}F-MRI. *Manuscript submitted for publication.* **2020**.

(96) Flaim, S. F. Pharmacokinetics and Side Effects of Perfluorocarbon-Based Blood Substitutes. *Artificial Cells, Blood Substitutes, and Biotechnology* **1994,** *22* (4), 1043-1054.

(97) Díaz-López, R.; Tsapis, N.; Fattal, E. Liquid Perfluorocarbons as Contrast Agents for Ultrasonography and 19F-MRI. *Pharmaceutical Research* **2009,** *27* (1), 1.

(98) Cosco, D.; Fattal, E.; Fresta, M.; Tsapis, N. Perfluorocarbon-loaded micro and nanosystems for medical imaging: A state of the art. *Journal of Fluorine Chemistry* **2015,** *171*, 18-26.

(99) Riess, J. G. Oxygen Carriers ("Blood Substitutes")Raison d'Etre, Chemistry, and Some Physiology Blut ist ein ganz besondrer Saft. *Chemical Reviews* **2001,** *101* (9), 2797-2920.

(100) Jacoby, C.; Temme, S.; Mayenfels, F.; Benoit, N.; Krafft, M. P.; Schubert, R.; Schrader, J.; Flögel, U. Probing different perfluorocarbons for in vivo inflammation imaging by ^{19}F MRI: image reconstruction, biological half-lives and sensitivity. *NMR in Biomedicine* **2014,** *27* (3), 261-271.

(101) Krafft, M. P.; Riess, J. G. Chemistry, Physical Chemistry, and Uses of Molecular Fluorocarbon−Hydrocarbon Diblocks, Triblocks, and Related Compounds—Unique "Apolar" Components for Self-Assembled Colloid and Interface Engineering. *Chemical Reviews* **2009,** *109* (5), 1714-1792.

(102) Stevens, T. K.; Ramirez, R. M.; Pines, A. Nanoemulsion Contrast Agents with Sub-picomolar Sensitivity for Xenon NMR. *Journal of the American Chemical Society* **2013,** *135* (26), 9576-9579.

(103) Lee, S.-J.; Olsen, B.; Schlesinger, P. H.; Baker, N. A. Characterization of Perfluorooctylbromide-Based Nanoemulsion Particles Using Atomistic Molecular Dynamics Simulations. *The Journal of Physical Chemistry B* **2010,** *114* (31), 10086-10096.

(104) Rossi, M. Use of lecithin and lecithin fractions. In *Bioactive egg compounds*, Springer: 2007; pp 229-239.

(105) Lim, Y. T.; Noh, Y.-W.; Kwon, J.-N.; Chung, B. H. Multifunctional perfluorocarbon nanoemulsions for ^{19}F-based magnetic resonance and near-infrared optical imaging of dendritic cells. *Chemical Communications* **2009,** (45), 6952-6954.

(106) Nienhaus, F.; Colley, D.; Jahn, A.; Pfeiler, S.; Flocke, V.; Temme, S.; Kelm, M.; Gerdes, N.; Flögel, U.; Bönner, F. Phagocytosis of a PFOB-Nanoemulsion for 19F Magnetic Resonance Imaging: First Results in Monocytes of Patients with Stable Coronary Artery Disease and ST-Elevation Myocardial Infarction. *Molecules* **2019,** *24* (11), 2058.

(107) Barres, A. R.; Molugu, S. K.; Stewart, P. L.; Mecozzi, S. Droplet Core Intermolecular Interactions and Block Copolymer Composition Heavily Influence Oil-In-Water Nanoemulsion Stability. *Langmuir* **2019,** *35* (39), 12765-12772.

(108) Patel, S. K.; Patrick, M.; Pollock, J.; Janjic, J. Two-color fluorescent (near-infrared and visible) triphasic perfluorocarbon nanoemulsions. *Journal of Biomedical Optics* **2013,** *18* (10), 101312.

(109) O'Hanlon, C. E.; Amede, K. G.; O'Hear, M. R.; Janjic, J. M. NIR-labeled perfluoropolyether nanoemulsions for drug delivery and imaging. *Journal of Fluorine Chemistry* **2012,** *137*, 27-33.

(110) Patel, S. K.; Beaino, W.; Anderson, C. J.; Janjic, J. M. Theranostic nanoemulsions for macrophage COX-2 inhibition in a murine inflammation model. *Clinical Immunology* **2015,** *160* (1), 59-70.

(111) Patel, S. K.; Zhang, Y.; Pollock, J. A.; Janjic, J. M. Cyclooxgenase-2 Inhibiting Perfluoropoly (Ethylene Glycol) Ether Theranostic Nanoemulsions—In Vitro Study. *PLOS ONE* **2013,** *8* (2), e55802.

(112) Hingorani, D. V.; Chapelin, F.; Stares, E.; Adams, S. R.; Okada, H.; Ahrens, E. T. Cell penetrating peptide functionalized perfluorocarbon nanoemulsions for targeted cell labeling and enhanced fluorine-19 MRI detection. *Magnetic Resonance in Medicine* **2020,** *83* (3), 974-987.

(113) Flögel, U.; Ding, Z.; Hardung, H.; Jander, S.; Reichmann, G.; Jacoby, C.; Schubert, R.; Schrader, J. In vivo monitoring of inflammation after cardiac and cerebral ischemia by ^{19}F magnetic resonance imaging. *Circulation* **2008,** *118* (2), 140.

(114) Wang, Y.-G.; Kim, H.; Mun, S.; Kim, D.; Choi, Y. Indocyanine green-loaded perfluorocarbon nanoemulsions for bimodal 19F-magnetic resonance/nearinfrared fluorescence imaging and subsequent phototherapy. *Quantitative imaging in medicine and surgery* **2013,** *3* (3), 132.

(115) Shin, S. H.; Park, E.-J.; Min, C.; Choi, S. I.; Jeon, S.; Kim, Y.-H.; Kim, D. Tracking perfluorocarbon nanoemulsion delivery by ^{19}F MRI for precise high intensity focused ultrasound tumor ablation. *Theranostics* **2017,** *7* (3), 562.

(116) Patel, S. K.; Williams, J.; Janjic, J. M. Cell labeling for 19F MRI: new and improved approach to perfluorocarbon nanoemulsion design. *Biosensors* **2013,** *3* (3), 341-359.

(117) Peng, Q.; Li, Y.; Bo, S.; Yuan, Y.; Yang, Z.; Chen, S.; Zhou, X.; Jiang, Z.-X. Paramagnetic nanoemulsions with unified signals for sensitive ^{19}F MRI cell tracking. *Chemical communications* **2018,** *54* (47), 6000-6003.

(118) Tirotta, I.; Mastropietro, A.; Cordiglieri, C.; Gazzera, L.; Baggi, F.; Baselli, G.; Bruzzone, M. G.; Zucca, I.; Cavallo, G.; Terraneo, G. A superfluorinated molecular probe for highly sensitive in vivo ^{19}F-MRI. *Journal of the American Chemical Society* **2014,** *136* (24), 8524-8527.

(119) Nieuwoudt, M.; Engelbrecht, G. H. C.; Sentle, L.; Auer, R.; Kahn, D.; van der Merwe, S. W. Non-toxicity of IV Injected Perfluorocarbon Oxygen Carrier in an Animal Model of Liver Regeneration Following Surgical Injury. *Artificial Cells, Blood Substitutes, and Biotechnology* **2009,** *37* (3), 117-124.

(120) Klein, D. H.; Jones, R. C.; Keipert, P. E.; Luena, G. A.; Otto, S.; Weers, J. G. Intravascular behavior of perflubron emulsions. *Colloids and Surfaces A: Physicochemical and Engineering Aspects* **1994,** *84* (1), 89-95.

(121) Criscione, J. M.; Le, B. L.; Stern, E.; Brennan, M.; Rahner, C.; Papademetris, X.; Fahmy, T. M. Self-assembly of pH-responsive fluorinated dendrimer-based particulates for drug delivery and noninvasive imaging. *Biomaterials* **2009,** *30* (23), 3946-3955.

(122) Jiang, Z.-X.; Liu, X.; Jeong, E.-K.; Yu, Y. B. Symmetry-Guided Design and Fluorous Synthesis of a Stable and Rapidly Excreted Imaging Tracer for 19F MRI. *Angewandte Chemie International Edition* **2009,** *48* (26), 4755-4758.

(123) Yu, Y. B. Fluorinated dendrimers as imaging agents for ^{19}F MRI. *Wiley Interdisciplinary Reviews: Nanomedicine and Nanobiotechnology* **2013,** *5* (6), 646-661.

(124) Yu, W.; Yang, Y.; Bo, S.; Li, Y.; Chen, S.; Yang, Z.; Zheng, X.; Jiang, Z.-X.; Zhou, X. Design and Synthesis of Fluorinated Dendrimers for Sensitive ^{19}F MRI. *The Journal of Organic Chemistry* **2015,** *80* (9), 4443-4449.

(125) Xiao, Q.; Rubien, J. D.; Wang, Z.; Reed, E. H.; Hammer, D. A.; Sahoo, D.; Heiney, P. A.; Yadavalli, S. S.; Goulian, M.; Wilner, S. E.; Baumgart, T.; Vinogradov, S. A.; Klein, M. L.; Percec, V. Self-Sorting and Coassembly of Fluorinated, Hydrogenated, and Hybrid Janus Dendrimers into Dendrimersomes. *Journal of the American Chemical Society* **2016,** *138* (38), 12655-12663.

(126) Liu, X.; Yuan, Y.; Bo, S.; Li, Y.; Yang, Z.; Zhou, X.; Chen, S.; Jiang, Z. X. Monitoring Fluorinated Dendrimer - Based Self - Assembled Drug - Delivery Systems with ^{19}F Magnetic Resonance. *European Journal of Organic Chemistry* **2017,** *2017* (30), 4461-4468.

(127) Zhang, H.; Bo, S.; Zeng, K.; Wang, J.; Li, Y.; Yang, Z.; Zhou, X.; Chen, S.; Jiang, Z.-X. Fluorinated porphyrin-based theranostics for dual imaging and chemo-photodynamic therapy. *Journal of Materials Chemistry B* **2020,** *8* (20), 4469-4474.

(128) Zhang, C.; Moonshi, S. S.; Han, Y.; Puttick, S.; Peng, H.; Magoling, B. J. A.; Reid, J. C.; Bernardi, S.; Searles, D. J.; Král, P.; Whittaker, A. K. PFPE-Based Polymeric ^{19}F MRI Agents: A New Class of Contrast Agents with Outstanding Sensitivity. *Macromolecules* **2017,** *50* (15), 5953-5963.

(129) Nurmi, L.; Peng, H.; Seppälä, J.; Haddleton, D. M.; Blakey, I.; Whittaker, A. K. Synthesis and evaluation of partly fluorinated polyelectrolytes as components in ^{19}F MRI-detectable nanoparticles. *Polymer Chemistry* **2010,** *1* (7), 1039-1047.

(130) Wang, K.; Peng, H.; Thurecht, K. J.; Puttick, S.; Whittaker, A. K. Segmented highly branched copolymers: Rationally designed macromolecules for improved and tunable ^{19}F MRI. *Biomacromolecules* **2015,** *16* (9), 2827-2839.

(131) Fu, C.; Zhang, C.; Peng, H.; Han, F.; Baker, C.; Wu, Y.; Ta, H.; Whittaker, A. K. Enhanced Performance of Polymeric ^{19}F MRI Contrast Agents through Incorporation of Highly Water-Soluble Monomer MSEA. *Macromolecules* **2018,** *51* (15), 5875-5882.

(132) Bo, S.; Song, C.; Li, Y.; Yu, W.; Chen, S.; Zhou, X.; Yang, Z.; Zheng, X.; Jiang, Z.-X. Design and Synthesis of Fluorinated Amphiphile as ^{19}F MRI/Fluorescence Dual-Imaging Agent by Tuning the Self-Assembly. *The Journal of Organic Chemistry* **2015,** *80* (12), 6360-6366.

(133) Arvizo, R.; Bhattacharya, R.; Mukherjee, P. Gold nanoparticles: opportunities and challenges in nanomedicine. *Expert opinion on drug delivery* **2010,** *7* (6), 753-763.

(134) Gentilini, C.; Boccalon, M.; Pasquato, L. Straightforward Synthesis of Fluorinated Amphiphilic Thiols. *European Journal of Organic Chemistry* **2008,** *2008* (19), 3308-3313.

(135) Niikura, K.; Iyo, N.; Higuchi, T.; Nishio, T.; Jinnai, H.; Fujitani, N.; Ijiro, K. Gold Nanoparticles Coated with Semi-Fluorinated Oligo(ethylene glycol) Produce Sub-100 nm Nanoparticle Vesicles without Templates. *Journal of the American Chemical Society* **2012,** *134* (18), 7632-7635.

(136) Boccalon, M.; Franchi, P.; Lucarini, M.; Delgado, J. J.; Sousa, F.; Stellacci, F.; Zucca, I.; Scotti, A.; Spreafico, R.; Pengo, P.; Pasquato, L. Gold nanoparticles protected by fluorinated ligands for ^{19}F MRI. *Chemical Communications* **2013,** *49* (78), 8794-8796.

(137) Michelena, O.; Padro, D.; Carrillo-Carrión, C.; del Pino, P.; Blanco, J.; Arnaiz, B.; Parak, W. J.; Carril, M. Novel fluorinated ligands for gold nanoparticle labelling with applications in ^{19}F-MRI. *Chemical Communications* **2017,** *53* (16), 2447-2450.

(138) Matsushita, H.; Mizukami, S.; Sugihara, F.; Nakanishi, Y.; Yoshioka, Y.; Kikuchi, K. Multifunctional Core–Shell Silica Nanoparticles for Highly Sensitive ^{19}F Magnetic Resonance Imaging. *Angewandte Chemie International Edition* **2014,** *53* (4), 1008-1011.

(139) Nakamura, T.; Sugihara, F.; Matsushita, H.; Yoshioka, Y.; Mizukami, S.; Kikuchi, K. Mesoporous silica nanoparticles for ^{19}F magnetic resonance imaging, fluorescence imaging, and drug delivery. *Chemical science* **2015,** *6* (3), 1986-1990.

(140) Bouchoucha, M.; van Heeswijk, R. B.; Gossuin, Y.; Kleitz, F.; Fortin, M.-A. Fluorinated mesoporous silica nanoparticles for binuclear probes in ^{1}H and ^{19}F magnetic resonance imaging. *Langmuir* **2017,** *33* (40), 10531-10542.

(141) Zhu, X.; Tang, X.; Lin, H.; Shi, S.; Xiong, H.; Zhou, Q.; Li, A.; Wang, Q.; Chen, X.; Gao, J. A Fluorinated Ionic Liquid-Based Activatable ^{19}F MRI Platform Detects Biological Targets. *Chem* **2020,** *6* (5), 1134-1148.

(142) Peterson, K. L.; Srivastava, K.; Pierre, V. C. Fluorinated Paramagnetic Complexes: Sensitive and Responsive Probes for Magnetic Resonance Spectroscopy and Imaging. *Frontiers in Chemistry* **2018,** *6* (160).

(143) Kislukhin, A. A.; Xu, H.; Adams, S. R.; Narsinh, K. H.; Tsien, R. Y.; Ahrens, E. T. Paramagnetic fluorinated nanoemulsions for sensitive cellular fluorine-19 magnetic resonance imaging. *Nature materials* **2016,** *15* (6), 662-668.

(144) Harvey, P.; Kuprov, I.; Parker, D. Lanthanide Complexes as Paramagnetic Probes for ^{19}F Magnetic Resonance. *European Journal of Inorganic Chemistry* **2012,** *2012* (12), 2015-2022.

(145) Jahromi, A. H.; Wang, C.; Adams, S. R.; Zhu, W.; Narsinh, K.; Xu, H.; Gray, D. L.; Tsien, R. Y.; Ahrens, E. T. Fluorous-Soluble Metal Chelate for Sensitive Fluorine-19 Magnetic Resonance Imaging Nanoemulsion Probes. *ACS nano* **2018,** *13* (1), 143-151.

(146) Barres, A. R.; Wimmer, M. R.; Mecozzi, S. Multicompartment theranostic nanoemulsions stabilized by a triphilic semifluorinated block copolymer. *Molecular pharmaceutics* **2017,** *14* (11), 3916-3926.

CHAPTER 2 – DEVELOPMENT OF IRGD CONJUGATED SEMIFLUORINATED NANOASSEMBLIES FOR TARGETED DRUG DELIVERY

This chapter has been submitted, in part, as a manuscript – Reference: Decato, S.E.[#], Tangsangasaksri, M.[#], Tucker, W.B., Madsen, E.J., Miura, Y., Matsumoto Y., Kataoka K., and Mecozzi, S. "Long-circulating, tumor-targeting drug nanocarriers: in vivo stability of triphilic polymer self-assemblies enhanced by branched semi-fluorinated cores". *Submitted*. ([#]equal contribution).

Abstract

The administration of small molecule anticancer drugs leads to inevitable side effects on patients due to nonselective properties of the drugs. Drug delivery carriers have been extensively studied to overcome the nonselective properties of chemotherapeutics and prolong their blood circulation time. Passive targeting of nanoparticles through the enhanced permeability and retention (EPR) effect allows an improved accumulation of nanoparticles at the tumor site; however, due to tumor heterogeneity, limited accumulation is still a major hurdle for achieving high therapeutic efficiency. Herein, an internalizing RGD (iRGD), an active targeting ligand, was utilized to improve tumor targeting and tissue penetration. The iRGD was covalently conjugated to our novel semifluorinated polymer containing a tri-perfluoro-*tert*-butyl ($PFtB_{TRI}$) group as a fluorophilic segment. Our previous studies have demonstrated that the use of a fluorocarbon moiety in triphilic copolymers provides enhanced stability to the corresponding self-assembled nanoparticles, thus allowing longer *in vivo* circulation times. The iRGD conjugated semifluorinated micelles exhibited a high cellular uptake in 2D monolayer cultured cells and deep penetration in 3D tumor spheroids. The increased circulation of the semifluorinated micelles, coupled with the enhanced accumulation and penetration abilities of the iRGD demonstrates the synergistic potential of the multifunctional micelle design.

2.1 Introduction

Currently, cancer is the second leading cause of death worldwide. The number of new cancer cases increased from 15.2 million in 2015 to 18.1 million in 2018 globally.[1-2] The World Health Organization (WHO) has estimated that the number of new cancer cases will keep increasing and it will reach 23.9 million new cases by 2035.[1] There are several methods being used for cancer treatment, with chemotherapy as one of the most common treatment methods.[3] This conventional method involves the use of small molecules that primarily interfere with the mitotic phase cell cycle (such as paclitaxel[4]) or DNA synthesis (such as doxorubicin[5] and 5-fluorouracil[6]), preventing cell replication processes and leading to the deaths of the fast growing and rapidly dividing cancer cells. There are several challenges associated with the delivery of these molecules for clinical application. For example, since many small molecule anticancer drugs are hydrophobic in nature, they are poorly water-soluble which limits their bioavailability.[7-9] Moreover, the small size of anticancer drugs allows for non-selective diffusion of the molecules across the cell membrane of both healthy and cancer cells, resulting in undesirable side effects.[10] Therefore, the development of delivery carriers is desirable to improve the water solubility and the selective properties of small molecules. Nanoparticles have been extensively studied for the past decades as a delivery carrier in cancer therapy. A wide range of nanomaterials has been developed and used for preparation of different types of nanoparticles, such as polymers, lipids, silica, gold, etc. The nanoparticle improves the hydrophobic drugs' solubility by encapsulating the hydrophobic molecules inside the hydrophilic shell. By increasing the overall size of the small molecules with nanoparticles, the non-selective diffusion to healthy tissue is avoided, thus, reducing the undesirable side effects. Moreover, the nanoparticle also improves therapeutic efficacy by selective accumulation at the tumor site through the enhanced permeability and retention (EPR) effect (as previously discussed in *Chapter 1.3*).

This passive targeting *via* EPR effect, however, also faces several challenges that lead to a limited accumulation of nanoparticles. Heterogeneity of the tumors is one of the main concerns for EPR

effectiveness. Different sizes and types of tumors, vasculature formation, and tumor necrosis, together, play a role in tumor heterogeneity which can lead to low passive targeting efficiency.[11-12] Moreover, the EPR effect is a slow and time-dependent process.[13-14] The extravasation of nanoparticles depends on its concentration in the bloodstream. Therefore, to achieve a high accumulation, nanoparticles are required to have a long systemic circulation half-life.[13] To improve the accumulation of nanoparticles, active targeting ligands such as antibodies, proteins, and peptides have been introduced. Active targeting, so-called ligand-mediated targeting, is a targeting method that incorporates various ligands on the nanoparticles which bind to specific receptors presented on the cell surface.[15] One of the commonly use targeting ligand is a small cyclic peptide called cyclic RGD (cRGD). This RGD (Arginine-Glycine-Aspartic acid) motif targets and binds to α_v integrins that are overexpressed on activated endothelial cells and tumor cells, thus, leading to an increased accumulation of the nanoparticles at the tumor site.[16-17] However, because of high interstitial fluid pressure (IFP) in the tumor, the distribution of these nanoparticles to the deeper tumor tissues is restricted. As a result, the treatment to those distant tumor tissues is impossible, leading to a reduced therapeutic efficacy.[18-20]

In recent years, researchers have reported a new small cyclic tumor-penetrating peptide, an internalizing RGD (iRGD), that showed a tumor permeability effect.[19, 21] Unlike normal cRGD where the peptide can only targets α_v integrins for improved accumulation, iRGD, in addition to the tumor-homing ability through the RGD motif, also possesses a C-end Rule (CendR) motif that can trigger receptor-mediated transcytosis pathway. This CendR motif is a C-terminal arginine residue with a sequence R/KXXR/K where X is any amino acid. It specifically binds to neuropilin-1 (NRP-1) receptor which triggers the transcytosis pathway, resulting in a penetration into the tumor tissue.[19, 21-23] Therefore, iRGD is a tumor specific penetrating peptide which actively targets tumors through a two-step mechanism. First, specific binding to α_v integrins overexpressed on tumor endothelial cells enhances tumor accumulation. Next, a subsequent proteolytic cleavage exposes the CendR motif, a sequence recognized by NRP-1 receptor, inducing transcytosis pathway, resulting in tissue penetration (**Figure 2.1**).[19-24]

The discovery of iRGD leads to numerous efforts exploiting the advantages of iRGD for improving therapeutic efficacy. iRGD can be co-administered with therapeutic compounds (e.g. small molecules[25], nanoparticles[26-27], or antibodies[26, 28]), where the payloads are transported through a bystander effect, or covalently conjugated to the cargos.[24, 29-30] Even though the co-administration of iRGD may be preferable due to its relatively simple preparation, the short half-life of the peptide serves as a major drawback that could reduce the overall efficacy.[20] To increase the half-life of the peptide, the iRGD can be covalently conjugated to a long circulating nanoparticle.

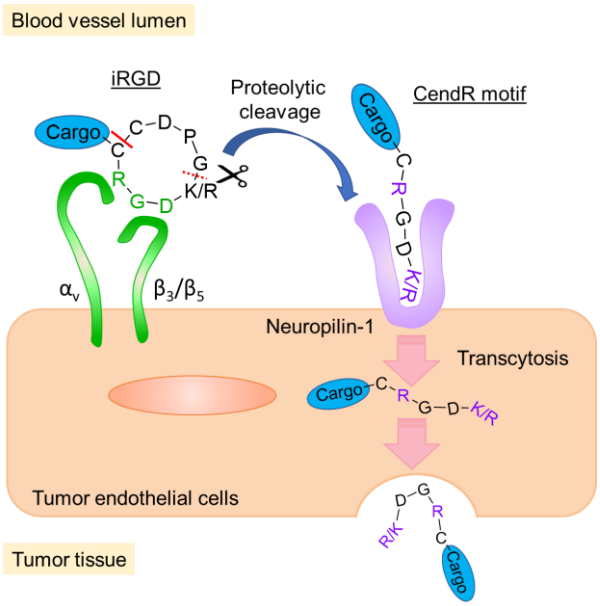

Figure 2.1 Mechanism of iRGD for nanocarrier delivery. The iRGD peptide binds to α_v integrins overexpressed on tumor endothelial cells through the RGD (Arg-Gly-Asp) motif, allowing the accumulation of the attached cargo (nanoparticles or drugs). The cleavage at C terminus along the red dotted line *via* a proteolytic cleavage exposes the CendR motif, a sequence specific to neuropilin-1 (NRP-1) binding. This binding results in cargo transportation through tissues and cells, enabling deep penetration of the attached cargo, since the cargo is attached to the N terminus of iRGD. The cleave of the disulfide bond at the black line can happen before internalization of the peptide. Figure adapted from Sugahara *et al*.[19]

Semifluorinated polymers are triblock copolymers consisting of a fluorocarbon, hydrocarbon, and poly(ethylene glycol) (PEG) segment. The dual hydrophobic and lipophobic properties of fluorocarbon can lead to self-aggregation of the fluorous segment, which provides the nanoaggregates with enhanced stability, allowing its beneficial usage in drug delivery system.[31-32] As shown in **Figure 2.2**, the nanoaggregates, called micelles, are formed from the self-assembly of semifluorinated triblock copolymers.

These semifluorinated micelles encapsulate hydrophobic molecules inside the hydrophobic segment, leaving PEG (a hydrophilic moiety) as a corona and providing water-solubility properties. It should be noted that the formation of fluorophilic core provides a stable micellar core due to the self-aggregation of fluorocarbon, leading to less unimer dynamics at the equilibrium.[33]

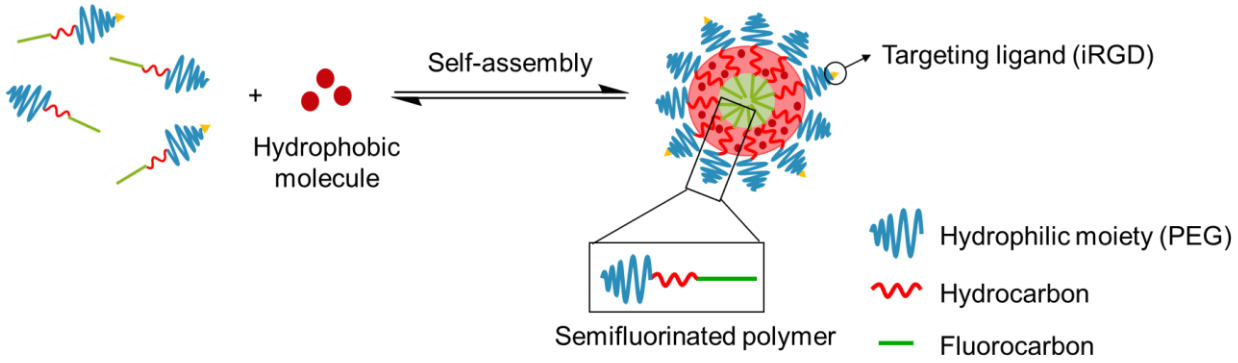

Figure 2.2 Semifluorinated micelle formation. Schematic of the hydrophobic molecule loaded micelle formation equilibrium. The semifluorinated polymer contains a fluorophilic core (green), a lipophilic shell (red), and a hydrophilic corona (blue).

Herein, we introduce a novel semifluorinated polymer containing tri-perfluoro-*tert*-butyl ($PFtB_{TRI}$) as the fluorocarbon block that, when formed as a micelle, can be used as a carrier in a drug delivery system.[32] Our previous studies have demonstrated that the use of a fluorocarbon moiety in triphilic copolymers provides enhanced stability to the corresponding self-assembled micelles, thus allowing longer *in vivo* circulation times (unpublished results). Since these long-circulating micelles only engage in passive targeting (EPR effect), the particles have limited accumulation at the tumor site. Therefore, iRGD was covalently conjugated to our semifluorinated polymers to enhance the accumulation and tissue penetration of the micelles and improve the pharmacokinetics properties of the iRGD peptide.

This chapter describes the synthetic methods of the iRGD conjugated semifluorinated polymer, iRGD-PMPI-P2H10$PFtB_{TRI}$ (**Figure 2.3**). The physicochemical characteristics of the polymer will be discussed. The formulation of iRGD micelles will be presented and evaluated *in vitro*. The improved accumulation and penetration properties of the iRGD functionalized micelles will be demonstrated in both traditional 2D monolayer culture cells and 3D multicellular spheroids.

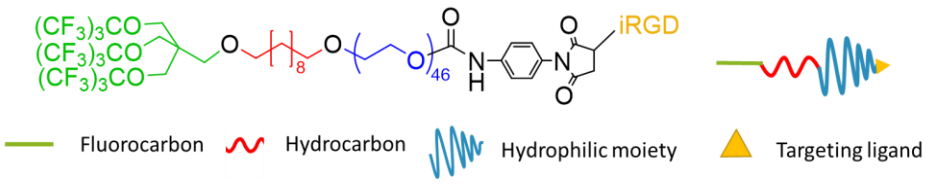

Figure 2.3 Structure of iRGD-PMPI-P2H10PFtB$_{TRI}$.

2.2 Results and Discussion

2.2.1 Synthesis of N-[(4-azidocarbonyl)phenyl]maleimide (ACPM)

To develop the functionalized polymer, a linker that possesses bifunctionality is essential. The specific linker, in this case, has to provide a good coupling with both iRGD (containing free thiol group) and the semifluorinated polymer (containing free hydroxyl group). *N*-[(4-azidocarbonyl)phenyl]maleimide (ACPM) was selected due to its specific bifunctionality consisting of maleimide and acyl azide functional groups for coupling with the thiol and hydroxyl groups, respectively. The maleimide group reacts specifically with the thiol moiety *via* click chemistry while acyl azide group can undergo a Curtius rearrangement, generating an isocyanate *in situ*, which can easily react with hydroxyl groups. ACPM was synthesized according to previously published paper by T. Oishi and M. Fujimoto[34] (**Scheme 2.1**) *via* three-step reaction. The reaction started by reacting maleic anhydride with *p*-amino-benzoic acid in DMF to give *N*-(4-carboxyphenyl)maleamic acid (*p*-CPMA, **2-1**). The ring closure of *p*-CPMA (**2-1**) was carried out in the presence of acetic anhydride (Ac_2O) and sodium acetate (AcONa), resulting in *N*-(4-carboxyphenyl)maleimide (*p*-CPMI, **2-2**). Finally, the carboxylic acid was transformed to an acyl azide moiety by reacting **2-2** with diphenylphosphoryl azide (DPPA) to give ACPM as yellow crystals. The linker was kept in an azide form due to its higher stability over an isocyanate. The isocyanate group will be generated *in situ* during the coupling reaction with the semifluorinated polymer.

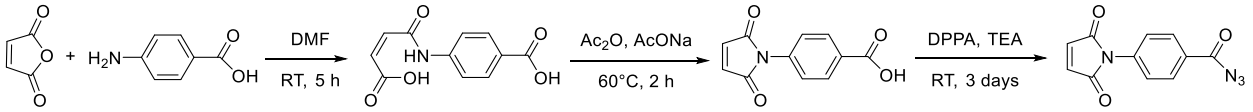

Scheme 2.1 Synthesis of ACPM linker.

2.2.2 Synthesis of iRGD-conjugated PFtB$_{TRI}$ polymer "iRGD-PMPI-P2H10PFtB$_{TRI}$"

The semifluorinated polymer with (iRGD-PMPI-P2H10PFtB$_{TRI}$) and without (M2H10PFtB$_{TRI}$) the iRGD ligand were synthesized. The nomenclatures for the polymers are as follows: i) P2 or M2 represents poly(ethylene glycol) (PEG) with hydroxy capped and methoxy capped at the α position, respectively, where 2 is the average molecular weight in the thousands, ii) H10 represents the hydrocarbon block where 10 is the number of carbon atoms substituted with hydrogens, and iii) PFtB$_{TRI}$ represents the fluorocarbon block with the tri-perfluoro-*tert*-butanol structure. The polymers were synthesized in a block manner. The first synthesized block was PFtB$_{TRI}$, the fluorocarbon block. PFtB$_{TRI}$-OH was synthesized according to the previously published paper in our group by Decato *et al*.[32] The fluorous alcohol was then coupled with the second hydrocarbon block, 9-decen-1-OMs, through a Williamson ether synthesis to give **2-4**, followed by a hydroboration reaction, resulting in the diblock HO-H10PFtB$_{TRI}$ (**2-5**, the synthesis was developed in our lab by Dr. Sarah Decato). Finally, to couple the last PEG block, the mesylated methoxy capped PEG (M2-OMs) was used to react with HO-H10PFtB$_{TRI}$ (**2-5**) through a Williamson ether synthesis under basic conditions to yield the final M2H10PFtB$_{TRI}$ polymer (**2-6**). M2H10PFtB$_{TRI}$ was purified by an automated CombiFlash system, resulting in a pure isolated polymer with high yield (**Scheme 2.2**).

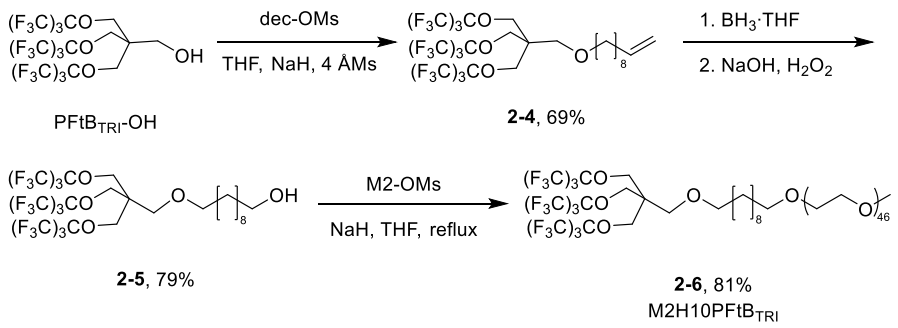

Scheme 2.2 Synthesis of M2H10PFtB$_{TRI}$.

The iRGD-PMPI-P2H10PFtB$_{TRI}$ was synthesized in a similar manner to M2H10PFtB$_{TRI}$ by using hydroxy capped PEG (P2) instead of methoxy capped PEG (M2). Changing the starting material to monoprotected PEG mesylate (**2-8**) allows an additional conjugation/modification to the polymer. A benzyl ether (-OBn) was selected as a protecting group due to its stability in different reaction conditions and its straightforward deprotection. The monobenzylated PEG was synthesized according to Bouzide, A., & Sauvé, G.[35] with some modifications. Briefly, PEG diol was reacted with benzyl bromide (BnBr, 1.1 eq) mediated by silver(I) oxide (Ag_2O) in the presence of KI as a catalyst. The resulting crude product was purified by column chromatography using MeOH/DCM (0 – 10%) as the eluent to yield BnO-P2-OH (**2-7**) (**Scheme 2.3a**). Compound **2-7** was mesylated under basic conditions to give **2-8**. The monobenzylated PEG mesylate (**2-8**) was then used to couple with HO-H10PFtB$_{TRI}$ (**2-5**) to yield the benzylated triblock copolymer intermediate, **2-9**. Hydrogenation of **2-9** using palladium on carbon (Pd/C) as the catalyst in the presence of hydrogen gas gave the alcohol of the triblock copolymer, HO-P2-H10-PFtB$_{TRI}$, **2-10**. The hydroxyl group was transformed to a maleimide linker by a reaction with *p*-maleimidophenyl isocyanate (PMPI) generated *in situ* through a thermal induced Curtius rearrangement of ACPM (**2-3**) to yield PMPI-P2H10PFtB$_{TRI}$, **2-11**. The iRGD peptide was then conjugated to the semifluorinated polymer through a thiol-maleimide coupling reaction, giving iRGD-PMPI-P2H10PFtB$_{TRI}$ (**2-12**) (**Scheme 2.3b**). The crude product was dialyzed against water to remove unreacted iRGD. The successful conjugation of iRGD to the semifluorinated polymer was confirmed by MALDI-MS.

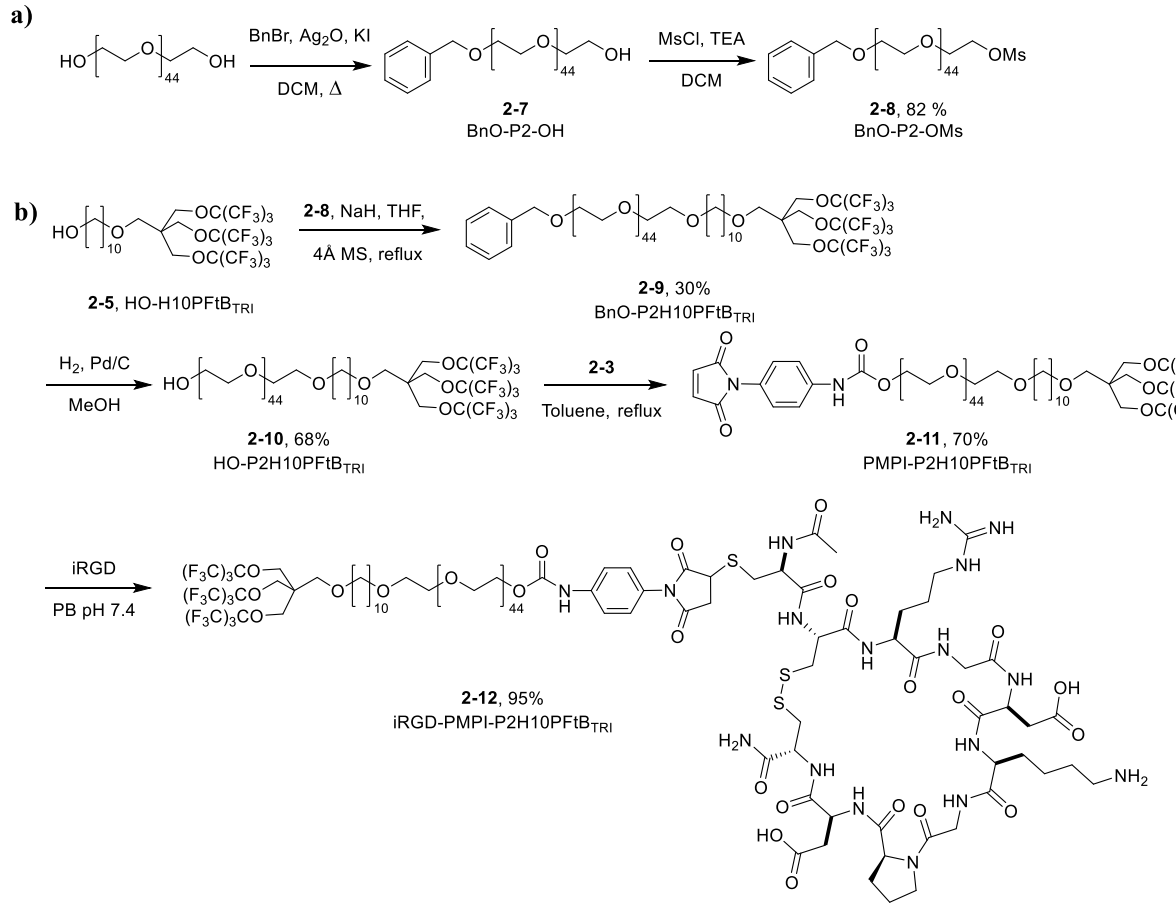

Scheme 2.3 Synthesis of a) Bn-P2-OMs and b) iRGD-PMPI-P2H10PFtB$_{TRI}$.

2.2.3 Physicochemical characterization of polymeric micelles

The M2H10PFtB$_{TRI}$ polymer was characterized and compared with a mono-branched fluorocarbon, M2H10PFtB$_{MONO}$, and a linear fluorocarbon, M2H10F13, shown in **Figure 2.4**. All three polymers can self-assemble to form small, discrete micelles in aqueous solution at a sub-millimolar critical micelle concentrations (CMCs). It is important to note that the semifluorinated micelles remained below 30 nm and maintained a narrow size distribution (**Table 2.1**). However, when carefully comparing the sizes of all aggregates, M2H10PFtB$_{TRI}$ and M2H10PFtB$_{MONO}$ showed similar aggregate sizes (11 and 14 nm, respectively) while the linear version of fluorous block, M2H10F13, demonstrated an increased in size (23 nm). These results agree well with the observed higher aggregation number of M2H10F13 compared to M2H10PFtB$_{TRI}$ and M2H10PFtB$_{MONO}$. This suggests that a larger amount of polymer is needed for

M2H10F13 to form a stable micellar core, thus, resulting in larger particles. In addition, all three polymers revealed different aggregation numbers with $N_{agg,M2H10PFtB_{TRI}} < N_{agg,M2H10PFtB_{MONO}} < N_{agg,M2H10F13}$, indicating that the shape of the fluorous block has an effect on the number of unimers that form a thermodynamically stable micelle.

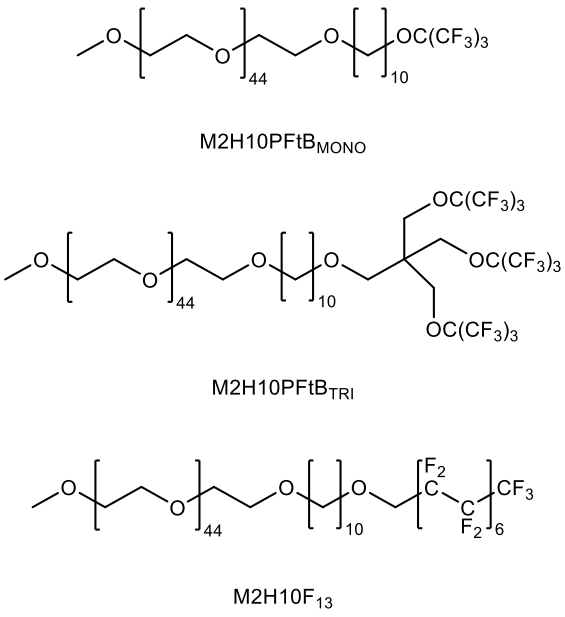

Figure 2.4 Structure of different semifluorinated polymers synthesized in the Mecozzi Lab.

Table 2.1 Physicochemical characterization of different semifluorinated polymers.

Compound	pCMC (-log(M))	Diameter (nm)[c]	Aggregation number (N_{agg})[d]
M2H10PFtB$_{MONO}$	4.82 ± 0.05[a]	11 ± 2	65 ± 4
M2H10PFtB$_{TRI}$	4.94 ± 0.01[b]	14 ± 5	56 ± 2
M2H10F13	4.49 ± 0.18[a]	23 ± 8	80 ± 1

[a]Critical micelle concentration (CMC) was determined by surface tensiometry. The experiments were performed by Dr. Sarah Decato. [b]CMC was determined by pyrene 1:3 ratio method. [c]The size of the micelles is reported by percent volume (%) to represent the hydrodynamic diameter, which was determined by dynamic light scattering (DLS) using spherical fits. [d]Aggregation number was measured by a steady-state fluorescence quenching of pyrene and coumarin 153.

2.2.4 Drug encapsulation

M2H10PFtB$_{TRI}$ was evaluated for its encapsulation efficiency using the following hydrophobic anticancer drugs: paclitaxel (PTX), docetaxel (DCX), and rapamycin (RAP). The drugs were encapsulated within the semifluorinated micelles via the thin-film solvent evaporation method. The concentration of polymer was fixed at 10 mg/mL (3.61 mM). The amount of encapsulated drug was quantified by HPLC immediately after formulation and after 24 h. The % drug loading can be calculated from

Equation 2-1: $$\textbf{\textit{Drug loading}}\ (\%) = \frac{\textbf{\textit{weight of drug in the micelles}}}{\textbf{\textit{weight of polymer+drug in the micelles}}} \times \mathbf{100}$$

M2H10PFtB$_{TRI}$ was able to solubilize all three drugs with the solubility ranging as follows: RAP > PTX > DCX (**Table 2.2**). Interestingly, the experimented logP value of these three drugs are $logP_{RAP}$ = 4.3 > $logP_{PTX}$ = 3 > $logP_{DCX}$ = 2.4 (Data obtained from DrugBank). A higher logP value represents a more hydrophobic compound. Therefore, this indicates that the core of the M2H10PFtB$_{TRI}$ micelle can encapsulate more hydrophobic molecules better than less hydrophobic molecules, suggesting a highly hydrophobic micellar core. After 24 h, negligible drug loss was observed and the micelles show more than 94 % retention for all three drugs. The wt% drug loading calculated from **Equation 2-1** shows the loading in the range of 9 – 12 wt%, suggesting a high loading efficiency with the M2H10PFtB$_{TRI}$ micelles.

Table 2.2 Various drug encapsulation properties of M2H10PFtB$_{TRI}$ micelles.

Anticancer drugs	Initial encapsulation (μg/mL)	Encapsulation after 24 h (μg/mL)	Drug retention (%)	Drug loading (wt%)
Paclitaxel (PTX)	1109.17 ± 25.05	1046.32 ± 30.41	94.32	9.47
Docetaxel (DCX)	952.36 ± 147.76	938.98 ± 135.24	98.60	7.17
Rapamycin (RAP)	1449.51 ± 95.28	1462.05 ± 54.68	100	11.94

2.2.5 Preparation of iRGD conjugated micelles

iRGD conjugated micelles were prepared using a thin-film solvent evaporation method by mixing M2H10PFtB$_{TRI}$ (**2-6**) with iRGD-PMPI-P2H10PFtB$_{TRI}$ (**2-9**) at different %iRGD; 0, 5, 10, and 20%. 0% iRGD represents a non-functionalized or control micelle, composed of solely M2H10PFtB$_{TRI}$. As shown in **Figure 2.5a and b**, iRGD functionalized semifluorinated polymer maintained a similar size with narrow size distribution (PDI ≈ 0.11 – 0.13) compared to that of the control (0% iRGD) micelles, regardless of iRGD concentrations. This suggests that the decoration with iRGD ligand did not alter the physical characteristics of the small semifluorinated micelles.

a)

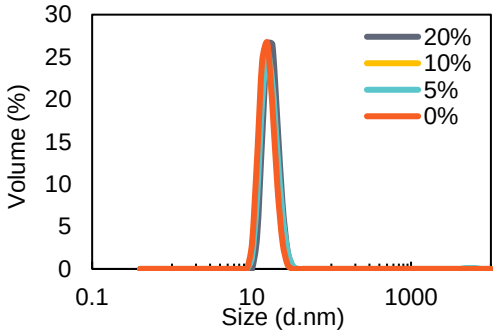

b)

%iRGD	Size (nm)	PDI
0%	15.08 ± 1.26	0.13 ± 0.01
5%	16.90 ± 0.23	0.11 ± 0.07
10%	16.92 ± 0.68	0.10 ± 0.03

Figure 2.5 Sizes of micelles with different %iRGD obtained from Dynamic Light Scattering (DLS). a) Overlay of the particle size distribution by volume and b) hydrodynamic diameter and polydispersity index (PDI).

2.2.6 In vitro cellular uptake: 2D 4T1-Luc monolayer cultured cells

The effect of the iRGD targeting was first evaluated *in vitro* using a 2D monolayer cultured 4T1-Luc cells. DiI, a fluorescent dye, was encapsulated in iRGD micelle formulations with various iRGD concentrations. The cellular uptake of each micelle was measured using confocal laser scanning microscopy (CLSM) after a 3 h incubation with 4T1-Luc cells. As shown in **Figure 2.6**, 0% iRGD micelles exhibited the lowest fluorescence intensity whereas 20% iRGD micelles showed the highest fluorescence intensity. Quantitative analysis of fluorescence intensity per cell demonstrated a 5-fold increase in intensity of 20% iRGD micelles compared to 0% iRGD (control) micelles (**Figure 2.7**). This suggests that the iRGD

functionalization significantly improved the uptake of these small semifluorinated micelles. It should be noted that increasing iRGD concentration from 5% to 20% resulted in an increase in fluorescence intensity with an observed non-linear trend. This is possibly due to the higher ligand density presented on the micellar surface, which can induce multivalent binding of integrins and iRGD ligands, resulting in an enhanced cellular uptake of these small aggregates into the cells.[36-37]

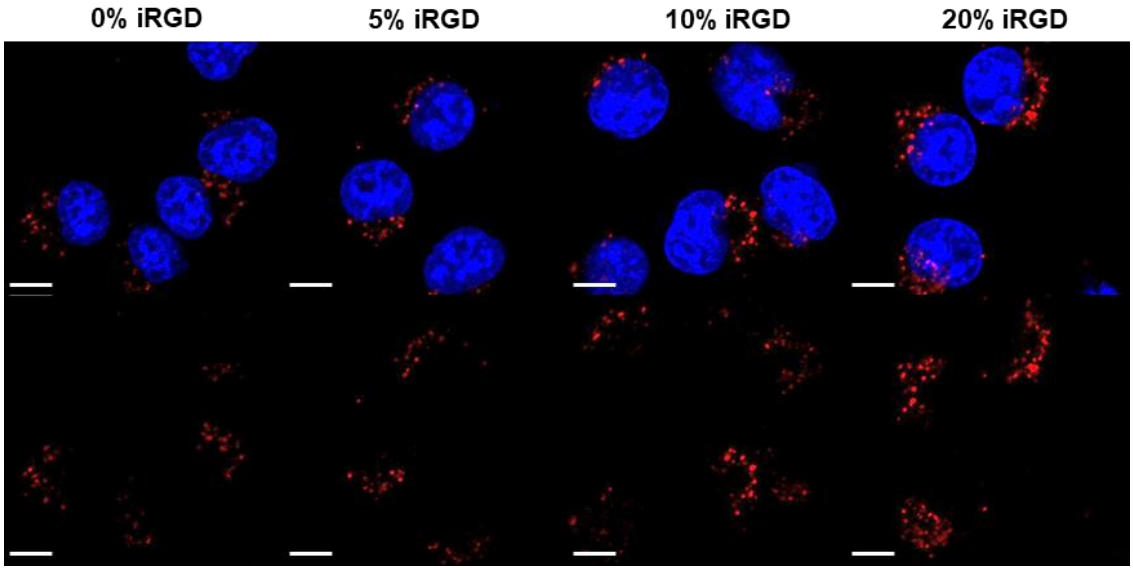

Figure 2.6 Representative CLSM images of 2D 4T1-Luc cells treated with different % iRGD micelles. Cells were incubated with DiI-loaded micelles for 3 h. Red: DiI. Blue: Hoechst 33342 (nuclei). Scale bar: 10 μm.

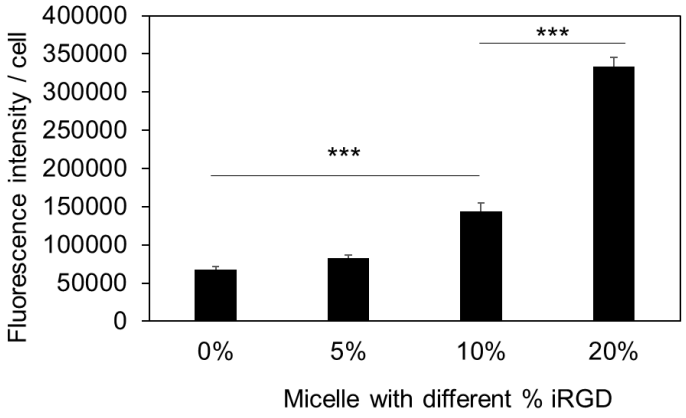

Figure 2.7 Quantitative analysis of cellular uptake studies on 2D monolayer cultured cells after 3 h incubation with DiI-loaded micelles. Fluorescence intensity was measured by CLSM. All images were analyzed by ImageJ. Data represents mean fluorescence ± SEM, n = 89. *** $p < 0.001$

2.2.7 Tumor spheroid penetration

Although there was an improved cellular uptake with iRGD functionalization in 2D cell cultures, it should be noted that these studies only confirm the improved accumulation of nanoparticles but do not provide information on whether iRGD can facilitate tissue penetration. Therefore, a better model is required to further evaluate the penetration effect of iRGD. To visualize the tumor penetration, 3D multicellular spheroids were used. 4T1-Luc tumor spheroids were prepared using a 3D Petri Dish® micromolds. The spheroids were incubated with DiI-loaded micelles and CLSM images were captured after a 24 h incubation. Without iRGD functionalization, 0% iRGD micelles were mostly observed around the periphery of the spheroid (**Figure 2.8**). The 5% iRGD micelles showed a low penetration into the spheroids, similar to the 0% iRGD micelles. Inward penetration was observed from the spheroids treated with 10% iRGD micelles, while 20% iRGD micelles exhibited the most prominent penetration throughout the spheroids. The increasing iRGD concentration showed an improved penetration ability in tumor spheroids similar to what was observed in 2D culture, suggesting a non-linear effect in the targeting ability of iRGD that can be explained though multivalent binding effects.

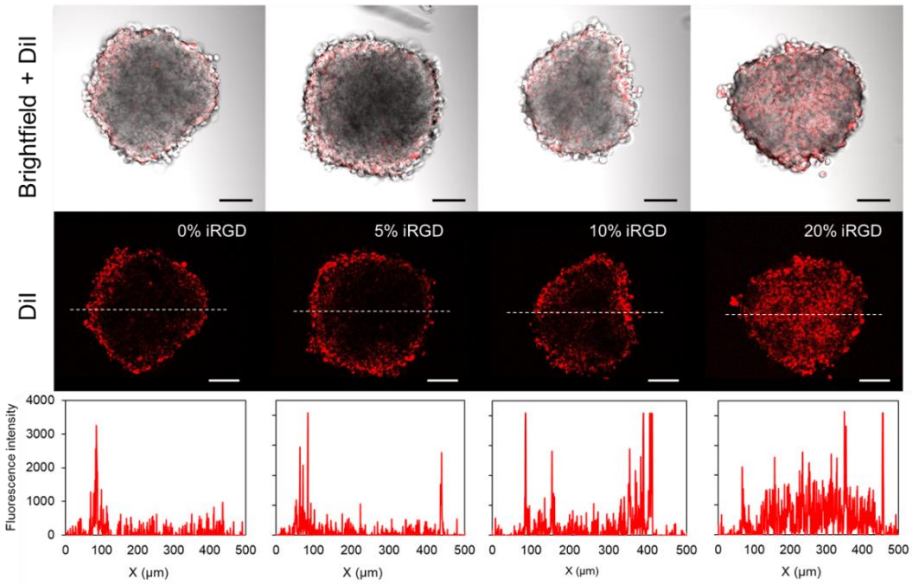

Figure 2.8 Representative CLSM images of 4T1-Luc spheroids after 24 h incubation with DiI-loaded micelles. Top; the overlay image of brightfield and DiI channel. Middle; DiI channel. Bottom: The corresponding fluorescence signal intensity along the dotted line across the spheroids. Scale bar: 100 μm.

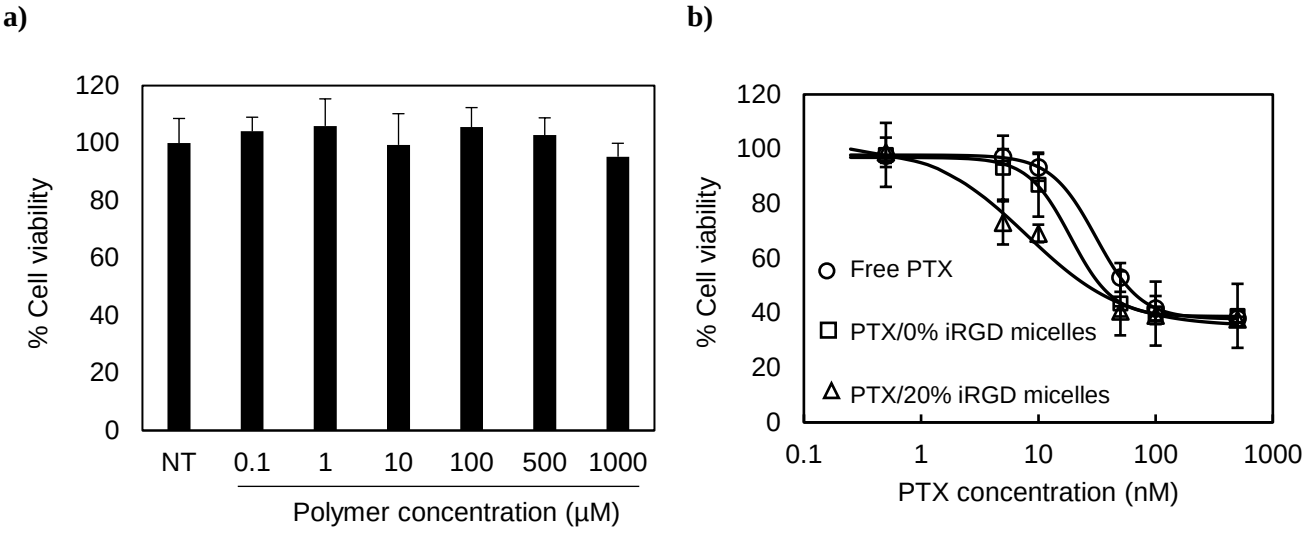

Figure 2.9 4T1-Luc cell viability after 48 h incubation with a) empty M2H10PFtB$_{TRI}$ micelles and b) PTX-loaded micelles after 48 h incubation. The representative data represent mean ± SD.

2.2.8 Cytotoxicity studies

The 20% iRGD micelles exhibited the highest accumulation and penetration efficiency in both 2D and 3D cultures. This micelle formulation was then selected to further evaluate its drug delivery capability and cytotoxic effects *in vitro*. The cytotoxicity was first evaluated using free polymers. 4T1-Luc cells were incubated with free M2H10PFtB$_{TRI}$ for 48 h at different polymer concentrations up to 1 mM. As shown in **Figure 2.9a**, negligible cytotoxicity of free M2H10PFtB$_{TRI}$ was observed even at high polymer concentration. This result suggests that the M2H10PFtB$_{TRI}$ polymer is biocompatible. To further study the formulation efficacy, paclitaxel (PTX) was selected as the model hydrophobic anticancer drug. Two micelle formulations containing PTX were prepared: PTX/0% iRGD and PTX/20% iRGD micelles. 4T1-Luc cells were incubated with free PTX, PTX/0% iRGD micelles and PTX/20% iRGD micelles for 48 h. As shown in **Figure 2.9b**, both micelles provided higher cytotoxic effect than free PTX, demonstrating that the encapsulation of the drug inside these semifluorinated micelles enhanced the drug's toxicity against cancer cells. A comparison between the two micelle formulations show that PTX/20% iRGD micelles were more toxic than PTX/0% iRGD micelles. This is expected due to the enhanced cellular uptake resulting from the

iRGD ligand. Quantitative comparison of IC_{50} values revealed a significantly lower IC_{50} in PTX/20% iRGD micelles than PTX/0% iRGD micelles ($p < 0.5$) and free paclitaxel ($p < 0.001$) (**Table 2.3**). This suggests an improvement of formulation efficacy due to the introduction of the iRGD targeting ligand.

Table 2.3 IC_{50} values of paclitaxel, PTX/0% iRGD micelle, and PTX/20% iRGD micelle on 4T1-Luc cells following 48 h treatment.

Polymer	IC_{50} (nM)
Paclitaxel (PTX)	33.6 ± 3.5
PTX/polymer 2 micelle	17.2 ± 2.4
PTX/20% iRGD-2 micelle	9.50 ± 1.3

Data represent mean ± SD from triplicate studies.

2.3 Conclusions

Our synthesized semifluorinated polymer, M2H10PFtB$_{TRI}$ (a branched fluorous segment) has been shown to be a good candidate as a promising drug delivery carrier. The formation of a small micelle from M2H10PFtB$_{TRI}$ allows a high encapsulation and retention of different hydrophobic molecules up to 12 wt%. The successful installation of iRGD, a targeting ligand, to the semifluorinated polymer resulted in an improved efficacy of PTX towards cancer cells *in vitro* due to the enhanced accumulation and penetration properties of the functionalized micelles. This demonstrates the synergistic potential of the multifunctional micelle design and suggests the potential of our formulation as a promising vehicle in a drug delivery system.

2.4 Experimental

2.4.1 Materials and Methods

Perfluoro-*tert*-butanol was purchased from SynQuest Laboratories Inc. (Alachua, FL). iRGD was purchased from ABI Scientific (Sterling, VA). Paclitaxel (PTX) was purchased from LC Laboratories (Woburn, MA). 4T1-Luc marine breast cancer cells were generously given by Dr. Glen S. Kwon. Solvents

and all other reagents were purchased from Sigma-Aldrich and were used as purchased, unless otherwise specified. Small molecule and polymer chromatography were accomplished with Silicycle 60 Å SiO_2 or using a Teledyne CombiFlash Rf 4× (Lincoln, NE) equipped with an ELSD for visualization and RediSep® Rf high performance silica or C18 columns.

^{1}H, ^{13}C, and ^{19}F NMR spectra were measured using a Bruker Avance III HD 400 MHz spectrometer or a Varian UI 500 MHz spectrometer. All spectra were measured with either $CDCl_3$, D_2O, or DMSO-d6 as the solvent. Polymer purity was confirmed by HPLC with a Gilson 321 Pump (Middleton, WI) equipped with a Jordi Gel DVB 500 Å (Bellingham, MA) column and a Gilson Prep-ELS detector, and by MALDI-MS on a Bruker Ultraflex III MALDI TOF/TOF using α-cyano-4-hydroxycinnamic acid matrix unless otherwise specified.

*2.4.2 Synthesis of N-(4-Carboxyphenyl)maleamic Acid (p-CPMA) (**2-1**)*

Maleic anhydride (5 g, 51 mmol) and 4-aminobenzoic acid (7 g, 51 mmol) were dissolved in 40 mL of dry DMF under Ar. The reaction was stirred at room temperature for 5 h. The reaction mixture was then poured into DI water (450 mL) to precipitate out the product. The solid was filtered and washed once again with DI water (3✕300 mL). The product was then collected and dried under high vacuum overnight to give *p*-CPMA as a yellow solid (11.23 g, 94% yield). ^{1}H NMR (400 MHz, DMSO-d6): δ 12.76 (s, 2H), 10.60 (s, 1H), 7.88 (d, 2H), 7.70 (d, 2H), 6.46 (d, 1H), 6.30 (d, 1H).

*2.4.3 Synthesis of N-(4-Carboxyphenyl)maleimide (p-CPMI) (**2-2**)*

AcONa (590.6 mg, 7.2 mmol, 0.15 eq) was added into a flask containing *p*-CPMA (**2-1**) (11.23 g, 48 mmol) under Ar. Ac_2O (22.7 mL, 240 mmol) was then added and the reaction was stirred at 60 °C using water bath for 2 h. After 2 h, the reaction solution was poured into cold DI water. The product clustered into yellow solid chunks and was filtered and washed with DI water several times. The collected solid was recrystallized in 50 mL of 6:1 MeOH-water twice. The crystals were collected, washed again with water,

and dried under high vacuum to give *p*-CPMI as pale-yellow crystals (5.37 g, 48% yield). ^{1}H NMR (400 MHz, DMSO-d6): δ 8.02 (d, 2H), 7.47 (d, 2H), 7.19 (s, 2H).

*2.4.4 Synthesis of N-[(4-azidocarbonyl)phenyl]maleimide (ACPM) (**2-3**)*

To a dry round bottom flask containing *p*-CPMI (**2-2**) (2 g, 9.2 mmol), 80 mL of dry toluene was added under Ar. TEA (1.4 mL, 10.12 mmol) was added followed by DPPA (2.2 mL, 10.12 mmol). The reaction was allowed to stir at room temperature for 3 days. After 3 days, the reaction solution was concentrated and purified by column chromatography using DCM as the eluent. The collected product fractions (R_f ~ 0.5) was concentrated and dried under high vacuum to give the product as yellow crystals (1.53 g, 70% yield). ^{1}H NMR (400 MHz, DMSO-d6): δ 8.05 (d, 2H), 7.56 (d, 2H), 7.21 (s, 2H). ^{1}H NMR (400 MHz, $CDCl_3$): δ 8.14 (d, 2H), 7.56 (d, 2H), 6.90 (s, 2H).

*2.4.5 Synthesis of "9-decen-1-OPFtB$_{TRI}$" (**2-4**)*

To a dry round bottom flask containing PFtB$_{TRI}$-OH (2.96 g, 3.75 mmol) was added 15 mL dry THF under Ar. 4 Å powdered molecular sieves (1 weight eq. to PFtB$_{TRI}$-OH) was then added and the mixture was stirred for 30 min. After that the mixture was cooled down to 0 °C using an ice bath and NaH (450 mg, 18.7 mmol) was added. The ice bath was removed, and the reaction was stirred for 30 min as it warmed up to room temperature. 9-decen-1-OMs (339 mg, 1.87 mmol), diluted in 2 mL dry THF, was then added dropwise into the reaction. The reaction was then brought to reflux and stirred at reflux conditions for 7 days. After this time, the reaction was diluted in 20 mL DCM. Saturated NH_4Cl solution was slowly added to quench the reaction. The aqueous layer was extracted with 100 mL diethyl ether (3x). The collected organic layers were filtered through Celite. The filtrate was washed with saturated NH_4Cl solution, dried over $MgSO_4$, and adsorbed on Celite. The crude product was purified by automated flash chromatography using a RediSep Rf Gold® Normal-phase Silica column with a hexane and ethyl acetate gradient. The collected fractions were then concentrated under reduced pressure to give the product as a clear liquid (1.2 g, 69% yield). ^{1}H NMR (500 MHz, $CDCl_3$) δ 5.81 (ddt, J = 17.0, 10.2, 6.7 Hz, 1H), 5.05 – 4.86 (m, 2H),

4.04 (s, 6H), 3.40 – 3.30 (m, 4H), 2.10 – 1.97 (m, 2H), 1.52 (t, J = 6.6 Hz, 2H), 1.37 (q, J = 7.1, 6.6 Hz, 2H), 1.28 (d, J = 3.0 Hz, 9H). ^{19}F NMR (470 MHz, $CDCl_3$) δ -70.37.

*2.4.6 Synthesis of "HO-H10PFtB$_{TRI}$" (**2-5**)*

To a dry round bottom flask, BH_3·THF (4 mL, 4 mmol) was added under Ar and diluted with 5 mL dry THF. The solution was cooled down to 0 °C using an ice bath. **2-4** (2.44 g, 2.67 mmol) diluted in 5 mL dry THF was added dropwise into the reaction flask. The ice bath was removed, and the reaction was stirred at room temperature overnight. The reaction was then cooled down to 10 °C. 3 M NaOH (5.7 mL, 13.4 mmol) was slowly added dropwise followed by 30% w/w H_2O_2 (996 µL, 13.4 mmol). The reaction was heated to 50 °C and stirred overnight. After this time, the reaction was diluted in water and extracted with diethyl ether 3x. The collected organic layers were washed with brine, dried over $MgSO_4$, and adsorbed on Celite. The crude product was purified by automated flash chromatography using a RediSep Rf Gold® Normal-phase Silica column with a hexane and ethyl acetate gradient. The collected fractions were then concentrated under reduced pressure to give the product as a clear liquid (2.01 g, 79% yield). ^{1}H NMR (500 MHz, $CDCl_3$) δ 4.04 (s, 6H), 3.64 (q, J = 6.2 Hz, 2H), 3.40 – 3.31 (m, 4H), 1.57 (dd, J = 7.9, 6.3 Hz, 2H), 1.52 (t, J = 6.7 Hz, 2H), 1.28 (s, 12H), 1.21 – 1.17 (m, 1H). ^{19}F NMR (470 MHz, $CDCl_3$) δ -70.35.

*2.4.7 Synthesis of "M2H10PFTB$_{TRI}$" (**2-6**)*

To a dry round bottom flask containing **2-5** (1.23 g, 1.3 mmol) was added 30 mL dry THF under Ar. The reaction solution was cooled down to 0 °C and NaH (312 mg, 13 mmol) was added followed by 4 Å powdered molecular sieves (1 weight eq. to **2-5**). This was allowed to stir for 30 min as it slowly warmed to room temperature. After this time, M2-OMs (4.08 g, 1.95 mmol) was added and the reaction mixture was stirred for 10 min before refluxing for 7 days. During the reaction time, NaH was added to facilitate the reaction. After 7 days, the reaction mixture was then diluted with 10 mL of DCM, slowly quenched with 1 mL of MeOH, followed by 1 mL of water, washed with saturated NH_4Cl solution, dried over $MgSO_4$, and adsorbed on Celite. The crude product was purified by automated flash chromatography using a

RediSep® C-18 reverse phase silica column with a water–MeOH (0.1% FA) to dichloromethane–MeOH gradient. The collected fractions were concentrated under reduced pressure to give the product as a white solid (3.14 g, 81% yield). ^{1}H NMR (500 MHz, $CDCl_3$) δ 4.04 (s, 6H), 3.64 – 3.54 (m, 177H), 3.59 – 3.53 (m, 4H), 3.50 (s, 1H), 3.44 (t, J = 6.8 Hz, 2H), 3.38 (s, 3H), 3.37 – 3.33 (m, 4H), 1.57 (d, J = 7.1 Hz, 2H), 1.51 (d, J = 6.6 Hz, 1H), 1.27 (s, 12H). ^{19}F NMR (470 MHz, $CDCl_3$) δ -70.34. MALDI MS: $[M + Na]^+$ calculated for $C_{112}H_{199}F_{27}NaO_{47}$ = 2832.26; found: 2832.633.

2.4.8 Synthesis of "BnO-P2-OH" monobenzylated poly(ethylene glycol) ***(2-7)***

PEG_{2k}-diol (20 g, 10 mmol) was dissolved in 600 mL dry DCM under Ar. Ag_2O (4.64 g, 20 mmol) was then added followed by KI (332 mg, 2 mmol). After a few minutes, benzyl bromide (BnBr) (1.3 mL, 11 mmol) was added dropwise into the reaction. The reaction was heated to reflux and stirred overnight. After this time, the reaction mixture was filtered through celite to remove Ag_2O. The collected filtrate was concentrated under reduced pressure. The crude solution was diluted in DCM, washed with saturated NH_4Cl solution (3x). The collected organic layer was collected, dried over $MgSO_4$, and concentrated under reduced pressure. The crude product was purified by silica gel column chromatography using MeOH/DCM in gradient (0 – 10%) as mobile phase. ^{1}H NMR (400 MHz, $CDCl_3$) δ 7.37 – 7.31 (m, 5H), 4.57 (s, 2H), 3.71 – 3.57 (m, 234H). MALDI MS: $[M + Na]^+$ calculated for $C_{103}H_{200}NaO_{49}$ = 2244.31; found: 2244.421.

2.4.9 Synthesis of "BnO-P2-OMs" monobenzylated poly(ethylene glycol) methanesulfonate ***(2-8)***

To a dry round bottom flask, 10 mL of dry DCM was added to dissolve BnO-PEG_{2k}-OH (**2-7**) (1.42 g, 0.6 mmol) under Ar. TEA (252 µL, 1.8 mmol) was then added followed by the addition of methanesulfonyl chloride (MsCl, 116.5 µL, 1.5 mmol) dropwise. The reaction was allowed to stir at room temperature overnight. After running overnight, the reaction was diluted with DCM and then washed with saturated NH_4Cl solution (3x). The collected organic layer was dried over $MgSO_4$ and concentrated under reduced pressure. The crude product was precipitated in cold ether. The collected white solid was freeze-

dried in a mixture of DCM and benzene to give the product as a white powder (1.2 g, 82% yield)**.** ^{1}H-NMR (400 MHz, $CDCl_3$): δ 7.35 (d, 5 H), 4.57 (s, 2 H), 4.39 (m, 2 H), 3.67 – 3.59 (m, 171 H), 3.09 (s, 3 H).

*2.4.10 Synthesis of "BnO-P2H10PFtB$_{TRI}$" (**2-9**)*

To a dry round bottom flask containing **2-5** (599 mg, 0.63 mmol) was added 10 mL dry THF under Ar. The reaction solution was cooled down to 0 °C and NaH (127 mg, 5.3 mmol) was added followed by 4 Å powdered molecular sieves (1 weight eq.). This was allowed to stir for 30 min as it warmed slowly to room temperature. After this time, BnO-PEG$_{2k}$-OMs (**2-8**) (1.2 g, 0.53 mmol) was added and the reaction mixture was stirred for 10 min before refluxing for 7 days. Each day 10 mg of NaH was added to facilitate the reaction. After 7 days, the reaction mixture was then diluted with 10 mL of DCM, slowly quenched with 1 mL of MeOH, followed by 1 mL of water, washed with saturated NH_4Cl solution, dried over $MgSO_4$, and adsorbed on Celite. The crude product was purified by automated flash chromatography using a RediSep® C-18 reverse phase silica column with a water–MeOH (0.1% FA) to dichloromethane–MeOH gradient. The collected fractions were then concentrated under reduced pressure to give the product as a white solid (491 mg, 31% yield). ^{1}H-NMR (400 MHz, $CDCl_3$): δ 7.35 (d, 3 H), 4.57 (s, 1 H), 4.04 (s, 6 H), 3.7-3.5 (m, 171 H), 3.44 (t, 2 H), 3.36 (t, 4 H), 1.27-1.25 (m, 16 H). ^{19}F-NMR (500 MHz, $CDCl_3$): δ -70.35 (s). MALDI MS: $[M + Na]^+$ calculated for $C_{122}H_{211}F_{27}NaO_{49}$ = 2996.35; found: 2996.74.

*2.4.11 Synthesis of "HO-P2H10PFtB$_{TRI}$" (**2-10**)*

MeOH (25 mL) was added to dissolve *BnO-P2H10PFtB$_{TRI}$* (**2-9**) (500 mg, 0.16 mmol). The solution was flushed with Ar for 1 h at room temperature. After this time, Pd/C was added, and the mixture was stirred under Ar for another 1 h. The mixture was then stirred under an H_2 atmosphere overnight. After this time, the reaction mixture was filtered through Celite. The collected organic filtrate was concentrated and dried under reduced pressure to give the product as a white solid (68% yield). ^{1}H-NMR (500 MHz, $CDCl_3$): δ 4.04 (s, 6H), 3.7-3.5 (m, 140H), 3.44 (t, 2H), 3.36 (t, 4H), 1.52, (t, 2), 1.27-1.25 (m, 14H). ^{19}F-

NMR (500 MHz, $CDCl_3$): δ -70.36 (s). MALDI MS: $[M + Na]^+$ calculated for $C_{115}H_{205}F_{27}NaO_{49}$ = 2906.30; found: 2905.22.

*2.4.12 Synthesis of "PMPI-P2H10PFtB$_{TRI}$" (**2-11**)*

To an oven-dried round bottom flask containing *HO-P2H10PFtB$_{TRI}$* (**2-10**) (50 mg, 0.017 mmol) and ACPM (**2-3**) (40.9 mg, 0.17 mmol) was added 5 mL of dry toluene. The reaction solution was brought to reflux for 3 h. After 3 h, heat was removed and the reaction solution was allowed to stir at room temperature overnight. After this time, toluene was evaporated and the crude product was redissolved in DCM. The crude product was then precipitated in cold ether. The collected white solid was freeze-dried in a mixture of DCM and benzene to give the product as a white powder (53% yield). ^{1}H-NMR (500 MHz, $CDCl_3$): δ 7.52 (d, 2 H), 6.84 (s, 1 H), 4.33 (t, 1 H) 4.04 (s, 6 H), 3.7-3.5 (m, 171 H), 3.44 (t, 2 H), 3.36 (t, 4 H), 1.52, (t, 2 H), 1.27-1.25 (m, 14 H) ^{19}F-NMR (500 MHz, $CDCl_3$): δ -70.35 (s). MALDI MS: $[M + Na]^+$ calculated for $C_{126}H_{211}F_{27}N_2NaO_{52}$ = 3120.34; found: 3119.25.

*2.4.13 Synthesis of "iRGD-PMPI-P2H10PFtB$_{TRI}$" (**2-12**)*

iRGD (10 mg, 0.0092 mmol) was dissolved in 3 mL PB buffer in a round bottom flask. Separately, PMPI-P2H10PFtB$_{TRI}$ (**2-11**) (27 mg, 0.0084) was dissolved in 0.5 mL DMF and immediately added into the round bottom flask containing iRGD. The reaction was allowed to stir at room temperature for 48 h. After this time, the reaction solution was transferred to a dialysis bag (MWCO: 2,000) and dialyzed against water for 5 days to remove unreacted iRGD. After 5 days, the solution was then lyophilized to give the product as a white powder (95% yield). MALDI MS: $[M + Na]^+$ calculated for $C_{170}H_{283}F_{27}N_{17}NaO_{69}S_3^-$ = 4298.79; found: 4294.35.

2.4.14 Critical Micelle Concentration (CMC): Pyrene 1:3 ratio method

Polymer solutions were prepared in water at different concentration from 0 – 2 mg/mL. Pyrene stock solution in pure ethanol was introduced into a dry vial. Ethanol was evaporated and the pyrene residue was dissolved with the polymer solution using sonication. The final pyrene concentration in the polymer

solution was 2 µM. Fluorescence intensity was measured by a SLM Luminescence Spectrometer Aminco-Bowman® Series 2 (Rochester, NY) using the excitation of pyrene at 337 nm. All measurements were done at 25 ± 1 °C. The intensities of the first and third vibronic bands (I_1 and I_3) were recorded at 374 and 384 nm. CMC of the polymer was calculated according to Aguiar, J. *et. al*.[38]

2.4.15 Aggregation Number Study

The aggregation number of micelles was determined using a steady-state fluorescence quenching method. Polymer solutions were prepared at 3 different concentrations (3 – 7 mg/mL) in MilliQ water. Pyrene stock solution in pure ethanol was introduced into a dry vial. Ethanol was evaporated and the pyrene residue was dissolved with the polymer solution using sonication in such a way that the final polymer solution contained 2 µM pyrene. Different amounts of C153 stock (1 mM in pure ethanol) was added into the pyrene/polymer solutions to obtain various quencher concentrations (0 – 20 µM). The concentration of ethanol in final solution was kept to be ≤ 2% without effecting the aggregation number.[39] Fluorescence intensity of each sample was measured by a SLM Luminescence Spectrometer Aminco-Bowman® Series 2 (Rochester, NY) using the excitation of pyrene at 337 nm. All measurements were done at 25 ± 1 °C. Error was reported as the standard deviation from triplicate measurements.

The aggregation number (N_s) can be calculated from the following equations[40]

Equation 2-2 $$\frac{I}{I_0} = exp\left(-\frac{[Q]}{[M]}\right)$$ **Equation 2-3** $$N_S = \frac{[S]-CMC}{[M]}$$

Where I and I_0 represent fluorescence intensity with and without the quencher, respectively, [Q] is the quencher concentration, [M] is the micelle concentration and [S] is the total bulk polymer concentration.

2.4.16 Dynamic light scattering (DLS)

Particle size was measured by dynamic light scattering (DLS) with a Zetasizer Nano-ZS (Malvern Instruments Ltd., UK) at 25 °C with a 173° detection angle. The micelle solutions were measured without dilution and in triplicate. The number of scans of each run was determined automatically by the instrument. The data were reported as volume weighted average diameters.

2.4.17 Drug encapsulation

2.4.17.1 Anticancer drug stock solution preparation (DCX, RAP, and PTX)

All anticancer drug stock solutions were prepared by dissolving the drug in ACN, aided by sonication for complete solubility. Docetaxel (DCX), rapamycin (RAP), and paclitaxel (PTX) were prepared at 4 mg/mL.

2.4.17.2 Micelle preparation

M2H10PFtB$_{TRI}$ polymer solution was prepared in ACN at 10 mg/mL concentration. Anticancer drug loaded micelles solutions were prepared in triplicate using the solvent evaporation method at a final polymer concentration of 10 mg/mL (3.6 mM). Briefly, 1 mL of polymer solution was added to a 10 mL round-bottom flask. The anticancer drug concentrations are as follows: DCX 250 µL (4 mg/mL stock solution), RAP 350 µL (4 mg/mL stock solution), and PTX 200 µL (4 mg/mL stock solution). The solution was rotated in a water bath at 60 °C for 5 min. The solvent was then evaporated under reduced pressure for 15 min to ensure a complete dried thin film. The film was resuspended with 1 mL hot PBS and sonicated for 5 – 10 min. The micelle sample was then centrifuged at 12,000 rpm for 5 min and passed through a 0.45-µm nylon syringe filter to remove any insoluble precipitates. A 100 µL aliquot of micelle solution was mixed with 900 µL of ACN and the remaining micelle solution was allowed to sit for 24 h at 4 °C. The sample was then re-centrifuged at 12,000 rpm for 5 min and passed through a 0.45-µm nylon syringe filter to remove any insoluble precipitates. A 100 µL aliquot of micelle solution was mixed with 900 µL of ACN for further analysis with HPLC.

2.4.17.3 HPLC method

The amount of anticancer drug loaded in the micelle was quantified by reverse phase HPLC (Shimadzu prominence HPLC system, Shimadzu, Japan), equipped with a LC-20AT pump, SIL-20 AC HT autosampler, CTO-20 AC column oven and an SPD-M20A diode array detector. Column temperature was maintained at 40°C. 20 µL of the mixture was injected into a C18 column (Agilent XDB-C8, 4.6 Å × 150

mm). The flow rate was 1.0 mL/min and the detection was set to 227 nm. For DCX, the samples were eluted with an isocratic mixture of 45% water in acetonitrile. The run time was 10 min and DCX eluted at 7.8 min. For RAP, the samples were eluted with an isocratic mixture of 20% water in acetonitrile. The run time was 10 min and RAP eluted at 7.29 min. For PTX, the samples were eluted with an isocratic mixture of 25% water in acetonitrile. The run time was 10 min and PTX eluted at 4.00 min.

2.4.18 Cellular uptake

4T1-Luc breast cancer cells were cultured at 37 °C in a humidified atmosphere containing 5% CO_2 and maintained in high glucose DMEM supplemented with 10% FBS and 1% penicillin/streptomycin. 4T1-Luc cells were seeded on 29 mm glass-bottom dishes (Cellvis, Mountain View, CA) at 2×10^4 cells/well/200 µL and incubated for 24 h. DiI-loaded iRGD-PFtB$_{TRI}$ micelles (DiI/iRGD micelles) were prepared by the thin-film hydration method using different iRGD concentrations (0%, 5%, 10%, and 20%). The cells were incubated with DiI loaded micelles at 37 °C for 3 h. After this time, the media was replaced with a fresh media containing Hoechst 33342 (Invitrogen, CA) for staining the nuclei. The cells were then incubated at 37 °C for 10 min. Finally, the cells were washed twice with PBS followed by an addition of fresh media prior to the image acquisition. All the images were acquired by confocal laser scanning microscope (Nikon A1R, Japan) and analyzed by ImageJ.

2.4.19 Tumor spheroid penetration

Three dimensional spheroids of 4T1-Luc were prepared by culturing the cells in 3D Petri Dish® micromolds (Microtissues, Inc., Providence, RI) using #12-81 series (8.1×10^4 cells in 190 µL of culture media). The micromolds were prepared according to the manufacturer's protocol. The cells in the micromolds were incubated at 37°C for 48 h. The spheroids were then incubated with DiI/iRGD-PFtB$_{TRI}$ micelles at different concentrations of iRGD (0%, 5%, 10%, and 20%) for 24 h. After this time, the spheroids were washed twice with fresh media and transferred, according to the manufacturer's protocol,

to a 29 mm glass-bottom dish before an image acquisition with confocal laser scanning microscope (Nikon A1R, Japan). All images were analyzed by ImageJ.

2.4.20 Cytotoxicity studies

4T1-Luc cells were seeded at 3,000 cells/well on 96-well plates and incubated for 24 h. PTX loaded micelles (PTX/0% iRGD micelle) and PTX loaded 20% iRGD micelles (PTX/20% iRGD micelle) were prepared by the solvent evaporation method. The cells were then incubated with free PTX, PTX/0% iRGD micelles, PTX/20% iRGD micelles, and free M2H10PFtB$_{TRI}$ polymer (empty micelles) for 48 h. After this time, the cytotoxic effects were analyzed by CellTiter-Blue® Cell Viability Assay (Promega, WI) according to the manufacturer's protocol. The fluorescence signal was measured at 560/590 nm using a SpectraMax® M2 microplate reader (Molecular Devices, CA). The results were repeated in triplicate and represented as percentages of cell viability normalized to the nontreated cells.

2.5 References

(1) Are, C.; McMasters, K. M.; Giuliano, A.; Yanala, U.; Balch, C.; Anderson, B. O.; Berman, R.; Audisio, R.; Kovacs, T.; Savant, D. Global forum of cancer surgeons: perspectives on barriers to surgical care for cancer patients and potential solutions. *Annals of surgical oncology* **2019,** *26* (6), 1577-1582.

(2) Norouzi, M.; Amerian, M.; Amerian, M.; Atyabi, F. Clinical applications of nanomedicine in cancer therapy. *Drug discovery today* **2019**.

(3) DeVita, V. T.; Chu, E. A history of cancer chemotherapy. *Cancer research* **2008,** *68* (21), 8643-8653.

(4) Horwitz, S. B. Taxol (paclitaxel): mechanisms of action. *Annals of oncology: official journal of the European Society for Medical Oncology* **1994,** *5*, S3-6.

(5) Thorn, C. F.; Oshiro, C.; Marsh, S.; Hernandez-Boussard, T.; McLeod, H.; Klein, T. E.; Altman, R. B. Doxorubicin pathways: pharmacodynamics and adverse effects. *Pharmacogenetics and genomics* **2011,** *21* (7), 440.

(6) Longley, D. B.; Harkin, D. P.; Johnston, P. G. 5-fluorouracil: mechanisms of action and clinical strategies. *Nature reviews cancer* **2003,** *3* (5), 330-338.

(7) Kakde, D.; Jain, D.; Shrivastava, V.; Kakde, R.; Patil, A. Cancer therapeutics-opportunities, challenges and advances in drug delivery. *Journal of Applied Pharmaceutical Science* **2011,** *1* (9), 1-10.

(8) Wang, H.; Wang, K.; Tian, B.; Revia, R.; Mu, Q.; Jeon, M.; Chang, F. C.; Zhang, M. Preloading of Hydrophobic Anticancer Drug into Multifunctional Nanocarrier for Multimodal Imaging, NIR-Responsive Drug Release, and Synergistic Therapy. *Small* **2016,** *12* (46), 6388-6397.

(9) Wicki, A.; Witzigmann, D.; Balasubramanian, V.; Huwyler, J. Nanomedicine in cancer therapy: challenges, opportunities, and clinical applications. *Journal of controlled release* **2015,** *200*, 138-157.

(10) Senapati, S.; Mahanta, A. K.; Kumar, S.; Maiti, P. Controlled drug delivery vehicles for cancer treatment and their performance. *Signal transduction and targeted therapy* **2018,** *3* (1), 1-19.

(11) Prabhakar, U.; Maeda, H.; Jain, R. K.; Sevick-Muraca, E. M.; Zamboni, W.; Farokhzad, O. C.; Barry, S. T.; Gabizon, A.; Grodzinski, P.; Blakey, D. C. Challenges and key considerations of the enhanced permeability and retention effect for nanomedicine drug delivery in oncology. *Cancer Research* **2013,** *73* (8), 2412-2417.

(12) Fang, J.; Nakamura, H.; Maeda, H. The EPR effect: unique features of tumor blood vessels for drug delivery, factors involved, and limitations and augmentation of the effect. *Advanced drug delivery reviews* **2011,** *63* (3), 136-151.

(13) Maeda, H. Toward a full understanding of the EPR effect in primary and metastatic tumors as well as issues related to its heterogeneity. *Advanced drug delivery reviews* **2015,** *91*, 3-6.

(14) Maeda, H. Macromolecular therapeutics in cancer treatment: the EPR effect and beyond. *Journal of Controlled Release* **2012,** *164* (2), 138-144.

(15) Bertrand, N.; Wu, J.; Xu, X.; Kamaly, N.; Farokhzad, O. C. Cancer nanotechnology: The impact of passive and active targeting in the era of modern cancer biology. *Advanced Drug Delivery Reviews* **2014,** *66*, 2-25.

(16) Zhan, C.; Gu, B.; Xie, C.; Li, J.; Liu, Y.; Lu, W., Cyclic RGD conjugated poly (ethylene glycol)-co-poly (lactic acid) micelle enhances paclitaxel anti-glioblastoma effect. *Journal of Controlled Release* **2010,** *143* (1), 136-142.

(17) Thumshirn, G.; Hersel, U.; Goodman, S. L.; Kessler, H. Multimeric cyclic RGD peptides as potential tools for tumor targeting: solid-phase peptide synthesis and chemoselective oxime ligation. *Chemistry–A European Journal* **2003,** *9* (12), 2717-2725.

(18) Ni, D.; Ding, H.; Liu, S.; Yue, H.; Bao, Y.; Wang, Z.; Su, Z.; Wei, W.; Ma, G. Superior intratumoral penetration of paclitaxel nanodots strengthens tumor restriction and metastasis prevention. *Small* **2015,** *11* (21), 2518-2526.

(19) Sugahara, K. N.; Teesalu, T.; Karmali, P. P.; Kotamraju, V. R.; Agemy, L.; Girard, O. M.; Hanahan, D.; Mattrey, R. F.; Ruoslahti, E. Tissue-penetrating delivery of compounds and nanoparticles into tumors. *Cancer cell* **2009,** *16* (6), 510-520.

(20) Ruoslahti, E. Tumor penetrating peptides for improved drug delivery. *Advanced drug delivery reviews* **2017,** *110*, 3-12.

(21) Teesalu, T.; Sugahara, K. N.; Ruoslahti, E. Tumor-penetrating peptides. *Front Oncol* **2013,** *3* (216).

(22) Teesalu, T.; Sugahara, K. N.; Kotamraju, V. R.; Ruoslahti, E. C-end rule peptides mediate neuropilin-1-dependent cell, vascular, and tissue penetration. *Proceedings of the National Academy of Sciences* **2009,** *106* (38), 16157-16162.

(23) Liu, X.; Jiang, J.; Ji, Y.; Lu, J.; Chan, R.; Meng, H. Targeted drug delivery using iRGD peptide for solid cancer treatment. *Molecular Systems Design & Engineering* **2017,** *2* (4), 370-379.

(24) Liu, X.; Lin, P.; Perrett, I.; Lin, J.; Liao, Y.-P.; Chang, C. H.; Jiang, J.; Wu, N.; Donahue, T.; Wainberg, Z. Tumor-penetrating peptide enhances transcytosis of silicasome-based chemotherapy for pancreatic cancer. *The Journal of clinical investigation* **2017,** *127* (5), 2007-2018.

(25) Akashi, Y.; Oda, T.; Ohara, Y.; Miyamoto, R.; Kurokawa, T.; Hashimoto, S.; Enomoto, T.; Yamada, K.; Satake, M.; Ohkohchi, N. Anticancer effects of gemcitabine are enhanced by co-administered iRGD peptide in murine pancreatic cancer models that overexpressed neuropilin-1. *British journal of cancer* **2014,** *110* (6), 1481-1487.

(26) Sugahara, K. N.; Teesalu, T.; Karmali, P. P.; Kotamraju, V. R.; Agemy, L.; Greenwald, D. R.; Ruoslahti, E. Coadministration of a tumor-penetrating peptide enhances the efficacy of cancer drugs. *Science* **2010,** *328* (5981), 1031-1035.

(27) Ma, S.; Zhou, J.; Zhang, Y.; He, Y.; Jiang, Q.; Yue, D.; Xu, X.; Gu, Z. Highly stable fluorinated nanocarriers with iRGD for overcoming the stability dilemma and enhancing tumor penetration in an orthotopic breast cancer. *ACS applied materials & interfaces* **2016,** *8* (42), 28468-28479.

(28) Zhang, Y.; Yang, J.; Ding, M.; Li, L.; Lu, Z.; Zhang, Q.; Zheng, J. Tumor-penetration and antitumor efficacy of cetuximab are enhanced by co-administered iRGD in a murine model of human NSCLC. *Oncology letters* **2016,** *12* (5), 3241-3249.

(29) Shen, J.; Meng, Q.; Sui, H.; Yin, Q.; Zhang, Z.; Yu, H.; Li, Y. iRGD conjugated TPGS mediates codelivery of paclitaxel and survivin shRNA for the reversal of lung cancer resistance. *Molecular pharmaceutics* **2013,** *11* (8), 2579-2591.

(30) Mao, X.; Liu, J.; Gong, Z.; Zhang, H.; Lu, Y.; Zou, H.; Yu, Y.; Chen, Y.; Sun, Z.; Li, W. iRGD-conjugated DSPE-PEG2000 nanomicelles for targeted delivery of salinomycin for treatment of both liver cancer cells and cancer stem cells. *Nanomedicine* **2015,** *10* (17), 2677-2695.

(31) Parlato, M. C.; Jee, J.-P.; Teshite, M.; Mecozzi, S. Synthesis, characterization, and applications of hemifluorinated dibranched amphiphiles. *The Journal of organic chemistry* **2011,** *76* (16), 6584-6591.

(32) Decato, S.; Bemis, T.; Madsen, E.; Mecozzi, S. Synthesis and characterization of perfluoro-tert-butyl semifluorinated amphiphilic polymers and their potential application in hydrophobic drug delivery. *Polymer chemistry* **2014,** *5* (22), 6461-6471.

(33) Tucker, W. B.; McCoy, A. M.; Fix, S. M.; Stagg, M. F.; Murphy, M. M.; Mecozzi, S. Synthesis, physicochemical characterization, and self-assembly of linear, dibranched, and miktoarm semifluorinated triphilic polymers. *Journal of Polymer Science Part A: Polymer Chemistry* **2014,** *52* (23), 3324-3336.

(34) Oishi, T.; Fujimoto, M. Synthesis and polymerization of N-[4-N′-(α-methylbenzyl) aminocarbonylphenyl] maleimide. *Journal of Polymer Science Part A: Polymer Chemistry* **1992,** *30* (9), 1821-1830.

(35) Bouzide, A.; Sauvé, G. Silver (I) oxide mediated highly selective monotosylation of symmetrical diols. Application to the synthesis of polysubstituted cyclic ethers. *Organic letters* **2002,** *4* (14), 2329-2332.

(36) Valencia, P. M.; Hanewich-Hollatz, M. H.; Gao, W.; Karim, F.; Langer, R.; Karnik, R.; Farokhzad, O. C. Effects of ligands with different water solubilities on self-assembly and properties of targeted nanoparticles. *Biomaterials* **2011,** *32* (26), 6226-6233.

(37) Montet, X.; Funovics, M.; Montet-Abou, K.; Weissleder, R.; Josephson, L. Multivalent effects of RGD peptides obtained by nanoparticle display. *Journal of medicinal chemistry* **2006,** *49* (20), 6087-6093.

(38) Aguiar, J.; Carpena, P.; Molina-Bolıvar, J.; Ruiz, C. C. On the determination of the critical micelle concentration by the pyrene 1: 3 ratio method. *Journal of Colloid and Interface Science* **2003,** *258* (1), 116-122.

(39) Tummino, P. J.; Gafni, A. Determination of the aggregation number of detergent micelles using steady-state fluorescence quenching. *Biophysical journal* **1993,** *64* (5), 1580-1587.

(40) Wolszczak, M.; Miller, J. Characterization of non-ionic surfactant aggregates by fluorometric techniques. *Journal of Photochemistry and Photobiology A: Chemistry* **2002,** *147* (1), 45-54.

CHAPTER 3 – A STUDY OF THE EFFECT OF DIFFERENT SEMIFLUORINATED POLYMER ARCHITECTURES ON SELF-ASSEMBLED NANOPARTICLES

This chapter is currently being prepared as a manuscript – Reference: Tangsangasaksri, M.; Galli, C.; Steinke, K.; Mecozzi, S., Synthesis, characterization, and self-assembly of linear and dibranched semifluorinated polymers and their application as delivery carriers. *Manuscript in preparation*. **2020**

Abstract

Two different dibranched semifluorinated triblock copolymers, one symmetric and one asymmetric, were synthesized. The aggregation behavior in aqueous solution of the polymers was investigated and compared to other polymer architectures: dibranched diblock, and linear diblock and triblock copolymers. The dibranched diblock and triblock copolymers showed a smaller aggregation number and microviscosity of the corresponding aggregates than their linear counterparts. For the linear copolymers, the introduction of the fluorocarbon block led to a tight packing while a loose aggregate was formed from the symmetric dibranched copolymer mostly due to the rigidity and higher volume of fluorocarbons. Interestingly, the asymmetric dibranched copolymer did not follow the same trend. Additionally, all polymers aggregated as micelles in aqueous solution with the ability to encapsulate hydrophobic drug paclitaxel (PTX). The encapsulation efficiency of the polymeric micelles solely depended on the hydrocarbon moiety of the corresponding micelles. The dibranched structures demonstrated a prolonged release due to better sealing of the drug in the micelle hydrophobic core through the intermediate extended fluorous shell. Finally, *in vitro* cytotoxicity showed that the presence of the fluorous shell in the micellar structures considerably reduced the cellular toxicity of the polymers. These results demonstrate the promising advantages of semifluorinated polymers for drug delivery application.

3.1 Introduction

The high stability of perfluorocarbon (PFC)-based nanoparticles has driven the development of semifluorinated polymers used as carriers in drug delivery system.[1-4] The design and architecture of polymers are crucial for determining the physicochemical properties of nanoparticles.[5] In drug delivery, because of the dual hydrophobicity and lipophobicity of PFCs,[3, 6] the semifluorinated polymer design necessitates the inclusion of a hydrophilic portion in the polymer to provide water-solubility. As a result, fluorinated polymers are often designed as semifluorinated multi-block copolymers. Typical semifluorinated block copolymers arrangements are diblock or triblock copolymers with linear or branched architectures. Semifluorinated triblock copolymers consist of hydrophilic, lipophilic, and fluorophilic segments. They have received a lot of attention and have been developed in various architectures to be used in biomedical applications.[1, 7-8] Triblock copolymers self-assemble in aqueous environments, resulting in water-soluble nanoparticles with specific morphologies. The order and arrangement of the blocks in the semifluorinated triblock copolymers can affect the properties and morphologies of self-assembled nanoparticles.[5, 9-11]

We have previously reported the effect of different architectures of triphilic semifluorinated polymers that have a terminal fluorous block (ABC structure where A is hydrophilic, B is lipophilic, and C is fluorophilic) on their physicochemical properties.[5] The introduction of a fluorocarbon block to linear and dibranched copolymers showed an improved thermodynamic stability and microviscosity due to the formation of a compact fluorous core. However, the design of a short hydrocarbon segment in the semifluorinated polymers led to a lower encapsulation of the hydrophobic species compared to commercially available phospholipid-based $mPEG_{2K}$-DSPE or $mPEG_{5K}$-DSPE polymers.[5] Herein, we seek to improve the encapsulation properties of the semifluorinated polymers by designing new polymers based on our novel M2F8H18 polymer that has been previously used for the successful preparation of a highly stable nanoemulsion.[12] The new polymer designs consist of a symmetrical dibranched semifluoriated triblock copolymer, M2diF8H18, and an asymmetrical dibranched semifluorinated triblock copolymer,

M2diF8H18/F8 (**Figure 3.1**). The nomenclatures for the polymer are as follows: i) M2 represents poly(ethylene glycol) (PEG) with a methoxy cap at the α position where 2 is the average molecular weight in the thousands, ii) F8 represents the fluorocarbon block where 8 is the number of carbon atoms substituted with fluorine atoms, and iii) H18 represents the hydrocarbon block where 18 is the number of carbon atoms substituted with hydrogen atoms. The hydrocarbon block was designed to have a similar -CH_2- repeating unit as the commercially available nonionic surfactant, $mPEG_{2K}$-DSG (**Figure 3.1**), providing similar hydrophobic capacity for solubilizing hydrophobic molecules. In this study, we report the synthesis of the dibranched semifluorinated polymers, M2diF8H18 and M2diF8H18/F8, and a characterization of their physicochemical properties compared to their linear counterpart, M2F8H18, a linear diblock copolymer, M2H18, and a commercially available phospholipid-based $mPEG_{2K}$-DSG (**Figure 3.1**). The syntheses of M2F8H18 and M2H18 can be found in our previous publications.[12-13] These polymers were used for micelle preparation (**Figure 3.2**) and the effect of polymer architectures (linear vs. dibranched and diblock vs. triblock) on the micellar properties were studied. The encapsulation of a model hydrophobic anticancer drug (paclitaxel), *in vitro* time release profiles, and cytotoxicity of these polymers were explored.

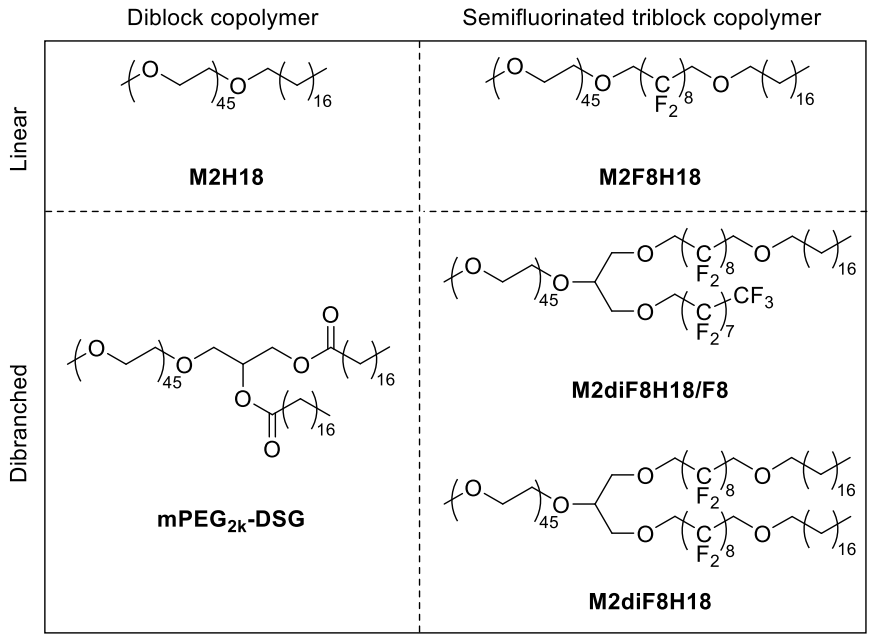

Figure 3.1 Chemical structure of dibranched semifluorinated and other related polymers.

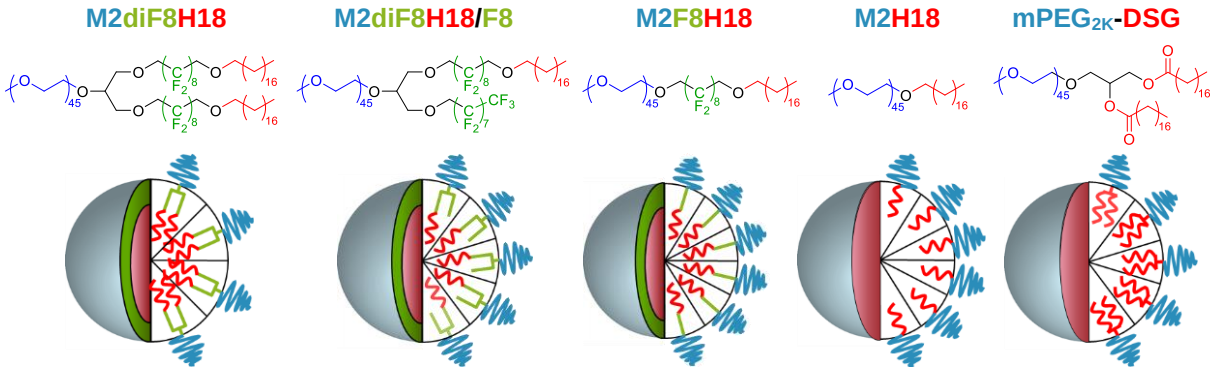

Figure 3.2 Schematic representation of micelles composed of linear and branched polymers.

3.2 Results and Discussion

3.2.1 Synthesis of semifluorinated dibranched polymers

We have previously reported the successful synthesis of semifluorinated dibranched polymers with a terminal fluorous block denoted as ABC structure.[5] A stable dibranched semifluorinated alcohol (HO-BC) was synthesized through an anionic synthesis and further coupled to a mono-methoxy capped poly(ethylene glycol) (mPEG) through a Williamson ether synthesis providing the final polymer in moderate to good yields.[5] The insertion of the hydrocarbon spacer between the reactive functionality and the fluorous tail of HO-BC led to an enhanced reactivity of the corresponding semifluorinated alcohols, driving the reaction to favor product formation.[14] Herein, we reported the synthesis of semifluorinated dibranched polymers with ACB structure, having a middle fluorous block. The semifluorinated dibranched polymers were designed to contain a symmetrical (M2diF8H18) and an asymmetrical (M2diF8H18/F8) branched structures (**Figure 3.1**). The synthesis of the dibranched semifluorinated alcohol (HO-CB) has been reported in the literature,[15] and a similar procedure was adopted for synthesizing HO-diF8H18 and HO-diF8H18/F8. The synthesis of HO-diF8H18 and HO-diF8H18/F8 were completed by Dr. Corinna Galli. The linear semifluorinated alcohol HO-F8H18 was first synthesized according to our previously published work.[12] HO-F8H18 was further reacted with epichlorohydrin and NaOH to generate the oxirane followed by an oxirane ring opening reaction with an additional alcohol to yield the corresponding dibranched

semifluorinated alcohols. However, the reactivity of these dibranched alcohols towards the coupling reaction with mPEG was greatly reduced due to the electron-withdrawing properties of the fluorocarbons which resulted in less than 10% of the PEGylated product (data not shown). Therefore, to circumvent the low reactivity of HO-CB, a new synthesis route was developed where the linear alcohol was separately attached to the branched mPEG (**Scheme 3.1**).

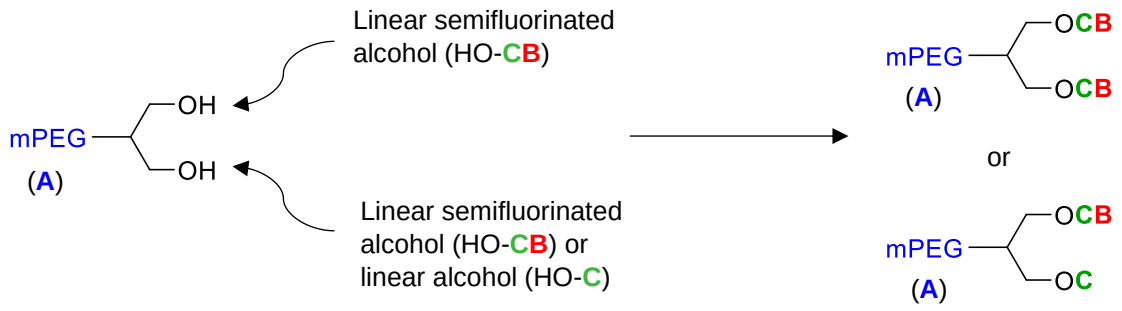

Scheme 3.1 Synthesis strategy for dibranched semifluorinated polymer with ACB structure.

The synthesis of the ACB triblock copolymer started with a functionalization methoxy capped poly(ethylene glycol) with average molecular weight of 2,000 (M2) with 2-phenyl-1,3-dioxan-5-ol (**3-1**). Compound **3-1** was synthesized through the acetal protection of the two primary alcohols of glycerol. This reaction proceeded with a low yield due to the mixture of the 1,2- and 1,3- protected products.[16] M2 was mesylated under basic condition to give **3-2**. Subsequent Williamson ether synthesis of compound **3-1** with **3-2** through a reflux reaction under basic conditions gave benzylidene acetal-M2, **3-3**, as a starting material for the synthesis of the dibranched polymers (**Scheme 3.2**). Compound **3-3** was used directly in subsequent reactions without further purification due to the difficulty in separating **3-3** and unreacted M2.

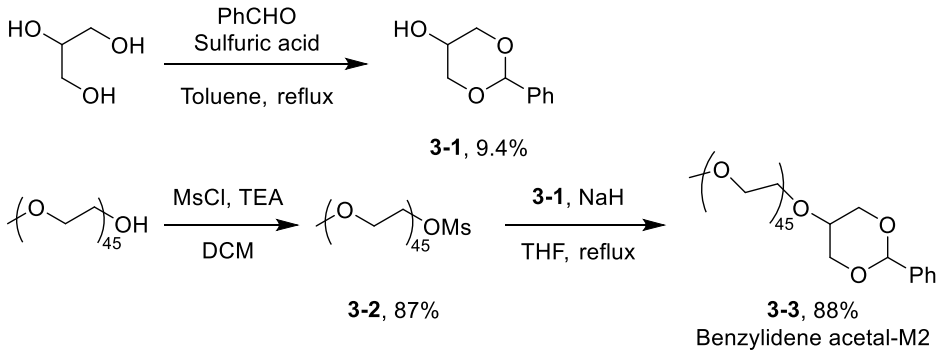

Scheme 3.2 Synthesis of Benzylidene acetal-M2.

The symmetric dibranched semifluorinated polymer, M2diF8H18, was prepared starting from compound **3-3** and proceeded with a deprotection reaction. The benzylidene acetal deprotection of compound **3-3** utilizes the method developed by Procopio *et al.*[17] through a microwave (MW)-assisted reaction in DI water at high temperature to give **3-4**. The mesylation of the two primary alcohols of **3-4** yielded **3-5**. Subsequent Williamson ether synthesis of **3-5** with a linear semifluorinated alcohol, HO-F8H18, through a reflux reaction under basic conditions yielded a final M2diF8H18 polymer, **3-6**. The crude polymer **3-6** was purified by an automated CombiFlash system, resulting in a pure isolated product with an improved yield (**Scheme 3.3**). The deprotection of the acetal exposed two free primary alcohols which further allowed the symmetrical addition of the highly reactive linear semifluorinated alcohols to both ends, providing a desired symmetrical dibranched semifluorinated polymer.

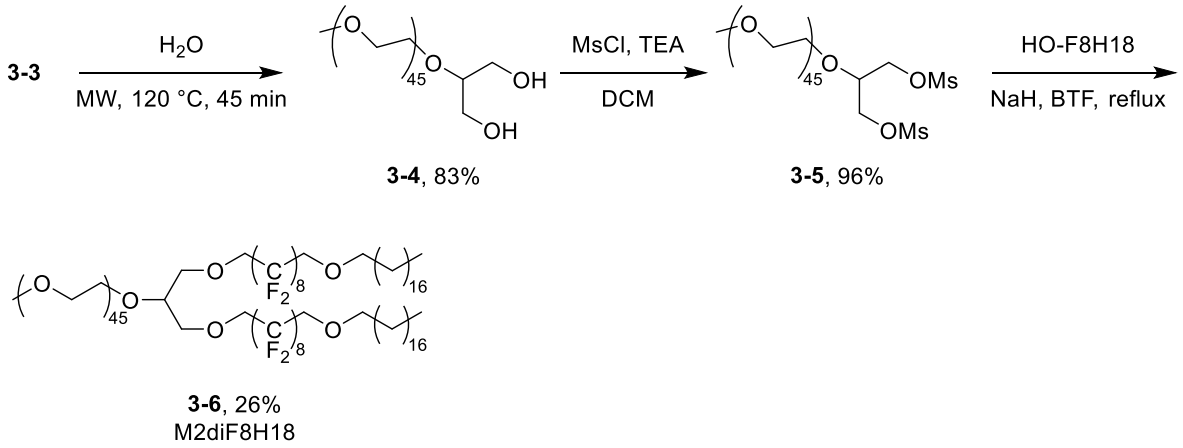

Scheme 3.3 Synthesis of M2diF8H18.

The asymmetrical dibranched semifluorinated polymer, M2diF8H18/F8, requires a conjugation of two different alcohols: HO-F8H18 and 1H,1H-perfluorononan-1-ol (HO-F8) on compound **3-3**. Reductive ring opening of compound **3-3** was first performed with BH_3·THF catalyzed by $Cu(OTf)_2$ to afford **3-7**. The reaction proceeded with 100% ring opening product which was observed from the absence of δ5.55 peak and the presence of δ4.54 from ^{1}H NMR, indicating 1 H next to the phenyl group (-C*H*C_6H_5) in starting material and 2 H from the benzyl group (-OC*H*$_2C_6H_5$) in the product, respectively. The free primary alcohol was mesylated under basic condition to produce **3-8**, and subsequently reacted with HO-F8 using MW-assisted synthesis to give **3-9**. The MW-assisted synthesis accelerated the coupling reaction of the semifluorinated alcohol to PEG where the reaction was run for 2 h compared to the conventional reflux reaction which was normally run for several days. Compound **3-9** (M2diOBn/F8) was purified using an automated Combiflash system and isolated as a pure polymer in a moderate yield. Deprotection of benzyl group through hydrogenation reaction in the presence of palladium on carbon (Pd/C) as a catalyst in the H_2 atmosphere was carried out in methanol resulted in the M2diOH/F8 intermediate, **3-10**. The mesylation reaction was once again performed on the primary alcohol of **3-10** to give **3-11**. Finally, the linear semifluorinated alcohol, HO-F8H18, was coupled to **3-11** through the MW-assisted synthesis to give a final asymmetric semifluorinated polymer, M2diF8H18/F8, **3-12** (**Scheme 3.4**). Compound **3-12** was purified by an automated CombiFlash system, resulting in a pure isolated product with a moderate yield.

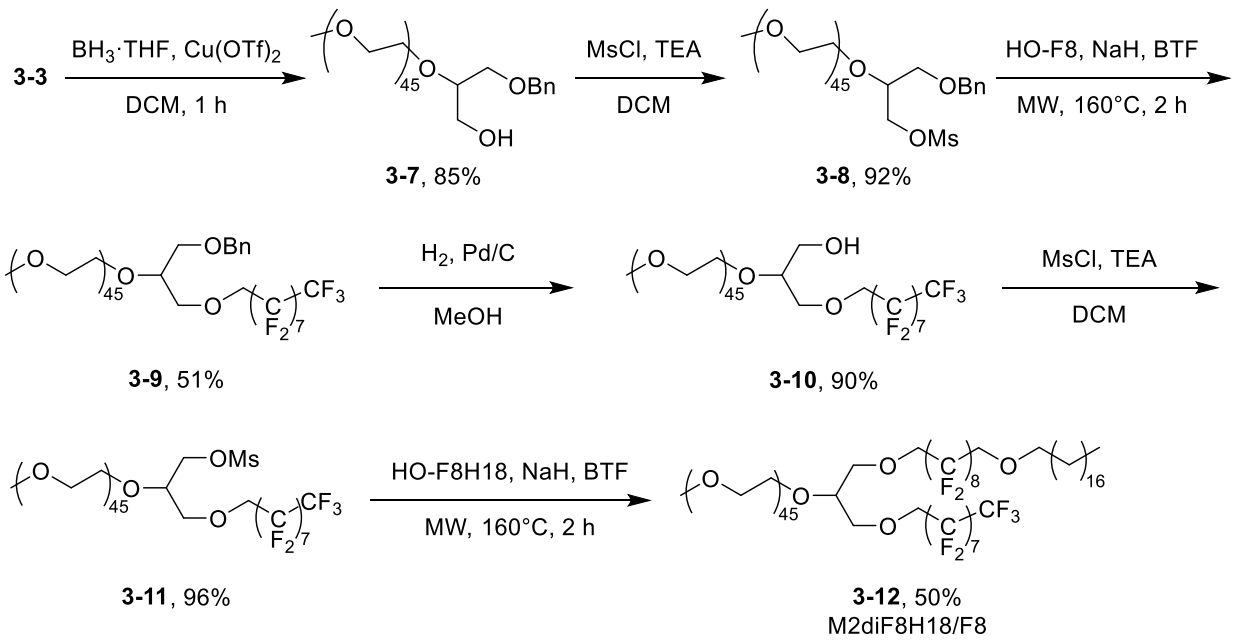

Scheme 3.4 Synthesis of M2diF8H18/F8.

3.2.2 Physicochemical characterization

The synthesized dibranched semifluorinated polymers, M2diF8H18 and M2diF8H18/F8 are water-soluble and can form micelles in aqueous solution. With the increase in the fluorophilic segment in the dibranched section, these polymers are more hydrophobic than their linear counterpart, M2F8H18, as observed from their partial solubility in acetonitrile (ACN). Physicochemical properties of dibranched semifluorinated polymers were studied and compared to the linear semifluorinated polymer, M2F8H18, and the linear and dibranched polymers without fluorous segment (diblock copolymer), M2H18, and $mPEG_{2K}$-DSG, respectively.

Table 3.1 Physicochemical properties of linear and dibranched polymers.

	CMC (μM)	Aggregation number (N_{agg})	Microviscosity (I_M/I_E)	Hydrodynamic diameter (nm)[a]
M2diF8H18	13.8 ± 1.1	55 ± 4	0.79 ± 0.05	27.4 ± 0.3
M2diF8H18/F8	20.5 ± 2.1	70 ± 3	3.47 ± 0.50	17.3 ± 0.4
M2F8H18	11.8 ± 0.1	84 ± 3	9.19 ± 0.82	15.7 ± 0.2
M2H18	9.7 ± 0.6	72 ± 7	5.20 ± 0.67	11.6 ± 0.7
$mPEG_{2K}$-DSG	7.7 ± 1.4	70 ± 4	3.99 ± 0.30	15.8 ± 1.2

[a] hydrodynamic diameter of polymer aggregates in Milli-Q water.

The critical micelle concentrations (CMCs) of the polymers were determined using a pyrene fluorescence method. This method was selected because of its convenience and low sample consumption. The hydrophobic nature of pyrene allows for its solubilization in the hydrophobic environment of the micelles. The intensity of I_1 and I_3 vibronic bands of pyrene (**Figure 3.3a**) was monitored and expressed as the I_1/I_3 ratio. This ratio reflects the microenvironment of micelles which are varied depending on the concentrations of polymers.[18-20] I_1/I_3 ratios were plotted against polymer concentrations and fitted by a Boltzmann-type sigmoid. CMCs were calculated from the middle of the sigmoid (**Figure 3.3a**) as described by Aguiar *et al*. for nonionic surfactants.[21] CMC values of all five polymers in aqueous solution are presented in **Table 3.1**. All polymers provide relatively similar CMC values, regardless of their architectures (linear vs. dibranched) or an addition of fluorophilic segment (diblock vs. triblock). The triblock copolymers are expected to form a corona-shell-core micelle structure due to the rigidity of fluorocarbon while the diblock copolymers are expected to form a shell-core structure. It should be noted that all polymers possess the same core forming hydrophobic moiety (H18). This results in relatively similar core stability as observed from comparable CMCs. However, a slightly higher CMC of M2diF8H18/F8 compared to M2diF8H18 was observed. This is due to a reduced hydrophobic H18 block which led to a lower core hydrophobicity, consequently resulting in a higher CMC.

Micelles aggregation numbers (N_{agg}) are reported in **Table 3.1**. N_{agg} was determined from a steady-state fluorescence quenching method using pyrene as a fluorescent probe and coumarin 153 (C153) as a quencher. The selection of C153 was based on its tendency to partition into micelles. This quenching mechanism has been thoroughly investigated by Tummino and Gafni.[22] M2F8H18 was found to have the highest aggregation number while M2diF8H18 showed the lowest value. This indicates that M2F8H18 micelles are composed of a greater number of linear semifluorinated polymers compared to the other polymer-forming micelles. This results in the tight packing of the M2F8H18 polymers when forming a micelle. In the case of M2diF8H18 micelles, the presence of the semifluorinated dibranched structure increases the chain's rigidity and, thus, restricts the polymer' mobility. As a result, an aggregate is formed with less polymers, leading to a loose packing. M2diF8H18/F8 micelles shared a similar N_{agg} as $mPEG_{2K}$-DSG micelles while a slightly higher N_{agg} was observed for M2H18 micelles. This suggests a more compact packing of M2H18 micelles than M2diF8H18/F8 and $mPEG_{2K}$-DSG micelles.

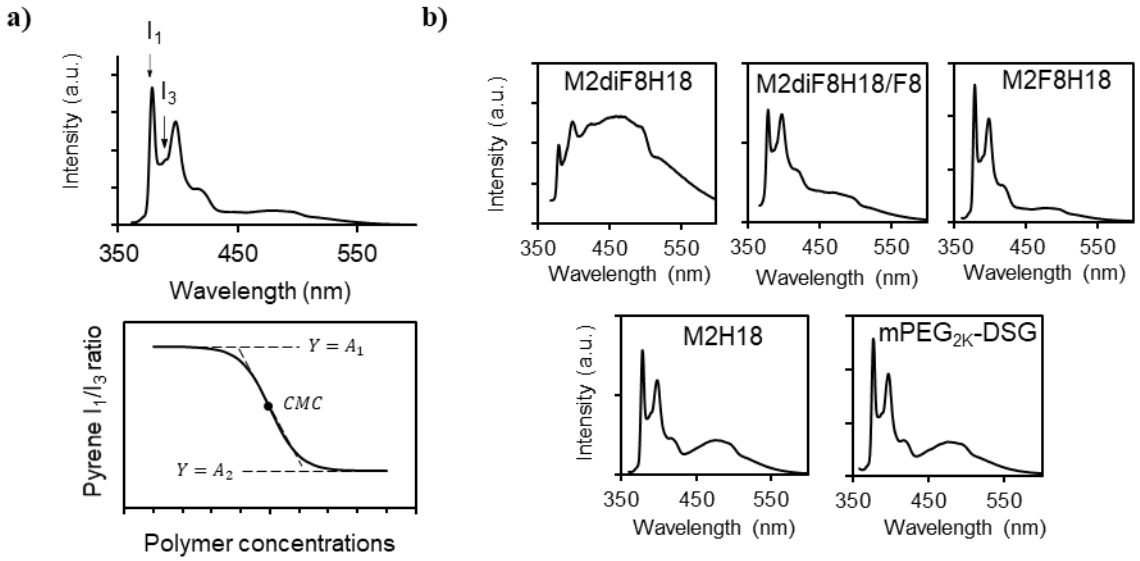

Figure 3.3 Fluorescence emission spectrum of micelles. a) Top: Fluorescence emission spectrum of pyrene in aqueous solution of M2F8H18. Bottom: A Boltzmann-type sigmoid of pyrene I_1/I_3 ratios plotted against polymer concentrations. CMC is calculated from the center of the sigmoid. b) Fluorescence emission spectra of the P3P probe in aqueous solutions of the five polymers.

P3P has been widely used as a tool for determining the microviscosity of micelles. P3P is a hydrophobic fluorescent probe that can incorporate into the micelle's hydrophobic domain where it can stay as a monomer or form an intramolecular excimer when excited. P3P is composed of two pyrenyl moieties connected by carbon bonds that can rotate freely. The extent of the excimer formation and emission depends on the viscosity of the micelle's environment. High viscosity will lead to a more restricted environment which impedes the conformational change of P3P. Therefore, a greater monomer to excimer fluorescent intensity ratio (I_M/I_E) represents a highly-dense microenvironment.[18, 20, 23-24] The P3P fluorescence spectra of each micelle are shown in **Figure 3.3b** and the I_M/I_E ratios are summarized in **Table 3.1**. As expected, M2F8H18 micelles had the highest microviscosity which corroborates well with its high aggregation number. The tight packing restricts the movement of the molecules, resulting in a highly viscous environment. Similarly, M2diF8H18 whose aggregation number is the smallest demonstrated the lowest I_M/I_E ratio. M2H18 micelles possess a slightly higher viscous core than M2diF8H18/F8 and $mPEG_{2K}$-DSG. It should be noted that the I_M/I_E ratio decreased when the polymer architecture changed from the linear to dibranched structure. This is probably due to the increased hydrophobicity and/or rigidity from the fluorocarbon of dibranched chains that form the loosely packed micellar core. As a result, the movement in the core is less restricted, lowering the microviscosity.

The average particle sizes of M2diF8H18, M2diF8H18/F8, M2F8H18, M2H18, and $mPEG_{2K}$-DSG micelles were determined by DLS and are summarized in **Table 3.1**. The linear diblock M2H18 polymer formed the smallest aggregate size due to its small hydrophobic portion (H18). Increasing the hydrophobic portion from linear (H18) to dibranched ($mPEG_{2K}$-DSG) or adding a fluorous block to the linear polymer (M2F8H18) leads to an increased in the micellar size. Interestingly, while an addition of two fluorous segments with one hydrocarbon chain (M2diF8H18/F8) did not have any effect on the size of the aggregate, the presence of two fluorocarbon-hydrocarbon chains (M2diF8H18) resulted in an almost two-fold increase in the aggregate size. This result corroborates well with its low aggregation number and microviscosity.

3.2.3 Drug encapsulation

The ability to encapsulate hydrophobic molecules is a core factor in determining whether these polymers can be used as a micellar drug delivery system. Therefore, the encapsulation of paclitaxel (PTX), a model hydrophobic drug, in the polymeric micelles was investigated. PTX is selected as it can only be solubilized in the hydrocarbon domain and not in the fluorophilic domain of micelles as previously reported.[5] Therefore, the effect of the middle fluorous block in the linear or dibranched polymers could be probed through the encapsulation of the hydrophobic PTX molecule in the hydrophobic domain of the micelles. PTX encapsulated micelles were prepared using a thin-film solvent evaporation method with equimolar amounts of polymers to allow for a direct comparison.[5, 25]

The sizes of PTX-loaded micelles are summarized in **Table 3.2**. PTX encapsulation did not lead to any increase in micellar sizes compared to the empty micelles. The concentrations of PTX encapsulated in the micelles at 0 h, 24 h, and 7 days are shown in **Figure 3.4**. M2diF8H18, M2F8H18, and $mPEG_{2K}$-DSG were initially able to encapsulate similar amount of PTX and showed full encapsulation (more than 97%) of initial PTX amount added (**Table 3.2**). M2diF8H18/F8 and M2H18 micelles, on the other hand, encapsulated only *ca*. 52% and 64% of initially added PTX. Interestingly, a lower PTX encapsulation was found in an asymmetric dibranched polymer, M2diF8H18/F8, and a linear diblock polymer, M2H18 which contain only one H18 chain. We have previously demonstrated that the fluorocarbon moiety of the micelles did not participate in the encapsulation of hydrophobic molecules and one of the key factors in the encapsulation of hydrophobic molecules is the hydrophobic carrying capacity.[5, 23] Compared to $mPEG_{2K}$-DSG which has a similar aggregation number, the presence of only one hydrophobic H18 chain per polymer in M2diF8H18/F8 and M2H18 (versus two from each $mPEG_{2K}$-DSG) leads to a smaller hydrophobic carrying capacity and results in a lower initial encapsulation. M2F8H18 contains only one H18 chain, but, unlike M2diF8H18/F8 and M2H18, has the highest aggregation number and microviscosity. This provides M2F8H18 micelles with strong hydrophobic cores, allowing a high encapsulation of hydrophobic species comparable to the dibranched structure of M2diF8H18 and $mPEG_{2K}$-DSG.

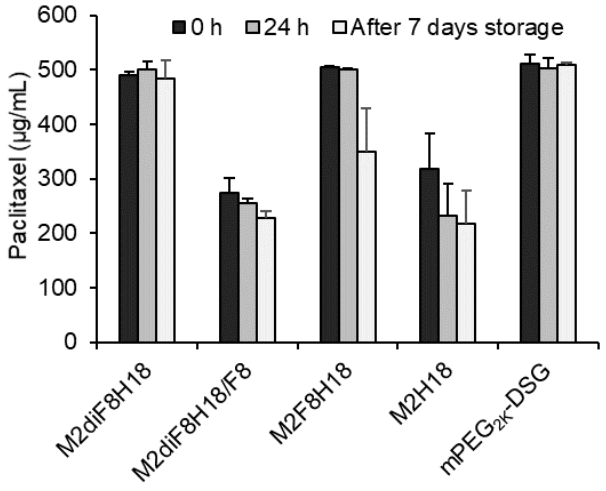

Figure 3.4 Amount of PTX encapsulated in polymeric micelles quantified by HPLC at 0 h, 24 h, and 7 days. Data represent mean ± S.D. (n = 3).

The retention of drug inside the micelles is also an important parameter for determining a good delivery carrier. The amount of PTX after 24 h was quantified to investigate the loss of the encapsulated drug.[5, 26] After 24 h, M2H18 showed a significant reduction of PTX. This suggests that due to the lower hydrophobic capacity, the hydrophobic molecules were poorly encapsulated inside the micellar core but were probably retained on the PEG corona which lead to a rapid loss of PTX.[5, 26] However, only a slight PTX content reduction was observed in M2diF8H18/F8 micelles, suggesting that, compared to M2H18, the fluorinated shell from M2diF8H18/F8 prevented the loss of PTX from the hydrophobic core.

Table 3.2 PTX encapsulation in polymeric micelles. Data represent mean ± S.D. (n = 3).

Polymer	Diameter of PTX-loaded micelle (nm)	PTX loading efficiency (%)	% changed at 24 h[a]	% changed at Day 7[a]
M2diF8H18	30.0 ± 0.7	97.9 ± 1.6	0.8 ± 2.2	-1.1 ± 6.9
M2diF8H18/F8	17.2 ± 0.2	51.8 ± 7.5	-7.3 ± 3.6	-16.7 ± 4.0
M2F8H18	14.7 ± 0.8	100.9 ± 0.4	-1.0 ± 0.6	-30.7 ± 15.9
M2H18	12.3 ± 0.2	63.5 ± 13.1	-41.9 ± 12.8	-44.8 ± 8.3
$mPEG_{2K}$-DSG	15.1 ± 0.4	102.1 ± 3.3	-1.4 ± 3.6	-0.3 ± 0.7

[a] % changed = (concentration at 24 h or Day 7 – initial concentration)/initial concentration × 100.

By monitoring the amount of PTX, one can look at the overall stability of the micelles in a storage condition (4 °C) through the drug retention. The PTX contents were monitored up to one week. At day 7, only M2diF8H18 and mPEG$_{2K}$-DSG micelles showed a negligible PTX loss (**Figure 3.4**), suggesting a high stability of the micelles. A slight PTX content reduction from 24 h was observed for M2diF8H18/F8 and M2H18 micelles at day 7. It should be noted that even though M2F8H18 micelles demonstrated a high retention of PTX after 24 h (1% decreased from day 0), a significant PTX reduction was observed on day 7 (31% decreased from day 0), despite the polymer's high microviscosity (**Table 3.2**). This suggests a lower stability during the storage condition.

3.2.4 In vitro time release

In vitro time release kinetics of PTX encapsulated micelles were investigated by dialyzing micelle solutions under sink condition in buffer for 48 h. The time release profiles were plotted for each polymer (**Figure 3.5**). M2H18, M2F8H18, M2diF8H18, M2diF8H18/F8, and mPEG$_{2K}$-DSG micelles released ca. 79%, 75%, 61%, 53%, and 36% of PTX after 48 h, respectively. M2H18 and M2F8H18 micelles showed the fastest PTX release followed by M2diF8H18 and M2diF8H18/F8 with the slowest PTX release from mPEG$_{2K}$-DSG. These results suggest that the semifluorinated dibranched structures form a better fluorous shell sealing the hydrophobic core content, thus prolonging PTX release.

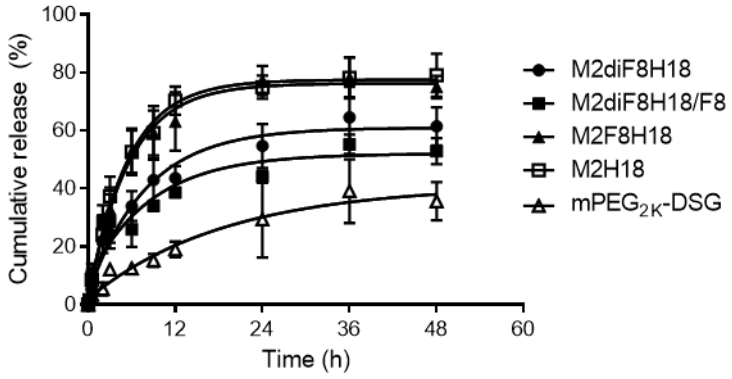

Figure 3.1 Time release profiles of PTX-loaded polymeric micelles. The amount of PTX was quantified by HPLC. Data represent mean ± S.D. (n = 3).

3.2.5 In vitro cytotoxicity of polymers

Safety is one of the most important aspects that determine the utility of formulations. Prior to *in vivo* administration of polymeric carriers, the biocompatibility of the polymers needs to be assessed. The *in vitro* cytotoxicity of all five polymers were evaluated on 4T1-Luc, murine breast carcinoma, cells. The cell viability was measured using the CellTiter-Blue® assay. As shown in **Figure 3.6**, negligible cell death was observed for M2diF8H18 and M2diF8H18/F8 after an 24 h incubation over the concentration range tested (10 μM – 1 mM). This suggests a high biocompatibility of the synthesized dibranched semifluorinated polymers. Interestingly, M2F8H18 and $mPEG_{2K}$-DSG showed a reduction in cell viability at 500 μM. In addition, when the cells were exposed to M2H18, the cell viability decreases to be less than 40% at a polymer concentration of 50 μM and reduces to 0% at 100 μM. The high cytotoxicity of M2H18 can be explained by a "detergent effect" of the nonionic surfactants with long hydrocarbon chains. The nonionic surfactant can mechanically destabilize the lipid bilayer by partitioning into the membrane.[27-28] It is worth noting that the addition of a fluorous block leads to a reduced cytotoxic effect in the linear architecture as shown by the higher cell viability of M2F8H18, compared to M2H18. This can be explained by the reduced partitioning of fluorinated polymers into lipid bilayers due to fluorous phase segregation.[29] As a result, the detergent-like properties of the polymer were reduced after an introduction of the fluorinated moiety, resulting in a reduced cytotoxicity.[14, 30-31]

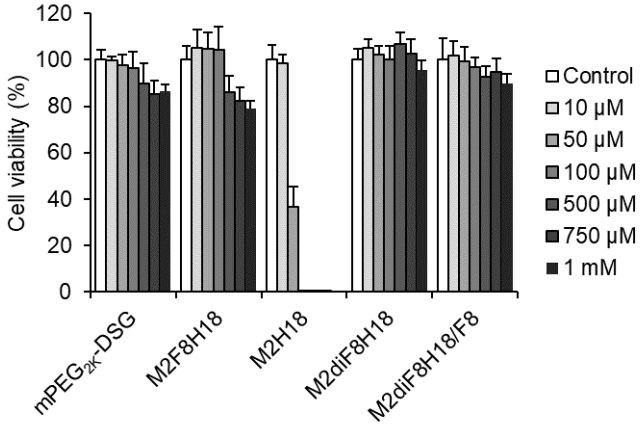

Figure 3.6 Cytotoxicity of polymers on 4T1-Luc cells after 24 h incubation.

3.3 Conclusions

We have reported the syntheses of two dibranched semifluorinated triblock copolymers: a symmetric, M2diF8H18, and an asymmetric, M2diF8H18/F8 polymers. We have characterized the physicochemical properties of these polymers and compared them to the linear triblock (M2F8H18) and the linear (M2H18) and dibranched ($mPEG_{2K}$-DSG) diblock copolymers. The introduction of a fluorocarbon in the ACB architecture led to the formation of a fluorous shell in a corona-shell-core micelle structure which bestows the aggregates with different physicochemical properties, depending on the polymer architecture. For the linear triblock copolymer, the introduction of a fluorous block allows for the formation of aggregates with a higher aggregation number and microviscosity compared to the corresponding polymer without a fluorocarbon block. For dibranched triblock copolymers, the symmetric dibranched forms a loose aggregate with lower microviscosity owing to the rigidity and higher volume of fluorocarbons. The asymmetric dibranched shares similar properties to the corresponding polymer without a fluorocarbon block. All polymers form micelles in an aqueous solution and can encapsulate PTX inside their structure. The encapsulation efficiency of the corresponding aggregates is determined by the hydrophobic capacity which solely depends on the hydrocarbon moiety. The prolonged release of PTX was enhanced in the dibranched structure compared to the linear structure due to the better sealing of the fluorocarbon segments. The fluorous shell in the micellar structures reduces the cellular toxicity, suggesting that the semifluorinated polymers are good candidates for drug delivery carriers.

3.4 Experimental

3.4.1 Materials and Methods

1H,1H-perfluoro-1-nonanol and 1H,1H,10H,10H-perfluorodecane-1,10-diol were purchased from SynQuest Laboratories Inc. (Alachua, FL). Distearoyl-rac-glycerol-PEG2K ($mPEG_{2K}$-DSG) was purchased from Avanti Polar Lipids (Alabaster, AL). 1,3-Bis-(1-pyrenyl)propane (P3P) was purchased from Life Technologies (Carlsbad, CA). Paclitaxel (PTX) was purchased from LC Laboratories (Woburn, MA).

Solvents and all other chemicals were purchased from Sigma-Aldrich and were used as purchased, unless otherwise specified. Small molecule and polymer chromatography were performed with Silicycle 60 Å SiO_2 or using a Teledyne CombiFlash Rf 4× (Lincoln, NE) equipped with an ELSD for visualization and RediSep® Rf high performance silica or C18 columns.

^{1}H, ^{13}C, and ^{19}F NMR spectra were measured using a Bruker Avance III HD 400 MHz spectrometer. All spectra were measured with either $CDCl_3$ as the solvent. Polymer purity was confirmed by MALDI-MS on a rapifleX MALDI TOF/TOF (Bruker, Billerica, MA) using α-cyano-4-hydroxycinnamic acid matrix unless otherwise specified.

*3.4.2 Synthesis of 2-phenyl-1,3-dioxan-5-ol (**3-1**)*

Using a Soxhlet extractor, a column was filled with anhydrous $CaCl_2$ (50 g). Glycerol (37.7 g, 0.41 mol) was dissolved in dry toluene (50 mL) under Ar. Benzaldehyde (32.7 mL, 0.32 mol) was then added followed by 10 drops of concentrated sulfuric acid. The reaction flask was connected to the Soxhlet extractor and the reaction was heated to reflux for 2 days. After this time, the solvent was removed from the reaction flask under reduced pressure. Diethyl ether (250 mL) was added to redissolve the residue and the solution was frozen at -80°C for at least 4 h. The white solid was vacuum filtered and the collected solid was recrystallized in 60 mL of toluene:petroleum ether (1:1). The white crystal was collected and dried under high vacuum (5.39 g, 9.4% yield). ^{1}H NMR (400 MHz, $CDCl_3$) δ 7.49 (d, J = 1.8 Hz, 2H), 7.42 – 7.33 (m, 3H), 5.56 (s, 1H), 4.17 (q, 4H), 3.63 (d, J = 10.7 Hz, 1H), 3.08 (d, J = 11.1 Hz, 1H). ^{13}C NMR (101 MHz, $CDCl_3$) δ 137.83, 129.13, 128.35, 125.89, 101.69, 72.32, 64.03.

*3.4.3 Synthesis of "M2-OMs" methoxypoly(ethylene glycol) methanesulfonate **(3-2)***

Poly(ethylene glycol) methyl ether (M2-OH) (10 g, 4.76 mmol) was dissolved in dry DCM (60 mL) under Ar. TEA (1.99 mL, 14.28 mmol) was then added followed by the addition of methanesulfonyl chloride (MsCl, 920 µL, 11.9 mmol) dropwise. The reaction was allowed to stir at room temperature overnight. After this time, the reaction was diluted in DCM and washed with saturated NH_4Cl solution (3x).

The collected organic layer was dried over $MgSO_4$ and concentrated under reduced pressure. The product was then freeze-dried in a mixture of DCM and benzene to give the product as a white powder (8.99 g, 87% yield). ^{1}H NMR (400 MHz, $CDCl_3$) δ 4.43 – 4.34 (m, 2H), 3.78 – 3.53 (m, 178H), 3.38 (s, 3H), 3.09 (s, 3H).

*3.4.4 Synthesis of Benzylidene acetal-M2 (**3-3**)*

3-1 (0.9 g, 5 mmol) was dissolved in dry THF (60 mL) under Ar. The solution was cooled down to 0 °C. NaH (480 mg, 20 mmol) was then added and the reaction mixture was allowed to warm up to room temperature for 30 min with vigorous stirring. After this time, **3-2** (4 g, 2 mmol) was added and the reaction was stirred under reflux for 2 days. After 2 days, the reaction mixture was quenched with water, diluted in DCM, and washed with saturated NH_4Cl solution (3x). The collected organic layer was dried over $MgSO_4$ and concentrated under reduced pressure. The crude product was precipitated in cold diethyl ether. The product was collected and freeze-dried under high vacuum to give the product as white powder (3.82 g, 88% yield, ~70% conjugation). The product was used without further purification for the next synthetic step. ^{1}H NMR (400 MHz, $CDCl_3$, contain free M2-OH) δ 7.56 – 7.33 (m, 4H), 5.55 (s, 1H), 4.36 (dd, J = 12.6, 1.7 Hz, 1H), 4.05 (dd, J = 12.7, 1.8 Hz, 1H), 3.78 – 3.53 (m, 184H), 3.38 (s, 3H).

*3.4.5 Synthesis of "M2-diol" (**3-4**)*

3-3 (1.52 g, 0.698 mmol) was dissolved in deionized water (10 mL) in a G30 microwave reaction vial. The reaction was run in a Monowave 300, Microwave Synthesis Reaction (Anton Paar, Austria) at 120 °C for 45 min. After this time, the reaction solution was extracted with DCM (3x). The collected DCM layer was dried over $MgSO_4$, and concentrated. The crude product was precipitated in cold diethyl ether. The white solid was collected and dried under high vacuum to give the intermediate product as a white powder (1.27 g, 100% deprotection, 95% yield). The product was used without further purification for the next synthetic step. ^{1}H NMR (400 MHz, $CDCl_3$, contain free M2-OH) δ 3.64 (m, 188H), 3.38 (d, J = 1.0 Hz, 3H).

*3.4.6 Synthesis of "M2-diOMs" (**3-5**)*

3-4 (1.27 g, 0.58 mmol) was dissolved in dry DCM (15 mL) under Ar. TEA (491.4 µL, 3.5 mmol) was then added followed by the addition of MsCl (225.7 µL, 2.92 mmol) dropwise. The reaction was allowed to stir at room temperature overnight. After this time, the reaction was diluted with DCM and washed with saturated NH_4Cl solution (3x). The collected organic layer was dried over $MgSO_4$ and concentrated under reduced pressure. The product was then freeze-dried in a mixture of DCM and benzene to give the product as a light-yellow powder (1.14 g, 88% yield). The product was used without further purification for the next synthetic step. ^{1}H NMR (400 MHz, $CDCl_3$, contain free M2-OH) δ 4.37 (qd, J = 11.1, 4.8 Hz, 4H), 3.78 – 3.53 (m, 275H (include free M2-OH)), 3.40 (s, 4H (include free M2-OH)), 3.11 (s, 6H).

*3.4.7 Synthesis of "M2diF8H18" (**3-6**)*

HO-F8H18 was synthesized according to previously published procedure.[12] HO-F8H18 (848 mg, 1.186 mmol) was dissolved in anhydrous benzotrifluoride (BTF, 15 mL). NaH (142 mg, 5.93 mmol) was added and the reaction mixture was stirred vigorously under Ar for 1 h. After this time, **3-5** (533 mg, 0.24 mmol) was added and the reaction was brought to reflux with vigorous stirring for 10 days. Small amounts of NaH were added throughout the 10 days to facilitate the reaction. After 10 days, water was slowly added to quench the reaction. The reaction was diluted in DCM, washed with saturated NH_4Cl solution, dried over $MgSO_4$, and concentrated under reduced pressure. The crude product was precipitated in cold diethyl ether. The solid was collected, redissolved in DCM, and adsorbed on Celite. The crude product was purified by automated flash chromatography, CombiFlash, using a RediSep® C-18 reverse phase silica column with a water (0.1% FA)–MeOH to dichloromethane–MeOH gradient. The collected fractions were then concentrated under reduced pressure and precipitated in cold diethyl ether. The brown solid was collected and dried under high vacuum (220 mg, 26% yield). ^{1}H NMR (400 MHz, $CDCl_3$) δ 4.00 (t, J = 13.7 Hz, 3H), 3.91 (t, J = 13.9 Hz, 4H), 3.78 – 3. 53 (m, 177H), 3.38 (s, 3H), 1.25 (s, 60H), 0.88 (t, J = 6.7 Hz, 6H). ^{19}F

NMR (376 MHz, $CDCl_3$) δ -119.70 (m), -121.96 (m), -123.46 (bs). MALDI MS: $[M + Na]^+$ calculated for $C_{146}H_{262}F_{32}NaO_{48}$ = 3414.74; found: 3414.706.

*3.4.8 Synthesis of "M2diOBn/OH" (**3-7**)*

3-3 (3 g, 1.38 mmol) was dissolved in dry DCM (30 mL) under Ar followed by an addition of BH_3·THF (1 M solution, 6.89 mL, 6.89 mmol). The reaction was allowed to stir for 10 min. $Cu(OTf)_2$ (74.87 mg, 15 mol%) was then added and the reaction was stirred at room temperature for 1 h. After this time, the reaction mixture was cooled down to 0 °C and quenched by adding 300 µL (2.1 mmol) TEA followed by 15 mL MeOH (caution: hydrogen gas was evolved). The crude solution was filtered through Celite. The filtrate was concentrated under reduced pressure. The residue was precipitate in cold diethyl ether. The solid was collected and dried under high vacuum to give the product as grey solid (2.94 g, 98% yield). The product was used without further purification for the next synthetic step. ^{1}H NMR (400 MHz, $CDCl_3$, contain free M2-OH) δ 7.33 (s, 5H), 4.54 (s, 2H), 3.78 – 3.53 (m, 280H), 3.38 (s, 4H).

*3.4.9 Synthesis of "M2diOBn/OMs" (**3-8**)*

3-7 (2.84 g, 1.3 mmol) was dissolved in dry DCM (20 mL) under Ar. TEA (543.6 µL, 3.9 mmol) was then added followed by the addition of MsCl (232 µL, 3 mmol) dropwise. The reaction was allowed to stir at room temperature overnight. After this time, the reaction was diluted with DCM and washed with saturated NH_4Cl solution (3x). The collected organic layer was dried over $MgSO_4$ and concentrated under reduced pressure. The product was then freeze-dried in a mixture of DCM and benzene to give the product as an off-white solid (2.71 g, 92% yield). The product was used without further purification for the next synthetic step. ^{1}H NMR (400 MHz, $CDCl_3$, contain free M2-OH) δ 7.44 – 7.28 (m, 5H), 4.54 (d, J = 2.1 Hz, 2H), 4.43 – 4.27 (m, 2H), 3.78 – 3.53 (m, 313H), 3.38 (s, 5H), 3.04 (s, 3H).

*3.4.10 Synthesis of "M2diOBn/F8" (**3-9**)*

1H,1H-Perfluorononan-1-ol (F8-OH, 748.3 mg, 1.66 mmol) was dissolved in anhydrous BTF (15 mL) under Ar in a G30 microwave reaction vial. NaH (159.6 mg, 6.65 mmol) was then added and the

reaction mixture was stirred for 1 h. After this time, **3-8** (1.5 g, 0.665 mmol) was added and the reaction was run in Monowave 300, Microwave Synthesis Reaction (Anton Paar, Austria) at 160 °C for 2 h. After the microwave reaction, water was slowly added to quench the reaction. The reaction was diluted in DCM, washed with saturated NH_4Cl solution (3x). The collected organic layer was dried over $MgSO_4$ and concentrated under reduced pressure. The crude product was adsorbed on Celite and purified by an automated flash chromatography using a RediSep® C-18 reverse phase silica column with a water (0.1% FA)–MeOH to dichloromethane–MeOH gradient. The collected fractions were then concentrated under reduced pressure and dried under high vacuum to give the product as an off-white solid (887 mg, 51% yield). ^{1}H NMR (400 MHz, $CDCl_3$) δ 7.33 (dd, J = 7.1, 1.6 Hz, 5H), 4.53 (s, 2H), 4.01 (dd, J = 15.3, 12.7 Hz, 2H), 3.78 – 3.53 (m, 191H), 3.38 (s, 3H). ^{19}F NMR (376 MHz, $CDCl_3$) δ -80.71 (t, J = 10.0 Hz), -119.74 (s), -121.93 (s), -122.66 (s), -123.32 (s), -126.07 (s). MALDI MS: $[M + Na]^+$ calculated for $C_{106}H_{189}F_{17}NaO_{46}$ = 2544.21; found: 2544.373.

*3.4.11 Synthesis of "M2diOH/F8" (**3-10**)*

3-9 (1.05 g, 0.4 mmol) was dissolved in methanol (12 mL). The solution was stirred under Ar for 30 min. Palladium on carbon (92.1 mg, 0.87 mmol) was then added and the mixture was flushed with Ar for another 30 min. Then, the reaction was flushed with hydrogen gas and was kept under a static hydrogen atmosphere overnight. Afterwards, the reaction mixture was filtered through Celite. The filtrate was concentrated and dried under high vacuum to give the intermediate as an off-white solid (925.8 mg, 90% yield). ^{1}H NMR (400 MHz, $CDCl_3$) δ 4.01 (t, *J* = 13.7 Hz, 2H), 3.78 – 3.53 (m, 170H), 3.38 (s, 3H). ^{19}F NMR (376 MHz, $CDCl_3$) δ -80.71 (t, J = 9.9 Hz), -119.65 (s), -121.87 (s), -122.66 (s), -123.33 (s), -126.05 (s). MALDI MS: $[M + Na]^+$ calculated for $C_{101}H_{187}F_{17}NaO_{47}$ = 2498.19; found: 2498.645.

*3.4.12 Synthesis of "M2diOMs/F8" (**3-11**)*

3-10 (1.41 g, 0.56 mmol) was dissolved in dry DCM (14 mL) under Ar. TEA (234.2 µL, 1.68 mmol) was then added followed by the addition of MsCl (99.5 µL, 1.29 mmol) dropwise. The reaction was

allowed to stir at room temperature overnight. After this time, the reaction was diluted with DCM and washed with saturated NH_4Cl solution (3x). The collected organic layer was dried over $MgSO_4$ and concentrated under reduced pressure. The product was then freeze-dried in a mixture of DCM and benzene to give the product as an off-white powder (1.39 g, 96% yield). ^{1}H NMR (400 MHz, $CDCl_3$) δ 4.37 (dd, *J* = 11.0, 4.0 Hz, 1H), 4.27 (dd, *J* = 11.1, 5.2 Hz, 1H), 4.05 (dd, *J* = 13.6, 5.8 Hz, 2H), 3.78 – 3.53 (m, 176H), 3.38 (s, 3H), 3.07 (s, 3H). ^{19}F NMR (376 MHz, $CDCl_3$) δ -80.70 (t, *J* = 10.0 Hz), -119.64 (s), -121.90 (s), -122.65 (s), -123.29 (s), -126.06 (s).

*3.4.13 Synthesis of "M2diF8H18/F8" (**3-12**)*

HO-F8OH18 was synthesized according to previously published procedure.[12] To a G30 microwave reaction vial, HO-F8H18 (804.4 mg, 1.13 mmol) was dissolved in anhydrous BTF (12 mL) under Ar. NaH (108 mg, 4.5 mmol) was then added and the reaction mixture was stirred for 1 h. After this time, **3-11** (1.17 g, 0.45 mmol) was added and the reaction was run in a Monowave 300, Microwave Synthesis Reaction (Anton Paar, Austria) at 160 °C for 2 h. After the microwave reaction, water was slowly added to quench the reaction. The reaction was diluted in DCM, washed with saturated NH_4Cl solution (3x). The collected organic layer was dried over $MgSO_4$ and concentrated under reduced pressure. The crude product was adsorbed on Celite and purified by automated flash chromatography using a RediSep® C-18 reverse phase silica column with a water (0.1% FA)–MeOH to dichloromethane–MeOH gradient. The collected fractions were then concentrated under reduced pressure and dried under high vacuum to give the product as an off-white solid (728.3 mg, 50% yield). ^{1}H NMR (400 MHz, $CDCl_3$) δ 4.00 (t, J = 13.8 Hz, 4H), 3.91 (t, J = 13.9 Hz, 2H), 3.78 – 3.53 (m, 177H), 3.38 (s, 3H), 1.65 – 1.54 (p, 2H), 1.25 (s, 30H), 0.88 (t, J = 6.8 Hz, 3H). ^{19}F NMR (376 MHz, $CDCl_3$) δ -80.75 (t, J = 9.9 Hz), -119.72 (dt, J = 26.9, 12.8 Hz), -121.95 (s), -122.71 (s), -123.43 (s), -126.11 (s). MALDI MS: $[M + Na]^+$ calculated for $C_{129}H_{227}F_{33}NaO_{48}$ = 3194.47; found: 3194.696.

3.4.14 Critical Micelle Concentration (CMC): Pyrene 1:3 ratio method

Polymer solutions were prepared in Milli-Q water at different concentration from 0 – 2 mg/mL. Pyrene stock solution in pure ethanol was introduced into a dry vial. The ethanol was evaporated and the pyrene residue was dissolved with the polymer solution using sonication. The samples were prepared in such a way that the final pyrene concentration in the polymer solution equals to 2 µM. Fluorescence intensity was measured by a SLM Luminescence Spectrometer Aminco-Bowman® Series 2 (Rochester, NY) using the excitation of pyrene at 337 nm. The emission spectra were recorded between 350 – 450 nm, with an increment of 1 nm. All measurements were done at 25 ± 1 °C. The intensities for the first and third vibronic bands (I_1 and I_3) were recorded at 374 and 384 nm. The CMC of the polymer was calculated according to the published paper by Aguiar *et al*.[21] Error was reported as the standard deviation from triplicate measurements.

3.4.15 Aggregation Number Study

The aggregation number of micelles was determined using a steady-state fluorescence quenching method. Polymer solutions were prepared at 3 different concentrations (3 – 5 mg/mL) in MilliQ water. Pyrene stock solution in pure ethanol was introduced into a dry vial. Ethanol was evaporated and the pyrene residue was dissolved with the polymer solution using sonication in such a way that the final polymer solution contained 2 µM pyrene. Different amounts of C153 stock (1 mM in pure ethanol) was added into the pyrene/polymer solutions to obtain various quencher concentration (0 – 20 µM). The concentration of ethanol in the final solution was kept to be ≤ 2% without effecting the aggregation number.[22] Fluorescence intensity of each sample was measured by a SLM Luminescence Spectrometer Aminco-Bowman® Series 2 (Rochester, NY) using the excitation of pyrene at 337 nm. The emission spectra were recorded between 350 – 500 nm, with an increment of 1 nm. All measurements were done at 25 ± 1 °C. Error was reported as the standard deviation from triplicate measurements.

The aggregation number (N_{agg}) can be calculated from the following equations[32]

Equation 3-1 $$\frac{I}{I_0} = exp\left(-\frac{[Q]}{[M]}\right)$$ **Equation 3-2** $$N_{agg} = \frac{[S]-CMC}{[M]}$$

Where I and I_0 represent fluorescence intensity with and without the quencher, respectively, [Q] is the quencher concentration, [M] is the micelle concentration and [S] is the total bulk polymer concentration.

3.4.16 Microviscosity

The relative microviscosity of the micelle cores were determined using a steady-state fluorescence method. 1,3-di-(1-pyrenyl)-propane (P3P) was chosen as a probe. Polymer solutions were prepared at a concentration of 0.5 mM in Milli-Q water. P3P stock solution in acetone was introduced into a dry empty vial. Acetone was evaporated and the polymer solution was introduced to give a final P3P concentration of 0.1 µM. The solutions containing the probe were sonicated for 30 min and left to equilibrate in the dark for 24 h before measurement. Fluorescence intensity of each sample was measured by a SLM Luminescence Spectrometer Aminco-Bowman® Series 2 (Rochester, NY) using the excitation of P3P at 346 nm. The emission spectra were recorded between 350 – 600 nm, with an increment of 1 nm. All measurements were done at 25 ± 1 °C. The intensity of the monomer emission (I_M) and the excimer emission (I_E) were recorded at *ca.* 378 and 480 nm, respectively. The microviscosity was presented as the I_M/I_E ratios which were determined from the average of three measurements.

3.4.17 Micelle preparation – Solvent evaporation method

The polymer was dissolved in acetonitrile (ACN) or DCM to a desired concentration. The polymer solution (1 mL) and additive (paclitaxel, PTX, in ACN) were added to a 10 mL round-bottom flask. The solution was rotated in a water bath at 60 °C for 5 min. The solvent was then evaporated under reduced pressure for 15 min to ensure a completely dried thin film. The film was redispersed with 1 mL hot PBS (60 °C), sonicated for 5 – 10 min, and filtered through a 0.45 µm RC filter.

3.4.18 Dynamic Light Scattering (DLS)

Particle size was measured by dynamic light scattering (DLS) with a Zetasizer Nano-ZS (Malvern Instruments Ltd., UK) at 25 °C with a 173° detection angle. The micelle solutions were measured without dilution and in triplicate. The number of scans of each run was determined automatically by the instrument. The data were reported as volume weighted average diameters.

3.4.19 Drug Encapsulation

Polymer solutions were prepared at 3.5 mM. A paclitaxel (PTX) stock solution was prepared in ACN at 4 mg/mL. PTX loaded micelles were prepared in triplicate using the solvent evaporation method where 1 mL of polymer solution was combined with 125 µL of PTX stock (500 µg total). After sonication, the micelle samples were centrifuged at 12,000 rpm for 5 min and then passed through a 0.20 µm RC syringe filter to remove any insoluble precipitate. A 100 µL aliquot of micelle solution was mixed with 900 µL of ACN and the remaining micelle solution was kept at 4 °C. The process was repeated on day 1 and 7. The amount of PTX loaded in the micelle was quantified by reverse phase HPLC (Shimadzu prominence HPLC system, Shimadzu, Japan), equipped with a LC-20AT pump, SIL-20 AC HT autosampler, CTO-20 AC column oven, and an SPD-M20A diode array detector. Column temperature was maintained at 40°C. 10 µL of the mixture was injected into a C18 column (Agilent XDB-C8, 4.6 Å × 150 mm). The flow rate was 1.0 mL/min and the detection was set to 227 nm. The samples were eluted with an isocratic mixture of 25% water (0.1% phosphoric acid, 1% MeOH) in acetonitrile. The run time was 7 min and PTX eluted at 3.98 min.

3.4.20 In vitro time release studies

Polymer solutions were prepared at 2.4 mM. PTX stock solution was prepared in ACN at 2 mg/mL. Micelle solutions were then prepared by the solvent evaporation method as described above using 4 mL of polymer solution and 400 µL of PTX solution. The micelles were prepared one day prior to the experiment. Immediately before the study, the micelles were centrifuged at 4,000 rpm for 5 min and filtered through

0.45 μm RC syringe filter to remove any precipitate. A t = 0 h time point was established by diluting 100 μL of micelle solution in 900 μL ACN. A 3 mL capacity Slide-A-Lyzer Dialysis cassette G2 2,000 MWCO (Thermo Fisher Scientific Inc, Fitchburg, WI) was hydrated by stirring in a 3L PBS bath at 37 °C overnight. After this time, 2.5 mL of micelle solution was added to the cassette which was then returned to the PBS bath and allowed to stir for 48 h. Time points were taken at 0.5, 2, 3, 6, 9, 12, 24, 36, and 48 h. For each time point, a 100 μL aliquot of the micelle solution was removed from the cassette and diluted in 900 μL ACN. The aliquot was then replaced in the cassette with 100 μL of fresh PBS solution. Sink conditions were maintained by replacing the 3L PBS baths at the 6, 12, and 24 h time points. The amount of PTX remaining was quantified by reverse phase HPLC using the same method as described earlier. Concentration was determined from the area under the curve and extrapolated from the standard curve. Curve-fitting analysis using one-phase exponential association was used to plot the data.

3.4.21 Cytotoxicity studies

4T1-Luc cells, luciferase-modified murine breast carcinoma cell line, (kindly provided by Dr. Glen S. Kwon) were cultured at 37 °C in a humidified atmosphere containing 5% CO_2. The cells were maintained in a high glucose Dulbecco's Modified Eagle Medium (DMEM) (Hyclone, Logan, UT) supplemented with 10% fetal bovine serum and 1% penicillin/streptomycin. For cytotoxicity study, 4T1-Luc cells were seeded at 5,000 cells/well on 96-well plates and incubated for 24 h. Polymer solutions were prepared in Milli-Q water at a concentration of 10 mM. The cells were incubated with polymer solutions at different concentrations ranging from 10 – 1,000 μM for 24 h. After this time, the cytotoxic effects were analyzed by a CellTiter-Blue® Cell Viability Assay (Promega, WI) according to the manufacturer's protocol. The fluorescence signal was measured at 560/590 nm using a SpectraMax® M2 microplate reader (Molecular Devices, CA). The results were represented as percentages of cell viability normalized to the nontreated cells.

3.5 References

(1) Krafft, M. P. Fluorocarbons and fluorinated amphiphiles in drug delivery and biomedical research. *Advanced drug delivery reviews* **2001,** *47* (2-3), 209-228.

(2) Riess, J. G. Highly fluorinated amphiphilic molecules and self-assemblies with biomedical potential. *Current Opinion in Colloid & Interface Science* **2009,** *14* (5), 294-304.

(3) Krafft, M. P.; Riess, J. G. Perfluorocarbons: Life sciences and biomedical uses Dedicated to the memory of Professor Guy Ourisson, a true RENAISSANCE man. *Journal of Polymer Science Part A: Polymer Chemistry* **2007,** *45* (7), 1185-1198.

(4) Decato, S.; Mecozzi, S. Chapter 16 - Highly fluorinated colloids in drug delivery and imaging. In *Colloid and Interface Science in Pharmaceutical Research and Development*, Ohshima, H.; Makino, K., Eds. Elsevier: Amsterdam, 2014; pp 319-345.

(5) Tucker, W. B.; McCoy, A. M.; Fix, S. M.; Stagg, M. F.; Murphy, M. M.; Mecozzi, S. Synthesis, physicochemical characterization, and self‐assembly of linear, dibranched, and miktoarm semifluorinated triphilic polymers. *Journal of Polymer Science Part A: Polymer Chemistry* **2014,** *52* (23), 3324-3336.

(6) Neil, E.; Marsh, G. Towards the nonstick egg: designing fluorous proteins. *Chemistry & biology* **2000,** *7* (7), R153-R157.

(7) Xu, B.; Yao, W.; Li, Y.; Zhang, S.; Huang, X. Perfluorocyclobutyl Aryl Ether-Based ABC Amphiphilic Triblock Copolymer. *Scientific Reports* **2016,** *6* (1), 39504.

(8) Miksa, B. Recent progress in designing shell cross-linked polymer capsules for drug delivery. *RSC advances* **2015,** *5* (107), 87781-87805.

(9) Bates, F. S.; Hillmyer, M. A.; Lodge, T. P.; Bates, C. M.; Delaney, K. T.; Fredrickson, G. H. Multiblock Polymers: Panacea or Pandora's Box? *Science* **2012,** *336* (6080), 434-440.

(10) Huo, M.; Zeng, M.; Li, D.; Liu, L.; Wei, Y.; Yuan, J. Tailoring the Multicompartment Nanostructures of Fluoro-Containing ABC Triblock Terpolymer Assemblies via Polymerization-Induced Self-Assembly. *Macromolecules* **2017,** *50* (20), 8212-8220.

(11) Amado, E.; Kressler, J. Triphilic block copolymers with perfluorocarbon moieties in aqueous systems and their biochemical perspectives. *Soft Matter* **2011,** *7* (16), 7144-7149.

(12) Barres, A. R.; Wimmer, M. R.; Mecozzi, S. Multicompartment theranostic nanoemulsions stabilized by a triphilic semifluorinated block copolymer. *Molecular pharmaceutics* **2017,** *14* (11), 3916-3926.

(13) Barres, A. R.; Molugu, S. K.; Stewart, P. L.; Mecozzi, S. Droplet Core Intermolecular Interactions and Block Copolymer Composition Heavily Influence Oil-In-Water Nanoemulsion Stability. *Langmuir* **2019,** *35* (39), 12765-12772.

(14) Parlato, M. C.; Jee, J.-P.; Teshite, M.; Mecozzi, S. Synthesis, characterization, and applications of hemifluorinated dibranched amphiphiles. *The Journal of organic chemistry* **2011,** *76* (16), 6584-6591.

(15) Hussein, W. M.; Ross, B. P.; Landsberg, M. J.; Lévy, D.; Hankamer, B.; McGeary, R. P. Synthesis of nickel-chelating fluorinated lipids for protein monolayer crystallizations. *The Journal of organic chemistry* **2009,** *74* (4), 1473-1479.

(16) Juaristi, E.; Antúnez, S. Conformational analysis of 5-substituted 1,3-dioxanes. 6. Study of the attractive gauche effect in O-C-C-O segments. *Tetrahedron* **1992,** *48* (29), 5941-5950.

(17) Procopio, A.; Gaspari, M.; Nardi, M.; Oliverio, M.; Tagarelli, A.; Sindona, G. Simple and efficient MW-assisted cleavage of acetals and ketals in pure water. *Tetrahedron Letters* **2007,** *48* (49), 8623-8627.

(18) Pispas, S. Self-assembled nanostructures in mixed anionic–neutral double hydrophilic block copolymer/cationic vesicle-forming surfactant solutions. *Soft Matter* **2011,** *7* (2), 474-482.

(19) Sadoqi, M.; Lau-Cam, C.; Wu, S. Investigation of the micellar properties of the tocopheryl polyethylene glycol succinate surfactants TPGS 400 and TPGS 1000 by steady state fluorometry. *Journal of colloid and interface science* **2009,** *333* (2), 585-589.

(20) Hierrezuelo, J.; Aguiar, J.; Ruiz, C. C. Micellar properties of a mixed surfactant system constituted by n-octyl-β-D-thioglucopyranoside and sodium dodecyl sulphate. *Colloids and Surfaces A: Physicochemical and Engineering Aspects* **2005,** *264* (1-3), 29-36.

(21) Aguiar, J.; Carpena, P.; Molina-Bolıvar, J.; Ruiz, C. C. On the determination of the critical micelle concentration by the pyrene 1: 3 ratio method. *Journal of Colloid and Interface Science* **2003,** *258* (1), 116-122.

(22) Tummino, P. J.; Gafni, A. Determination of the aggregation number of detergent micelles using steady-state fluorescence quenching. *Biophysical journal* **1993,** *64* (5), 1580-1587.

(23) Jee, J.-P.; McCoy, A.; Mecozzi, S. Encapsulation and release of Amphotericin B from an ABC triblock fluorous copolymer. *Pharmaceutical Research* **2012,** *29* (1), 69-82.

(24) Zana, R. Microviscosity of Aqueous Surfactant Micelles: Effect of Various Parameters. *The Journal of Physical Chemistry B* **1999,** *103* (43), 9117-9125.

(25) Decato, S.; Tangsangasaksri, M.; Tucker, W. B.; Madsen, E. J.; Miura, Y.; Matsumoto, Y.; Kataoka, K.; Mecozzi, S. Long-circulating, tumor-targeting drug nanocarriers: in vivo stability of

triphilic polymer self-assemblies enhanced by branched semifluorinated cores. *Manuscript submitted for publication.* **2020**.

(26) Vakil, R.; Kwon, G. S. Poly(ethylene glycol)-b-Poly(ε-caprolactone) and PEG-Phospholipid Form Stable Mixed Micelles in Aqueous Media. *Langmuir* **2006,** *22* (23), 9723-9729.

(27) Ekelund, K.; Östh, K.; Påhlstorp, C.; Björk, E.; Ulvenlund, S.; Johansson, F. Correlation Between Epithelial Toxicity and Surfactant Structure as Derived From the Effects of Polyethyleneoxide Surfactants on Caco-2 Cell Monolayers and Pig Nasal Mucosa. *Journal of Pharmaceutical Sciences* **2005,** *94* (4), 730-744.

(28) Henriksen, J. R.; Andresen, T. L.; Feldborg, L. N.; Duelund, L.; Ipsen, J. H. Understanding Detergent Effects on Lipid Membranes: A Model Study of Lysolipids. *Biophysical Journal* **2010,** *98* (10), 2199-2205.

(29) Popot, J.-L. Alternatives to Detergents for Handling Membrane Proteins in Aqueous Solutions. In *Membrane Proteins in Aqueous Solutions: From Detergents to Amphipols*, Springer International Publishing: Cham, 2018; pp 97-149.

(30) Breyton, C.; Chabaud, E.; Chaudier, Y.; Pucci, B.; Popot, J.-L. Hemifluorinated surfactants: a non-dissociating environment for handling membrane proteins in aqueous solutions? *FEBS Letters* **2004,** *564* (3), 312-318.

(31) Valdés, K.; Morilla, M. J.; Romero, E.; Chávez, J. Physicochemical characterization and cytotoxic studies of nonionic surfactant vesicles using sucrose esters as oral delivery systems. *Colloids and Surfaces B: Biointerfaces* **2014,** *117*, 1-6.

(32) Wolszczak, M.; Miller, J. Characterization of non-ionic surfactant aggregates by fluorometric techniques. *Journal of Photochemistry and Photobiology A: Chemistry* **2002,** *147* (1), 45-54.

CHAPTER 4 – DEVELOPMENT OF FLUORINATED NANOASSEMBLIES AS NEW IMAGING AGENTS FOR ^{19}F MRI

Part A of this chapter has been submitted, in part, as a manuscript – Reference: Barres, A. R.; Lechuga, L.M.; Tangsangasaksri, M.; Ludwig, K.D.; Fain, S.B.; Mecozzi, S. A stable fluorous nanoemulsion formulation for *in vivo* cancer imaging via ^{19}F-MRI. *ACS Biomaterials Science & Engineering.* Under review. **2020**. M.T. contributed to the design and implementation of *in vivo* study and stability of nanoemulsion under different conditions.

Abstract

Magnetic resonance imaging (MRI) is a non-invasive imaging technique that can provide three-dimensional and high-resolution images. Conventional ^{1}H MRI looks at different relaxation times of protons from water and lipids present in the body to develop darker and brighter spots in black and white images. However, the abundance of water and lipids in the body can lead to significant background noises that impede image interpretations. Fluorine has a 100% natural abundance as the isotope ^{19}F and has an 83% sensitivity to that of ^{1}H. ^{19}F MRI has been extensively studied as an alternative to ^{1}H MRI due to its many advantages. For example, ^{19}F possesses negligible background noises in physiological conditions and its signals are presented as "hot spots" (i.e., a second color), thereby facilitating clearer image interpretations. However, the intrinsically high T_1 relaxation of fluorine as well as the concentration-dependent signal intensity lead to a low signal sensitivity that impedes its clinical translation. To improve the signal intensity and sensitivity, two different approaches were explored. We developed a nanoemulsion formulation containing a large volume of perfluoro-15-crown-5-ether (PFCE), allowing for improved signal intensity as a result of the high density of fluorine atoms. The PFCE nanoemlusion was stabilized by our novel M2F8H18 polymer and demonstrated long-lasting stability under different storage conditions. We demonstrated that our concentrated PFCE nanoemulsions accumulated at tumor sites *in vivo*, where the ^{19}F signal was retained for at least two weeks. Furthermore, we demonstrated the enhanced ^{19}F sensitivity by using paramagnetic Fe^{3+} in the form of Extremely Small Iron Oxide Nanoparticles (ESIONs) and magnetic ionic liquids (MILs). Our preliminary results demonstrated that the incorporation of our novel $PFtB_{TRI}$ structure, which contains 27 chemically equivalent fluorine atoms, with ESIONs and a commercially available perfluoropolyether (PFPE) with MIL led to a decreased in T_1 relaxation, suggesting the enhanced signal sensitivity.

4.1 Introduction

Magnetic resonance imaging (MRI) has become a popular imaging technique due to its non-invasive properties.[2-4] Unlike other diagnostic tools such as PET (positron emission tomography) or CT (computed tomography) that require radioactive materials or radiation, MRI uses strong external magnetic fields, magnetic field gradients, and radio frequency (RF) waves to affect the precession of protons in anatomical water and fats to generate magnetic resonance (MR) images. Different relaxation properties of protons provide the contrast to MR images, resulting in dark and bright spots on gray scale images. This conventional process is called ^{1}H MRI. The two important parameters that play a major role in the contrasts of MR images are longitudinal (T_1) relaxation and transverse (T_2) relaxation. T_1 relaxation refers to a time at which the net magnetization restores to its own original value. Clinically, the T_1 relaxation means the time between each scan. Therefore, a short T_1 time is preferred in order to enhance the signal intensity, resulting in bright spots on the images. T_2 relaxation, on the other hand, refers to the time at which the signal decays. A short T_2 will reduce the signal intensity, resulting in dark spots on the images. Development of contrast agents (CAs) lead to the improvement of images' contrast quality by shortening the T_1 or T_2 relaxations. These CAs are called T_1 or T_2 agents, depending on which parameter is strongly affected. Commonly used CAs are paramagnetic metal ions, such as gadolinium (Gd^{3+}) and manganese (Mn^{2+}), which are T_1 agents, and superparamagnetic iron oxide nanoparticles (SPIONs), which are T_2 agents. Even though these CAs can provide better contrast for MR images, the abundance of water and fats in the body can still lead to significant background noise, which is a major hurdle for accurately interpreting an image. Moreover, the commonly used Gd^{3+}-based contrast agents (GBCAs) have been shown to cause some toxicities such as nephrogenic systemic fibrosis (NSF) in patients with impaired renal function. In healthy patients with a normal renal function, Gd^{3+} deposits have been found in the brain, skin, liver, and bone which are tied to the gadolinium deposition disease (GDD).[5-7]

To bypass the need for contrast agents especially GBCAs, an alternative multinuclear MRI approach is being studied. Fluorine has a 100% natural abundance as the isotope ^{19}F and has a sensitivity

of 83% to that of proton. Therefore, ^{19}F has been extensively studied as an alternative nuclei to ^{1}H.[8-10] The identification of a second nuclei species by MRI allows for those nuclei to be presented as a "hot spot" or "second color", providing additional information apart from an anatomical grayscale ^{1}H images.[3-4, 11] In addition, the low physiological abundance of ^{19}F in the body provides another advantage over conventionally used ^{1}H nuclei. In the human body, the main sources of fluorine are in bones and teeth. The signals from these immobilized fluorine atoms are undetectable by MRI due to the fast signal decay (very short T_2 relaxation time), thus, resulting in negligible background noises. Furthermore, due to the similar Larmor frequency to ^{1}H, ^{19}F nuclei can be detected with clinical scanners by incorporating a tunable RF coil for ^{19}F frequency, showcasing its clinical translatability.[9, 11-12] However, due to the low physiological abundance of fluorine, the detectable ^{19}F signal solely depends on the fluorine density/concentration from exogenous sources, namely, perfluorocarbons (PFCs). Additionally, an intrinsically high T_1 relaxation of fluorine necessitates long image acquisition time, leading to a limited scan cycles in a given scanning interval. This results in a low signal intensity, which is a major hurdle for clinical translation.[9, 13] Increasing the sensitivity of ^{19}F MRI can be accomplished through various strategies, including the delivery of large amounts of PFCs as well as reducing the intrinsically long T_1 relaxation times of fluorine.[9, 13-14]

Perfluoro-15-crown-5-ether (PFCE) is a perfluorocarbon oil which has been widely used as the source of fluorine for ^{19}F MRI. The macrocyclic structure of PFCE provides 20 chemically equivalent fluorine atoms which give rise to one strong ^{19}F signal. This single ^{19}F resonance is advantageous to MRI as it increases the sensitivity and the signal intensity. PFCE is highly stable in physiological conditions and is non-toxic which allows its usage in biomedical application.[15-16] Due to its high hydrophobicity and lipophobicity, PFCE is normally formulated as a nanoemulsion and has been used in various ^{19}F MRI applications such as cell labeling, cell tracking, and the imaging of inflammation sites.[16-18] A nanoemulsion is a colloidal nanoparticle prepared from two immiscible liquids stabilized by surfactants with an average droplet size below 500 nm.[19-21] The preparation of PFCE as a nanoemulsion allows for the incorporation of

a large amount of PFCE, enabling the delivery of a large quantity of fluorocarbon as the fluorine source for ^{19}F MRI.

Extremely small-sized iron oxide nanoparticles (ESIONs) are magnetic nanoparticles that are considered to be potential candidates as T_1 agents. Interestingly, iron oxide nanoparticles themselves have been used as T_2 contrast agents such as Feridex® which is a dextran-coated superparamagnetic iron oxide nanoparticles (SPIONs). Since SPIONs are larger than ESIONs, they provide a stronger magnetic moment that induces magnetic inhomogeneity and causes a rapid dephasing of the nuclei.[22-23] This results in a rapid signal loss, lowering the T_2 relaxation time. Decreasing the size of iron oxide nanoparticles to be less than 3 nm, which is the case for ESIONs, significantly reduces their magnetic properties, leading to an enhanced T_1 effect while suppressing the T_2 effect.[22] Additionally, iron ions can improve the sensitivity of PFCs in ^{19}F MRI. Kislukhin *et al.*[14] demonstrated that when a nanoemulsion was prepared with chelated Fe^{3+} and PFPE, the T_1 relaxation time of PFPE was reduced with a modest T_2 effect. This suggests that the incorporation of paramagnetic Fe^{3+} improves ^{19}F signal sensitivity.

In this work, we present two strategies to improve the sensitivity of PFCs for ^{19}F MRI. The first strategy is to employ a high concentration of the fluorine source which results in an increased ^{19}F density (**Part A**). This high fluorine density comes from a highly concentrated PFCE nanoemulsion prepared using our novel semifluorinated polymer M2F8H18. The PFCE oil forms the core droplet of the nanoemulsion, allowing for the incorporation of a large volume of PFCE that is then stabilized by the M2F8H18 polymer. The highly concentrated and highly stable PFCE nanoemulsions were evaluated for their stability and toxicity *in vitro*. An *in vivo* study was performed on tumor-bearing mice with a focus on cancer imaging application. The second strategy is to incorporate paramagnetic metal ions, namely Fe^{3+}, and ESIONs, with different fluorinated agents to reduce the intrinsically high T_1 relaxation of fluorine (**Part B**). Syntheses of ESIONs and fluorinated agents were explored. The effects of ESION and paramagnetic metal ions on T_1 and T_2 relaxations were evaluated.

Part A: Incorporation of high PFCE concentration in nanoemulsions for MR imaging

4.2A Results and Discussion

4.2A.1 Highly concentrated PFCE nanoemulsion preparation and characterization

The PFCE nanoemulsion was prepared with our novel semifluorinated polymer, M2F8H18. The nomenclatures for the polymer are as follows: i) M2 represents poly(ethylene glycol) (PEG) with methoxy cap at the α position where 2 is the average molecular weight in the thousands, ii) F8 represents the fluorocarbon block where 8 is the number of carbon atoms substituted with fluorine atoms, and iii) H18 represents the hydrocarbon block where 18 is the number of carbon atoms substituted with hydrogen atoms. The polymer was synthesized according to a previously published article from our group.[24] The PFCE nanoemulsion was prepared by Dr. Alexa R. Barres.[1] In brief, the highly concentrated PFCE nanoemulsion was formulated via a two-step high energy input method; homogenization at 21,500 rpm for 1 min followed by microfluidization at 5,000 psi for 2 min. The first homogenization step disperses the oil phase into small droplets which are then stabilized by the polymer, resulting in the formation of micron-sized particles. The second microfluidization step further refines and reduces particle size with high pressure, creating uniform nano-sized particles with a narrow size distribution. Following this two-step high energy input method, the resulting PFCE nanoemulsion was an opaque/milky colloidal solution, consisting of 6.3 mL or 35% v/v PFCE stabilized by 20 mM M2F8H18 in normal saline (**Figure 4.1a**). The nanoemulsion has a small particle size and a narrow size distribution of 210 ± 38 nm (day 0, data not shown) measured by dynamic light scattering (DLS). The long-term stability of PFCE nanoemulsion was monitored *via* DLS. As shown in **Figure 4.1b**, almost no particle growth was observed over the course of 320 days (detailed long-term stability from day 0 – 98 was reported by Barres *et al*.[1]) with average particle sizes at day 98 and 320 of 218 ± 31 nm and 254 ± 32 nm, respectively. These results showcase the high stability of the nanoemulsion in storage conditions (4 °C). Similarly, the storage of the nanoemulsion at 25 and 37 °C showed a negligible change in the nanoemulsion size for at least 3 weeks (**Figure 4.1c**). In addition, the PFCE nanoemulsion demonstrated high stability while incubating in cell culture media and fetal bovine serum (FBS) at 37 °C,

with no phase separation occurring for at least one week (**Figure 4.1d**). These results suggest a highly stable PFCE nanoemulsion where a large amount of PFCE was stabilized by the novel M2F8H18 polymer. This is due to the unique properties of the semifluorinated M2F8H18 polymer having an increased fluorophilicity as well as hydrophobicity, allowing for a favorable interaction with PFCE that has less fluorophilicity and hydrophobicity compared to pure perfluorocarbons.[25] Treatment of 4T1-Luc cells (luciferase-expressing murine breast cancer cells) with the PFCE nanoemulsion revealed negligible cytotoxicity up to 20 mg/mL PFCE concentration (**Figure 4.1e**). However, some toxicity was observed at higher PFCE concentrations of 40 and 60 mg/mL and the cytotoxic effect was more pronounced with a longer incubation period. At 40 and 60 mg/mL PFCE, the concentration of M2F8H18 polymer is higher than 1 mM. The apparent toxicity of the nanoemulsion at high PFCE concentration could possibly be associated with the increased concentration of the polymer.

4.2A.2 In vitro ^{19}F phantom images

The *in vitro* MRI phantom images of PFCE nanoemulsion were taken at different concentrations of PFCE starting from the neat 35% v/v (1.07 M) PFCE down to 5% v/v (0.15 M) PFCE. ^{1}H phantom image (**Figure 4.1f**-inset) shows a high-water content from all nanoemulsions with the lowest intensity observed for 1.07 M PFCE nanoemulsion (top circle). This is due to the nanoemulsion having the highest PFCE volume in the sample which results in the lowest amount of water content. To calculate the signal to noise ratio (SNR) of ^{19}F, a region of interest (ROI) was drawn on the raw magnitude ^{19}F phantom image (**Figure 4.1f**) for each PFCE concentration. The background noise was determined from a region away from all ^{19}F sources to avoid bias related to Rician noise distribution which is a probability distribution of the measured signal intensity.[26] The SNR was then calculated by **Equation 4-1**, which can be found in section **4.4A.6**, and was plotted against PFCE concentration. As shown in **Figure 4.1g**, a linear correlation ($R^2 = 0.997$) was observed between ^{19}F SNR and PFCE concentration, suggesting a concentration-dependent ^{19}F signal. At the lowest PFCE concentration of 0.15 M, the ^{19}F signal could still be observed and the signal intensity

was much higher than the background noise, indicating a low limit of detection of our PFCE nanoemulsion formulation.

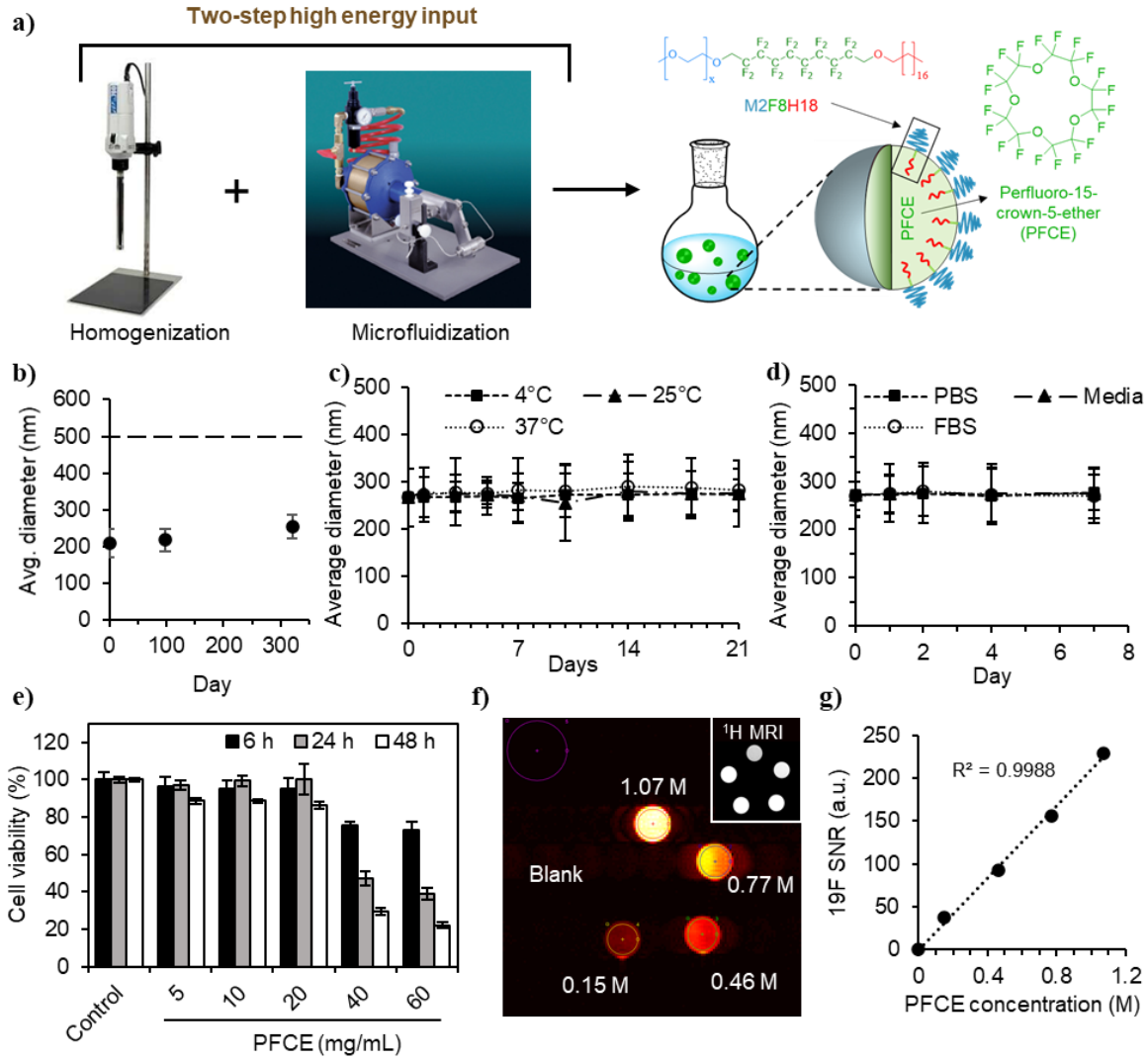

Figure 4.1 PFCE nanoemulsion formulation and the *in vitro* characterizations. a) The illustration demonstrates the formulation of the o/w nanoemulsion that consists of PFCE oil (green), M2F8H18 polymer and aqueous phase (blue) prepared from a two-step high energy input method. The PFCE oil droplet composes the core of the nanoemulsion and is stabilized by the M2F8H18 polymer. Figure adapted from Barres *et al.*[1] b) PFCE nanoemulsion stability over time measured by dynamic light scattering (DLS) shows negligible particle growth over 300 days, maintaining the size below the 500 nm cutoff according to USP <729> (dashed line). c) Stability of the PFCE nanoemulsion at different storage temperatures: 4, 25, and 37 °C. d) Serum stability of PFCE nanoemulsion incubated at 37 °C. e) 4T1-Luc cell viability after PFCE nanoemulsion treatment. f) *In vitro* ^{19}F MR phantom images showing ^{19}F MR raw magnitude image with 4 ROIs drawn for PFCE nanoemulsion at different concentrations. A 5th ROI was drawn in a region away from all ^{19}F sources (purple circle; top left corner) to represent background noise. The inset image shows ^{1}H MR image of the corresponding PFCE nanoemulsions. g) Linear correlation of ^{19}F signal to PFCE concentration. MRI data were acquired by Lawrence M. Lechuga.

4.2A.3 In vivo ^{19}F MRI

In vivo study was performed using immunocompetent mice. The tumor model was prepared by subcutaneously inoculating 4T1-Luc cells on the right flank of female BALB/c mice (n = 5). When the tumor size reached ~100 mm^3, the imaging study was initiated. The study timeline is shown in **Figure 4.2**. ^1H images of all mice were acquired one day prior to the formulation injection as a pre-contrast anatomical background image. To each mouse was intravenously injected 200 µL of neat 35% v/v PFCE nanoemulsion through the tail vein on day 0. Six hours after the injection, the first ^1H and ^{19}F MR images were acquired. MR images were periodically obtained on day 1, 4, 7, and 14 to assess nanoemulsion distribution and accumulation.

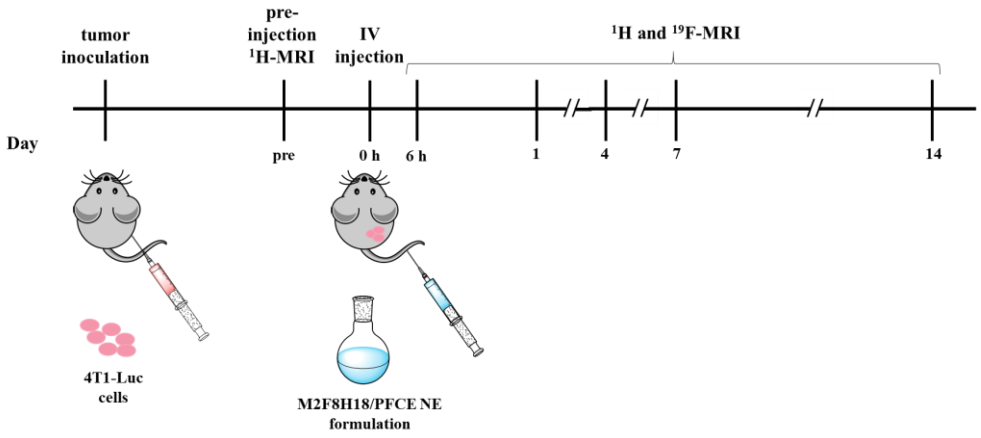

Figure 4.2 *In vivo* study timeline. 4T1-Luc cells were inoculated at the right flank of female BALB/c mice. After the tumor volume reached ~ 100 mm^3, ^1H MR image was taken one day prior to intravenously administration of PFCE nanoemulsions. ^1H and ^{19}F MR images were taken at 6 h, 1, 4, 7, and 14 days after injection. Figure from Barres *et al*.[1]

As predicted, the ^{19}F signal can be clearly observed from all major organs, especially the heart, liver, spleen, kidneys, inferior vena cava, and tumor as early as 6 h post injection (**Figure 4.3c**). The observed ^{19}F signal in inferior vena cava indicates that the PFCE nanoparticles circulated inside the body, suggesting that the formulation is stable under physiological conditions *in vivo*. The highest ^{19}F signal intensity was shown in the liver and spleen which are the major filtering organs in the body (**Figure 4.3c – g**). This was due to the quick uptake of nanoemulsion particles by circulating monocytes and macrophages

after intravenous administration of the PFCE nanoemulsion.[27-28] This can be explained by the nature of the monocytes and macrophages which are homed to the reticuloendothelial system (RES). After these cells engulf the particles, they typically bring the particles back to the RES organs, which include the liver and spleen, resulting in a high ^{19}F signal intensity in those organs. A gradual reduction of ^{19}F intensity was observed overtime, suggesting that the PFCE was slowly eliminated from the body. The accumulation of the PFCE nanoemulsions in the tumor was observed at 6 h and was pronounced at 24 h (day 1) post injection (**Figure 4.3d**). This is expected as the PFCE nanoemulsion passively targeted the tumor through the EPR effect which is a slow and time-dependent process.[29-30] The ^{19}F signal was retained in the tumor for at least 14 days (**Figure 4.3g**). This result suggests that our PFCE nanoemulsion formulation can be used as a powerful imaging tool for tumor diagnosis and long-term monitoring.

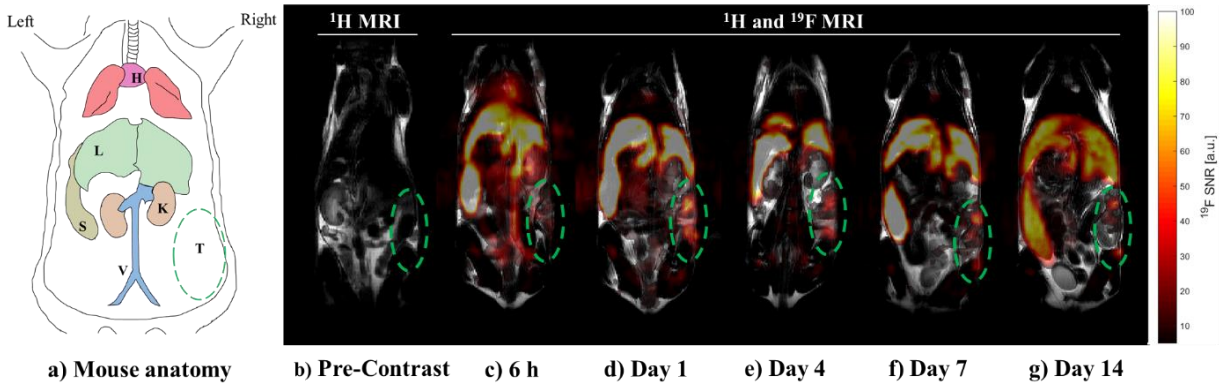

Figure 4.3 Representative MR images of tumor-bearing BALB/c mouse injected with PFCE nanoemulsion. a) Mouse anatomy showing major organs; heart (H), lung, liver (L), spleen (S), kidneys (K), inferior vena cava (V), and tumor (T). b) ^{1}H MR image of the mouse before injection. c) – g) overlay of ^{1}H and ^{19}F MR images taken at 6 h, day 1, 4, 7, and 14. Tumor is shown in green dashed line. Figure from Barres *et al.*[1]

4.2A.4 Excretion of PFCE nanoparticles

The main elimination pathway of PFCs from living organisms is through exhalation *via* the lungs.[27] The study from Klein *et al.*[31] demonstrated that the elimination of perfluorooctyl bromide (PFOB or Perflubron) from blood circulation underwent two-phase kinetics. The initial phase corresponds to the capture of particles by the RES, resulting in the reduction of PFOB concentration in bloodstream. The

uptake of the emulsion is independent of the types of PFCs but depends on the physicochemical properties of the emulsions such as size and surface charge. This initial phase obeys first-order kinetics, suggesting a dose-dependent elimination.[28, 31] The second phase, on the other hand, does not follow first-order kinetics. This phase relates to the release of PFCs from the RES back into circulation *via* blood lipids, such as lipoproteins, and subsequent elimination through exhalation. This is a much slower process and, therefore, is the rate-limiting step. Unlike the initial phase, the elimination rate of the second phase depends on the physicochemical properties of PFCs, e.g. lipophobicity and molecular weight, which determine how well PFC molecules can diffuse back across the cell membrane, be taken up by the lipids and eventually be excreted through the lung alveoli.[27-28, 31-32] Other elimination pathways for PFCs are through the deposition of PFCs in adipose tissue with subsequent elimination through the lungs or direct vaporization of PFCs from the emulsion. The latter mainly depends on the vapor pressure and molar mass of the PFC molecules.[27-28] Through these elimination pathways, a four-compartment pharmacokinetics model can be used to showcase the excretion pathways (**Figure 4.4**).[28]

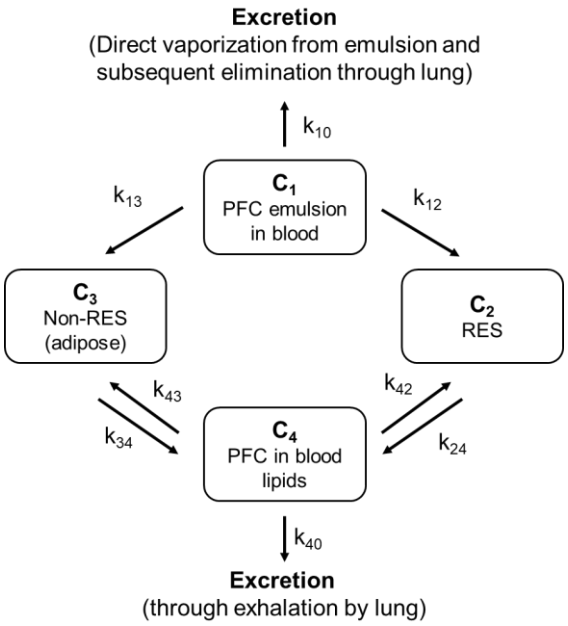

Figure 4.4 A four-compartment pharmacokinetic model for PFC emulsion. First-order kinetics was assumed where k_{ij} represents the rate constant from compartment C_i to compartment C_j and k_{i0} represents the excretion of PFC through exhalation. Figure adapted from Reiss J.G.[28]

As shown in **Figure 4.3**, after intravenous administration of the highly concentrated 35% v/v PFCE nanoemulsion formulation, the nanoemulsion particles had distributed throughout the body with the highest accumulation observed in the liver and spleen, indicating the possible elimination of the nanoemulsion from the bloodstream through the RES. No ^{19}F signal was observed in the lungs, suggesting that the direct vaporization might not be a dominant mechanism for PFCE elimination which could be due to the moderate vapor pressure (13.2 mmHg)[27] and the high molar mass (580.072 g/mol) of PFCE. Even though the observed ^{19}F signal intensity gradually decreased overtime in the liver and spleen, no significant reduction of the calculated mean SNR of liver was observed over the course of 14 days (**Figure 4.5**). This indicates that the deposition of PFCE in the liver remained unchanged. In fact, no evidence of PFCE metabolism has been reported due to its highly stable C-F bonds and the dense electron clouds of fluorine which make the molecules become biologically inert and difficult to degrade.[16, 28] Several literature sources have shown that the PFCE signal can persist in organs for several months, resulting in an extremely long biological half-life of PFCE.[16, 27-28] This suggests the advantage of using PFCE as a cell labeling agent for cell tracking applications.

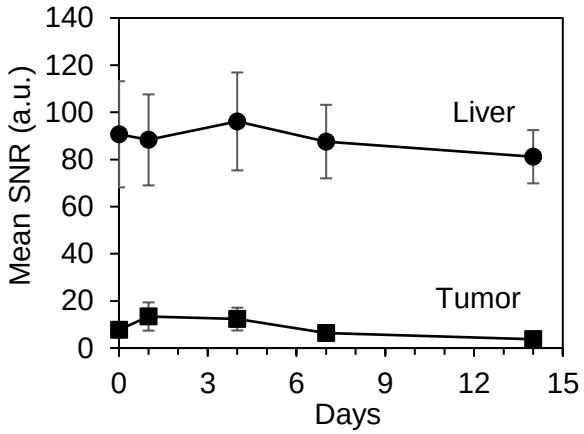

Figure 4.5 Liver and tumor mean SNR. The average SNR was calculated (n = 5) from the ROI drawn on the livers and the tumors (drawn region can be found from Barres *et al.*[1]). Mean SNR of the livers (solid circle). Mean SNR of the tumors (solid square). Data represent mean ± standard deviation. MR images and data were acquired by Lawrence M. Lechuga.

4.3A Conclusion

Herein, the sensitivity of ^{19}F MRI was improved by using a high density of fluorine atoms which was provided by a high concentration of liquid PFCE. The nanoemulsion containing a large volume of PFCE (35% v/v) was successfully prepared using our novel semifluorinated polymer, M2F8H18. The PFCE nanoemulsions were prepared through a two-step high energy input method, resulting in a nanoemulsion with a size of 200 nm. The nanoemulsion showed a long-term stability at 4 °C storage conditions. Additionally, the nanoemulsions exhibited a high stability at higher storage temperatures of 25 and 37 °C for at least 3 weeks, and in the presence of serum with an incubation at 37 °C for at least one week. This highly stable PFCE nanoemulsion demonstrated a negligible cytotoxic effect to 4T1-Luc cells at the concentration up to 20 mg/mL PFCE. The *in vitro* phantom images of PFCE nanoemulsion at different concentrations revealed a high SNR and suggested a concentration-dependent ^{19}F signal. Tail vein injection of concentrated PFCE nanoemulsion (35% v/v) into tumor-bearing mice showed no sign of toxicity in all mice during the 14-day study period. ^{19}F signal was clearly detected by MRI in all major organs including the tumor at 6 h post injection. The accumulation of nanoemulsion in the tumor was the highest on day 1, suggesting a slow passive targeting process through the EPR effect. The ^{19}F signal was retained in the tumor for up to two weeks, providing an advantage for multiple imaging sessions after one injection. The high ^{19}F signal intensity observed in liver and spleen suggested that the nanoemulsion was mainly cleared from the bloodstream by RES after I.V. injection. The small decrease in ^{19}F signal reduction in the liver and spleen on day 14 indicates that PFCE has a long biological half-life. These results suggest that our PFCE nanoemulsion formulation can be used as a powerful imaging tool for tumor diagnosis and long-term monitoring of tumors as well as in cell labeling for cell tracking application.

Part B: Improving ^{19}F sensitivity by decreasing T_1 relaxation

4.2B Results and Discussion

4.2B.1 Improving sensitivity of PFC through ESIONs

Extremely small-sized iron oxide nanoparticles (ESIONs) are typically synthesized by the thermal decomposition of iron precursors in organic solvent.[22] The surface of prepared ESIONs are then stabilized by hydrocarbon, improving their solubility in the corresponding solvent. However, the hydrophobic properties of ESIONs prevent the use of these particles in biomedical applications. Therefore, changing the surface properties from hydrophobic to hydrophilic is a crucial step for developing these particles for clinical use. Ligand exchange is one of the most common methods used to modify the iron oxide surface, where different functional group linkers with higher affinity toward the iron surface have been utilized to remove the original hydrophobic ligand from the iron oxide surface. The example of these functional groups are amine,[33-34] carboxylic acid,[33, 35-36] silane,[37] cysteine residue,[38] phosphonic/phosphoric acid,[33, 35, 39] and catechol.[33, 35, 40-42] Herein, our novel $PFtB_{TRI}$ or the tri-perfluoro-*tert*-butyl group was selected as the fluorine source because the $PFtB_{TRI}$ molecule possesses 27 chemically equivalent fluorine atoms which give rise to one strong ^{19}F signal. We first explored the functionalization of the $PFtB_{TRI}$ molecule with phosphoric acid ($PFtB_{TRI}$ phosphoric acid) as the synthetic method required the least number of steps. Phosphoric acid has been widely used for hydrophilic ligand exchange with iron oxide particles.[43-44] However, the $PFtB_{TRI}$ phosphoric acid could not be obtained due to the difficulty in the deprotection reaction of the molecule (detailed synthesis can be found in **Appendix 1**). Therefore, a new synthesis route was pursued with the use of a catechol group, which has been proved to have a very high and irreversible affinity towards iron oxide surfaces.[33, 40] Among catechol derivatives, nitrocatechol provided higher particle stability which is due to its lower pK_a compared to its counterpart.[40] Thus the nitrocatechol group was selected for iron oxide surface functionalization.

4.2B.1.1 Synthesis of M2-NDA and NitroDOPET-PFtB$_{TRI}$

To synthesize M2-NDA, dopamine was used as a precursor catechol group for nitrocatechol linker synthesis due to its primary amine functionality which can be used in various coupling reactions. Nitrodopamine (**4-1**, NDA) was synthesized through a nitration reaction of dopamine with sodium nitrite and concentrated sulfuric acid (**Scheme 4.1**). M2-NHS was synthesized according to Harris J.M. and Kozlowski A.[45] and was used to react with **4-1** through NHS-amine coupling reaction to yield M2-NDA (**4-2**).

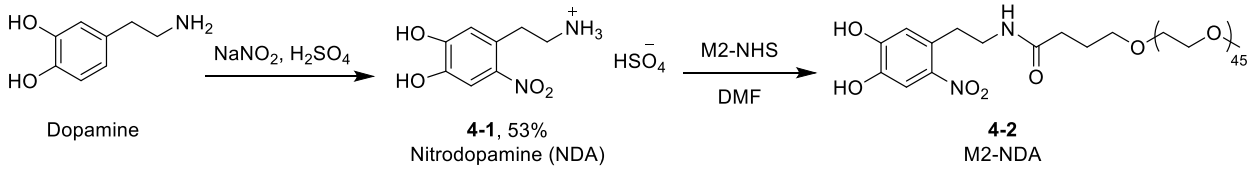

Scheme 4.1 Synthesis of M2-NDA.

NitroDOPET-PFtB$_{TRI}$ was synthesized as shown in **Scheme 4.2**. Unlike M2-NDA, the same nitrocatechol linker (NDA) was not utilized. Due to the free hydroxyl functionality of PFtB$_{TRI}$, a new nitrocatechol based linker was synthesized to contain a free hydroxyl group (**4-4**), which can facilitate the coupling reaction with PFtB$_{TRI}$ through a Williamson ether synthesis (**Scheme 4.2**). This new linker was synthesized according to Gambacorta *et al.*[46] with some modifications. First, the carboxylic acid functional group of 3,4-dihydroxyphenylacetic acid (DOPAC) was protected by an esterification reaction with MeOH under acidic conditions to give **4-3**. The dihydroxyl group of the catechol was further protected with 2,2-dimethoxypropane and the methyl ester was subsequently reduced to expose hydroxyl group to give **4-4** in high yield. The introduction of NO_2 by a nitration reaction to **4-4** resulted in a non-reactive nitrocatechol linker, which led to an unsuccessful coupling reaction with PFtB$_{TRI}$-OH (data not shown). Therefore, a Williamson ether reaction was carried out prior to the nitration step. PFtB$_{TRI}$-OH was synthesized according to a previously published paper in our group by Decato *et al.*[47] **4-4** was mesylated under basic conditions and subsequently coupled with PFtB$_{TRI}$-OH through a reflux reaction under basic conditions to yield **4-5**. Nitration of **4-5** was carried out in a 1:1 mixture of nitric acid (HNO_3) and water in the presence of MeOH

to help with the solubility of the compound, yielding **4-6**. Deprotection of the acetonide from **4-6** was done in 25% trifluoroacetic acid (TFA) to give nitroDOPET-PFtB$_{TRI}$ (**4-7**).

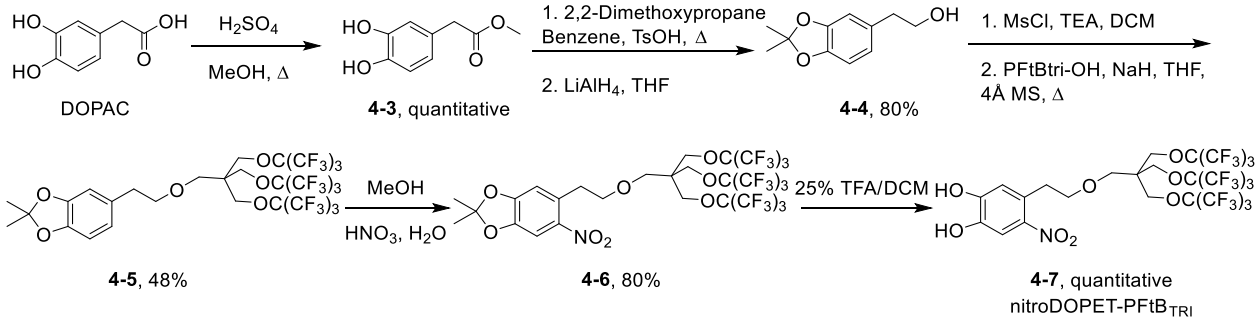

Scheme 4.2 Synthesis of nitroDOPET-PFtB$_{TRI}$.

4.2B.1.2 Synthesis of extremely small-sized iron oxide nanoparticles (ESIONs)

Iron oxide nanoparticles can be synthesized through various method depending on their application. For example, the co-precipitation method allows for simple and fast rate of production but usually generates polydispersed particles. Hydrothermal synthesis is another method that uses high temperature and pressure, resulting in small size and monodispersed particles.[48] Another method that is used to produce very small size particles with narrow size distribution is a thermal decomposition method. This method requires a high temperature to decompose the organometallic compound, and thus is performed under an inert atmosphere in the presence of surfactants and an organic solvent with a high boiling point.[22, 48-49] Therefore, to synthesize extremely small-sized iron oxide nanoparticles (ESIONs) with narrow size distribution, a thermal decomposition of iron-oleate complex was used.[22, 50] Iron-oleate complex was synthesized according to Park *et al*.[49] by reacting iron(III)chloride hexahydrate ($FeCl_3 \cdot 6H_2O$) with sodium oleate at 70 °C (**Scheme 4.3**). Thermal decomposition of the complex was achieved through a microwave reactor by heating the complex with oleyl alcohol in diphenyl ether to 200 °C (synthesis was adapted from Lu *et al.*[50]). After precipitation of the particles in acetone, the collected particles were redispersed in hexane (**Figure 4.6a**). The size of the iron oxide nanoparticles was measured using dynamic light scattering (DLS), which measures the hydrodynamic diameter of the particles. The results revealed a size of 4.7 ± 0.3 nm with a

monodispersed distribution (**Figure 4.6b**). As mentioned, the observed size by DLS refers to the hydrodynamic diameter of the particle, which is not the actual iron oxide core. The size measured by DLS includes the length of the hydrocarbon stabilizing the particles plus the iron oxide core. Therefore, the actual iron oxide core was expected to be less than 4.7 nm, suggesting the successful synthesis of ESIONs.

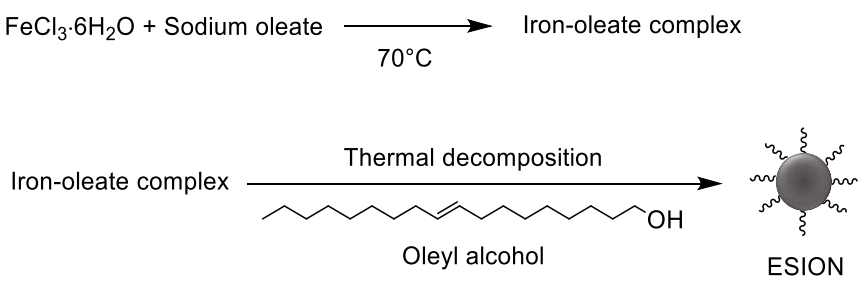

Scheme 4.3 Synthesis of extremely small-sized iron oxide nanoparticle.

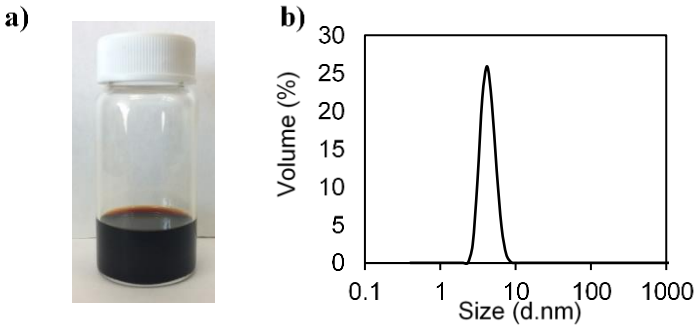

Figure 4.6 Iron oxide nanoparticle solution and the hydrodynamic diameter. a) Iron oxide nanoparticle solution in hexane. b) Hydrodynamic diameter of the iron oxide particles in hexane measured by DLS with a size of 4.7 ± 0.3 nm. Data represent mean ± standard deviation from three independent runs. Value reported as volume based %.

4.2B.1.3 Ligand exchange with M2-NDA and nitroDOPET-PFtB$_{TRI}$ and the effect on relaxations

M2-NDA (**4-2**) and nitroDOPET-PFTB$_{TRI}$ (**4-7**) were conjugated to the iron oxide surface through a ligand exchange method to provide colloidal stability and fluorine content to the ESIONs, respectively. The nitrocatechol group on these molecules binds irreversibly to the iron oxide surface, allowing for high particle staility.[33] Our preliminary ligand exchange was carried out in chloroform in the presence of a 1:2.5

of M2-NDA and nitroDOPET-PFtB$_{TRI}$. The solution was sonicated at 45 °C for 24 h to promote the ligand exchange. The resulting solution was kept in chloroform and used without further purification. As shown in **Figure 4.7**, the ^{19}F NMR signal of mPEG/PFtB$_{TRI}$-decorated ESIONs showed a split peak with $\Delta\delta$ = 0.05, which is probably due to the different signals of free and attached PFtB$_{TRI}$. These split signals can be neglected since they do not affect relaxation parameters due to the small $\Delta\delta$. T_1 and T_2 relaxations of ^{19}F were measured through NMR using inversion recovery and a Carr–Purcell–Meiboom–Gill (CPMG) pulse sequence, respectively. As expected, high T_1 and T_2 were observed for free PFtB$_{TRI}$ (PFtB$_{TRI}$-OH) at around 1 s (**Table 4.1**). The conjugation of PFtB$_{TRI}$ to ESIONs (mPEG/PFtB$_{TRI}$-decorated ESIONs) showed a decreased in both T_1 and T_2 values to 0.55 s and 0.17 s, respectively. These preliminary results demonstrated a promising effect on improving ^{19}F sensitivity of the PFtB$_{TRI}$ molecule. However, the conjugation of two different ligands on the iron oxide surface can lead to a competitive binding between PEG and PFtB$_{TRI}$ which can eventually lead to a problem with the colloidal stability of particles. Therefore, a new strategy for ligand preparation was employed by synthesizing both PFtB$_{TRI}$ and PEG on the same molecule.

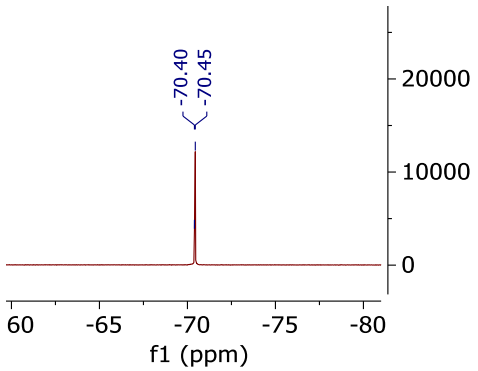

Figure 4.7 ^{19}F NMR signal of PEG/PFtB$_{TRI}$ decorated ESIONs in CDCl$_3$.

Table 4.1 Relaxation parameters for $PFtB_{TRI}$-OH and mPEG/$PFtB_{TRI}$ decorated ESIONs. Measurements were run in $CDCl_3$.

	T_1 (s)	T_2 (s)
$PFtB_{TRI}$-OH	1.36	1.1
mPEG/$PFtB_{TRI}$ decorated ESIONs	0.545	0.168

4.2B.1.4 Synthesis of M2diDOPET/$PFtB_{TRI}$

To synthesize the linker that has both $PFtB_{TRI}$ and PEG on the same molecule, the same synthetic strategy as presented in *Chapter 3* for the dibranched polymer was employed here. The asymmetric dibranched polymer was synthesized with $PFtB_{TRI}$ and catechol functional group, resulting in the M2diDOPET/$PFtB_{TRI}$ polymer. As shown in **Scheme 4.4**, the synthesis of M2diDOPET/$PFtB_{TRI}$ started from the functionalization of M2 with 2-phenyl-1,3-dioxan-5-ol (**4-8**). 2-phenyl-1,3-dioxan-5-ol (**4-8**) was synthesized through the acetal protection of the two primary alcohols of glycerol. This reaction proceeded with a low yield due to the mixture of the 1,2- and 1,3- protection products.[51-52] M2-OH was mesylated under basic conditions and subsequently coupled with **4-8** through a reflux reaction under basic conditions to give benzylidene acetal-M2 (**4-9**). Compound **4-9** was directly used in subsequent reactions without further purification due to the difficulty in separating **4-9** and unreacted M2. For the conjugation of $PFtB_{TRI}$-OH and compound **4-4**, a reductive ring opening of compound **4-9** was first performed with BH_3·THF catalyzed by $Cu(OTf)_2$ to give **4-10** with one free primary alcohol. The free primary alcohol was mesylated under basic conditions to give **4-11**, and subsequently reacted with compound **4-4** to introduce the protected catechol group to the PEG using a reflux reaction under basic conditions, yielding **4-12**. Compound **4-12** was purified using an automated Combiflash system with a reverse phase C18 column. However, compound **4-12** could not be isolated as a pure product. The result from MALDI MS showed that the isolated fractions contained M2-OH and compound **4-12** (**Appendix 3 – A.3.2.3**). This is due to the similar mass and polarity of the desired product and M2-OH.

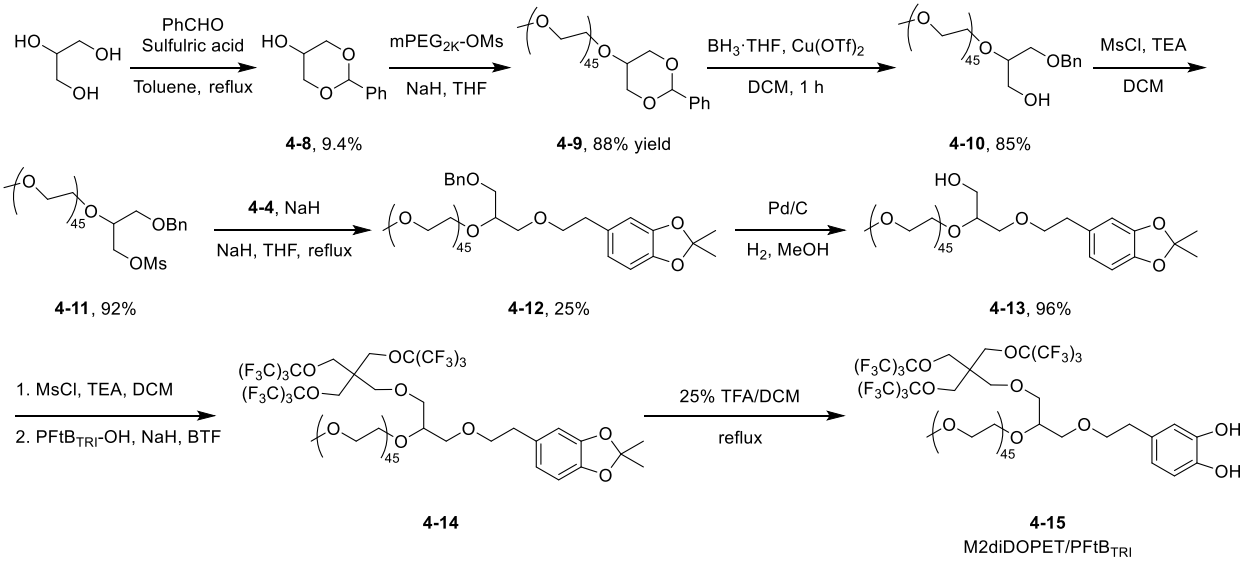

Scheme 4.4 Synthesis of M2diDOPET/PFtB$_{TRI}$.

To continue the synthetic process, compound **4-12** was used without reattempting the purification. We also explored the possibility to add the nitration step here. Hydrogenation and nitration reactions were first run with compound **4-12** to remove the benzyl protecting group and add the nitro group to the catechol, respectively, yielding M2dinitroDOPET(acetonide)/OH. Then, a coupling reaction with PFtB$_{TRI}$-OH was performed. It should be noted that the product, M2dinitroDOPET(acetonide)/OH, was only observed when the hydrogenation reaction was performed prior to the nitration reaction. Running the nitration reaction followed by the hydrogenation reaction led to the cleavage of the benzyl protecting group and the nitrocatechol (data not shown). However, due to the high yield of the nitration reaction, we decided to first proceed with the hydrogenation reaction followed by the coupling reaction with PFtB$_{TRI}$-OH (**Scheme 4.4**). The hydrogenation reaction on compound **4-12** was performed in MeOH in the presence of palladium on carbon (Pd/C) under the H_2 atmosphere to give **4-13**. The primary alcohol of compound **4-13** was mesylated under basic conditions followed by a coupling reaction with PFtB$_{TRI}$-OH using microwave-assisted synthesis at 160 °C for 2 h under basic conditions to afford **4-14**. Compound **4-14** was purified by an automated Combiflash system to afford a pure M2diDOPET(acetonide)/PFtB$_{TRI}$. Even though this step provided a low yield, more efforts are underway to optimize the reaction condition in order to improve the

yield. Acetonide deprotection of compound **4-14** was proceeded using trifluoroacetic acid (TFA) in DCM under reflux conditions to give **4-15**, M2diDOPET/PFtB$_{TRI}$, as the final polymer. This polymer consists of PEG as the hydrophilic segment, PFtB$_{TRI}$ as the fluorine source, and the catechol group as the linker for binding to the iron oxide surface.

4.2B.1.5 Future studies

The successful synthesis of M2diDOPET/PFtB$_{TRI}$ encouraged us to further improve the binding affinity of the molecule by introducing a nitro functional group to the catechol moiety[40] presenting on the polymer to give M2dinitroDOPET/PFtB$_{TRI}$ (**Figure 4.8a**). M2dinitroDOPET/PFtB$_{TRI}$ will be synthesized and the ligand exchange of ESIONs with M2dinitroDOPET/PFtB$_{TRI}$ will be carried out. We expect that the modification of the ESIONs' surface with our polymer will lead to particles having an irreversible ligand binding and improved water-solubility. The effect of the ESIONs on the ^{19}F signal sensitivity will be investigated using ^{19}F NMR. The polymer will be synthesized with various linker lengths between PFtB$_{TRI}$ and the catechol group to study the relationship between the distance of the fluorine atoms from the ESIONs' surface and its effect on the relaxation parameters. The example of the polymer is shown in **Figure 4.8b** where an H10 spacer (10-repeating unit of CH_2) is added to increase the distance of PFtB$_{TRI}$ from the catechol.

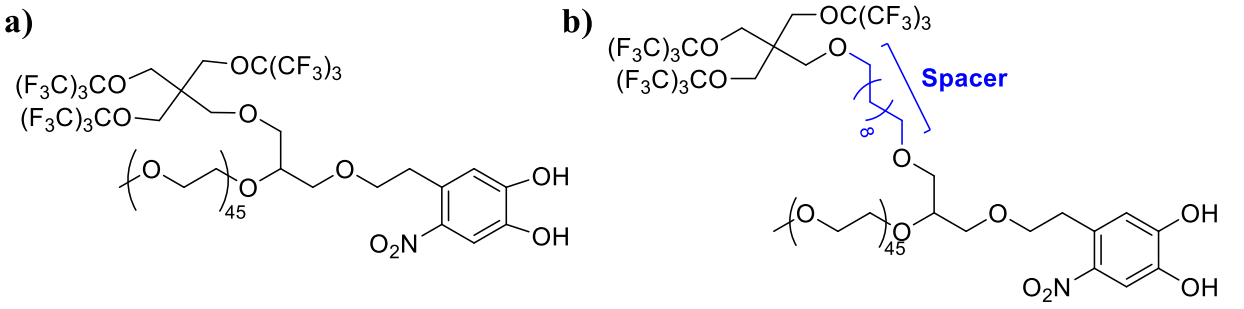

Figure 4.8 Structure of a) M2dinitroDOPET/PFtB$_{TRI}$ and b) M2dinitroDOPET/PFtB$_{TRI}$ with an addition of the H10 spacer.

4.2B.2 Improving sensitivity of PFC through Fe^{3+}

Another method for introducing iron ions for improving sensitivity of PFC is to directly add Fe^{3+} to the liquid PFC. However, due to the incompatibility of PFC and Fe^{3+}, different chelators have been synthesized to contain fluorine for improving the solubility of chelated Fe^{3+} in PFC oils.[14, 53-54] As noted before, the commonly used PFC oils include PFCE and PFPE. These oils are normally prepared in the form of nanoemulsions. One of the methods to increase the solubility of chelated Fe^{3+} is to introduce the chelating group to the same PFC oil used for emulsion preparation.

4.2B.2.1 Effect of magnetic ionic liquids (MILs) on T_1 and T_2 relaxation of PFPE

Ionic liquids (ILs) are salts in a liquid state below 100 °C[60] and have been used in various fields such as separation process,[55-56] catalysis,[57-58] electrochemistry,[59-60] or even biomedical applications.[61-63] They are normally composed of organic or inorganic cations/anions which can be deliberately tuned to provide distinct properties depending on cationic and anionic structures. ILs possess unique physicochemical properties such as high thermal and chemical stability. One class of ILs is metal-containing ionic liquids. These ionic liquids can be designed to contain Fe^{3+}, thus, providing a strong response to an external magnetic field. This type of IL is called a magnetic ionic liquid (MIL). Similar to normal ILs, MILs have high thermal and chemical stability which can be exploited to improve the sensitivity of PFC without any introduction of chelating group on PFC molecules.

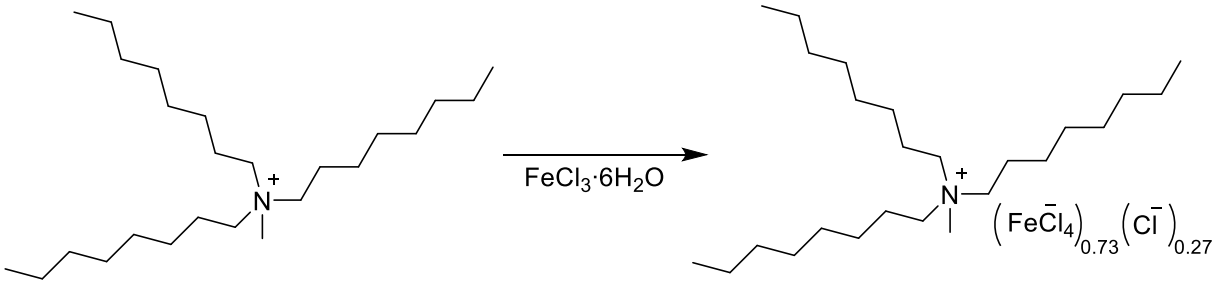

Scheme 4.5 Synthesis of $[A336][FeCl_4]_{0.73}[Cl]_{0.27}$.

The MIL was prepared from vigorous stirring of tricaprylylmethylammonium chloride (Aliquot®336) and $FeCl_3$ with a slight excess of the Aliquot®336, as described according to Kogelnic *et al.*[64], generating $[A336][FeCl_4]_{0.73}[Cl]_{0.27}$ (**Scheme 4.5**). $[A336][FeCl_4]_{0.73}[Cl]_{0.27}$ is a binary salt which has a higher stability than tricaprylylmethylammonium tetrachloroferrate $[A336][FeCl_4]$.[64]

Table 4.2 Relaxation parameters of PFPE with MIL in acetone.

PFPE + MIL (Fe concentration; mM)	T_1 (s)	T_2 (s)
0	665	580
12.8	312	207
24	246	155
40	167	104
104	76	46

To evaluate the effect of the MIL on PFPE, ^{19}F NMR relaxation parameters of PFPE and MIL in acetone were measured as a function of Fe^{3+} concentration. Acetone was selected as it solubilizes both components. ^{19}F relaxation times measured by NMR are summarized in **Table 4.2**. As expected, increasing the concentration Fe^{3+} with the MIL leads to a decreased in T_1 as well as T_2 relaxations. The reduction of T_2 relaxation did not lead to any severe line broadening effect. The longitudinal relaxation rate (R_1) and transverse relaxation rate (R_2) which can be calculated from $1/T_1$ and $1/T_2$, respectively, were plotted against Fe^{3+} concentration (**Figure 4.9**). The r_1 and r_2 parameters, so called relaxivity with a unit of $mM^{-1}s^{-1}$, are calculated from the slope of the graph and are used to describe the effectiveness of the individual contrast agent which are normally expressed as the r_2/r_1 ratio.[65] A low r_2/r_1 ratio is an indication of a good T_1 contrast agent.[44, 65-67] Typical paramagnetic T_1 contrast agents such as Gd^{3+} and Mn^{2+} possess a low r_2/r_1 ratio which is normally in 1 – 2 range. As shown in **Figure 4.9**, the calculated r_1 and r_2 of PFPE with MIL are 0.111 $mM^{-1}s^{-1}$ and 0.189 $mM^{-1}s^{-1}$, respectively, resulting in a r_2/r_1 ratio of 1.7. The results suggest that the

incorporation of Fe^{3+} through the MIL with PFPE leads to improved properties of PFPE, resulting in an enhanced sensitivity of ^{19}F signal.

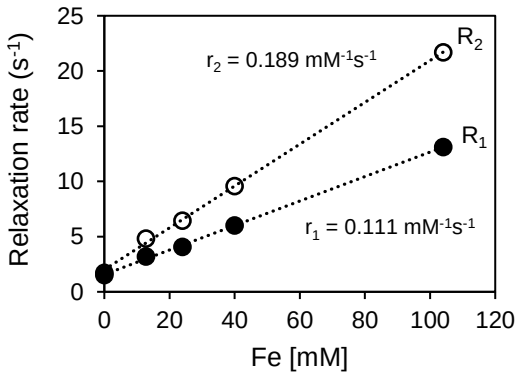

Figure 4.9 Fluorine-19 relaxometry of PFPE with MIL. R_1 (solid circle) and R_2 (opened circle) of PFPE after adding different concentration of MIL. A concentration-dependent effect is shown for both parameters.

We have attempted to prepare a nanoemulsion incorporating the MIL and PFPE as the oil phase stabilized by a commercially available $mPEG_{2K}$-DSG, a hydrophilic-hydrophobic diblock copolymer. Barres *et al*. has previously demonstrated that the diblock copolymers can be used to stabilized perfluoropolyether oils, resulting in stable nanoemulsions.[25] With a small-scale preparation, the MIL+PFPE nanoemulsion was prepare using a homogenization method. After mixing MIL and PFPE, which resulted in a biphasic solution, saline was added, and the mixture was homogenized. However, due to the large amount of saline used compared to the MIL, the MIL was solubilized in the aqueous solution. This suggests that the prepared MIL was not hydrophobic enough. Therefore, a new MIL has to be designed to increase its hydrophobicity. One strategy is to prepare a fluorinated magnetic ionic liquid (FMIL). This will not only increase the hydrophobicity of the molecule but also improve its miscibility with the fluorinated oil.

4.2B.2.2 Future studies

The observed T_1 relaxation improvement from the mixture of PFPE and the MIL encourages us to look further into the preparation of a more hydrophobic MIL. We plan to design a new MIL that contains fluorine atoms, so-called a fluorinated magnetic ionic liquid (FMIL), to increase the hydrophobicity as well as the miscibility with fluorinated oil. We expect that the FMIL will incorporate well with PFPE, leading

to a preparation of a stable paramagnetic fluorinated nanoemulsion. Additionally, the effect of the relaxations will be explored using ^{19}F NMR. The *in vitro* cytotoxicity will be investigated with the new paramagnetic fluorinated nanoemulsion. Furthermore, the *in vivo* ^{19}F MRI will be studied. Altogether, these results will allow us to determine the clinical translatability of this new formulation.

4.3B Conclusion

We focused on addressing the intrinsically high T_1 relaxation properties of fluorine. The high T_1 relaxation was reduced by using a paramagnetic metal ion, Fe^{3+}. Herein, the Fe^{3+} was introduced into the imaging agents in two different forms: i) the extremely small-sized iron oxide nanoparticles (ESIONs) and ii) the magnetic ionic liquids (MILs). The ESIONs, containing Fe^{3+}, were used due to its properties as a T_1 agent. Nitrocatechol functionality was selected as the ligand for iron oxide surface binding due to its high stability over other functional groups. M2-NDA and nitroDOPET-PFtB$_{TRI}$ were successfully synthesized to express the nitrocatechol group. The thermal decomposition method using microwave-assisted synthesis was employed for the successful synthesis of ESIONs. The synthesized ESIONs had a hydrodynamic diameter of 4.7 ± 0.3 nm, suggesting that the actual iron oxide core size is less than 4.7 nm. The preliminary ligand exchange results using M2-NDA and nitroDOPET-PFtB$_{TRI}$ with the ESIONs revealed an improved ^{19}F sensitivity as demonstrated by a reduced T_1 relaxation with a modest line broadening effect. However, the limited water-solubility of the resulting particles hampered its translatability, leading to a new design of the nanoparticles.

As two different molecules possess different binding affinities to the iron oxide surface, the competitive binding of M2-NDA and nitroDOPET-PFtB$_{TRI}$ poses a complication for the surface modification. Therefore, the M2diDOPET/PFtB$_{TRI}$ was synthesized to circumvent the aforementioned problem. The M2diDOPET/PFtB$_{TRI}$ was successfully synthesized to contain PEG, PFtB$_{TRI}$, and the catechol group. The addition of the nitro group to the polymer was not presented here but will be explored in the future.

Another approach for introducing Fe^{3+} to the fluorocarbon is through the magnetic ionic liquids (MILs). We have successfully synthesized the hydrophobic MIL, $[A336][FeCl_4]_{0.73}[Cl]_{0.27}$. The effect of the MIL to the relaxations of fluorine was demonstrated. Preliminary results from the mixture of the MIL and PFPE in acetone revealed that the T_1 relaxation was reduced with increasing Fe^{3+} concentration, suggesting a concentration-dependent effect. We attempted to prepare the nanoemulsion with MIL and PFPE using a commercially available $mPEG_{2K}$-DSG polymer. However, we were not able to incorporate the MIL as an oil phase due to MIL's solubility in aqueous solution at the concentration we used. This was due to a low hydrophobicity of the synthesized MIL. Therefore, we are currently working on improving the hydrophobicity of the MIL by designing a new MIL to contain fluorine, a so-called fluorinated magnetic ionic liquid (FMIL), in order to increase the hydrophobicity of the ionic liquid as well as improve its miscibility with fluorocarbon.

4.4 Experimental

Part A: Incorporation of high PFCE concentration in nanoemulsions for MR imaging

4.4A.1 Nanoemulsion stability using dynamic light scattering (DLS)

For different storage conditions, nanoemulsions were stored at temperatures of 4, 25, and 37 °C. At each time point, 10 µL of the stock nanoemulsion was added into 3 mL of Milli-Q water. The size of the nanoemulsion particles was measured by dynamic light scattering (NICOMP 380ZLS, Particle Sizing Systems, Santa Barbara, CA). Each particle size analysis was run for 5 min at room temperature and repeated three times. The data was analyzed using Gaussian analysis and reported as the intensity weighted average diameters.

For measuring the stability of the nanoemulsion in serums, 100 µL of the nanoemulsion was mixed with 100 µL of PBS (as a control), media (DMEM media supplemented with 10% fetal bovine serum (FBS) and 1% penicillin/streptomycin), or FBS alone. The samples were incubated at 37 °C. The size of the nanoemulsion particles was measured on day 0, 1, 4, and 7 via DLS by adding 20 µL of the sample into 3 mL of Milli-Q water. Each particle size analysis was run for 5 min at room temperature and repeated three

times. The data was analyzed using Gaussian analysis and reported as the intensity weighted average diameters.

4.4A.2 Cell culture

4T1-Luc cells, luciferase-modified murine breast carcinoma cell line, (kindly provided by Dr. Glen S. Kwon) were cultured at 37°C in a humidified atmosphere containing 5% CO_2. The cells were maintained in a high glucose Dulbecco's Modified Eagle Medium (DMEM) (Hyclone, Logan, UT) supplemented with 10% fetal bovine serum and 1% penicillin/streptomycin.

4.4A.3 Cytotoxicity studies

4T1-Luc cells were seeded at 5,000 cells/well/100 µL on 96-well plates and incubated at 37 °C for 24 h. The cells were treated with the PFCE nanoemulsion at various concentrations and incubated for 6, 24, and 48 h. After each timepoint, the cytotoxic effects were quantified by using a CellTiter-Blue® cell viability assay (Promega, WI) according to the manufacturer's protocol. The fluorescence signal was measured at 560/590 nm using a SpectraMax® M2 microplate reader (Molecular Devices, CA). The results were represented as percentage of cell viability normalized to the nontreated cell control group.

4.4A.4 In vivo tumor model preparation

All *in vivo* experiments with mice were performed using protocols approved by the University of Wisconsin Institutional Animal Care and Use Committees. Six to eight-week-old female BALB/c mice were obtained from Harlan Laboratories (Envigo, Indianapolis, IN). Mice were acclimated to their environment for at least 1 week prior to tumor inoculation. 4T1-Luc cells were harvested from sub-confluent cultures after trypsinization. Mice were subcutaneously inoculated with 4T1-Luc cells (1×10^6 cells per 100 µL in serum-free DMEM) on the right flank. Tumors were allowed to reach approximately 100 mm^3 before beginning the following *in vivo* experiment.

4.4A.5 In vivo ^{19}F MRI studies

Female tumor-bearing BALB/c mice (n = 5) were intravenously injected with 200 μL of the 35% v/v PFCE nanoemulsion through the tail vein. *In vivo* ^{1}H images were acquired prior to nanoemulsion injection, followed by ^{1}H and ^{19}F images at 6 hours, 1, 4, 7, and 14 days post-injection to monitor the nanoemulsion distribution. Mice were induced with 3% isoflurane and placed in a supine position in the $^{1}H/^{19}F$ homebuilt coil. During all imaging sessions, mice were maintained at 37 °C with 1.5% isoflurane. Anatomic ^{1}H images were acquired using a T_2-weighted fast spin echo pulse sequence with a 0.28 × 0.28 × 2.0 mm^3 spatial resolution, 72 × 36 mm^2 FOV, 3000/20 ms TR/TE, 90° flip angle, 3 averages, and a total scan time of 1 min and 12 sec. ^{19}F images of the injected PFCE nanoemulsion were acquired with a fast spin echo sequence with a 1.1 × 1.1 × 2.0 mm^3 spatial resolution, 72 × 64 mm^2 FOV, 1250/20.0 ms TR/TE, echo train length of 8 echoes, 128 averages, 10 min 40 s imaging time, and an isoflurane saturation RF pulse at +2150 Hz (relative to the ^{19}F Larmor frequency of PFCE) to avoid any anesthetic signal contamination in the image.

4.4A.6 MRI data procession

All image reconstructions and analyses were performed on MATLAB 2015b (MathWorks, Natick, MA). ^{19}F images were scaled in arbitrary units (a.u.) of SNR according to **Equation 4-1**:

Equation 4-1 $$SNR=(0.655)\cdot S/\sigma$$

where S is the pixel intensity value of the magnitude image, σ is the standard deviation of a noise measurement obtained from a region of interest (ROI) in the image background, and 0.655 is a correction factor to account for the Rician noise distribution of the background noise. Once scaled to SNR, the ^{19}F images were resized (bicubic interpolation) to match the anatomic image size and overlaid with the $_{1}H$ images to produce composite images. For visualization and comparison, the ^{19}F signal within the fused images were windowed and leveled to display pixel SNR values ranging from 10% – 100% of the maximum pixel value in the image as indicated in the corresponding colorbars

Part B: Improving ^{19}F sensitivity by decreasing T_1 relaxation

4.4B.1 Materials and Methods

Perfluoro-*tert*-butanol was purchased from SynQuest Laboratories Inc. (Alachua, FL). 3,4-dihydroxyphenylacetic acid was purchased from Accela ChemBio Inc. (San Diego, CA). Diphenyl ether was purchased from Alfa Aesar (Haverhill, MA). Sodium nitrite was purchased from Santa Cruz Biotechnology (Dallas, TX). F-PEG600 diol-perfluorinated polyethylene glycol diol was generously given by Exfluor Research Corporation (Round Rock, TX). Solvents and all other chemicals were purchased from Sigma-Aldrich and were used as purchased, unless otherwise specified. Small molecule and polymer chromatography was accomplished with Silicycle 60 Å SiO_2 or using a Teledyne CombiFlash Rf 4× (Lincoln, NE) equipped with an ELSD for visualization and RediSep® Rf high performance silica or C18 columns.

^1H, ^{13}C, and ^{19}F NMR spectra were measured using a Bruker Avance III HD 400 MHz spectrometer. All spectra were measured with either $CDCl_3$ or DMSO-d6 as the solvent. Polymer purity was confirmed by MALDI-MS on a rapifleX MALDI TOF/TOF (Bruker, Billerica, MA) using α-cyano-4-hydroxycinnamic acid matrix unless otherwise specified.

*4.4B.2 Synthesis of Nitrodopamine (NDA, **4-1**)*

NDA was synthesized according to Bixner *et al*.[41] Briefly, dopamine hydrochloride (1.5 g, 7.9 mmol) was dissolved in MilliQ water (45 mL). $NaNO_2$ (2.18 g, 31.6 mmol) was then added into the solution under vigorous stirring. The reaction solution was then cooled down to 0 °C using an ice bath followed by dropwise addition of 20% v/v sulfuric acid (7.5 mL). The ice bath was then removed and the reaction was stirred at room temperature overnight. After this time, the reaction mixture was filtered. The collected solid was washed extensively with ice-cold water, EtOH, and diethyl ether. The resulting solid was collected and dried under high vacuum to give the product as a yellow solid (1.24 g, 53% yield). ^1H NMR (400 MHz, DMSO-d6) δ 7.44 (s, 1H), 6.52 (s, 1H), 3.03 (d, J = 2.8 Hz, 4H).

*4.4B.3 Synthesis of M2-NDA (**4-2**)*

M2-NHS (1 g, 0.455 mmol) was dissolved in dry DMF (20 mL) under Ar. NDA (**4-1**, 270 mg, 0.910 mmol) was then added and the reaction was stirred at room temperature overnight. After this time, the reaction solution was diluted with water (20 mL) and extracted with DCM (3x). The organic layers were combined, dried over $MgSO_4$, and filtered. The organic filtrate was concentrated under reduced pressure and precipitated in cold ether. The collected solid was freeze-dried in a mixture of DCM and benzene to give the product as a slightly dark yellow powder. ^{1}H NMR (400 MHz, $CDCl_3$) δ 7.65 (s, 1H), 6.82 (s, 1H), 3.67 – 3.59 (m, 178H), 3.38 (s, 3H), 3.08 (t, J = 6.6 Hz, 2H), 2.29 (t, J = 6.8 Hz, 2H).

*4.4B.4 Synthesis of (3,4-Dihydroxyphenyl)acetic acid methyl ester (**4-3**)*

3,4-dihydroxyphenylacetic acid (DOPAC, 5 g, 29.73 mmol) was dissolved in MeOH (450 mL) under Ar. Concentrated H_2SO_4 (20 drops) was added and the reaction was brought to reflux in the dark for 2 h. The completion of the reaction was monitored by TLC using 20% EtOAc/hexane as a mobile phase. After the reaction was completed, the solvent was evaporated. The residue was redissolved in EtOAc, washed with saturated $NaHCO_3$. The aqueous layer was extracted with EtOAc (3x). The combined organic layers were washed with brine, dried over $MgSO_4$, filtered, concentrated, and dried under high vacuum to give the product as a faint red liquid (5.77 g, quantitative). ^{1}H NMR (400 MHz, $CDCl_3$) δ 6.82 – 6.71 (m, 2H), 6.66 (dd, J = 8.1, 2.0 Hz, 1H), 5.78 (s, 1H), 5.56 (s, 1H), 3.71 (s, 3H), 3.52 (s, 2H).

*4.4B.5 Synthesis of Hydroxytyrosol(acetonide) (DOPET(acetonide), **4-4**)*

Using a Soxhlet extractor, the column was filled with anhydrous $CaCl_2$ (10 g). To the flask containing **4-3** (5.77 g, 31.67 mmol) was added benzene (70 mL) under Ar. 2,2-dimethoxypropane (DMP, 35 mL, 0.29 mol) was then added followed by *p*-Toluenesulfonic acid (TsOH, 904 mg, 4.75 mmol). The reaction flask was connected to the Soxhlet extractor and the reaction was heated to reflux. TLC was used to confirm the completed reaction using 1% aqueous $FeCl_3$ solution stain. After the reaction was completed (~ 6 h), the reaction solution was washed with water (2x) and brine (1x). The organic layer was then

concentrated and purified by column chromatography using hexane/EtOAc gradient to give the intermediate product as a yellow liquid (7.18 g). ^{1}H NMR (400 MHz, $CDCl_3$) δ 6.75 – 6.61 (m, 3H), 3.69 (s, 3H), 3.52 (s, 2H), 1.66 (s, 6H).

The intermediate was then dissolved in dry THF (500 mL) under Ar. $LiAlH_4$ (1 M in THF, 32.3 mL, 32.3 mmol) was added and the reaction solution was heated to reflux for 3 h. After this time, the mixture of water and diethyl ether was used to quench the remaining $LiAlH_4$, resulting in the formation of precipitates. The precipitates were then filtered. The collected filtrate was dried over $MgSO_4$, concentrated under reduced pressure, and adsorbed on Celite. The crude product was purified by automated flash chromatography using a RediSep® silica column with a EtOAc/hexane gradient. The collected fractions were then concentrated under reduced pressure to give the product as a yellow liquid (4.94 g, 80% yield). ^{1}H NMR (400 MHz, $CDCl_3$) δ 6.70 – 6.58 (m, 3H), 3.81 (t, J = 6.6 Hz, 2H), 2.77 (t, J = 6.5 Hz, 2H), 1.67 (s, 6H).

*4.4B.6 Synthesis of DOPET(acetonide)-PFtB$_{TRI}$ (**4-5**)*

4-4 (461 mg, 2.37 mmol) was dissolved in dry DCM (7 mL) under Ar. TEA (794 µL, 5.7 mmol) was added and the solution was cooled down to 0 °C using an ice bath and stirred for 10 min. Methanesulfonyl chloride (MsCl, 238 µL, 3.08 mmol) was slowly added. The reaction was allowed to stir in the ice bath until it melted and continued to stir at room temperature for 2 h. After this time, the reaction was diluted in DCM, washed with saturated NH_4Cl solution (3x), dried over $MgSO_4$, and filtered. The filtrate was concentrated under reduced pressure and dried under high vacuum overnight to give the intermediate, DOPET(acetonide)-OMs, as a yellow liquid.

PFtB$_{TRI}$-OH was synthesized according to a previously published procedure.[47] In a different dry round bottom flask, PFtB$_{TRI}$-OH (189.6 mg, 0.24 mmol) was dissolved in dry THF (7 mL) under Ar. 4 Å powdered molecular sieves (1 weight eq.) were added and the reaction flask was cooled down to 0 °C using an ice bath. NaH (57 mg, 2.37 mmol) was added and the ice bath was then removed. The reaction was allowed to stir for 30 min as it warmed up to room temperature. DOPET(acetonide)-OMs was separately

dissolved in dry THF (2 mL) and added dropwise into the reaction. The reaction was then heated to reflux for 7 days. Small amounts of NaH were added throughout the 7 days to facilitate the reaction. After 7 days, MeOH was added dropwise to quench the remaining NaH. The reaction solution was diluted in DCM and filtered through Celite to remove the molecular sieves. The filtrate was concentrated to half of the volume, washed with saturated NH_4Cl solution (2x), dried over $MgSO_4$, and filtered. The organic layer was concentrated to nearly 10 mL and was extracted with perfluorohexane (3x; total of 25 mL). The perfluorohexane layer was collected, concentrated, and dried under high vacuum to give the product as a slightly yellow solid (112 mg, 48% yield). ^{1}H NMR (400 MHz, $CDCl_3$) δ 6.67 – 6.50 (m, 3H), 4.02 (s, 6H), 3.53 (t, J = 6.9 Hz, 2H), 3.38 (s, 2H), 2.73 (t, J = 6.9 Hz, 2H), 1.65 (s, 6H). ^{19}F NMR (376 MHz, $CDCl_3$) δ -70.43.

*4.4B.7 Synthesis of nitroDOPET(acetonide)-PFtB$_{TRI}$ (**4-6**)*

4-5 (163.9 mg, 0.17 mmol) was dissolved in MeOH (2.5 mL). Heat was applied to help solubilize the compound. The reaction was heated to 50 °C and a cold solution of HNO_3 and water (1:1, 5 mL) was added dropwise. The reaction was allowed to stir at 50 °C overnight. The next day, saturated $NaHCO_3$ was slowly added dropwise to neutralize the solution. The reaction mixture after neutralized was passed through filter paper. The solid was collected and dried under high vacuum to give the product as a yellow solid (137.9 mg, 80% yield). ^{1}H NMR (400 MHz, $CDCl_3$) δ 7.40 (s, 1H), 6.56 (s, 1H), 4.01 (s, 7H), 3.65 (t, J = 6.2 Hz, 2H), 3.38 (s, 2H), 3.11 (t, J = 6.2 Hz, 2H), 1.70 (s, 6H). ^{19}F NMR (376 MHz, $CDCl_3$) δ -70.43.

*4.4B.8 Synthesis of nitroDOPET-PFtB$_{TRI}$ (**4-7**)*

4-6 (137.9 mg, 0.136 mmol) was dissolved in DCM (7.5 mL). TFA (2.5 mL) was added followed by an addition of water (0.1 mL). The reaction was heated to reflux and monitored for completion by TLC (mobile phase: 20% EtOAc/hexane or 1% aqueous $FeCl_3$ solution stain). After 7 h, no starting material was observed. The solvent was then evaporated from the reaction. The remaining residual was co-evaporated with toluene (2x) to completely remove the solvent. The residue was dried under high vacuum to give the

product as a dark yellow solid (138.6 mg, quantitative). ^{1}H NMR (400 MHz, $CDCl_3$) δ 7.63 (s, 1H), 6.75 (s, 1H), 5.80 (s, 1H), 5.42 (s, 1H), 4.01 (s, 6H), 3.63 (t, J = 6.5 Hz, 2H), 3.38 (s, 2H), 3.13 (t, J = 6.5 Hz, 2H). ^{19}F NMR (376 MHz, $CDCl_3$) δ -70.45.

*4.4B.9 Synthesis of 2-phenyl-1,3-dioxan-5-ol (**4-8**)*

Using a Soxhlet extractor, a column was filled with anhydrous $CaCl_2$ (50 g). Glycerol (37.7 g, 0.41 mol) was dissolved in dry toluene (50 mL) under Ar. Benzaldehyde (32.7 mL, 0.32 mol) was then added followed by 10 drops of concentrated sulfuric acid. The reaction flask was connected to the Soxhlet extractor and the reaction was heated to reflux for 2 days. After this time, the solvent was removed from the reaction flask under reduced pressure. Diethyl ether (250 mL) was added to redissolve the residue and the solution was frozen at -80°C for at least 4 h. The white solid was vacuum filtered and the collected solid was recrystallized in 60 mL of toluene:petroleum ether (1:1). The white crystals were collected and dried under high vacuum (5.39 g, 9.4% yield). ^{1}H NMR (400 MHz, $CDCl_3$) δ 7.49 (d, J = 1.8 Hz, 2H), 7.42 – 7.33 (m, 3H), 5.56 (s, 1H), 4.17 (q, 4H), 3.63 (d, J = 10.7 Hz, 1H), 3.08 (d, J = 11.1 Hz, 1H). ^{13}C NMR (101 MHz, $CDCl_3$) δ 137.83, 129.13, 128.35, 125.89, 101.69, 72.32, 64.03.

4.4B.10 Synthesis of "mPEG$_{2K}$-OMs" methoxypoly(ethylene glycol) methanesulfonate

Poly(ethylene glycol) methyl ether (mPEG$_{2K}$-OH) (10 g, 4.76 mmol) was dissolved in dry DCM (60 mL) under Ar. TEA (1.99 mL, 14.28 mmol) was then added followed by the addition of MsCl (920 µL, 11.9 mmol) dropwise. The reaction was allowed to stir at room temperature overnight. After this time, the reaction was diluted with DCM and washed with saturated NH_4Cl solution (3x). The organic layer was dried over $MgSO_4$ and concentrated under reduced pressure. The product was then freeze-dried in a mixture of DCM and benzene to give the product as a white powder (8.99 g, 87% yield). ^{1}H NMR (400 MHz, $CDCl_3$) δ 4.43 – 4.34 (m, 2H), 3.78 – 3.53 (m, 178H), 3.38 (s, 3H), 3.09 (s, 3H).

*4.4B.11 Synthesis of Benzylidene acetal-M2 (**4-9**)*

4-8 (0.9 g, 5 mmol) was dissolved in dry THF (60 mL) under Ar. The solution was cooled down to 0 °C. NaH (480 mg, 20 mmol) was then added and the reaction mixture was allowed to warm up to room temperature for 30 min with vigorous stirring. After this time, $mPEG_{2K}$-OMs (4 g, 2 mmol) was added and the reaction was stirred under reflux for 2 days. After 2 days, the reaction mixture was quenched by a slow addition of water. The reaction solution was diluted in DCM and washed with saturated NH_4Cl solution (3x). The organic layer was dried over $MgSO_4$ and concentrated under reduced pressure. The crude product was precipitated in cold diethyl ether. The product was collected and freeze-dried under high vacuum to give the product as white powder (3.82 g, 88% yield, ~70% conjugation). The product was used without further purification for the next synthetic step. ^{1}H NMR (400 MHz, $CDCl_3$, contain free M2-OH) δ 7.56 – 7.33 (m, 4H), 5.55 (s, 1H), 4.36 (dd, J = 12.6, 1.7 Hz, 1H), 4.05 (dd, J = 12.7, 1.8 Hz, 1H), 3.78 – 3.53 (m, 184H), 3.38 (s, 3H).

*4.4B.12 Synthesis of "M2diOBn/OH" (**4-10**)*

4-9 (3 g, 1.38 mmol) was dissolved in dry DCM (30 mL) under Ar followed by an addition of BH_3·THF (1 M solution, 6.89 mL, 6.89 mmol). The reaction was allowed to stir for 10 min. $Cu(OTf)_2$ (74.87 mg, 15 mol%) was then added and the reaction was stirred at room temperature for 1 h. After this time, the reaction mixture was cooled down to 0 °C and quenched by adding 300 µL (2.1 mmol) TEA followed by 15 mL MeOH (caution: hydrogen gas was evolved). The crude solution was filtered through Celite. The filtrate was concentrated under reduced pressure. The residue was precipitate in cold diethyl ether. The solid was collected and dried under high vacuum to give the product as grey solid (2.94 g, 98% yield). The product was used without further purification for the next synthetic step. ^{1}H NMR (400 MHz, $CDCl_3$, contain free M2-OH) δ 7.33 (s, 5H), 4.54 (s, 2H), 3.78 – 3.53 (m, 280H), 3.38 (s, 4H).

*4.4B.13 Synthesis of "M2diOBn/OMs" (**4-11**)*

4-10 (2.84 g, 1.3 mmol) was dissolved in dry DCM (20 mL) under Ar. TEA (543.6 µL, 3.9 mmol) was then added followed by the addition of MsCl (232 µL, 3 mmol) dropwise. The reaction was allowed to stir at room temperature overnight. After this time, the reaction was diluted with DCM and washed with saturated NH_4Cl solution (3x). The organic layer was dried over $MgSO_4$ and concentrated under reduced pressure. The corresponding solution was then freeze-dried in a mixture of DCM and benzene to give the product as an off-white solid (2.71 g, 92% yield). The product was used without further purification for the next synthetic step. ^{1}H NMR (400 MHz, $CDCl_3$, contain free M2-OH) δ 7.44 – 7.28 (m, 5H), 4.54 (d, J = 2.1 Hz, 2H), 4.43 – 4.27 (m, 2H), 3.78 – 3.53 (m, 313H), 3.38 (s, 5H), 3.04 (s, 3H).

*4.4B.14 Synthesis of "M2diDOPET(acetonide)/OBn" (**4-12**)*

4-4 (588 mg, 3.02 mmol) was dissolved in dry THF (27 mL) under Ar. The solution was cooled down to 0 °C followed by an addition of NaH (291 mg, 12.1 mmol). The reaction was stirred vigorously for 1 h as it warmed up to room temperature. **4-11** (2.73 g, 1.21 mmol) was then added and the reaction was heated to reflux with vigorous stirring for 2 days. After this time, the reaction was quenched with water and diluted in DCM. The reaction solution was washed with saturated NH_4Cl solution (3x). The collected organic layer was dried over $MgSO_4$ and concentrated under reduced pressure. The crude product was adsorbed on Celite and purified by automated flash chromatography using a RediSep® C-18 reverse phase silica column with a water (0.1% FA)–MeOH to dichloromethane–MeOH gradient. The collected fractions were then concentrated under reduced pressure and dried under high vacuum to give the product as a yellow solid (784 mg, 25% yield). The purified product still contained free $mPEG_{2K}$-OH. The product was used without further purification for the next synthetic step. ^{1}H NMR (400 MHz, $CDCl_3$, contain free $mPEG_{2K}$-OH) δ 7.38 – 7.28 (m, 4H), 6.66 – 6.55 (m, 3H), 4.52 (s, 2H), 3.64 (s, 191H), 3.38 (s, 3H), 2.76 (t, J = 7.1 Hz, 2H), 1.65 (d, J = 3.2 Hz, 6H). MALDI MS: $[M + Na]^+$ calculated for $C_{112}H_{208}NaO_{50}$ = 2376.36; found: 2376.295.

*4.4B.15 Synthesis of "M2diDOPET(acetonide)/OH" (**4-13**)*

4-12 (634.8 mg, 0.27 mmol) was dissolved in methanol (15 mL). The solution was stirred under Ar for 30 min. Palladium on carbon (52.2 mg, 0.49 mmol) was then added and the mixture was flushed with Ar for another 30 min. Then, the reaction was flushed with hydrogen gas and was kept under a static hydrogen atmosphere overnight. Afterwards, the reaction mixture was filtered through Celite. The filtrate was concentrated and dried under high vacuum to give the product as a yellow solid (587 mg, 96% yield). The product was used without further purification for the next synthetic step. ^{1}H NMR (400 MHz, CDCl3, contain free mPEG$_{2K}$-OH) δ 6.69 – 6.55 (m, 3H), 3.64 (s, 193H), 3.38 (s, 3H), 2.77 (t, J = 7.1 Hz, 2H), 1.65 (s, 6H).

*4.4B.16 Synthesis of "M2diDOPET(acetonide)/PFtB$_{TRI}$" (**4-14**)*

A mesylation reaction was performed by dissolving **4-13** (587mg, 0.26 mmol) in dry DCM (10 mL) under Ar. TEA (110 µL, 0.78 mmol) was then added followed by the addition of MsCl (46 µL, 0.6 mmol) dropwise. The reaction was allowed to stir at room temperature overnight. After this time, the reaction was diluted with DCM and washed with saturated NH_4Cl solution (3x). The organic layer was dried over $MgSO_4$ and concentrated under reduced pressure. The product was then freeze-dried in a mixture of DCM and benzene to give the intermediate (M2diDOPET(acetonide)/OMs) as a yellow powder (588 mg, 97% yield). ^{1}H NMR (400 MHz, $CDCl_3$, contain free mPEG$_{2K}$-OMs) δ 6.71 – 6.50 (m, 3H), 4.41 – 4.35 (m, 1H), 4.24 (dd, J = 11.0, 5.7 Hz, 1H), 3.64 (s, 181H), 3.38 (s, 3H), 3.08 (s, 1H), 3.03 (s, 2H), 2.77 (t, J = 6.9 Hz, 2H).

The subsequent Williamson ether synthesis was proceeded by dissolving PFtB$_{TRI}$-OH (496 mg, 0.63 mmol) in anhydrous BTF (6 mL) under Ar in a G30 microwave reaction vial. 4Å molecular sieve (500 mg) was added followed by NaH (60.2 mg, 2.51 mmol). The reaction mixture was allowed to stir for 1 h. After this time, the intermediate (M2diDOPET(acetonide)/OMs, 588 mg, 0.251 mmol) was added and the reaction was run in a Monowave 300, Microwave Synthesis Reaction (Anton Paar, Austria) at 160 °C for 2 h. After the microwave reaction, water was slowly added to quench the reaction. The reaction was diluted

in DCM and washed with saturated NH_4Cl solution (3x). The organic layer was dried over $MgSO_4$ and filtered through Celite. The filtrate was collected and concentrated under reduced pressure. The crude product was adsorbed on Celite and purified by an automated flash chromatography, CombiFlash, using a RediSep® C-18 reverse phase silica column with a water (0.1% FA)–MeOH to dichloromethane–MeOH gradient. The collected fractions were then concentrated under reduced pressure and dried under high vacuum to give the product as a yellow solid (57.2 mg, 7.5% yield). ^{1}H NMR (400 MHz, $CDCl_3$) δ 6.66 – 6.55 (m, 3H), 4.05 (s, 6H), 3.64 (s, 185H), 3.47 (dd, J = 6.0, 4.0 Hz, 5H), 3.43 (s, 2H), 3.38 (s, 3H), 2.76 (t, J = 7.1 Hz, 2H), 1.65 (s, 6H). ^{19}F NMR (376 MHz, $CDCl_3$) δ -70.35. MALDI MS: $[M + Na]^+$ calculated for $C_{118}H_{201}F_{27}NaO_{51}$ = 2970.26; found: 2970.058.

*4.4B.17 Synthesis of "M2diDOPET/PFtB$_{TRI}$" (**4-15**)*

4-14 (52.8 mg, 0.017 mmol) was dissolved in DCM (7.4 mL). Trifluoro acetic acid (2.5 mL) was added followed by an addition of water (0.1 mL). The reaction was heated to reflux overnight. The next day, the solvent was concentrated under reduced pressure. The remaining residue was co-evaporated with toluene (2x) to remove the remaining solvent. The residue was once again redissolved in toluene. The mixture was passed through a 0.2 µm nylon filter. The filtrate was collected, concentrated under reduced pressure, and dried under high vacuum to give the product as a yellow solid (47.8 mg). This reaction was a test reaction where the starting material contained a mixture of M2PFtB$_{TRI}$ and M2diDOPET(acetonide)/ PFtB$_{TRI}$. Therefore, the yield could not be calculated. ^{1}H NMR (400 MHz, $CDCl_3$) observed a disappearance of a singlet peak at δ 1.65 which corresponded to the protons from acetonide. ^{19}F NMR (376 MHz, $CDCl_3$) δ -70.40 (from M2PFtB$_{TRI}$), -70.36 (from the product, M2diDOPET/PFtB$_{TRI}$). MALDI MS: $[M + Na]^+$ calculated for $C_{119}H_{205}F_{27}NaO_{53}$ = 3018.28 ; found: 3018.280.

4.4B.18 Synthesis of iron oxide nanoparticles

Iron-oleate complex was synthesized according to Park *et al.*[49] Iron oxide nanoparticles were prepared through thermal decomposition using iron-oleate complex according to Lu *et al.*[50] with some

modifications. Briefly, iron-oleate complex (0.9 g, 1 mmol) was weighed into a G30 microwave reaction vial. Oleyl alcohol (1.61 g, 6 mmol) was then added followed by 5 g of diphenyl ether. The mixture was stirred vigorously until dissolved. The reaction was flushed with Ar to keep an inert atmosphere before it was placed in a Monowave 300, Microwave Synthesis Reaction (Anton Paar, Austria). The reaction was heated to 200 °C within 15 min (10 °C/min) and immediately cooled down to 55 °C (without holding at high temperature). Acetone was then added to the reaction solution to precipitate the particles. The particles were separated out by centrifugation, the supernatant was removed, and the particles were dispersed in 10 mL hexane.

*4.4B.19 Ligand exchange of ESIONs with M2-NDA (**4-2**) and nitroDOPET-PFtB$_{TRI}$ (**4-7**)*

The ESIONs solution in hexane (20 µL) was added into a glass vial. The solvent was evaporated out and the residue was re-dispersed in 5 mL chloroform. NitroDOPET-PFtB$_{TRI}$ (**4-7**) was prepared as a solution in DMF at 10 mg/mL. **4-7** in DMF (500 µL, 5 mg) was added into a separate vial and the solvent was evaporated out. The compound was redissolved in 1 mL chloroform. M2-NDA (**4-2**, 2 mg) was separately dissolved in 1 mL chloroform. The ESION solution in chloroform was sonicated at 45 °C. While sonicating, the nitroDOPET-PFtB$_{TRI}$ solution in chloroform was added followed by the M2-NDA solution. The solution mixture was sonicated for 24 h. After 24 h, the solution mixture was removed and used directly for relaxation measurements.

4.4B.20 Synthesis of magnetic ionic liquid (MIL): [A336][FeCl$_4$]$_{0.73}$[Cl]$_{0.27}$

[A336][FeCl$_4$]$_{0.73}$[Cl]$_{0.27}$ was synthesized according to Kogelnic *et al*.[64] Briefly, $FeCl_3 \cdot 6H_2O$ (1.08 g, 3.98 mmol) was added into Aliquat®336 (1.77 g, 4.38 mmol). The reaction was stirred vigorously at room temperature for two days. After this time, the reaction mixture was washed with water (3x). The collected liquid was heated to remove the remaining solvent overnight and dried under high vacuum to give the product as a rust color viscous liquid (1.76 g, 78% yield).

4.4B.21 Preparation of PFPE + MIL solution

Samples were prepared at different concentrations of the MIL. Briefly, PFPE (60 µL) was mixed with 5, 10, 20, or 40 µL MIL which corresponds 0.0128, 0.024, 0.04 and 0.104 M MIL, respectively. The mixture was then dissolved in 500 µL acetone-d6 in a 2 mL glass vial and the solution was transferred to an NMR tube for the relaxation measurement. A sample without MIL was prepared as the above but without the MIL.

4.4B.22 T_1 and T_2 measurements

The ^{19}F relaxation parameters T_1 and T_2 of PFPE were measured on a Varian Unity-Inova 500 MHz (11.7 T) NMR spectrometer with the internal temperature maintained at 25 °C. The T_1 parameter was determined using an inversion recovery experiment acquired with 18 independent, quadratically spaced variable (tau) values covering a range up to 5 time the estimated T_1 value. The T_2 parameter was determined using a Carr–Purcell–Meiboom–Gill (CPMG) pulse sequence experiment acquired with 18 independent, quadratically spaced variable (tau) values covering a range up to 5 time the estimated T_2 value.

4.5 References

(1) Barres, A. R.; Lechuga, L. M.; Tangsangasaksri, M.; Ludwig, K. D.; Fain, S. B.; Mecozzi, S. A stable, highly concentrated fluorous nanoemulsion formulation for in vivo cancer imaging via ^{19}F-MRI. *Manuscript submitted for publication.* **2020**.

(2) Strijkers, G. J.; M. Mulder, W. J.; F. van Tilborg, G. A.; Nicolay, K. MRI Contrast Agents: Current Status and Future Perspectives. *Anti-Cancer Agents in Medicinal Chemistry- Anti-Cancer Agents)* **2007,** *7* (3), 291-305.

(3) Tirotta, I.; Dichiarante, V.; Pigliacelli, C.; Cavallo, G.; Terraneo, G.; Bombelli, F. B.; Metrangolo, P.; Resnati, G. ^{19}F Magnetic Resonance Imaging (MRI): from design of materials to clinical applications. *Chemical reviews* **2014,** *115* (2), 1106-1129.

(4) Pirogov, Y. A. Multinuclear Magnetic Resonance Imaging and NMR Spectroscopy in Biomedical Investigations. *Physics Procedia* **2016,** *82*, 3-7.

(5) Ramalho, M.; Ramalho, J.; Burke, L. M.; Semelka, R. C. Gadolinium Retention and Toxicity—An Update. *Advances in Chronic Kidney Disease* **2017,** *24* (3), 138-146.

(6) Rogosnitzky, M.; Branch, S. Gadolinium-based contrast agent toxicity: a review of known and proposed mechanisms. *BioMetals* **2016,** *29* (3), 365-376.

(7) Harvey, H. B.; Gowda, V.; Cheng, G. Gadolinium Deposition Disease: A New Risk Management Threat. *Journal of the American College of Radiology* **2020,** *17* (4), 546-550.

(8) Bober, Z.; Aebisher, D.; Ożóg, Ł.; Tabarkiewicz, J.; Tutka, P.; Bartusik-Aebisher, D. ^{19}F MRI As a tool for imaging drug delivery to tissue and individual cells. *European Journal of Clinical and Experimental Medicine* **2017,** *15*, 109-119.

(9) Ruiz-Cabello, J.; Barnett, B. P.; Bottomley, P. A.; Bulte, J. W. Fluorine (^{19}F) MRS and MRI in biomedicine. *NMR in Biomedicine* **2011,** *24* (2), 114-129.

(10) Bartusik, D.; Aebisher, D. ^{19}F applications in drug development and imaging–a review. *Biomedicine & Pharmacotherapy* **2014,** *68* (6), 813-817.

(11) Srinivas, M.; Heerschap, A.; Ahrens, E. T.; Figdor, C. G.; de Vries, I. J. M. ^{19}F MRI for quantitative in vivo cell tracking. *Trends in biotechnology* **2010,** *28* (7), 363-370.

(12) Darçot, E.; Colotti, R.; Pellegrin, M.; Wilson, A.; Siegert, S.; Bouzourene, K.; Yerly, J.; Mazzolai, L.; Stuber, M.; van Heeswijk, R. B. Towards Quantification of Inflammation in Atherosclerotic Plaque in the Clinic – Characterization and Optimization of Fluorine-19 MRI in Mice at 3 T. *Scientific Reports* **2019,** *9* (1), 17488.

(13) Peterson, K. L.; Srivastava, K.; Pierre, V. C. Fluorinated Paramagnetic Complexes: Sensitive and Responsive Probes for Magnetic Resonance Spectroscopy and Imaging. *Frontiers in Chemistry* **2018,** *6* (160).

(14) Kislukhin, A. A.; Xu, H.; Adams, S. R.; Narsinh, K. H.; Tsien, R. Y.; Ahrens, E. T. Paramagnetic fluorinated nanoemulsions for sensitive cellular fluorine-19 magnetic resonance imaging. *Nature materials* **2016,** *15* (6), 662-668.

(15) Jacoby, C.; Oerther, T.; Temme, S.; Schrader, J.; Flögel, U. Simultaneous ^{19}F MR imaging at different resonance frequencies using multi chemical shift selective RARE. In *International Society for Magnetic Resonance in Medicine*, 2014; p 2927.

(16) Flögel, U.; Ding, Z.; Hardung, H.; Jander, S.; Reichmann, G.; Jacoby, C.; Schubert, R.; Schrader, J. In vivo monitoring of inflammation after cardiac and cerebral ischemia by ^{19}F magnetic resonance imaging. *Circulation* **2008,** *118* (2), 140.

(17) Shin, S. H.; Park, E.-J.; Min, C.; Choi, S. I.; Jeon, S.; Kim, Y.-H.; Kim, D. Tracking perfluorocarbon nanoemulsion delivery by ^{19}F MRI for precise high intensity focused ultrasound tumor ablation. *Theranostics* **2017,** *7* (3), 562.

(18) Wang, Y.-G.; Kim, H.; Mun, S.; Kim, D.; Choi, Y. Indocyanine green-loaded perfluorocarbon nanoemulsions for bimodal ^{19}F-magnetic resonance/nearinfrared fluorescence imaging and subsequent phototherapy. *Quantitative imaging in medicine and surgery* **2013,** *3* (3), 132.

(19) Chime, S.; Kenechukwu, F.; Attama, A. Nanoemulsions—advances in formulation, characterization and applications in drug delivery. In *Application of Nanotechnology in Drug Delivery*, Sezer, A. D., Ed. IntechOpen: 2014.

(20) Pharmacopea, U. Globule size distribution in lipid injectable emulsions. *US Pharm. Rockv. MD US Pharm* **2011,** *1*, 297-299.

(21) Singh, Y.; Meher, J. G.; Raval, K.; Khan, F. A.; Chaurasia, M.; Jain, N. K.; Chourasia, M. K. Nanoemulsion: Concepts, development and applications in drug delivery. *Journal of Controlled Release* **2017,** *252*, 28-49.

(22) Kim, B. H.; Lee, N.; Kim, H.; An, K.; Park, Y. I.; Choi, Y.; Shin, K.; Lee, Y.; Kwon, S. G.; Na, H. B. Large-scale synthesis of uniform and extremely small-sized iron oxide nanoparticles for high-resolution T_1 magnetic resonance imaging contrast agents. *Journal of the American Chemical Society* **2011,** *133* (32), 12624-12631.

(23) Lee, N.; Yoo, D.; Ling, D.; Cho, M. H.; Hyeon, T.; Cheon, J. Iron oxide based nanoparticles for multimodal imaging and magnetoresponsive therapy. *Chemical Reviews* **2015,** *115* (19), 10637-10689.

(24) Barres, A. R.; Wimmer, M. R.; Mecozzi, S. Multicompartment theranostic nanoemulsions stabilized by a triphilic semifluorinated block copolymer. *Molecular pharmaceutics* **2017,** *14* (11), 3916-3926.

(25) Barres, A. R.; Molugu, S. K.; Stewart, P. L.; Mecozzi, S. Droplet Core Intermolecular Interactions and Block Copolymer Composition Heavily Influence Oil-In-Water Nanoemulsion Stability. *Langmuir* **2019,** *35* (39), 12765-12772.

(26) Gudbjartsson, H.; Patz, S. The Rician distribution of noisy MRI data. *Magnetic resonance in medicine* **1995,** *34* (6), 910-914.

(27) Jacoby, C.; Temme, S.; Mayenfels, F.; Benoit, N.; Krafft, M. P.; Schubert, R.; Schrader, J.; Flögel, U. Probing different perfluorocarbons for in vivo inflammation imaging by 19F MRI: image reconstruction, biological half-lives and sensitivity. *NMR in Biomedicine* **2014,** *27* (3), 261-271.

(28) Riess, J. G. Oxygen Carriers ("Blood Substitutes")Raison d'Etre, Chemistry, and Some Physiology Blut ist ein ganz besondrer Saft. *Chemical Reviews* **2001,** *101* (9), 2797-2920.

(29) Maeda, H. Macromolecular therapeutics in cancer treatment: the EPR effect and beyond. *Journal of Controlled Release* **2012,** *164* (2), 138-144.

(30) Maeda, H. Toward a full understanding of the EPR effect in primary and metastatic tumors as well as issues related to its heterogeneity. *Advanced drug delivery reviews* **2015,** *91*, 3-6.

(31) Klein, D. H.; Jones, R. C.; Keipert, P. E.; Luena, G. A.; Otto, S.; Weers, J. G. Intravascular behavior of perflubron emulsions. *Colloids and Surfaces A: Physicochemical and Engineering Aspects* **1994,** *84* (1), 89-95.

(32) Díaz-López, R.; Tsapis, N.; Fattal, E. Liquid Perfluorocarbons as Contrast Agents for Ultrasonography and 19F-MRI. *Pharmaceutical Research* **2009,** *27* (1), 1.

(33) Davis, K.; Qi, B.; Witmer, M.; Kitchens, C. L.; Powell, B. A.; Mefford, O. T. Quantitative measurement of ligand exchange on iron oxides via radiolabeled oleic acid. *Langmuir* **2014,** *30* (36), 10918-10925.

(34) Portet, D.; Denizot, B.; Rump, E.; Lejeune, J.-J.; Jallet, P. Nonpolymeric coatings of iron oxide colloids for biological use as magnetic resonance imaging contrast agents. *Journal of colloid and interface science* **2001,** *238* (1), 37-42.

(35) Davis, K.; Cole, B.; Ghelardini, M.; Powell, B. A.; Mefford, O. T. Quantitative measurement of ligand exchange with small-molecule ligands on iron oxide nanoparticles via radioanalytical techniques. *Langmuir* **2016,** *32* (51), 13716-13727.

(36) Li, F.; Liang, Z.; Liu, J.; Sun, J.; Hu, X.; Zhao, M.; Liu, J.; Bai, R.; Kim, D.; Sun, X. Dynamically Reversible Iron Oxide Nanoparticle Assemblies for Targeted Amplification of T1-Weighted Magnetic Resonance Imaging of Tumors. *Nano letters* **2019**.

(37) Sun, L.; Huang, C.; Gong, T.; Zhou, S. A biocompatible approach to surface modification: Biodegradable polymer functionalized super-paramagnetic iron oxide nanoparticles. *Materials Science and Engineering: C* **2010,** *30* (4), 583-589.

(38) Huang, G.; Zhang, C.; Li, S.; Khemtong, C.; Yang, S.-G.; Tian, R.; Minna, J. D.; Brown, K. C.; Gao, J. A novel strategy for surface modification of superparamagnetic iron oxide nanoparticles for lung cancer imaging. *Journal of materials chemistry* **2009,** *19* (35), 6367-6372.

(39) Lu, C.; Bhatt, L. R.; Jun, H. Y.; Park, S. H.; Chai, K. Y. Carboxyl–polyethylene glycol–phosphoric acid: a ligand for highly stabilized iron oxide nanoparticles. *Journal of Materials Chemistry* **2012,** *22* (37), 19806-19811.

(40) Amstad, E.; Gillich, T.; Bilecka, I.; Textor, M.; Reimhult, E. Ultrastable iron oxide nanoparticle colloidal suspensions using dispersants with catechol-derived anchor groups. *Nano letters* **2009,** *9* (12), 4042-4048.

(41) Bixner, O.; Lassenberger, A.; Baurecht, D.; Reimhult, E. Complete exchange of the hydrophobic dispersant shell on monodisperse superparamagnetic iron oxide nanoparticles. *Langmuir* **2015,** *31* (33), 9198-9204.

(42) Lassenberger, A.; Bixner, O.; Gruenewald, T.; Lichtenegger, H.; Zirbs, R.; Reimhult, E. Evaluation of high-yield purification methods on monodisperse PEG-grafted iron oxide nanoparticles. *Langmuir* **2016,** *32* (17), 4259-4269.

(43) Na, H. B.; Lee, I. S.; Seo, H.; Park, Y. I.; Lee, J. H.; Kim, S.-W.; Hyeon, T. Versatile PEG-derivatized phosphine oxide ligands for water-dispersible metal oxide nanocrystals. *Chemical communications* **2007,** (48), 5167-5169.

(44) Tromsdorf, U. I.; Bruns, O. T.; Salmen, S. C.; Beisiegel, U.; Weller, H. A highly effective, nontoxic T_1 MR contrast agent based on ultrasmall PEGylated iron oxide nanoparticles. *Nano letters* **2009,** *9* (12), 4434-4440.

(45) Harris, J. M.; Kozlowski, A. Poly (ethylene glycol) and related polymers monosubstituted with propionic or butanoic acids and functional derivatives thereof for biotechnical applications. US Patent 5,672,662, **1997**.

(46) Gambacorta, A.; Tofani, D.; Bernini, R.; Migliorini, A. High-yielding preparation of a stable precursor of hydroxytyrosol by total synthesis and from the natural glycoside oleuropein. *Journal of agricultural and food chemistry* **2007,** *55* (9), 3386-3391.

(47) Decato, S.; Bemis, T.; Madsen, E.; Mecozzi, S. Synthesis and characterization of perfluoro-tert-butyl semifluorinated amphiphilic polymers and their potential application in hydrophobic drug delivery. *Polymer chemistry* **2014,** *5* (22), 6461-6471.

(48) Demirer, G. S.; Okur, A. C.; Kizilel, S. Synthesis and design of biologically inspired biocompatible iron oxide nanoparticles for biomedical applications. *Journal of Materials Chemistry B* **2015,** *3* (40), 7831-7849.

(49) Park, J.; An, K.; Hwang, Y.; Park, J.-G.; Noh, H.-J.; Kim, J.-Y.; Park, J.-H.; Hwang, N.-M.; Hyeon, T. Ultra-large-scale syntheses of monodisperse nanocrystals. *Nature materials* **2004,** *3* (12), 891-895.

(50) Lu, Y.; Xu, Y.-J.; Zhang, G.-b.; Ling, D.; Wang, M.-q.; Zhou, Y.; Wu, Y.-D.; Wu, T.; Hackett, M. J.; Kim, B. H. Iron oxide nanoclusters for T_1 magnetic resonance imaging of non-human primates. *Nature Biomedical Engineering* **2017,** *1* (8), 637.

(51) Juaristi, E.; Antúnez, S. Conformational analysis of 5-substituted 1,3-dioxanes. 6. Study of the attractive gauche effect in O-C-C-O segments. *Tetrahedron* **1992,** *48* (29), 5941-5950.

(52) Tucker, W. B.; McCoy, A. M.; Fix, S. M.; Stagg, M. F.; Murphy, M. M.; Mecozzi, S. Synthesis, physicochemical characterization, and self-assembly of linear, dibranched, and miktoarm semifluorinated triphilic polymers. *Journal of Polymer Science Part A: Polymer Chemistry* **2014,** *52* (23), 3324-3336.

(53) Peng, Q.; Li, Y.; Bo, S.; Yuan, Y.; Yang, Z.; Chen, S.; Zhou, X.; Jiang, Z.-X. Paramagnetic nanoemulsions with unified signals for sensitive ^{19}F MRI cell tracking. *Chemical communications* **2018,** *54* (47), 6000-6003.

(54) Jahromi, A. H.; Wang, C.; Adams, S. R.; Zhu, W.; Narsinh, K.; Xu, H.; Gray, D. L.; Tsien, R. Y.; Ahrens, E. T. Fluorous-Soluble Metal Chelate for Sensitive Fluorine-19 Magnetic Resonance Imaging Nanoemulsion Probes. *ACS nano* **2018,** *13* (1), 143-151.

(55) Ventura, S. P. M.; e Silva, F. A.; Quental, M. V.; Mondal, D.; Freire, M. G.; Coutinho, J. A. P. Ionic-Liquid-Mediated Extraction and Separation Processes for Bioactive Compounds: Past, Present, and Future Trends. *Chemical Reviews* **2017,** *117* (10), 6984-7052.

(56) Dai, Z.; Noble, R. D.; Gin, D. L.; Zhang, X.; Deng, L. Combination of ionic liquids with membrane technology: A new approach for CO_2 separation. *Journal of Membrane Science* **2016,** *497*, 1-20.

(57) Xun, S.; Zhu, W.; Chang, Y.; Li, H.; Zhang, M.; Jiang, W.; Zheng, D.; Qin, Y.; Li, H. Synthesis of supported SiW12O40-based ionic liquid catalyst induced solvent-free oxidative deep-desulfurization of fuels. *Chemical Engineering Journal* **2016,** *288*, 608-617.

(58) Bobbink, F. D.; Dyson, P. J. Synthesis of carbonates and related compounds incorporating CO_2 using ionic liquid-type catalysts: State-of-the-art and beyond. *Journal of Catalysis* **2016,** *343*, 52-61.

(59) Ehsani, A.; Mohammad Shiri, H.; Kowsari, E.; Safari, R.; Torabian, J.; Hajghani, S. High performance electrochemical pseudocapacitors from ionic liquid assisted electrochemically synthesized p-type conductive polymer. *Journal of Colloid and Interface Science* **2017,** *490*, 91-96.

(60) Abo-Hamad, A.; AlSaadi, M. A.; Hayyan, M.; Juneidi, I.; Hashim, M. A. Ionic Liquid-Carbon Nanomaterial Hybrids for Electrochemical Sensor Applications: a Review. *Electrochim. Acta* **2016,** *193*, 321-343.

(61) Monti, D.; Egiziano, E.; Burgalassi, S.; Chetoni, P.; Chiappe, C.; Sanzone, A.; Tampucci, S. Ionic liquids as potential enhancers for transdermal drug delivery. *International Journal of Pharmaceutics* **2017,** *516* (1), 45-51.

(62) Moniruzzaman, M.; Tahara, Y.; Tamura, M.; Kamiya, N.; Goto, M. Ionic liquid-assisted transdermal delivery of sparingly soluble drugs. *Chemical communications* **2010,** *46* (9), 1452-1454.

(63) Esson, M. M.; Mecozzi, S. Preparation, Characterization, and Formulation Optimization of Ionic-Liquid-in-Water Nanoemulsions toward Systemic Delivery of Amphotericin B. *Molecular Pharmaceutics* **2020,** *17* (6), 2221-2226.

(64) Kogelnig, D.; Stojanovic, A.; v.d. Kammer, F.; Terzieff, P.; Galanski, M.; Jirsa, F.; Krachler, R.; Hofmann, T.; Keppler, B. K. Tetrachloroferrate containing ionic liquids: Magnetic- and aggregation behavior. *Inorganic Chemistry Commuication.* **2010,** *13* (12), 1485-1488.

(65) Taboada, E.; Rodriguez, E.; Roig, A.; Oro, J.; Roch, A.; Muller, R. N. New ultrasmall iron-oxide nanoparticles with high magnetisation as potential T_1-MRI contrast agents for molecular imaging. *arXiv preprint cond-mat/0611243* **2006**.

(66) Cho, S.-J.; Jarrett, B. R.; Louie, A. Y.; Kauzlarich, S. M. Gold-coated iron nanoparticles: a novel magnetic resonance agent for T_1 and T_2 weighted imaging. *Nanotechnology* **2006,** *17* (3), 640.

(67) Hu, F.; Jia, Q.; Li, Y.; Gao, M. Facile synthesis of ultrasmall PEGylated iron oxide nanoparticles for dual-contrast T_1-and T_2-weighted magnetic resonance imaging. *Nanotechnology* **2011,** *22* (24), 245604.

CHAPTER 5 – CONCLUSIONS

5.1 Primary findings and conclusions

This thesis research was built upon the Mecozzi semifluorinated polymer, M2H10PFtB$_{TRI}$. M2H10PFtB$_{TRI}$ possesses the PFtB$_{TRI}$ (tri-perfluoro-*tert*-butyl) structure, as a novel fluorous block, which was used to improve the stability of micelles. PFtB$_{TRI}$ has 27 chemically symmetrical fluorine atoms that provide an advantage as a potential fluorinated probe for ^{19}F MRI applications. M2H10PFtB$_{TRI}$ micelles demonstrate a high encapsulation efficiency as well as a high stability *in vivo* with a longer circulation half-life than normal PEG-hydrocarbon block copolymers (unpublished results, Chapter 3, Sarah Decato Ph.D. Thesis, 2015). To further improve the targeting properties of M2H10PFtB$_{TRI}$ micelles, internalizing RGD (iRGD), an active targeting ligand, was conjugated to the polymer. The conjugation of iRGD to the polymer resulted in an enhanced accumulation and penetration of the micelles into tumor cells *in vitro* as demonstrated in 2D and 3D cultured cells. Paclitaxel (PTX), a hydrophobic anticancer drug, was successfully encapsulated inside these micelles. The PTX-loaded iRGD micelles showed an enhanced PTX's efficacy, compared to the free PTX or PTX-loaded non-modified micelles (without a targeting ligand). In addition, with a focus on the micelle preparation, different architectures of semifluorinated polymers were designed to study the impact of the architectures on micelle stabilities, drug encapsulation, *in vitro* time release, and *in vitro* cytotoxicity. The dibranched architecture showed a prolonged release of PTX, compared to the linear counterparts, and the introduction of the fluorocarbon block led to a reduced cellular toxicity. Additionally, as noted before, fluorinated materials can also serve as the fluorine sources for ^{19}F MRI. Preparation of the nanoemulsion with our novel semifluorinated M2F8H18 polymer allowed for the incorporation of an unprecedented amount of PFCE. This large amount of encapsulated PFCE led to a high ^{19}F sensitivity due to the immense density of fluorine atoms in the nanoemulsion formulation. Furthermore, the improved ^{19}F sensitivity was accomplished through an integration of paramagnetic Fe^{3+}. For the first time in the Mecozzi group, we incorporated extremely small-sized iron oxide nanoparticles (ESIONs) with our novel PFtB$_{TRI}$ molecules through a ligand exchange method. Preliminary results showed that PFtB$_{TRI}$ decorated ESIONs led to a reduced T_1 relaxation, suggesting an improvement of the ^{19}F

sensitivity. Finally, paramagnetic Fe^{3+} was also incorporated with perfluoropolyether (PFPE) in the form of the magnetic ionic liquids (MILs). Preliminary results demonstrated the improved ^{19}F sensitivity with an Fe^{3+} concentration-dependent effect. These promising results suggest potential strategies for incorporating Fe^{3+} into the fluorinated imaging agent for improving ^{19}F sensitivity.

5.1.1 Development of iRGD conjugated semifluorinated nanoassemblies for targeted drug delivery

The novel semifluorinated polymer with a branched fluorous $PFtB_{TRI}$ segment was synthesized to possess a maleimide functional group, PMPI-P2H10$PFtB_{TRI}$. The addition of the maleimide functional group enables further functionalization of the polymer with the targeting ligand. An internalizing RGD (iRGD), a cyclic peptide containing a free thiol moiety (-SH), was conjugated to the polymer through a thiol-maleimide coupling reaction, producing the iRGD-PMPI-P2H10$PFtB_{TRI}$ polymer in high yield. iRGD was used as an active targeting ligand for improving accumulation and penetration of the particles. iRGD binds to α_v integrins which are overexpressed on the tumor endothelial and tumor cells, allowing for an improved accumulation of nanoparticles at the tumor. iRGD undergoes a subsequent cleavage exposing a CendR motif that targets the neuropilin-1 (NRP-1) receptor, leading to deep penetration of the nanoparticles through the transcytosis pathway initiated by NRP-1. The micelles prepared from iRGD-conjugated polymers have a size similar to non-modified micelles (0% iRGD), regardless of the iRGD concentration (5, 10, and 20%). This suggests that the introduction of iRGD did not alter the physical properties of the particles. The iRGD concentration of the micelles was optimized through *in vitro* cell studies. The cellular uptake and tumor spheroid penetration studies revealed a significantly improved cellular uptake and spheroid penetration from the 20% iRGD-conjugated micelles. This optimized formulation was further evaluated for *in vitro* cytotoxicity with PTX. PTX was successfully encapsulated in 20% iRGD-conjugated micelles. The PTX efficacy was evaluated in 4T1-Luc, a murine breast carcinoma, cells. The results revealed improved PTX efficacy toward the cancer cells from the PTX-loaded 20% iRGD formulation, compared to PTX-loaded non-modified micelles and free PTX, due to the enhanced accumulation and penetration properties of the functionalized micelles. This demonstrates the synergistic potential of the

multifunctional micelle design and suggests the potential of our formulation as a promising vehicle for a drug delivery system.

5.1.2 A study of the effect of different semifluorinated polymer architectures on self-assembled nanoparticles

The dibranched semifluorinated triblock copolymers were synthesized. These dibranched triblock copolymers were designed to have a middle fluorocarbon block denoted as an ACB structure where A is hydrophilic, B is lipophilic, and C is fluorophilic. We have previously reported the syntheses of the dibranched triblock copolymers with ABC structure (with a terminal fluorocarbon block) where the dibranched fluorinated alcohol, HO-BC, was first synthesized and further coupled with the hydrophilic segment (A) to produce ABC triblock copolymer. However, the synthesis of the ACB triblock copolymer from the dibranched fluorinated alcohol, HO-CB, resulted in a very low yield of the final product (less than 5%). This is due to the instability and/or the non-reactivity of the corresponding dibranched fluorinated alcohol. Therefore, the synthesis of the dibranched semifluorinated triblock copolymer was pursued through a coupling reaction of the linear alcohol, which has a higher reactivity, to the branched PEG. Two different dibranched semifluorinated triblock copolymers were successfully synthesized: a symmetric, M2diF8H18, and an asymmetric, M2diF8H18/F8, triblock copolymers. The introduction of a fluorocarbon in the ACB architecture led to the formation of a fluorous shell in a corona-shell-core micelle structure which bestows the aggregates with different physicochemical properties, depending on the polymer architecture. The physicochemical properties of the polymers were characterized and compared to the linear triblock (M2F8H18), the linear diblock (M2H18), and the dibranched diblock ($mPEG_{2K}$-DSG) copolymers. The presence of the dibranched architecture in the diblock and triblock copolymers led to a formation of the aggregates with a smaller aggregation number and microviscosity than their linear counterparts. The introduction of the fluorocarbon block in the linear triblock copolymers provided the corresponding aggregates with a compact core and tight packing. Due to the rigidity and higher volume of the fluorocarbons, a loose aggregate was formed from the symmetric dibranched copolymer. Interestingly,

despite the two fluorocarbon blocks in the structure, the asymmetric dibranched architecture shares similar properties to the corresponding polymer without the fluorocarbon block ($mPEG_{2K}$-DSG). All polymers aggregated as micelles in aqueous solution and could encapsulate PTX. As PTX is only solubilized in the hydrocarbon segment, the encapsulation efficiency of PTX in polymeric micelles solely depends on the hydrocarbon capacity of the corresponding micelles. High retention of PTX inside the polymeric micelles was observed in M2diF8H18 and $mPEG_{2K}$-DSG after one week. These polymers have a dibranched structure with two H18 chains, suggesting a stronger hydrophobic core than the other polymers. The *in vitro* time release profiles showed that the dibranched structures demonstrated a prolonged release due to the better sealing of the drug in the micellar hydrophobic core through the intermediate extended fluorous shell. In addition, *in vitro* cytotoxicity studies revealed that the fluorous shell in the micellar structures considerably reduced the cellular toxicity of the polymers. This result suggests that the addition of a fluorocarbon block leads to the improved biocompatibility of the polymers. Based on these promising results, looking into different polymer architecture designs would be a valuable next step to discover new biomaterials for drug delivery system.

5.1.3 Development of fluorinated nanoassemblies as new imaging agents for ^{19}F MRI

5.1.3.1 Part A: Incorporation of high PFCE concentration in nanoemulsions for MR imaging

The first strategy for improving sensitivity of ^{19}F MRI is through the introduction of high-density fluorine atoms to the desired imaging area. This was accomplished through the preparation of a highly concentrated PFCE nanoemulsion. The PFCE nanoemulsion, containing 35% v/v PFCE, was prepared using the Mecozzi novel semifluorinated M2F8H18 polymer by a two-step high energy input method. The size of the nanoemulsion was around 200 nm as measured by dynamic light scattering (DLS). The size of the nanoemulsion was well below the 500 nm cutoff according to USP <729> for its usage in biomedical application to avoid pulmonary embolism. In addition, this size range also enables a passive tumor targeting process through the enhanced permeability and retention (EPR) effect. The PFCE nanoemulsion demonstrated a long-term stability at the 4 °C storage condition for more than 300 days. In addition, the

storage of the nanoemulsion at elevated temperatures, (25 and 37 °C), and at 37 °C with fetal bovine serum (FBS) and cell culture media showed negligible particle size change and no phase separation for a minimum of three weeks and one week, respectively. These results suggest an extremely stable PFCE nanoemulsion formulation. An *in vitro* cytotoxicity study of the PFCE nanoemulsion against 4T1-Luc cells showed minute toxicity up to 20 mg/mL PFCE concentration. *In vitro* MR phantom images of the PFCE nanoemulsions were acquired at 4.7 T. The phantom images revealed a high ^{19}F signal to noise ratio (SNR) with a concentration-dependent relationship. The *in vivo* studies were performed with 4T1-Luc tumor-bearing mice. The concentrated PFCE nanoemulsion (35% v/v PFCE) was intravenously injected through the tail vein. No signs of toxicity were observed after the injection and during the 14-day study period. At 6 h post injection, ^{19}F signal was detected in all major organs including the tumor. The observed ^{19}F intensity in the tumor was the highest on day 1 post injection, suggesting a slow passive tumor targeting of the PFCE nanoemulsion through the EPR effect. The ^{19}F signal in the tumor was retained for up to two weeks, suggesting the capability for multiple imaging sessions after one injection. The high ^{19}F signal intensity in the liver and spleen indicated a high accumulation of the nanoemulsion in the reticuloendothelial system (RES) organs. The particles were observed in the bloodstream after 6 h and were cleared from the bloodstream within the first day. The high ^{19}F signal in the RES organs suggests that the majority of the PFCE nanoemulsion was taken up by monocytes and macrophages. Since these monocytes and macrophages are located in the RES organs, the particles taken up by those cells were brought to the liver and spleen, resulting in high ^{19}F intensity. Furthermore, over the course of 14-days, only a slight decrease of ^{19}F signal was observed in the liver and spleen, suggesting a long biological half-life of PFCE. These results suggest that our PFCE nanoemulsion formulation can be used as a powerful imaging tool for tumor diagnosis and long-term monitoring of tumor as well as in cell labeling for cell tracking application.

5.1.3.2 Part B: Improving ^{19}F sensitivity by decreasing T_1 relaxation

The second strategy focuses on decreasing the intrinsically high T_1 relaxation of fluorine to increase its signal sensitivity. The high T_1 relaxation was reduced by using a paramagnetic metal ion, Fe^{3+}. Fe^{3+} was introduced as a part of the imaging agents in two different forms: i) extremely small-sized iron oxide nanoparticles (ESIONs) and ii) magnetic ionic liquids (MILs). Even though iron oxide nanoparticles are typically used as T_2 agents, the small iron oxide core of ESIONs allows its usage as a T_1 agent. To prepare the fluorinated imaging agent with ESIONs, the fluorocarbons were conjugated on to the surface of ESIONs. A nitrocatechol group was selected as a binding ligand due to its high affinity towards the iron oxide surface. We have successfully introduced the nitrocatechol group to $mPEG_{2K}$ (molecular weight of 2,000) and $PFtB_{TRI}$ to give M2-NDA and nitroDOPET-$PFtB_{TRI}$, respectively. We selected $PFtB_{TRI}$ due to its 27 chemically equivalent fluorine atoms that give rise to one strong ^{19}F signal. ESIONs were successfully synthesized through a thermal decomposition method, producing iron oxide nanoparticles with a hydrodynamic diameter of 4.7 ± 0.3 nm. M2-NDA and nitroDOPET-$PFtB_{TRI}$ were attached on the surface of ESION through a ligand exchanged method. The T_1 and T_2 relaxations of the decorated ESIONs were determined using ^{19}F NMR. Our preliminary results revealed that the T_1 relaxation of $PFtB_{TRI}$/PEG-decorated ESIONs was reduced compared to free $PFtB_{TRI}$-OH without Fe^{3+}. This promising result suggests the positive effect of ESIONs on the relaxation of fluorine. However, the $PFtB_{TRI}$/PEG-decorated ESIONs showed a low water solubility. This was due to the competitive binding of M2-NDA and nitroDOPET-$PFtB_{TRI}$ to the iron oxide surface. Therefore, a new molecule, M2diDOPET/$PFtB_{TRI}$, was designed based on the dibranched structure to contain mPEG as the hydrophilic segment, $PFtB_{TRI}$ as the fluorine source, and catechol as the binding ligand. The synthesis of M2diDOPET/$PFtB_{TRI}$ was successfully carried out with a low yield. The final product was confirmed by MALDI MS. The optimization for different reaction conditions to improve the final product's yield and further addition of a nitro group to enhance the binding affinity are currently being pursued.

For the introduction of Fe^{3+} through the use of MILs, we have successfully synthesized a hydrophobic MIL containing Fe^{3+}, $[A336][FeCl_4]_{0.73}[Cl]_{0.27}$. The effect of the MIL on PFPE was evaluated by dissolving MIL and PFPE in acetone and measuring the relaxations through ^{19}F NMR. Preliminary results showed the reduced T_1 relaxation with increasing Fe^{3+} concentration, suggesting a concentration-dependent effect. This promising result was followed by the preparation of nanoemulsion composed of the MIL and PFPE. However, due to the low hydrophobicity of the MIL, it could not be incorporated as the oil phase due to its miscibility with water at the concentration used for nanoemulsion preparation. Therefore, a new MIL designed with an improved hydrophobicity is needed. We are currently working on designing a new MIL that contains fluorine, a so-called fluorinated magnetic ionic liquid (FMIL). We expect that the presence of fluorine will increase the overall hydrophobicity of the ionic liquid as well as introducing the fluorophilicity properties for better miscibility with PFPE.

5.2 Final remarks

Semifluorinated polymers represent an ideal biomaterial used in biomedical applications, especially for therapeutic and diagnostic purposes due to their unique properties. For the therapeutic purpose, the presence of a fluorocarbon block in the semifluorinated triblock copolymer has been shown to improve the physicochemical properties of the corresponding aggregates. Typical orientations of the triblock copolymers are ABC or ACB structure, with the fluorocarbon block as the terminal and the middle block, respectively. The semifluorinated polymers self-assemble in aqueous solution forming micelles where the polymer architectures control the properties of these micelles. Delivery of hydrophobic molecules was achieved through the presence of the hydrocarbon block in the copolymer, where the encapsulation efficiency solely depended on the hydrophobic moiety. In addition, the biocompatibility of the polymer was improved with the addition of the fluorocarbon block. For the diagnostic purposes, the preparation of a nanoemulsion using the semifluorinated triblock copolymer, M2F8H18, allowed for the encapsulation of a large quantity of the fluorocarbon oil (PFCE). The PFCE nanoemulsion demonstrated a high particle

stability both in storage conditions (4 °C) and *in vivo* and provided a high biocompatibility *in vivo*. With PFCE as exogenous fluorine source, this PFCE nanoemulsion allowed for the delivery of highly concentrated fluorinated molecules, resulting in the improved signal intensity for ^{19}F MRI applications. Furthermore, the semifluorinated polymer itself can act as the fluorine source which was demonstrated through the use of $PFtB_{TRI}$-containing semifluorinated polymers in ^{19}F MRI applications.

APPENDIX 1 – INTRODUCTION OF PHOSPHORIC ACID FUNCTIONALITY TO PEG AND $PFTB_{TRI}$-OH

A1.1 Introduction

Phosphoric acid was first selected as a binding ligand for iron oxide surfaces. The coupling of phosphoric acid to PEG and $PFtB_{TRI}$ was performed separately.

A1.2 Results and Discussion

A1.2.1 Synthesis of mPEG-PO_3H_2

mPEG-PO_3H_2 was synthesized according to Tromsdorf *et al.*[1] Methoxy-capped poly(ethylene glycol) with various molecular weights of 1,000, 2,000, and 5,000 g/mol were phosphorylated with $POCl_3$ to give **A1-1 (Scheme A1.1**). This reaction was proceeded with high yield and no further purification was performed.

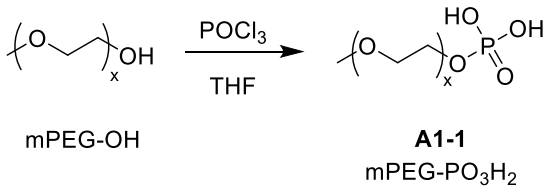

mPEG-OH **A1-1** mPEG-PO_3H_2

Scheme A1.1 Synthesis of mPEG-PO_3H_2.

A1.2.2 Synthesis of $PFtB_{TRI}$ phosphoric acid

We first attempted the synthesis of $PFtB_{TRI}$ phosphoric acid using a similar synthetic protocol as above. $PFtB_{TRI}$-OH was phosphorylated with $POCl_3$ in the presence of triethylamine (TEA) in an equimolar amount to $POCl_3$ (**Scheme A1.2**). The phosphorylation product was characterized by ESI MS. The result revealed the mixture of the mono- and di-substituted $PFtB_{TRI}$ products. This reaction was further optimized to maximize the product formation by varying the ratio of $POCl_3$ and TEA to the $PFtB_{TRI}$-OH. However, no pure product could be prepared. The maximum mono- to di-substitution we could achieve was 2:1 using 1.5 equivalent of $POCl_3$ and TEA to $PFtB_{TRI}$-OH. Due to the difficulty in separating the two products, we decided to pursue a different synthetic route.

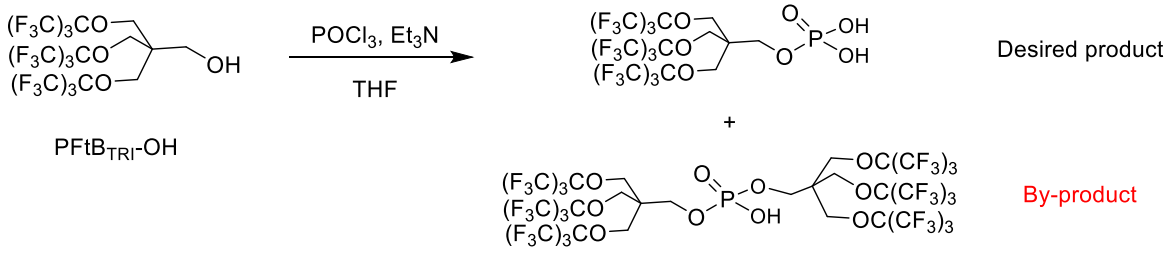

Scheme A1.2 Synthesis of $PFtB_{TRI}$ phosphoric acid using $POCl_3$.

The second phosphorylation reaction used the *o*-xylenyl phosphoryl chloride (*o*-XPCL) as the phosphorylating agent. *o*-XPCl was synthesized according to Murray *et al*.[2] Phosphorylation of $PFtB_{TRI}$-OH with *o*-XPCl was carried out in the presence of pyridine-*N*-oxide as an oxidizing agent and TEA as a base. However, no product was observed from ESI MS. Changing the reaction conditions by heating up the reaction or changing the base from TEA to DBU (1,8-Diazabicyclo[5.4.0]undec-7-ene) did not lead to the product formation (**Scheme A1.3**).

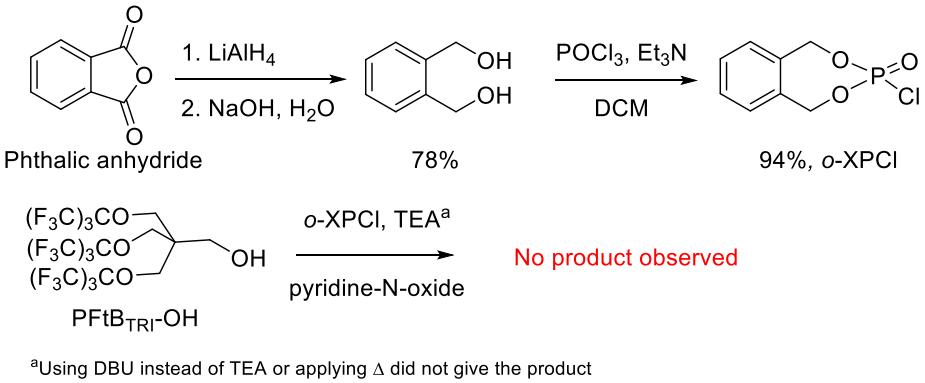

Scheme A1.3 Synthesis of $PFtB_{TRI}$ phosphoric acid using *o*-XPCl.

The third phosphorylation reaction was investigated using diphenyl phosphoryl chloride (DPPCl). With two phenyl protecting groups in DPPCl, the problem with di-substituted product could be eliminated. $PFtB_{TRI}$-OH was successfully phosphorylated with DPPCl under basic conditions to give **A1-2** (**Scheme**

A1.4). Compound **A1-2** was purified by an automated chromatography to give the pure isolated product in high yield.

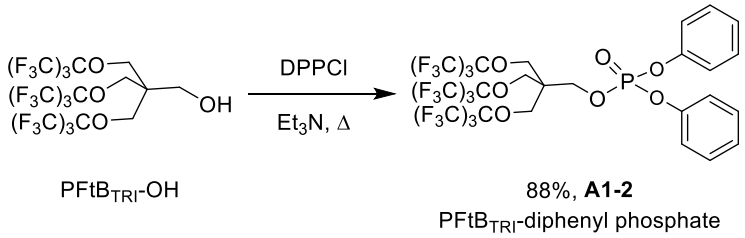

Scheme A1.4 Synthesis of PFtB$_{TRI}$-diphenyl phosphate.

The two phenyl groups were further deprotected under different conditions as summarized in **Table A1.1**. The phenyl groups in PFtB$_{TRI}$-diphenyl phosphate could not be removed through the acid hydrolysis. Even though the heat was applied to the reaction, only the starting material (diphenyl phosphate product) was recovered from the reaction. We further deprotected the two phenyl groups through the hydrogenation reaction using platinum oxide (PtO_2) or palladium on carbon (Pd/C) as a catalyst. Only one phenyl group was deprotected from **A1-2** under the acidic conditions with PtO_2 or the basic conditions with Pd/C. Even though one phenyl group was removed, further deprotection using the same condition did not result in the removal of the remaining phenyl group. The deprotection of phenyl groups through a basis hydrolysis was also investigated. The reaction using NaOH in THF resulted in a deprotection of only one phenyl group. Interestingly, when the solvent was changed from THF to MeOH, the remaining phenyl group was substituted with a methyl group, yielding PFtB$_{TRI}$-monomethyl phosphate as the reaction product. Similarly, when a stronger base, a sodium methoxide (CH_3ONa), was used, the PFtB$_{TRI}$-monomethyl phosphate was also observed from the reaction. Given all the reaction conditions we have tried, none of the conditions could provide the PFtB$_{TRI}$ phosphate as the final product. Therefore, we decided to synthesize PFtB$_{TRI}$-monophenyl phosphate, **A1-3**, as the intermediate (**Scheme A1.5**) and further optimized the deprotection of the remaining phenyl group.

Table A1.1 Deprotection reaction summary.

Starting material	Deprotection condition	Result
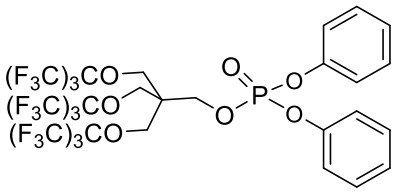 PFtB$_{TRI}$-diphenyl phosphate	Acetic acid, HCl, Δ	No reaction
	TFA, HCl, Δ	No reaction
	PtO_2, H_2, MeOH	No reaction
	PtO_2, H_2, acetic acid	Mixture of PFtB$_{TRI}$ phosphate and PFtB$_{TRI}$-monophenyl phosphate[a]
	Pd/C, TEA, Δ, MeOH	PFtB$_{TRI}$-monophenyl phosphate
	NaOH, Δ, THF	PFtB$_{TRI}$-monophenyl phosphate
	NaOH, Δ, MeOH	PFtB$_{TRI}$-monomethyl phosphate with PFtB$_{TRI}$-OH
	CH_3ONa, MeOH, Δ	PFtB$_{TRI}$-monomethyl phosphate
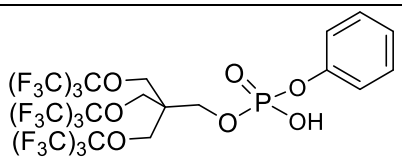 PFtB$_{TRI}$-monophenyl phosphate	PtO_2, H_2, TFA/acetic acid	No observed ^{31}P signal
	NaOH, Δ, THF or TBA	No reaction
	CH_3ONa, MeOH, Δ	PFtB$_{TRI}$-monomethyl phosphate

[a] A consistent result could not be achieved with this reaction condition.

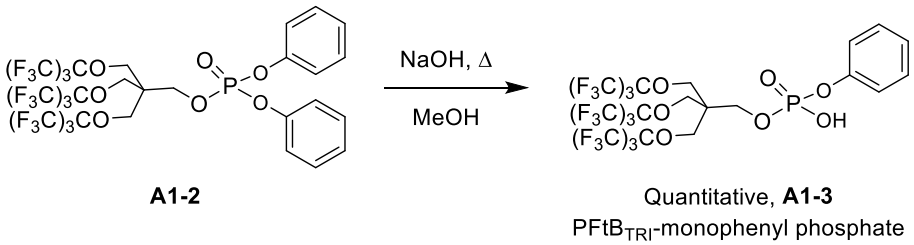

Scheme A1.5 Synthesis of PFtB$_{TRI}$-monophenyl phosphate.

The deprotection of the remaining phenyl group using PFtB$_{TRI}$-monophenyl phosphate as the starting material was carried out as shown in **Table A1.1**. The hydrogenation in the presence of PtO_2 in acidic conditions led to the cleavage of the phenyl group as no benzyl protons was observed from the product's ^1H NMR. However, the ^{31}P NMR did not show any signal, suggesting that the PFtB$_{TRI}$ phosphate could not be successfully prepared. In addition, a basic hydrolysis was also investigated as an alternative

route for the deprotection of the phenyl group where NaOH was used as a base in THF or TBA. Unfortunately, the NMR of the product from the reaction showed only the presence of the starting material. It should be noted that, the basic hydrolysis with a stronger base, CH_3ONa, led to a formation of $PFtB_{TRI}$-monomethyl phosphate. This suggests that the substitution reaction of phenyl with methyl group was favorable over the hydrolysis reaction.

Table A1.2 A summary of phosphorylating agents used in synthesizing $PFtB_{TRI}$ phosphoric acid.

Compound	Structure	Problem(s)
Phosphoryl chloride	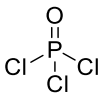	• Products contain both mono- and di-substituted $PFtB_{TRI}$ phosphate. • Difficult purification of mono- and di-substituted products.
o-xylenyl phosphoryl chloride (*o*-XPCL)	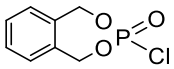	• No reaction occurred.
Diphenyl phosphoryl chloride (DPPCl)	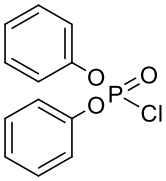	• Difficult deprotection of the diphenyl groups. • Only achieved $PFtB_{TRI}$-monophenyl phosphate product. • Deprotection of monophenyl product could not be performed.

A1.3 Conclusions

We have successfully synthesized mPEG-PO_3H_2 through the phosphorylation reaction using $POCl_3$. The synthesis of $PFtB_{TRI}$ phosphate was also pursued. Different phosphorylating agents were used to introduce the phosphate group to the fluorocarbon. **Table A1.2** summarizes problems for each phosphorylation reaction. Due to the difficulty in achieving the final product, we decided not to pursue the synthesis of this molecule. A new binding ligand was proposed which was presented in *Chapter 4*.

A1.4 Experimental

*A1.4.1 Synthesis of methoxy poly(ethylene glycol) phosphoric acid (M2-PO_3H_2, **A1-1**)*

Phosphorylation was proceeded according to Tromsdorf *et al.*[1] with some modification. Briefly, $mPEG_{2k}$-OH (2 g, 0.95 mmol) was weighed into a dry round bottom flask. The flask was heated to 80 °C under high vacuum to degass PEG for 1 h. After this time, the flask was cooled down to room temperature and 5 mL dry THF was wadded under Ar. The solution was then cooled with an ice bath. $POCl_3$ (98 µL, 1.05 mmol) was added dropwise under vigorous stirring. The reaction was stirred at room temperature overnight. Next day, 2 mL water was added to quench the reaction. The reaction solution was extracted with DCM (3x). The collected organic layer was dried over $MgSO_4$ and filtered. The filtrate was concentrated under reduced pressure and precipitated in cold ether. The precipitate was collected and dried under high vacuum to give the product as a white solid. ^{1}H NMR (400 MHz, $CDCl_3$) δ 4.23 (s, 2H), 3.80 – 3.50 (m, 176H), 3.38 (s, 3H), 1.92 – 1.76 (m, 4H). ^{31}P NMR (162 MHz, $CDCl_3$) δ -0.08.

*A1.4.2 Synthesis of $PFtB_{TRI}$-diphenyl phosphate (**A1-2**)*

$PFtB_{TRI}$-OH (500 mg, 0.63 mmol) was dissolved in dry DCM (10 mL) under Ar. The reaction flask was heated under reflux condition to solubilize the starting material. TEA (440 µL, 3.16 mmol) was slowly added followed by an addition of DPPCl (656 µL, 3.16 mmol) dropwise. The reaction was heated under reflux conditions with vigorous stirring for two days. After this time, MeOH (1.5 mL) was added to quench the reaction. The reaction solution was concentrated under reduced pressure. The crude product was adsorbed on Celite and purified by an automated flash chromatography, CombiFlash, using a RediSep® silica column with EtOAc-hexane gradient. The collected fractions were then concentrated under reduced pressure and dried under high vacuum to give the product as a white solid (569.7 mg, 88% yield). ^{1}H NMR (400 MHz, $CDCl_3$) δ 7.35 (t, J = 7.8 Hz, 4H), 7.25 – 7.15 (m, 6H), 4.30 (d, J = 4.1 Hz, 2H), 4.08 (s, 6H). ^{19}F NMR (376 MHz, $CDCl_3$) δ -70.36. ^{31}P NMR (162 MHz, $CDCl_3$) δ -12.88.

*A1.4.3 Synthesis of PFtB$_{TRI}$-monophenyl phosphate (**A1-3**)*

A1-2 (220 mg, 0.215 mmol) was dissolved in THF (8 mL). NaOH (3M, 4 mL) was added to the reaction solution. The reaction was heated under reflux conditions with vigorous stirring overnight. Next day, the reaction solvent was concentrated under reduced pressure. The white solid was filtered and the flask was rinsed with water. The white solid was washed down with MeOH. The filtrate was concentrated and pass through a 0.45 μm nylon filter. The solution was once again concentrated and dried under high vacuum to give the product as a white solid (216 mg, quantitative yield). ^{1}H NMR (400 MHz, Methanol-d4) δ 7.39 – 6.97 (m, 5H), 4.23 (s, 6H), 4.08 (d, J = 4.3 Hz, 2H). ^{19}F NMR (376 MHz, Methanol-d4) δ -71.55. ^{31}P NMR (162 MHz, Methanol-d4) δ -5.92.

A1.5 References

(1) Tromsdorf, U. I.; Bruns, O. T.; Salmen, S. C.; Beisiegel, U.; Weller, H. A highly effective, nontoxic T_1 MR contrast agent based on ultrasmall PEGylated iron oxide nanoparticles. *Nano letters* **2009,** *9* (12), 4434-4440.

(2) Murray, J. I.; Woscholski, R.; Spivey, A. C. Highly efficient and selective phosphorylation of amino acid derivatives and polyols catalysed by 2-aryl-4-(dimethylamino) pyridine-*N*-oxides–towards kinase-like reactivity. *Chemical Communications* **2014,** *50* (88), 13608-13611.

APPENDIX 2 – A DIRECT ENCAPSULATION OF SPIONS IN M2H10PFTB$_{TRI}$ MICELLES

A2.1 Introduction

This preliminary study was conducted to evaluate the effect of superparamagnetic iron oxide nanoparticles (SPIONs) on longitudinal (T_1) and transverse (T_2) relaxations of M2H10PFtB$_{TRI}$. Commercially available SPIONs with an average size of 5 nm were used to test the hypothesis. The preparation of SPION-encapsulated micelles is shown in **Figure A2.1**. T_1 and T_2 relaxations were measured using ^{19}F NMR. Preliminary *in vitro* MR imaging studies were also performed on 4.7 T MRI.

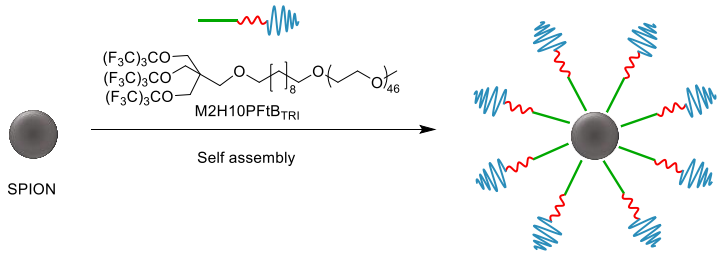

Figure A2.1 Schematic of SPION-encapsulated M2H10PFtB$_{TRI}$ micelle.

A2.2 Results and discussion

A2.2.1 SPION-encapsulated M2H10PFtB$_{TRI}$ micelles

A commercially available SPIONs was purchased from Sigma-Aldrich (St. Louis, MO) with an average particle size of 5 nm at 5 mg/mL concentration in toluene. The SPION-encapsulated micelles were prepared using an emulsion-solvent evaporation method. This method was adopted for the micelle preparation due to its advantage in removing high boiling point solvent. M2H10PFtB$_{TRI}$ polymer was selected here because of the unique properties of PFtB$_{TRI}$ that contains 27 chemically equivalent fluorine atoms, giving rise to one strong ^{19}F NMR signal (**Figure A2.2a**). The SPIONs, stabilized by hydrophobic oleic acid, were encapsulated inside the polymer through the hydrophobic interaction. The iron concentrations were varied from 0 – 75 µg Fe/mL. As shown in **Table A2.1**, a negligible change in the size of micelles was observed with increasing Fe concentration. The micelle solution was clear after preparation, however, brown precipitate at the bottom was gradually observed overtime. The brown precipitates were most likely the SPION aggregates. This suggests that the prepared formulation was not stable.

Table A2.1 Hydrodynamic diameter of SPION-encapsulated M2H10PFtB$_{TRI}$ micelles. Polymer concentration was 10 mg/mL. Size was measured by DLS. Data represent mean ± standard deviation from three different runs.

Fe concentration (µg/mL)	Hydrodynamic diameter (nm)
0	14.2 ± 0.3
25	14.0 ± 0.9
50	16.0 ± 0.1
75	16.5 ± 0.4

A2.2.2 T_1 & T_2 relaxations and in vitro ^{19}F MRI phantom images

The fresh SPION-encapsulated micelles were prepared and evaluated for the SPIONs effect on the relaxations. The ^{19}F NMR signals were acquired for the micelles with different Fe concentrations. As expected, the highest signal was observed for M2H10PFtB$_{TRI}$ micelles without an addition of SPIONs (**Figure A2.2a**). The signal intensity was gradually decreased with increasing Fe concentration (**Figure A2.2b – d**). It should be noted that a line broadening was observed from the samples containing SPIONs. This was due to the effect of paramagnetic metal ions, Fe^{3+}, on T_2 relaxation which led to a faster signal lost, thus reducing the signal to noise ratio (SNR).

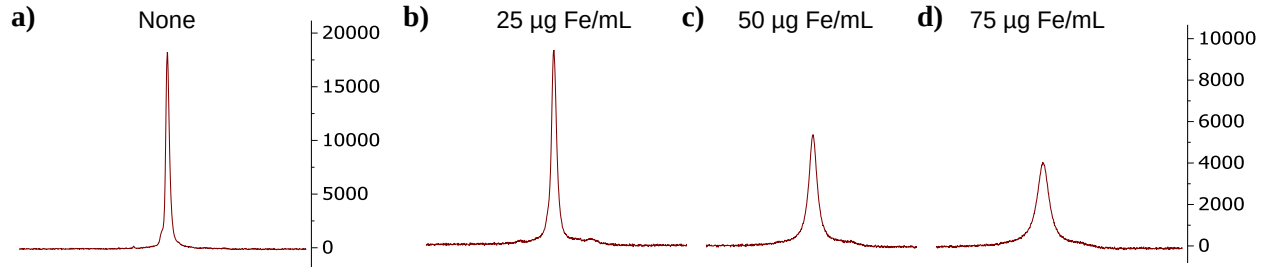

Figure A2.2 ^{19}F NMR signal of SPION-encapsulated micelles. a) M2H10PFtB$_{TRI}$ micelles in D_2O b) – d) M2H10PFtB$_{TRI}$ micelles with 25, 50, and 75 µg Fe/mL in D_2O, respectively. Polymer concentration was 10 mg/mL. δ -71.49 ppm. $\Delta\delta \approx 2$ ppm.

Table A2.2 T_1 and T_2 of SPION-encapsulated micelles. Measured in D_2O at 10 mg/mL M2H10PFTB$_{TRI}$.

Fe concentration (μg/mL)	T_1 (ms)	T_2 (ms)
0	534.0	60.5
25	448.9	56.5
50	439.6	11.1
75	533.3	11.6

As shown in **Table A2.2**, the addition of SPIONs to the M2H10PFtB$_{TRI}$ micelles did not have any effect on T_1 relaxation. However, a reduction of T_2 relaxation was observed especially at higher Fe concentration (50 and 75 μg Fe/mL). This phenomenon correlates well with the lower ^{19}F NMR signal intensity and the line broadening effect (**Figure A2.2b – d**). Preliminary study of the SPION-encapsulated micelles by the *in vitro* phantom images at 4.7 T also confirmed the reduction of T_2 with the addition of SPIONs. For the phantom study, the SPION-encapsulated micelles were prepared at two different polymer concentrations, 10 and 25 mg/mL, with a concentration of SPIONs at 25 and 50 μg Fe/mL. The SPION-encapsulated micelles showed a darker spot in ^{1}H phantom image (**Figure A2.3** – Left), suggesting the T_2 shortening effect of SPIONs on ^{1}H. M2H10PFtB$_{TRI}$ micelles at 25 mg/mL exhibited the brightest (highest SNR) spot on ^{19}F phantom image. This agrees well with the highest number of ^{19}F atoms in the solution. The incorporation of SPIONs to the 25 mg/mL M2H10PFtB$_{TRI}$ micelles provided a lower ^{19}F SNR than M2H10PFtB$_{TRI}$ micelles alone, suggesting a faster signal loss effect from the SPIONs. These results indicate that the iron oxide core of 5 nm is probably too large for the SPIONs to act as the T_1 agent. It should be noted that the size of SPIONs is a critical parameter for determining the magnetic effect and the magnetic moment of the particles. The low magnetization of the SPIONs allows the suppression of T_2 effect while enhanced T_1 effect.[1] Therefore, a smaller size of the SPIONs has to be prepared as well as a new formulation design to exploit the advantages of the SPIONs for enhancing sensitivity of ^{19}F signal.

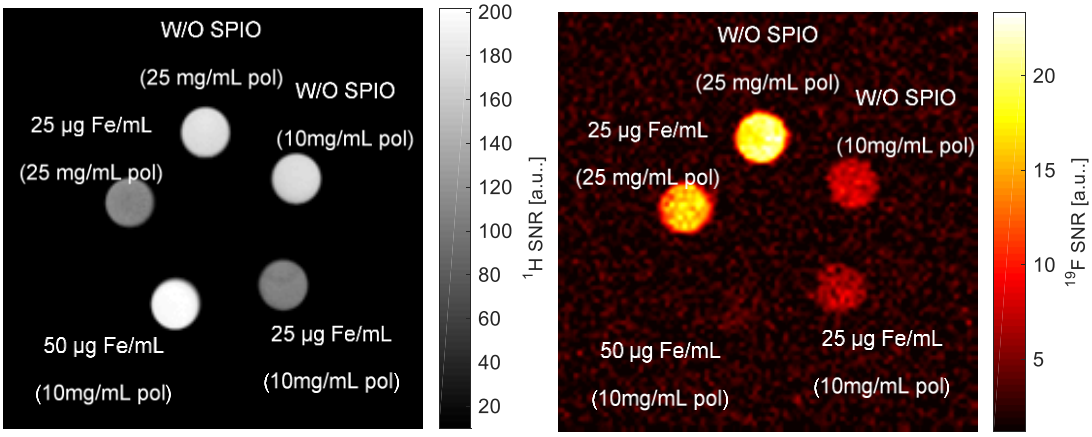

Figure A2.3 Phantom images of SPION-encapsulated M2H10PFtB$_{TRI}$. Left: ^{1}H phantom image. Right: ^{19}F phantom image. Polymers were prepared at two different concentrations: 10 and 25 mg/mL. MRI data were acquired by Dr. Kai D. Ludwig.

A2.3 Conclusion

SPIONs were encapsulated in M2H10PFtB$_{TRI}$ micelles, with a clear initial micelle solution. However, the brown precipitates were gradually observed over time, indicating the aggregation of the SPIONs. This is possibly due to the short hydrophobic portion of the M2H10PFtB$_{TRI}$ polymer that could not provide the total encapsulation of SPION particles, thus leading to the aggregation of the SPIONs overtime. The size of the SPION used in this study (5 nm) was not able to provide T_1 effect to both ^{1}H and ^{19}F. The *in vitro* phantom images confirmed the T_2 reduction with an addition of the SPIONs as observed from a darker spot in both ^{1}H and ^{19}F phantom images. These results suggest that the smaller size of iron oxide (< 5 nm) should be used in order to improve the ^{19}F sensitivity.

A2.4 Experimental

A2.4.1 SPION-encapsulated M2H10PFtB$_{TRI}$ micelle preparation

SPION-encapsulated M2H10PFtB$_{TRI}$ micelles were prepared using an emulsion-solvent evaporation method. Briefly, M2H10PFtB$_{TRI}$ (the synthesis of this polymer can be found in *Chapter 2*) was dissolved in Milli-Q water at 10 mg/mL. SPION solution in toluene (5 nm average particle size, 5 mg/mL in toluene, Sigma-Aldrich, St. Louis, MO) was added to the polymer solution to get the final Fe

concentration of 25, 50, and 75 μg/mL. The solution mixture was sonicated for 30 min followed by a solvent evaporation using rotary evaporator to yield SPION-encapsulated M2H10PFtB$_{TRI}$ micelles. For relaxation measurement, all samples were prepared in D_2O instead of Milli-Q water.

A2.4.2 Dynamic light scattering (DLS)

Particle size was measured by dynamic light scattering (DLS) with a Zetasizer Nano-ZS (Malvern Instruments Ltd., UK) at 25 °C with a 173° detection angle. The micelle solutions were measured directly without dilution and run in triplicate. The number of scans of each run was determined automatically by the instrument. The data were reported as volume weighted average diameters.

A2.4.3 T_1 and T_2 measurement

The ^{19}F relaxation parameters T_1 and T_2 were measured on a Varian Unity-Inova 500 MHz (11.7 T) NMR spectrometer with the internal temperature maintained at 25 °C. The T_1 parameter was determined using an inversion recovery experiment acquired with 18 independent, quadratically spaced variable (tau) values covering a range up to 5 time the estimated T_1 value. The T_2 parameter was determined using a Carr–Purcell–Meiboom–Gill (CPMG) pulse sequence experiment acquired with 18 independent, quadratically spaced variable (tau) values covering a range up to 5 time the estimated T_2 value.

A2.4.4 In vitro ^{19}F MRI phantom experiments

The samples were loaded in microcentrifuge tubes and MR images were acquired using a $^{1}H/^{19}F$ quadrature volumetric RF MRI coil on the 4.7 T Agilent small animal horizontal bore MRI (Agilent Technologies, Santa Clara, CA). ^{1}H images were acquired using 2D multi-slice gradient echo with 8.82/4.43 ms TR/TE, 16° flip angle, 0.19 × 0.19 mm^2 in-plane spatial resolution, 2 mm thickness, 48 × 48 mm^2 field-of-view (FOV), 256 × 256 data matrix, 195.3 Hz/voxel bandwidth, and 36.1 s scan time. ^{19}F images were acquired using 2D multi-slice fast spin echo with 1.15/12.51 ms TR/TE, 8 echo train length, 0.5 × 0.5 mm^2 in-plane spatial resolution, 2 mm thickness, 48 × 48 mm^2 FOV, 96 × 96 data matrix, 156.9 Hz/voxel bandwidth, and 7 min 22 s scan time.

A2.5 References

(1) Kim, B. H.; Lee, N.; Kim, H.; An, K.; Park, Y. I.; Choi, Y.; Shin, K.; Lee, Y.; Kwon, S. G.; Na, H. B. Large-scale synthesis of uniform and extremely small-sized iron oxide nanoparticles for high-resolution T_1 magnetic resonance imaging contrast agents. *Journal of the American Chemical Society* **2011,** *133* (32), 12624-12631.

APPENDIX 3 – SUPPLEMENTARY DATA

Table of Contents

A3.1 NMRs

A3.1.1 Chapter 2: ^{1}H NMRs, ^{19}F NMRs, and ^{13}C NMRs

N-(4-Carboxyphenyl)maleamic Acid (*p*-CPMA) (**2-1**)

^{1}H NMR

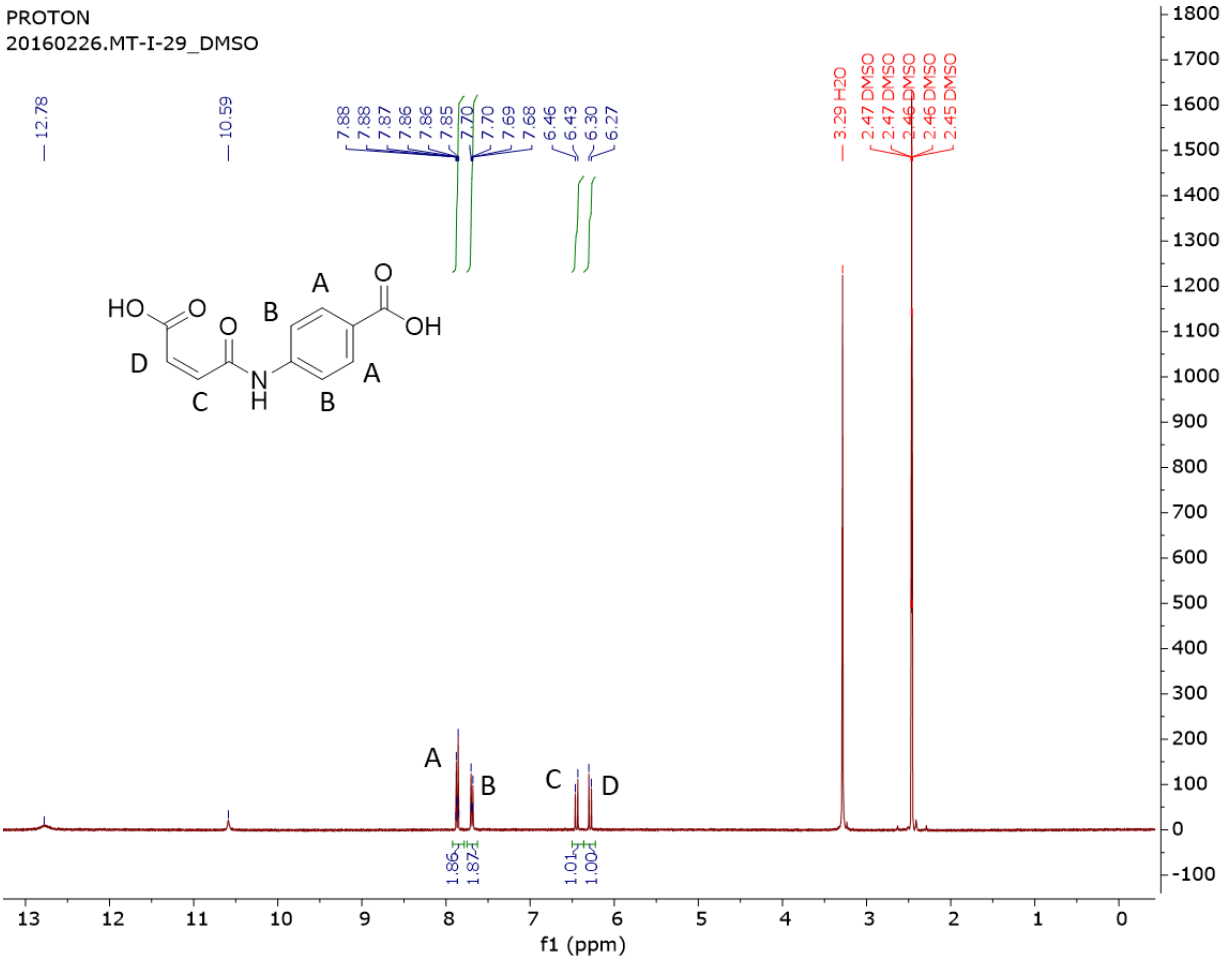

N-(4-Carboxyphenyl)maleimide (*p*-CPMI) (**2-2**)

^{1}H NMR

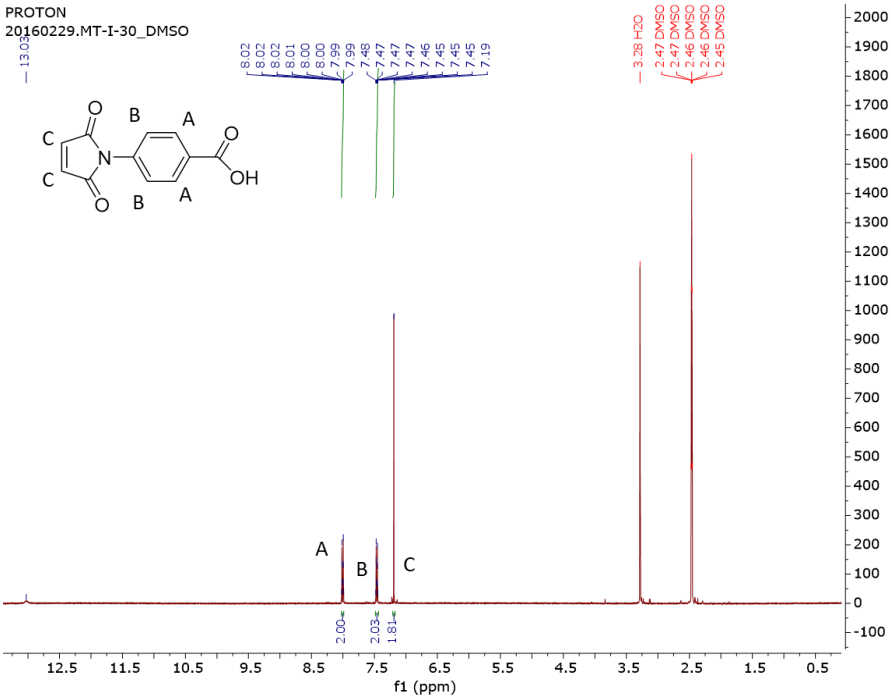

N-[(4-azidocarbonyl)phenyl]maleimide (ACPM) (**2-3**)

^{1}H NMR

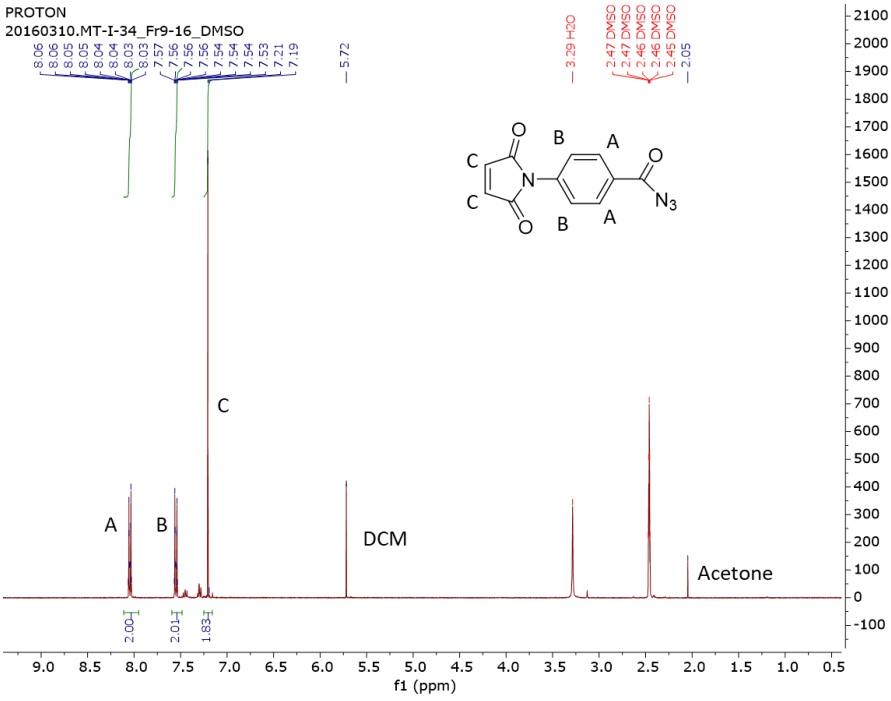

9-decen-1-OPFtB$_{TRI}$ (**2-4**)

^{1}H NMR

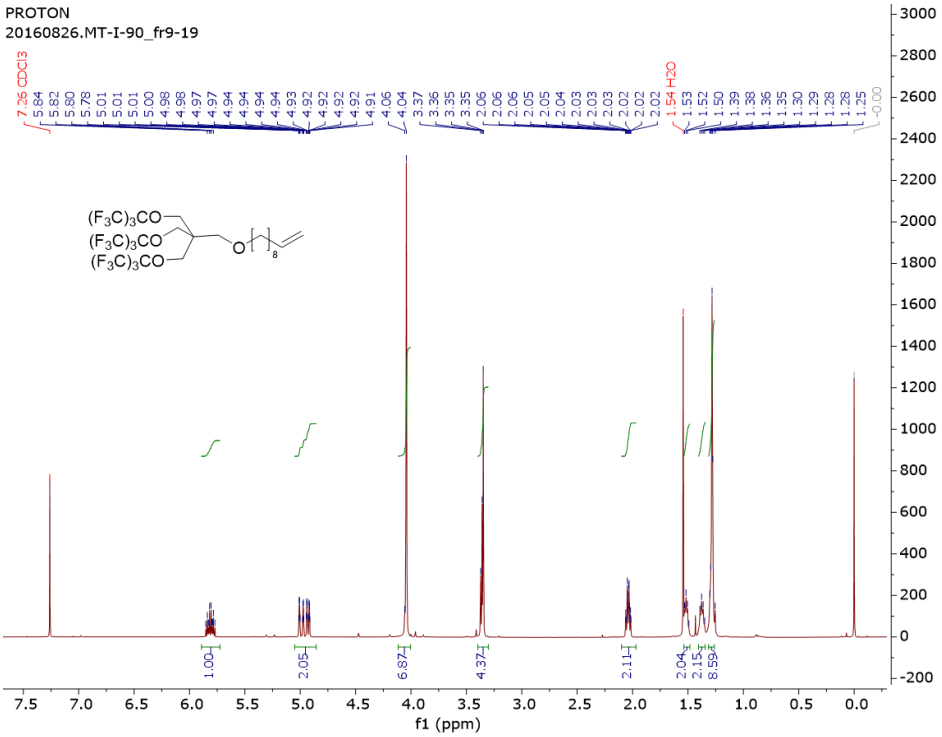

^{19}F NMR

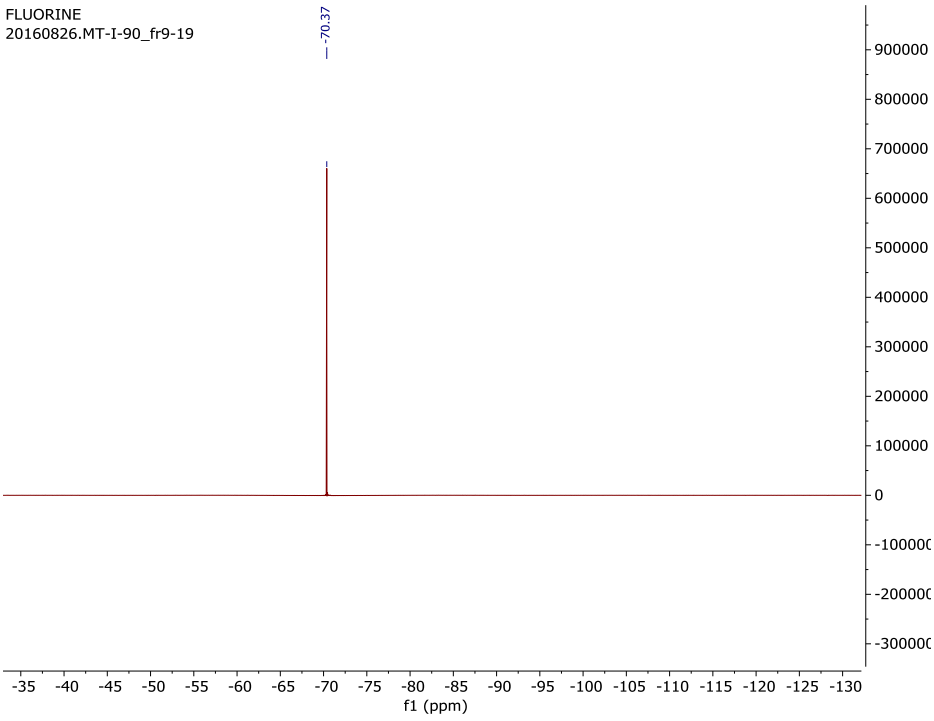

HO-H10PFTB$_{TRI}$ (**2-5**)

^{1}H NMR

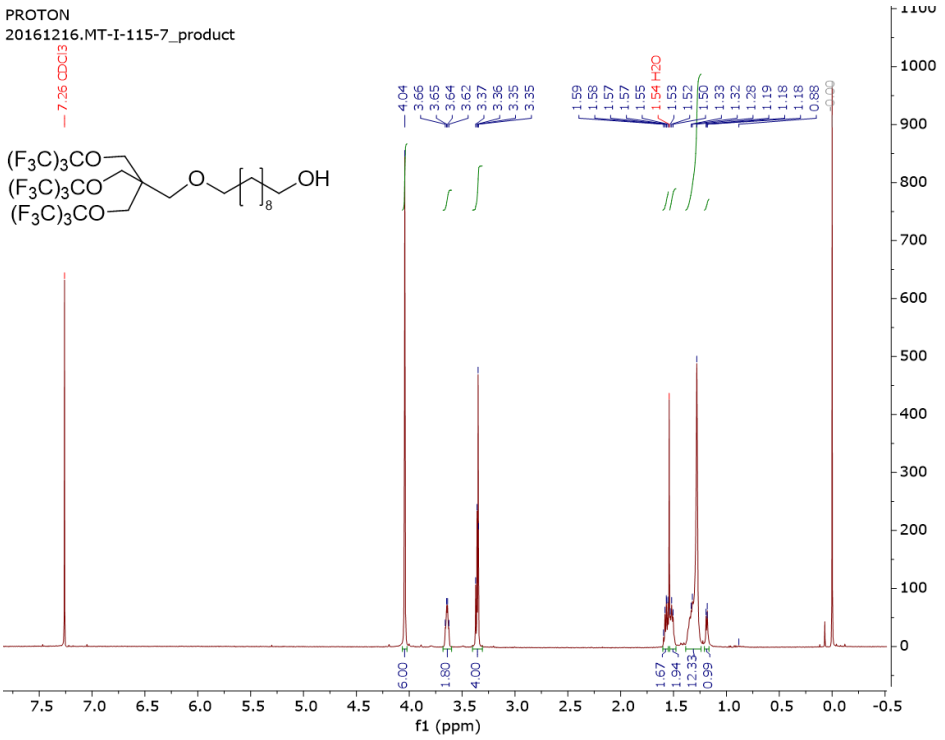

^{19}F NMR

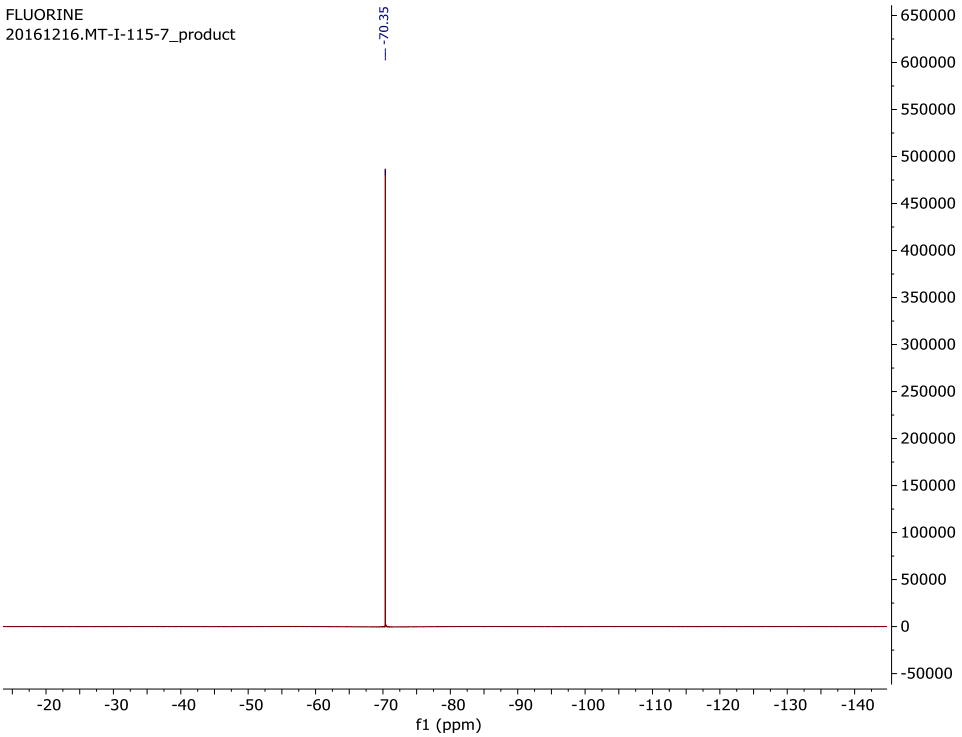

M2H10PFtB$_{TRI}$ (**2-6**)

^{1}H NMR

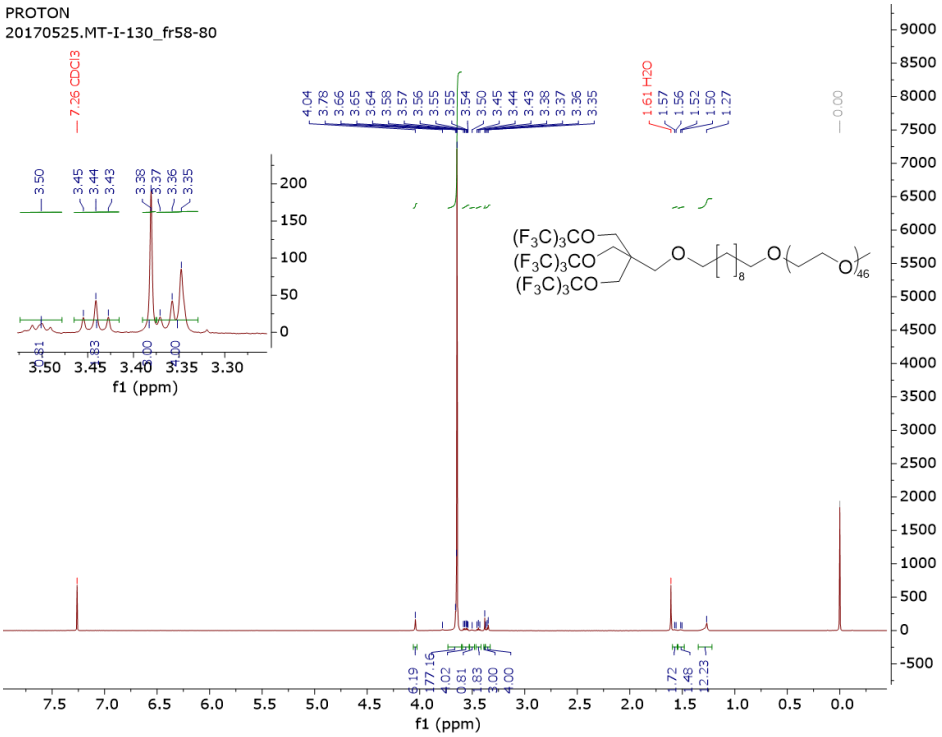

^{19}F NMR

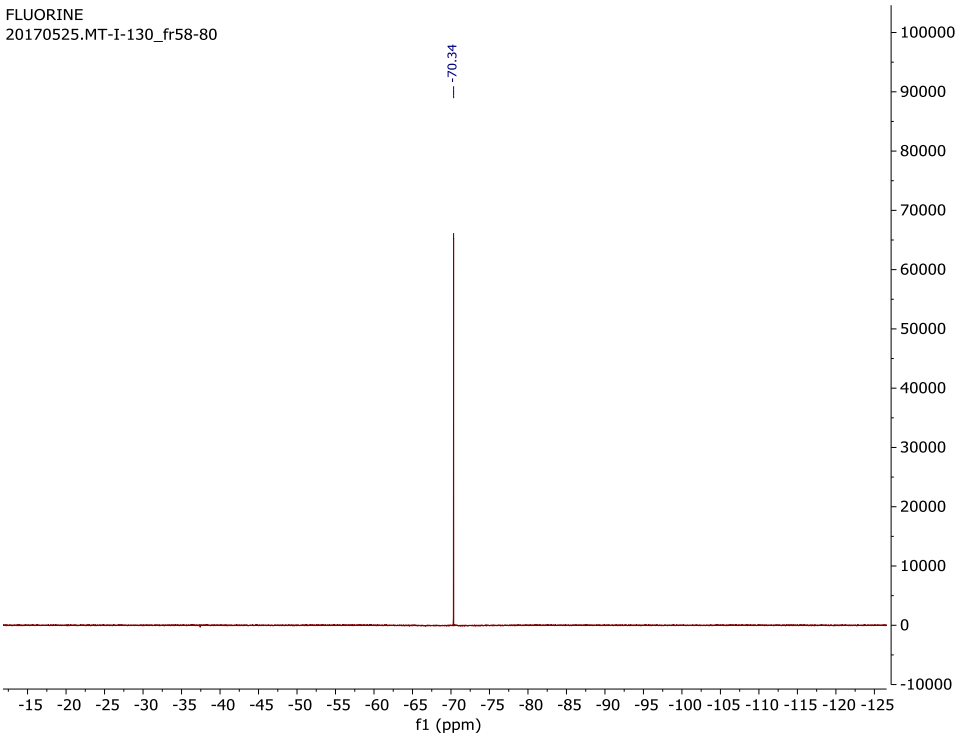

BnO-P2-OH (**2-7**)

^{1}H NMR

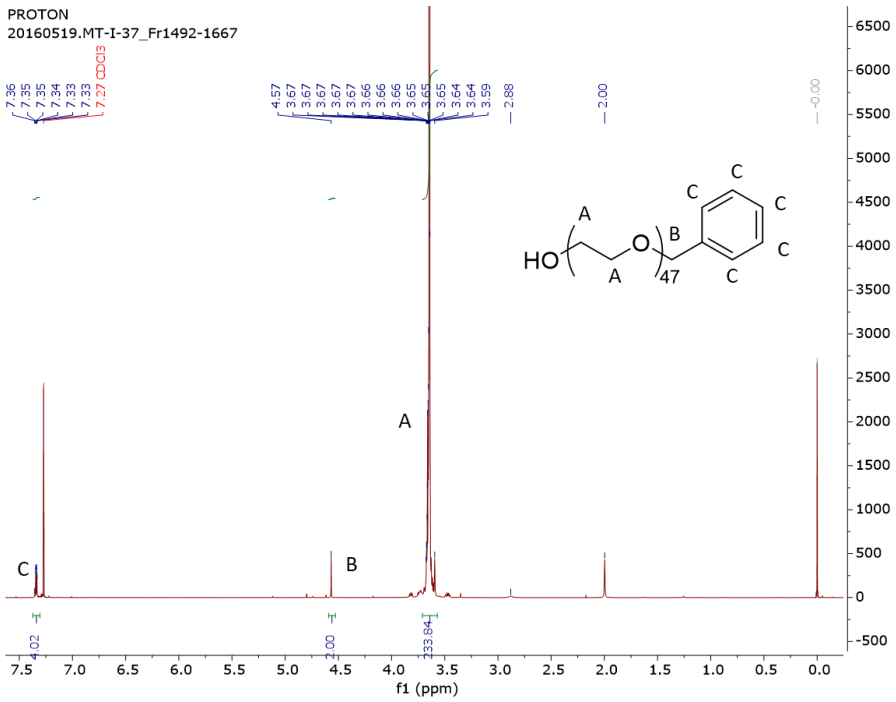

BnO-P2-OMs (**2-8**)

^{1}H NMR

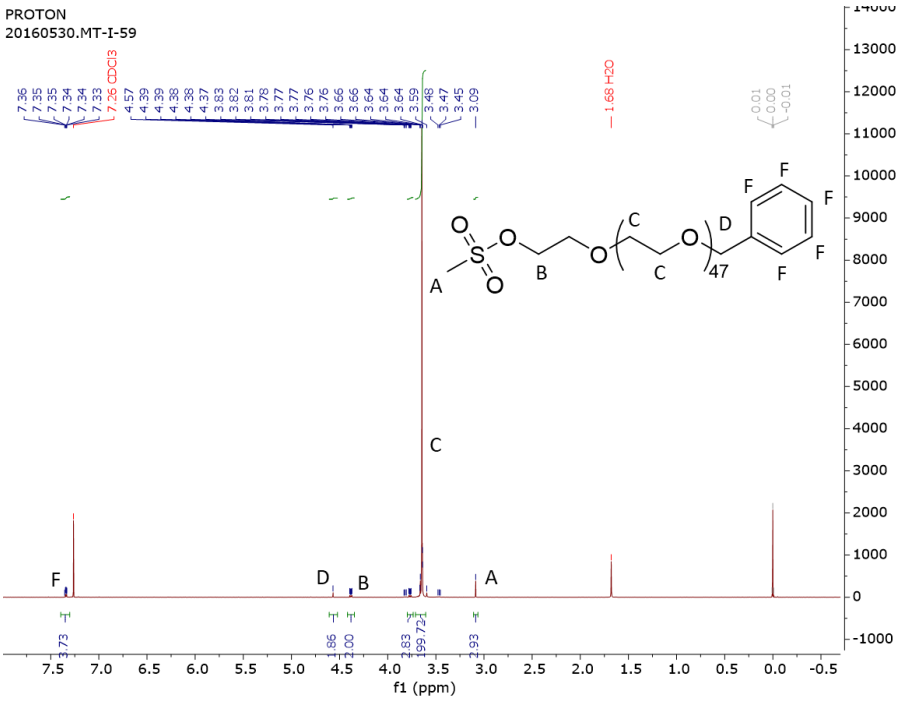

BnO-P2H10PFtB$_{TRI}$ (**2-9**)

^{1}H NMR

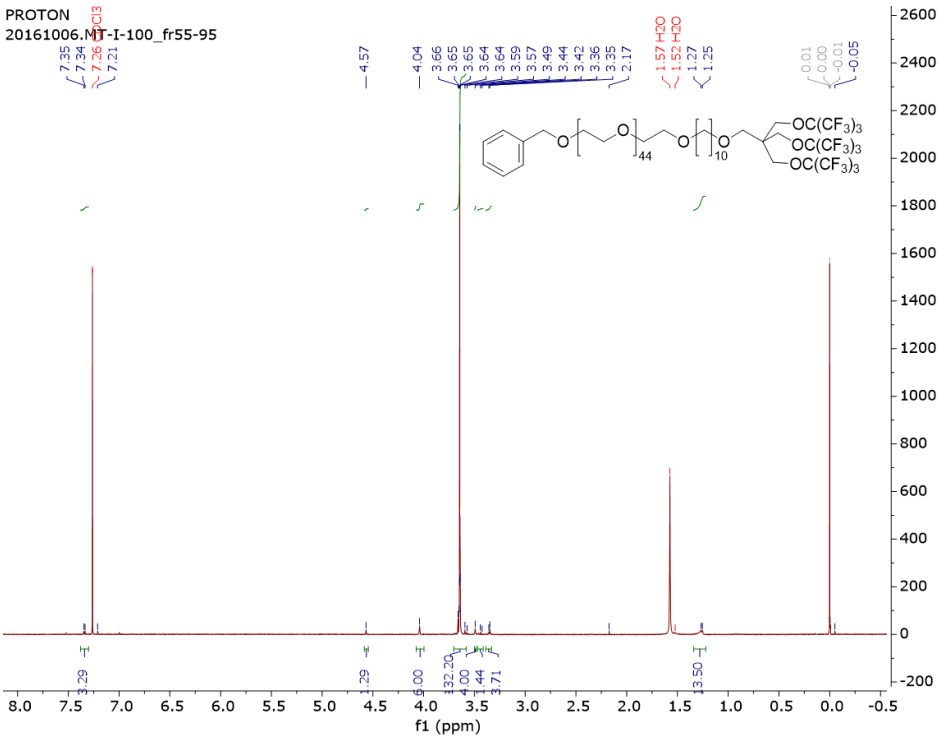

^{19}F NMR

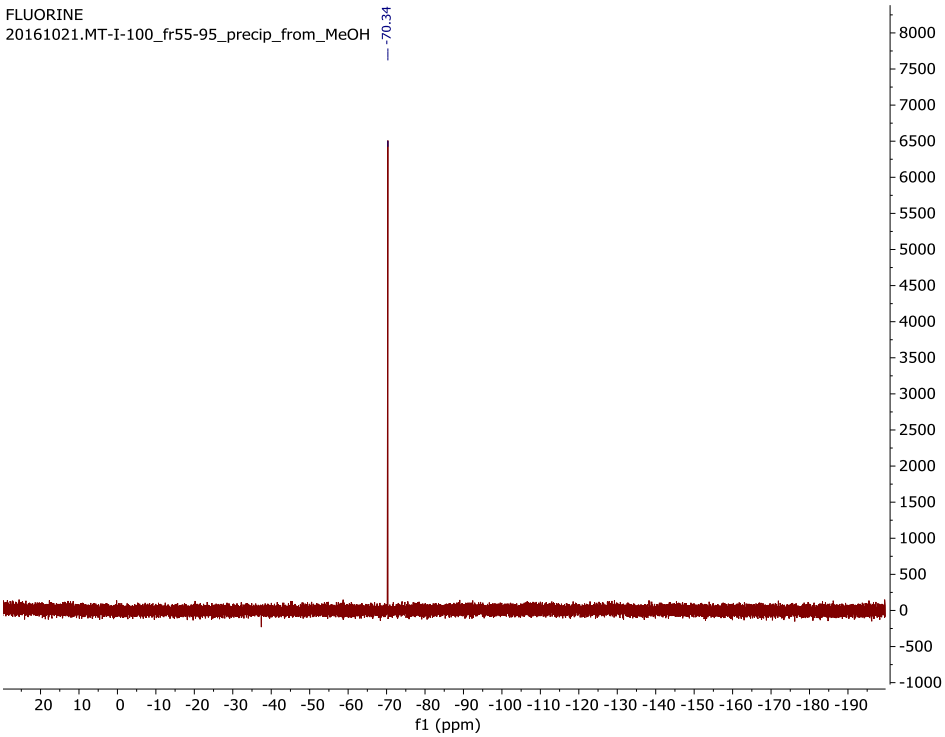

HO-P2H10PFtB$_{TRI}$ (**2-10**)

^{1}H NMR

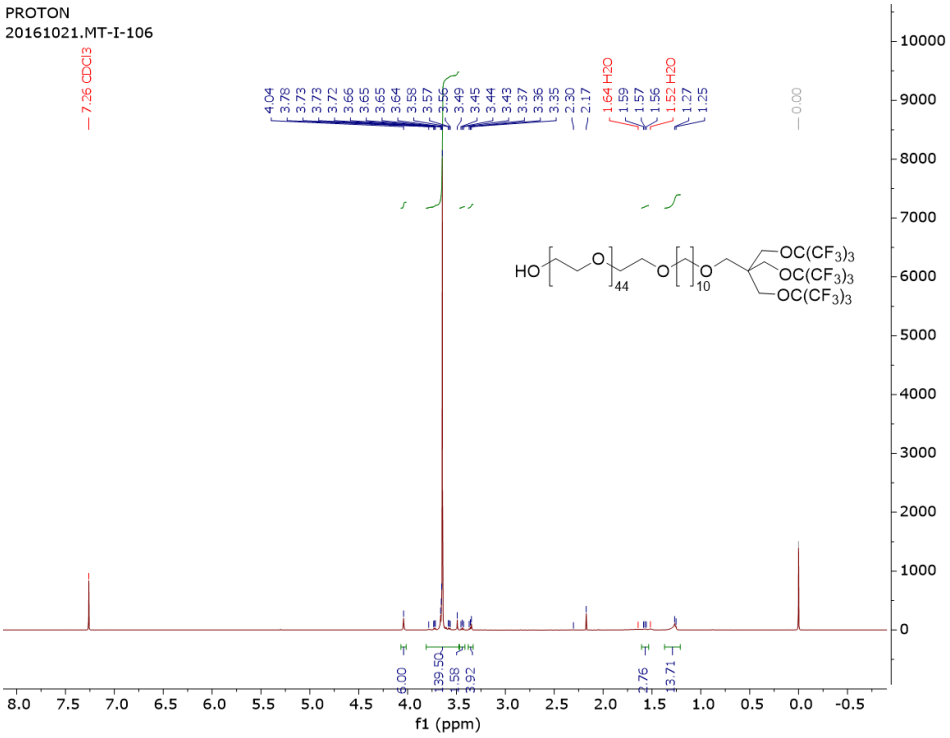

^{19}F NMR

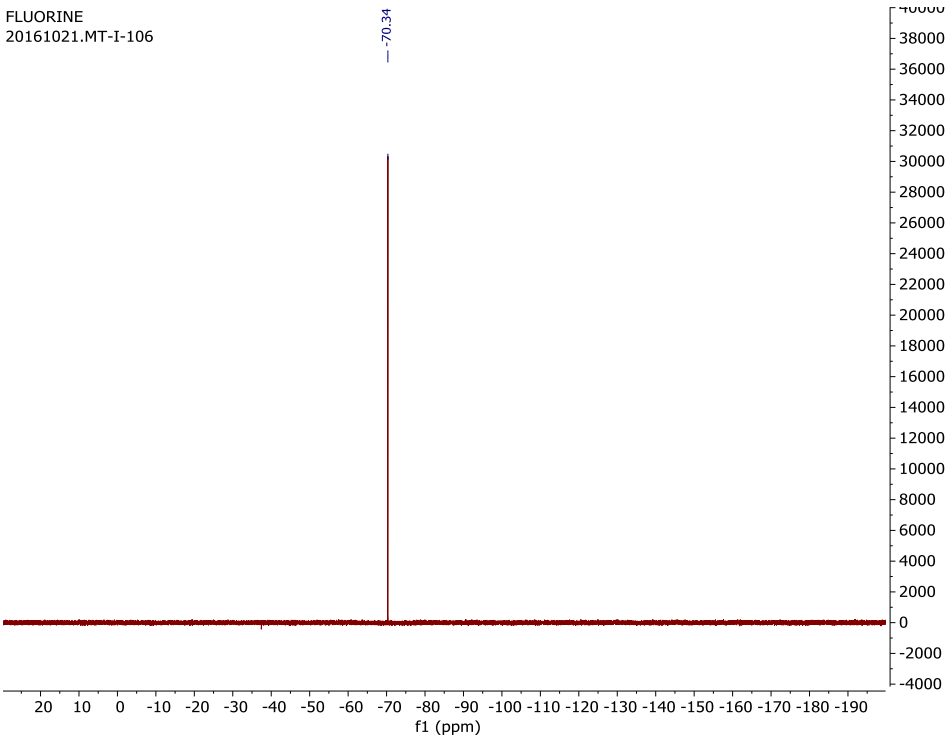

PMPI-P2H10PFtB$_{TRI}$ (**2-11**)

^{1}H NMR

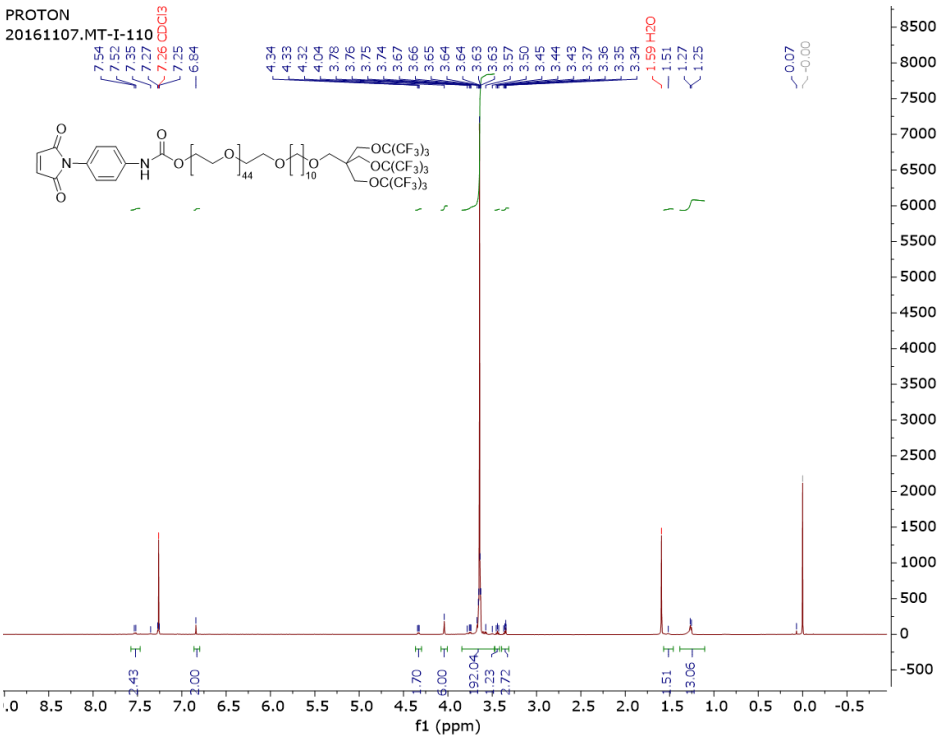

^{19}F NMR

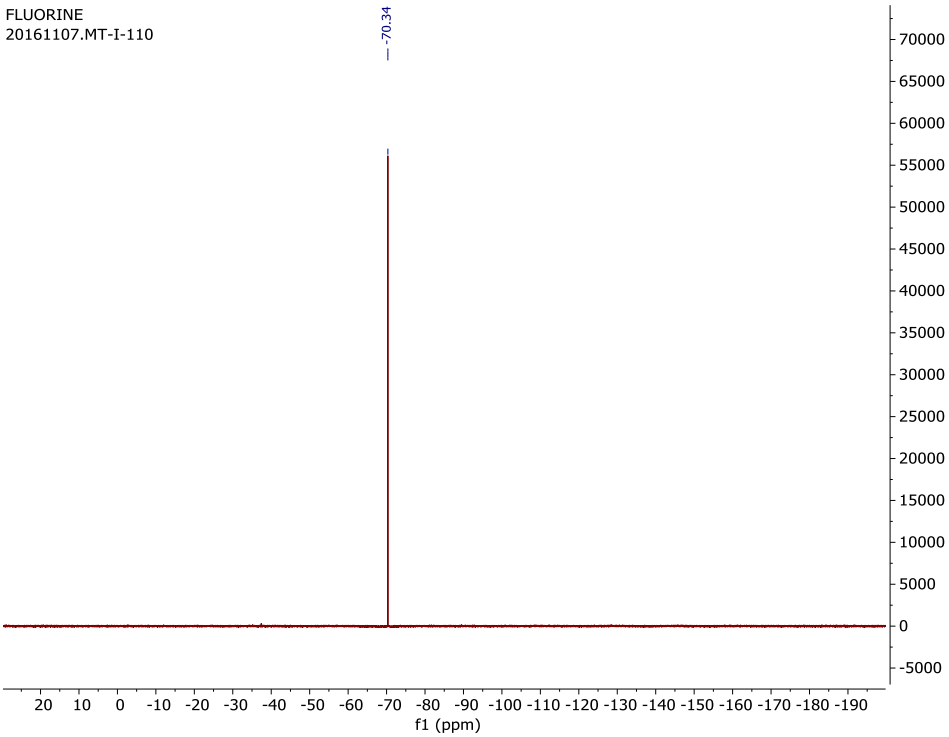

A3.1.2 Chapter 3: ^{1}H NMRs, ^{19}F NMRs, and ^{13}C NMRs

2-phenyl-1,3-dioxan-5-ol (**3-1**)

^{1}H NMR

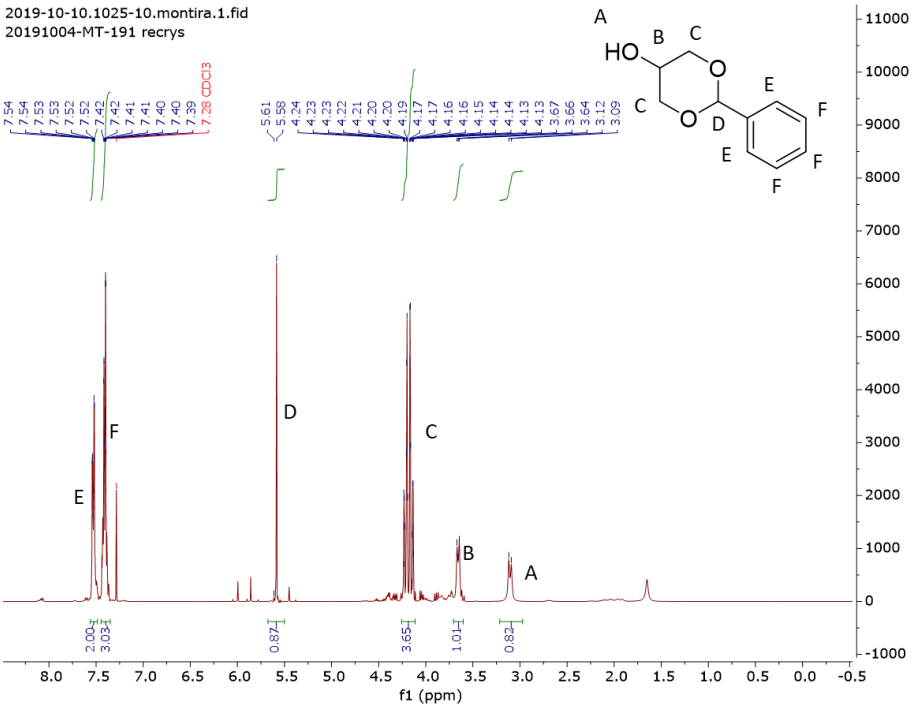

^{13}C NMR

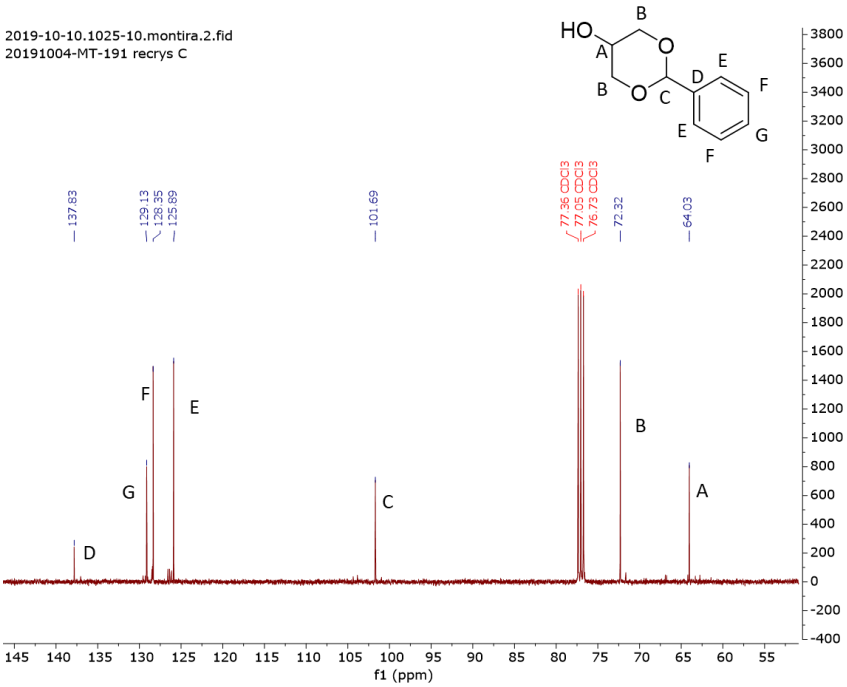

M2-OMs (**3-2**)

^{1}H NMR

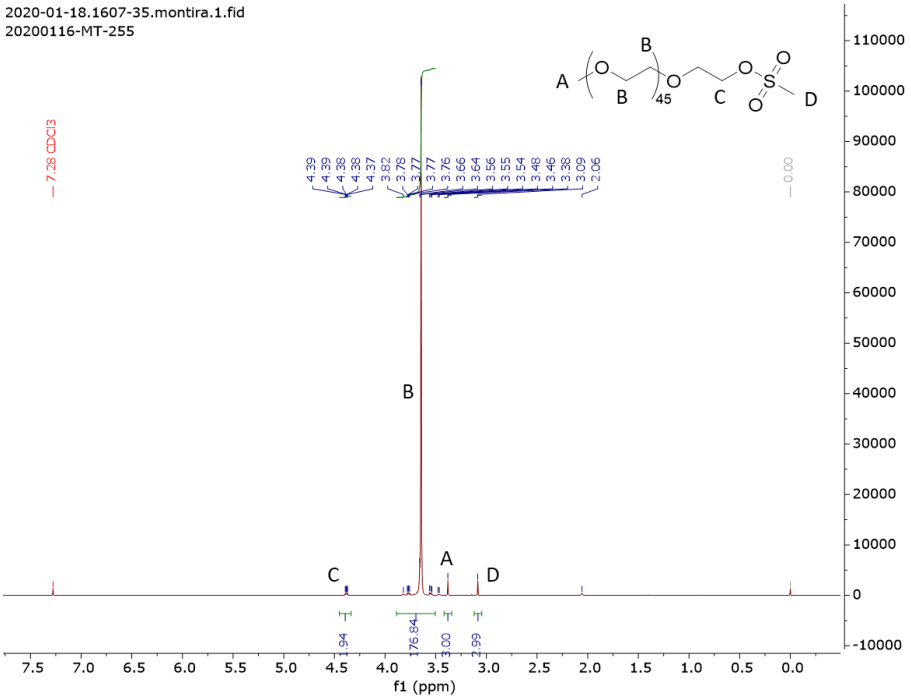

Benzylidene acetal-M2 (**3-3**), contains free M2-OH

^{1}H NMR

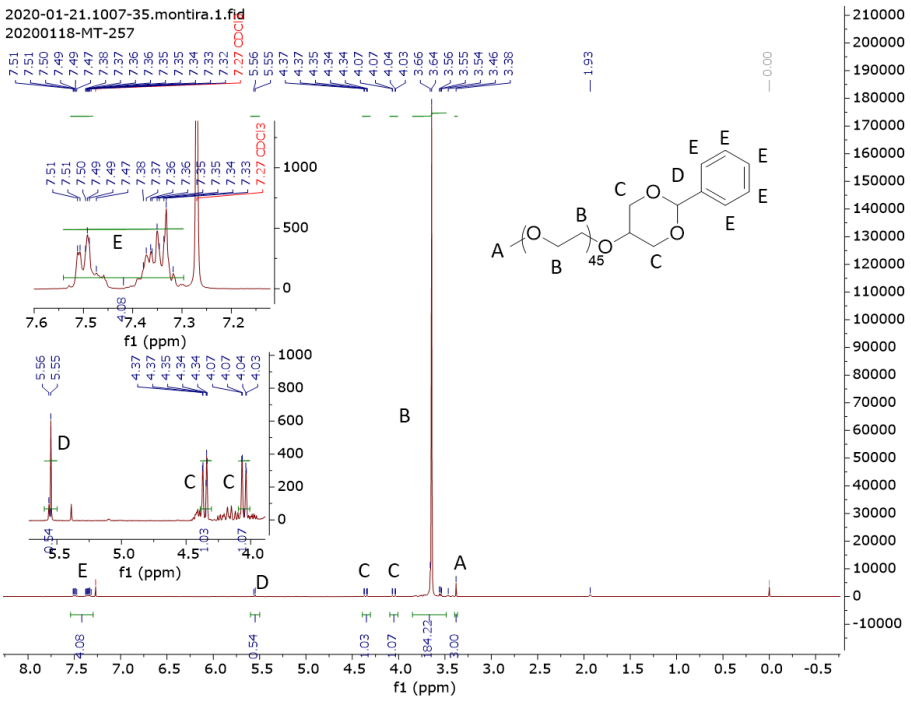

M2-diOH (**3-4**), contains free M2-OH

^{1}H NMR

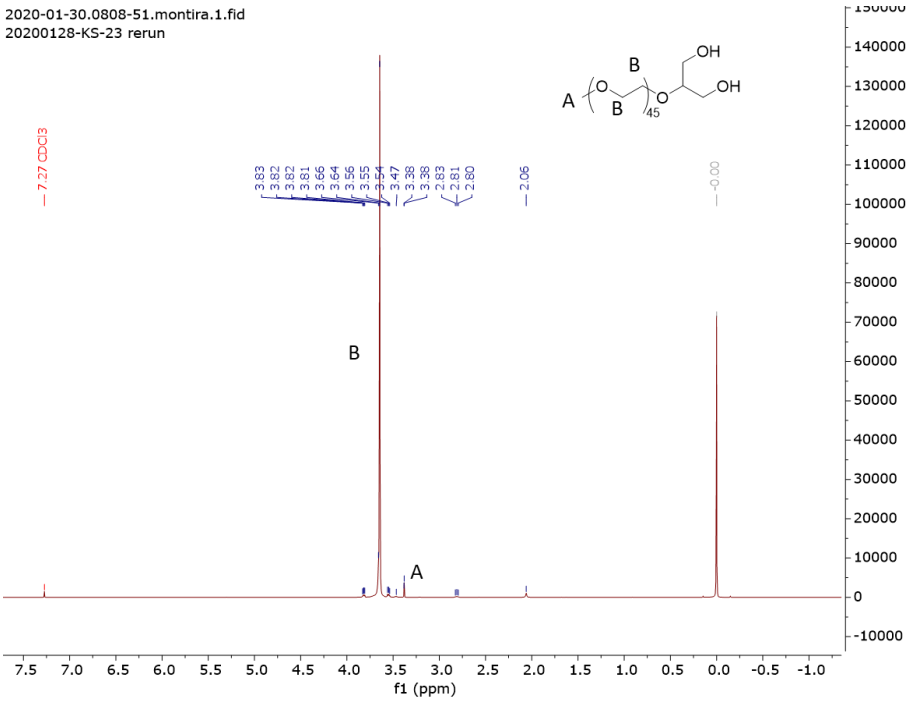

M2-diOMs (**3-5**), contains free M2-OMs

^{1}H NMR

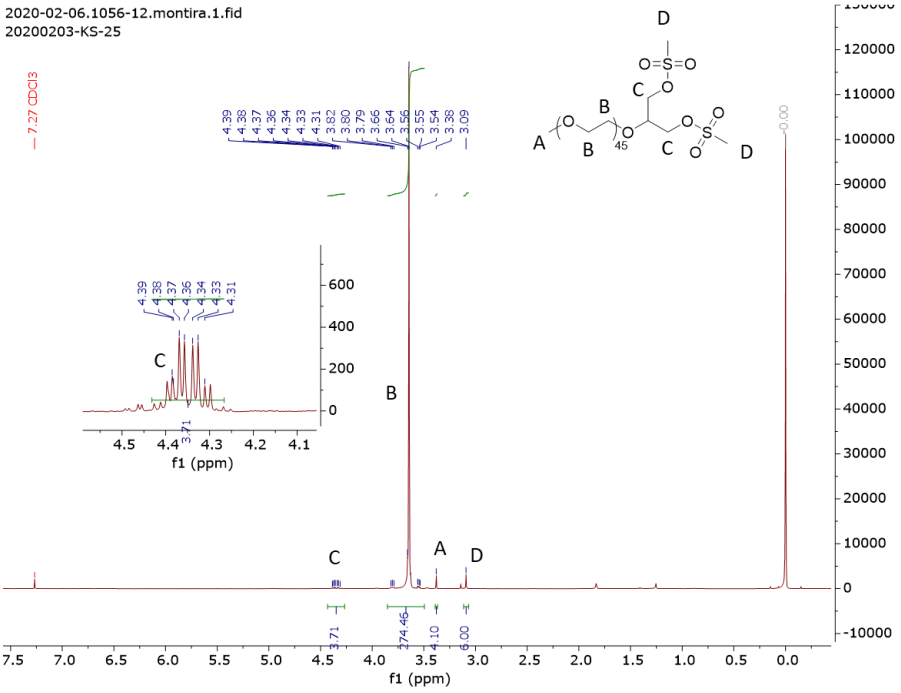

M2diF8H18 (**3-6**)

^{1}H NMR

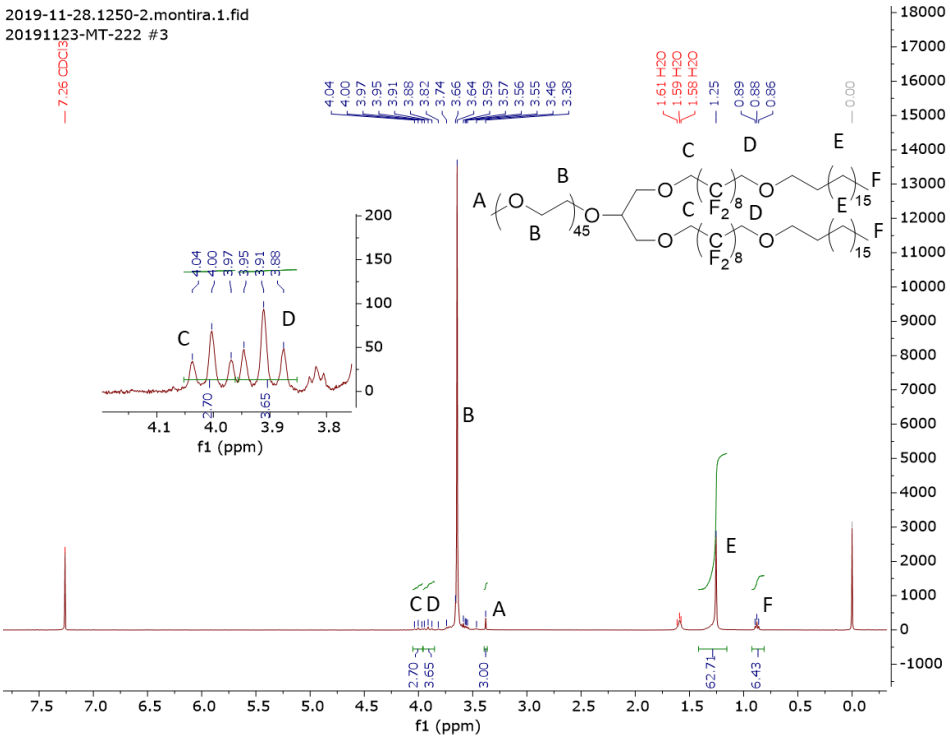

^{19}F NMR

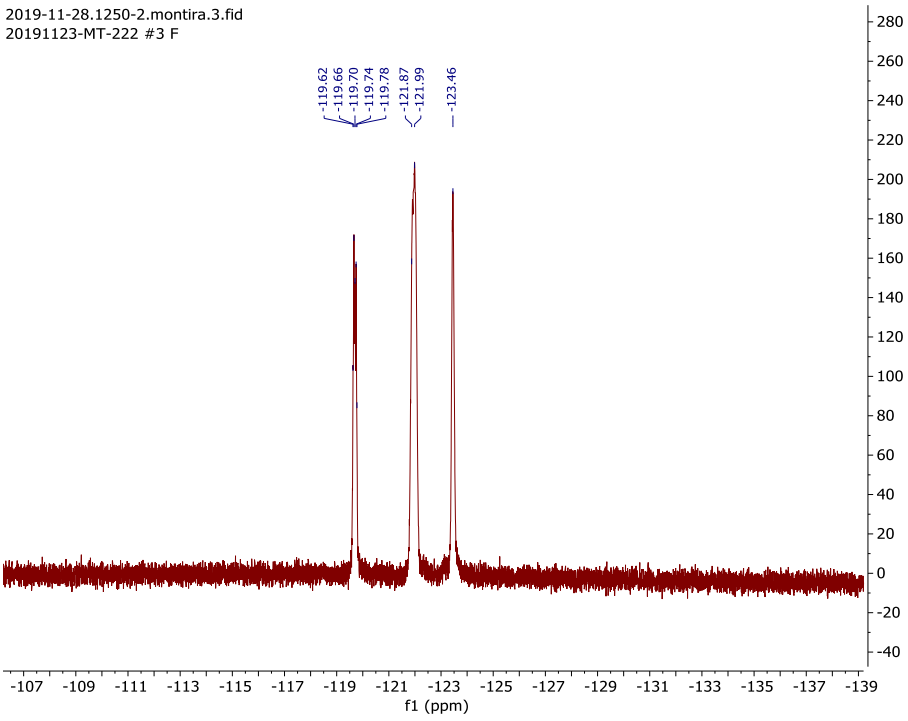

M2diOBn/OH (**3-7**), contains free M2-OH

^{1}H NMR

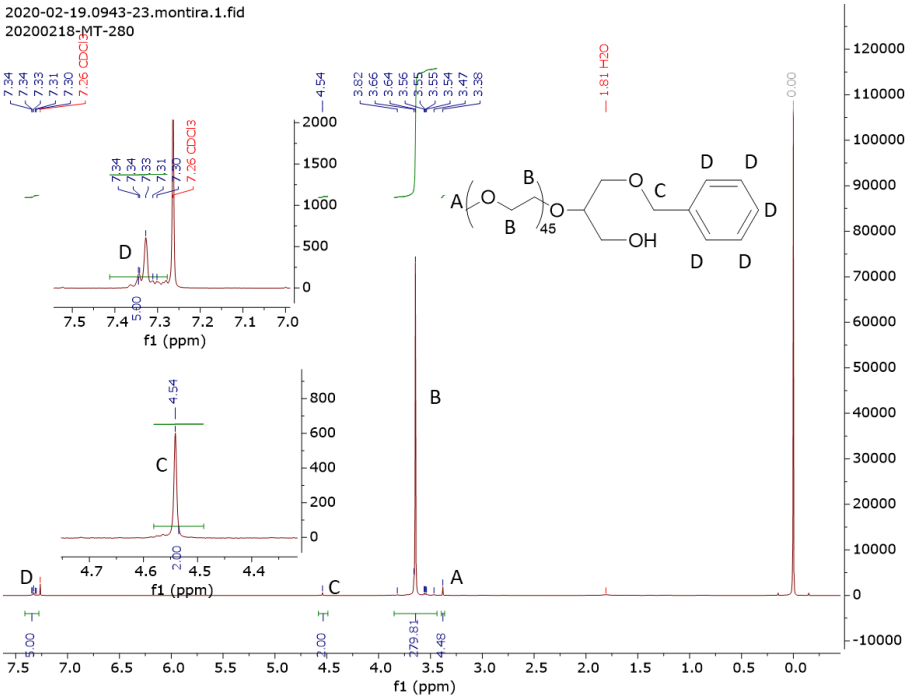

M2diOBn/OMs (**3-8**), contains free M2-OMs

^{1}H NMR

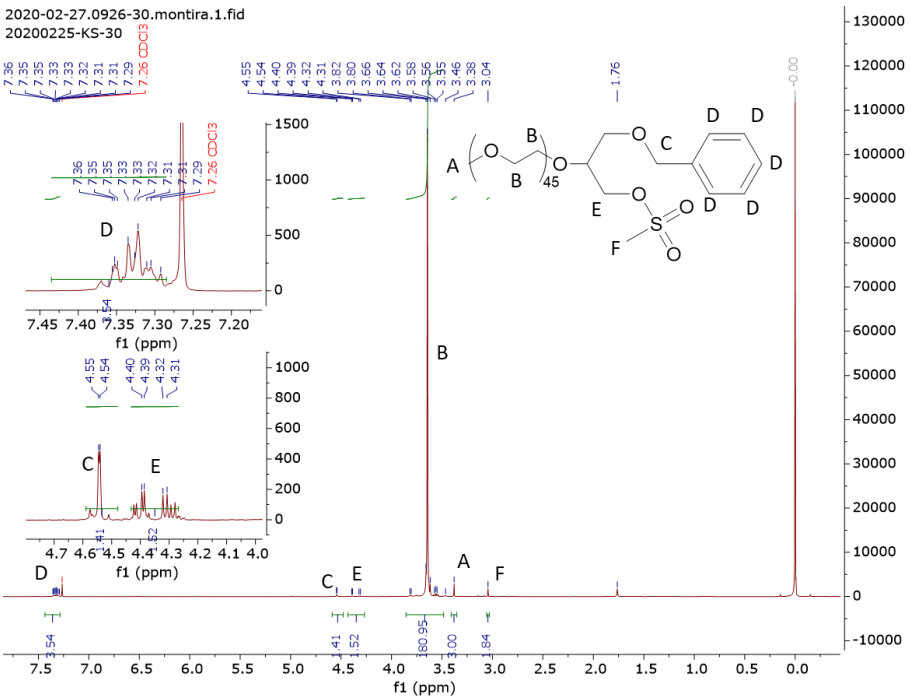

M2diOBn/F8 (**3-9**)

^{1}H NMR

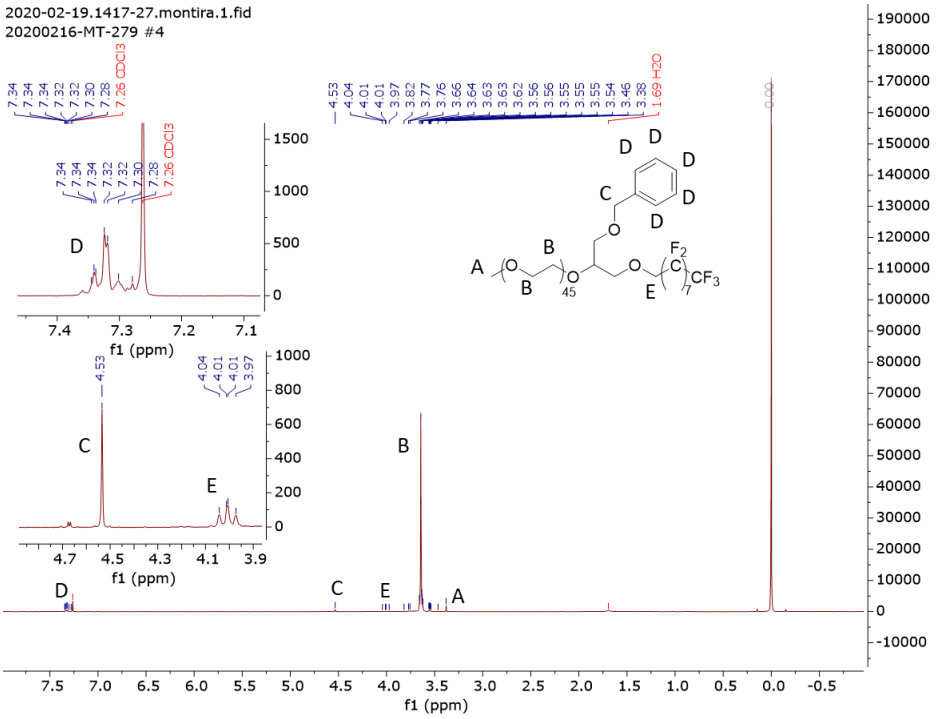

^{19}F NMR

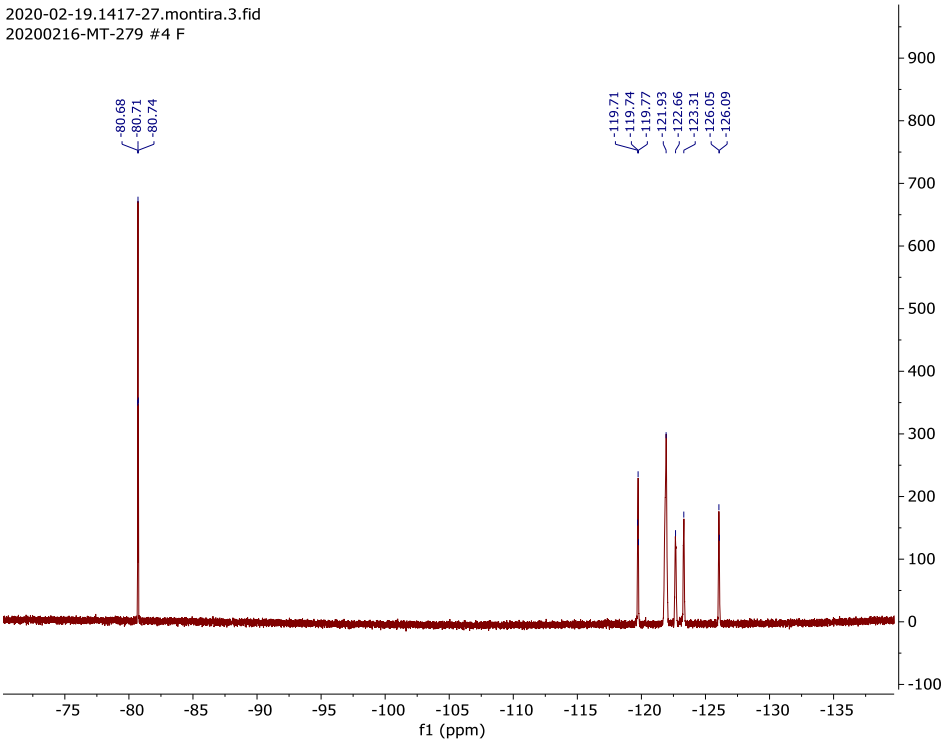

M2diOH/F8 (**3-10**)

^{1}H NMR

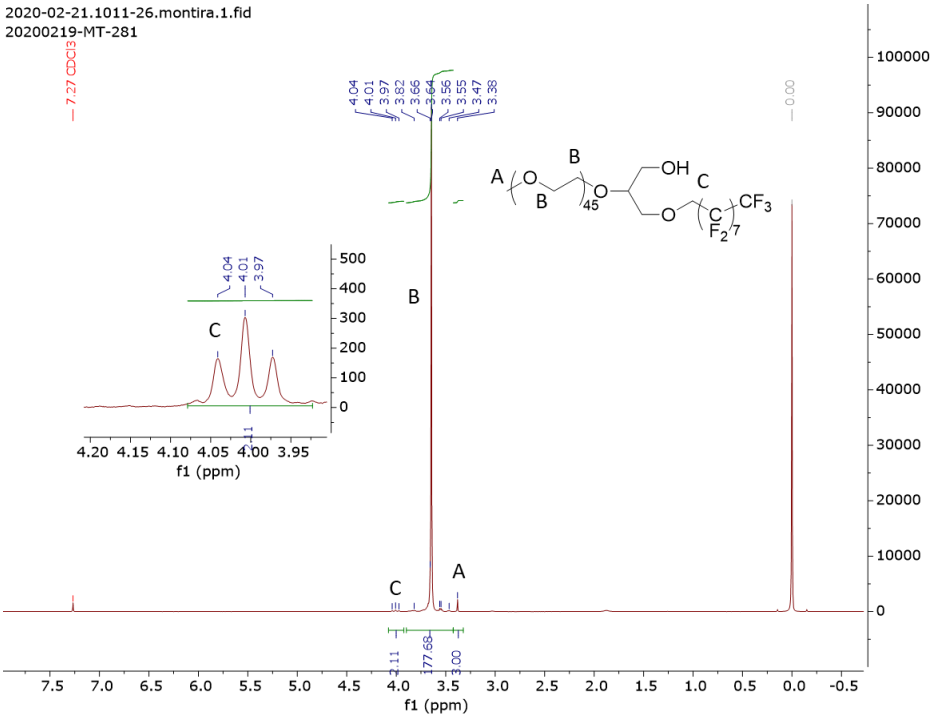

^{19}F NMR

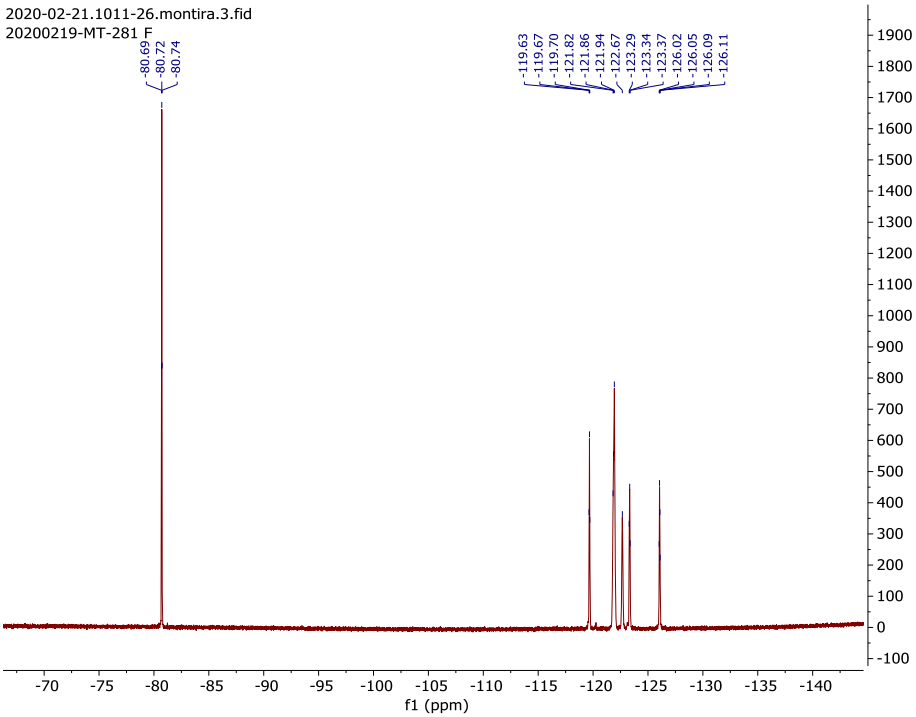

M2diOMs/F8 (**3-11**)

^{1}H NMR

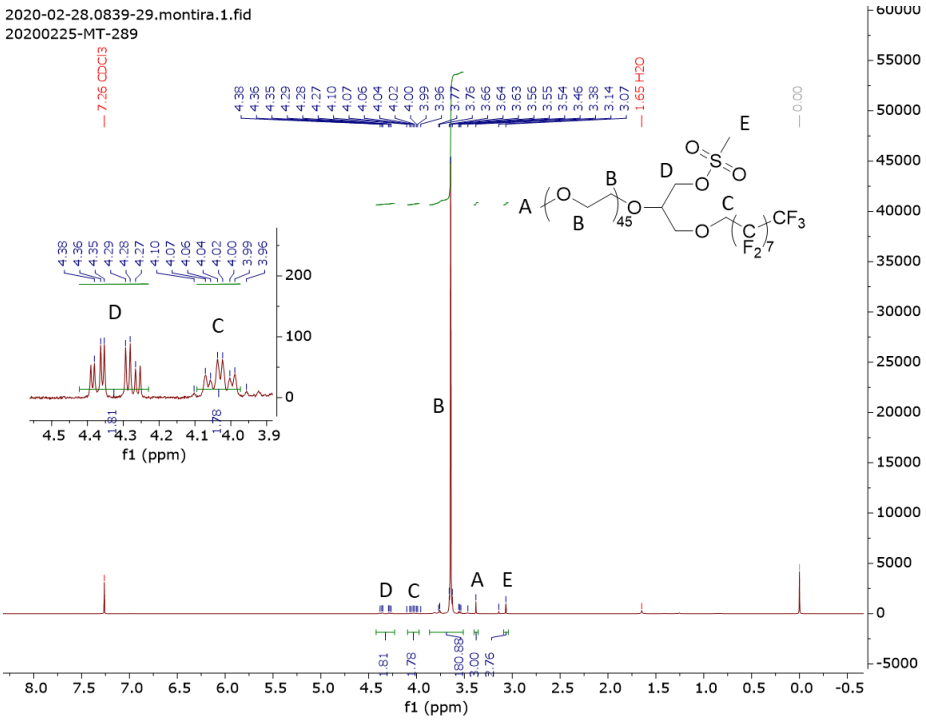

^{19}F NMR

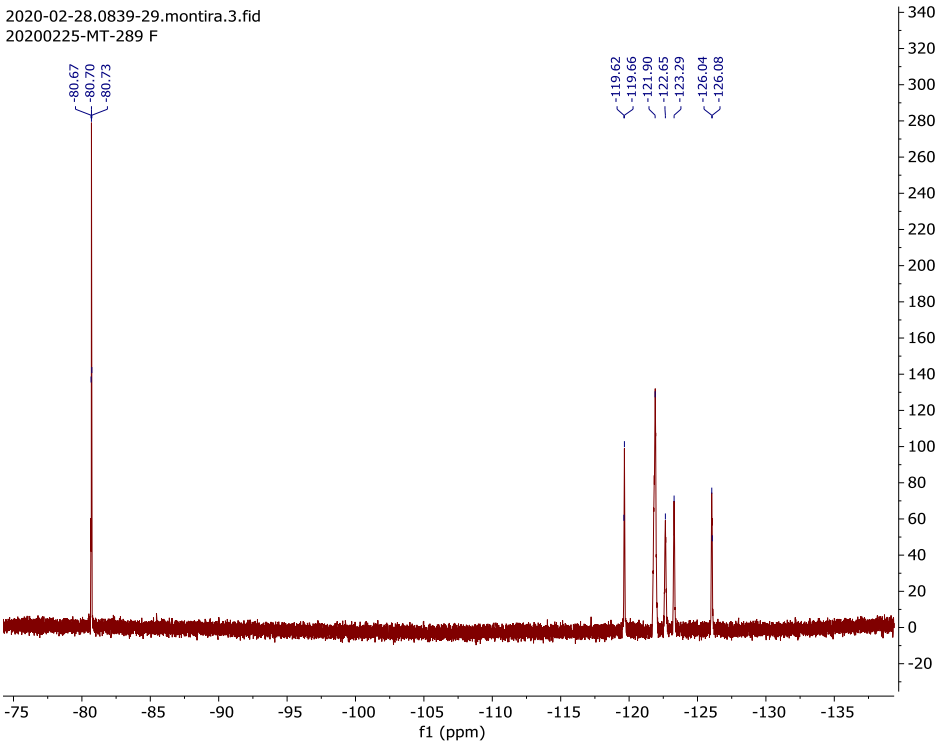

M2diF8H18/F8 (**3-12**)

^{1}H NMR

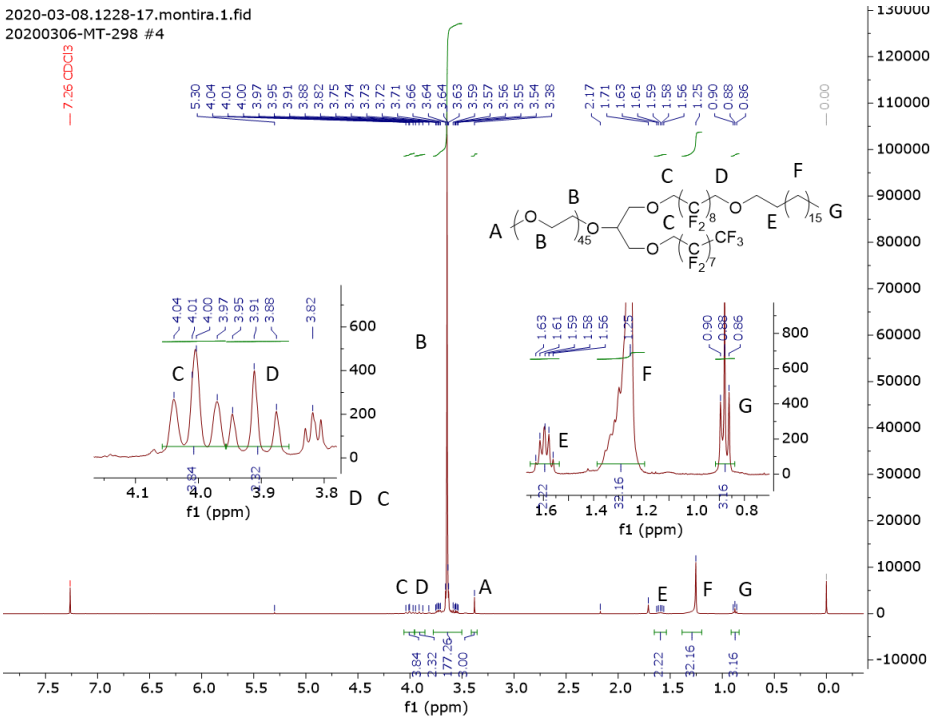

^{19}F NMR

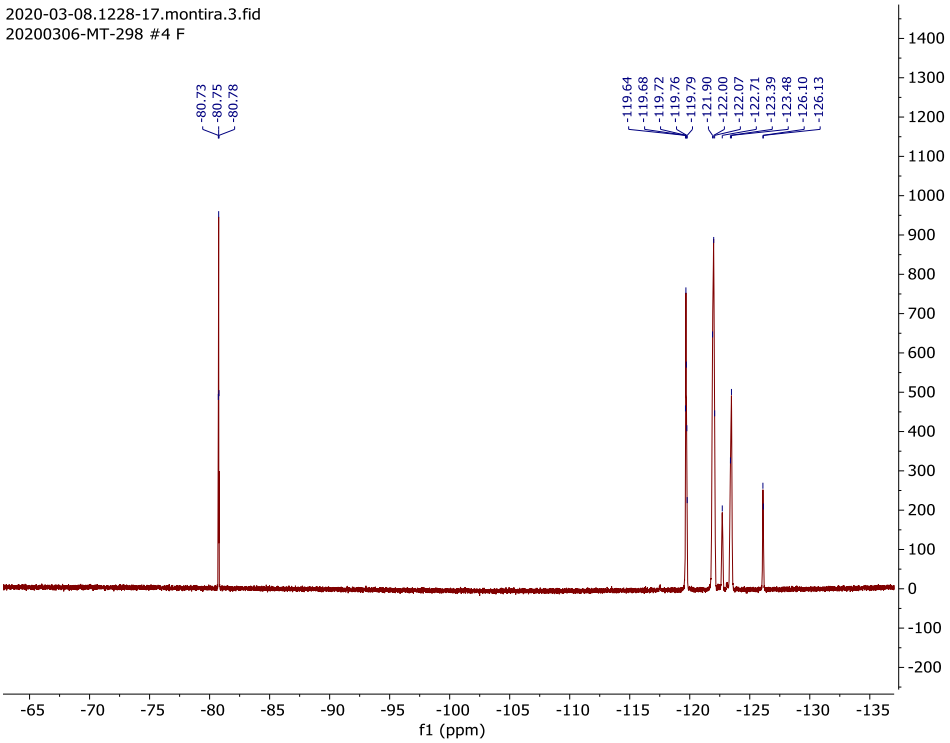

A3.1.3 Chapter 4: ^{1}H NMRs, ^{19}F NMRs, and ^{13}C NMRs

Nitrodopamine (NDA, **4-1**)

^{1}H NMR

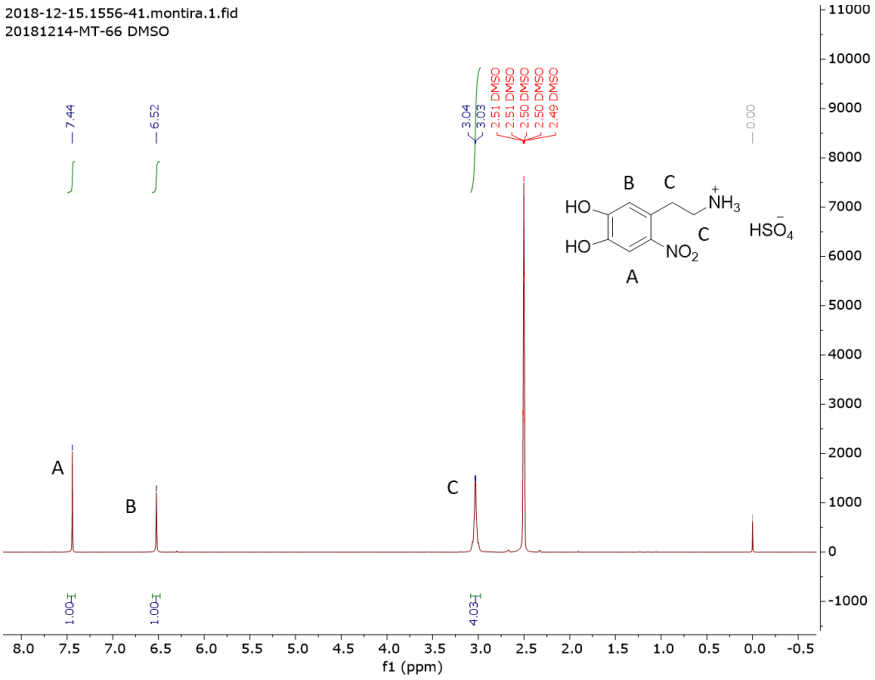

M2-NDA (**4-2**)

^{1}H NMR

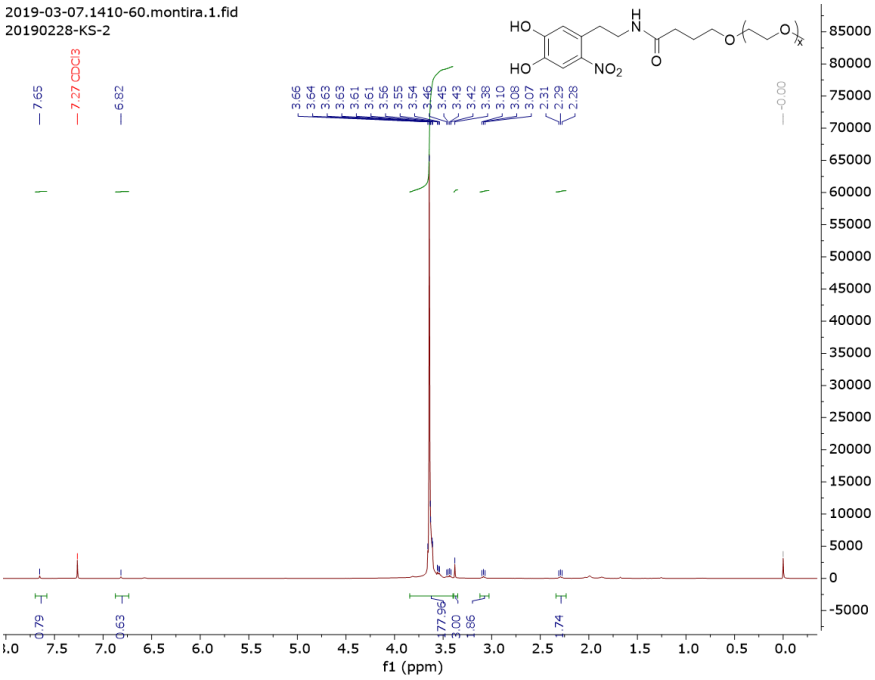

(3,4-Dihydroxyphenyl)acetic acid methyl ester (**4-3**)

^{1}H NMR

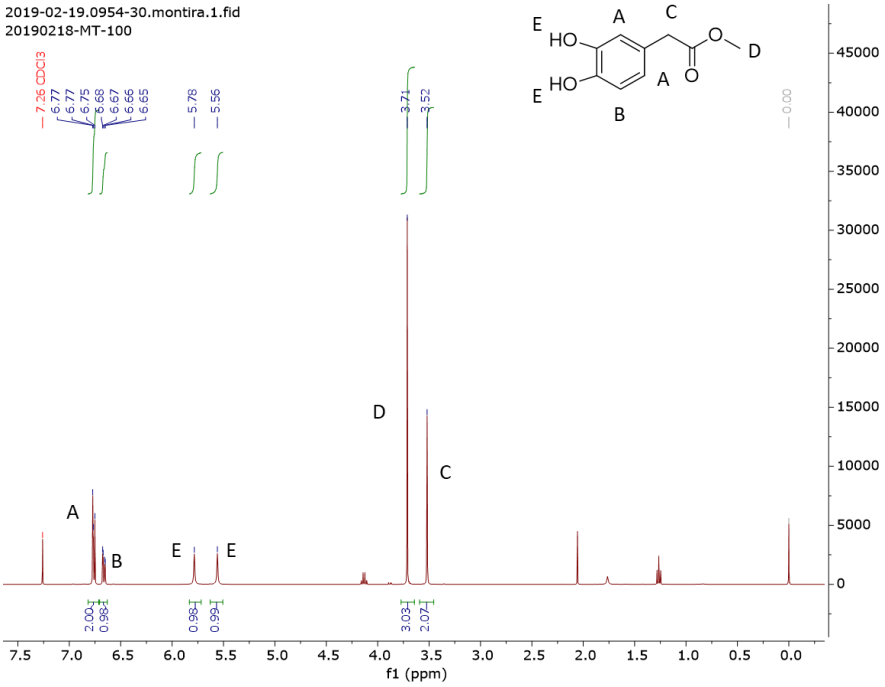

Hydroxytyrosol(acetonide) (DOPET(acetonide), **4-4**)

^{1}H NMR

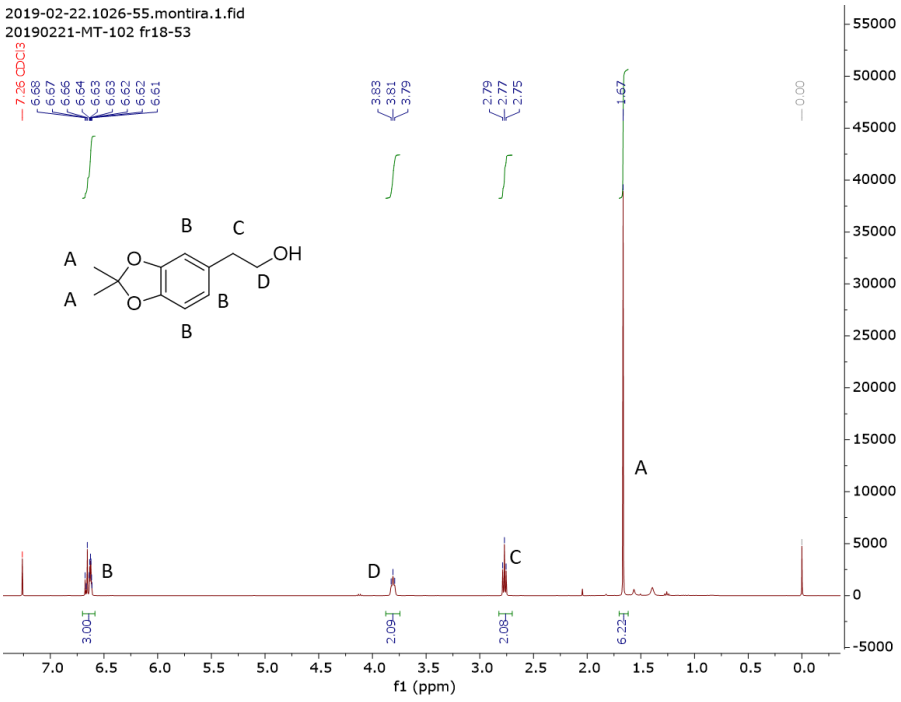

DOPET(acetonide)-PFtB$_{TRI}$ (**4-5**)

^{1}H NMR

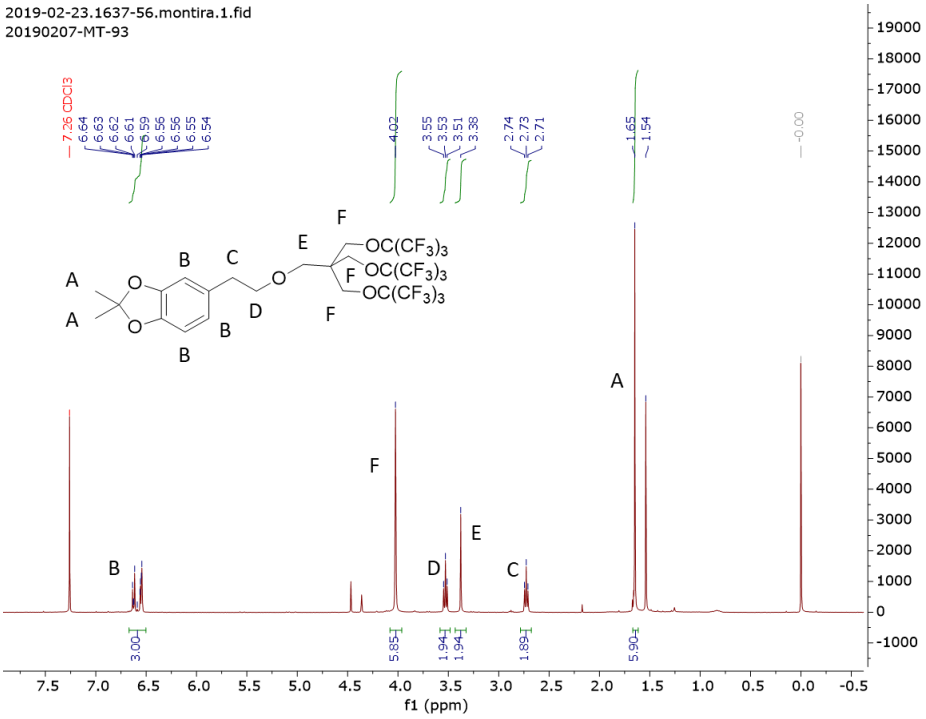

^{19}F NMR

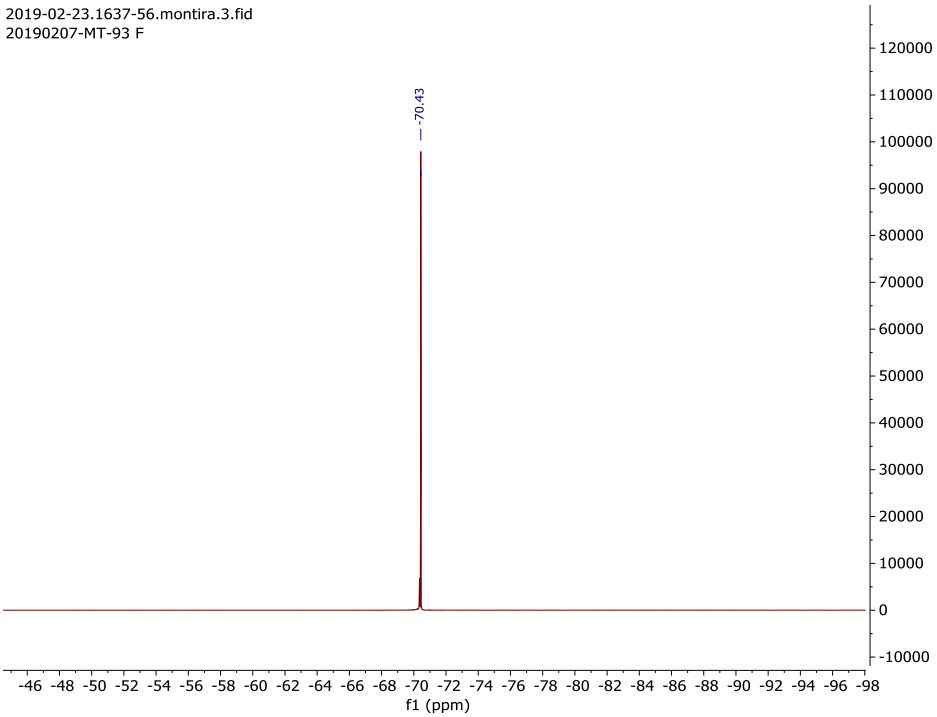

NitroDOPET(acetonide)-PFtB$_{TRI}$ (**4-6**)

^{1}H NMR

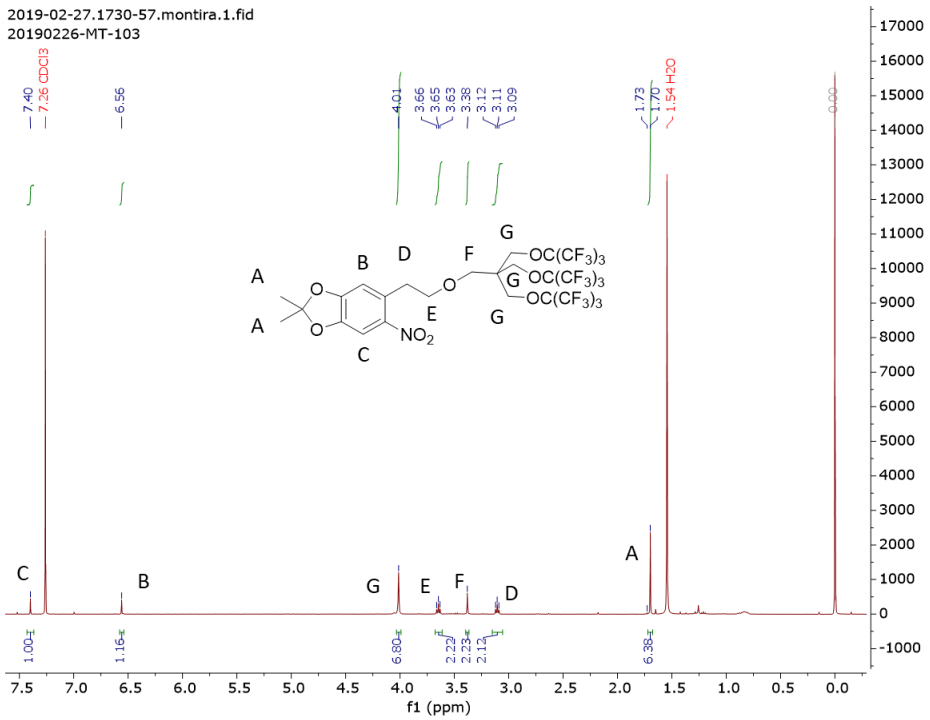

^{19}F NMR

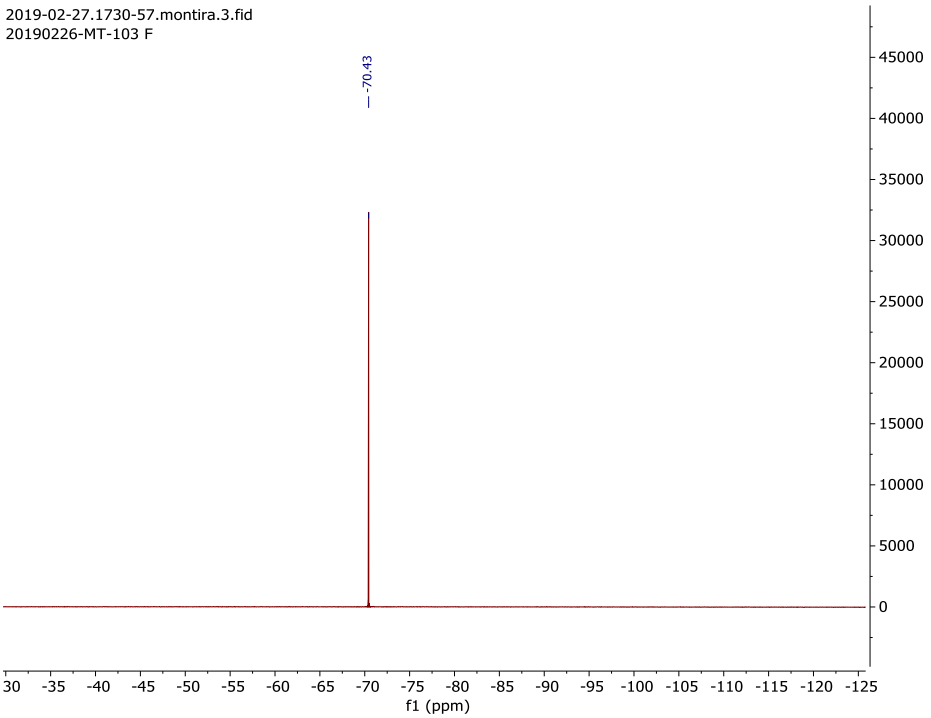

NitroDOPET-PFtB$_{TRI}$ (**4-7**)

^{1}H NMR

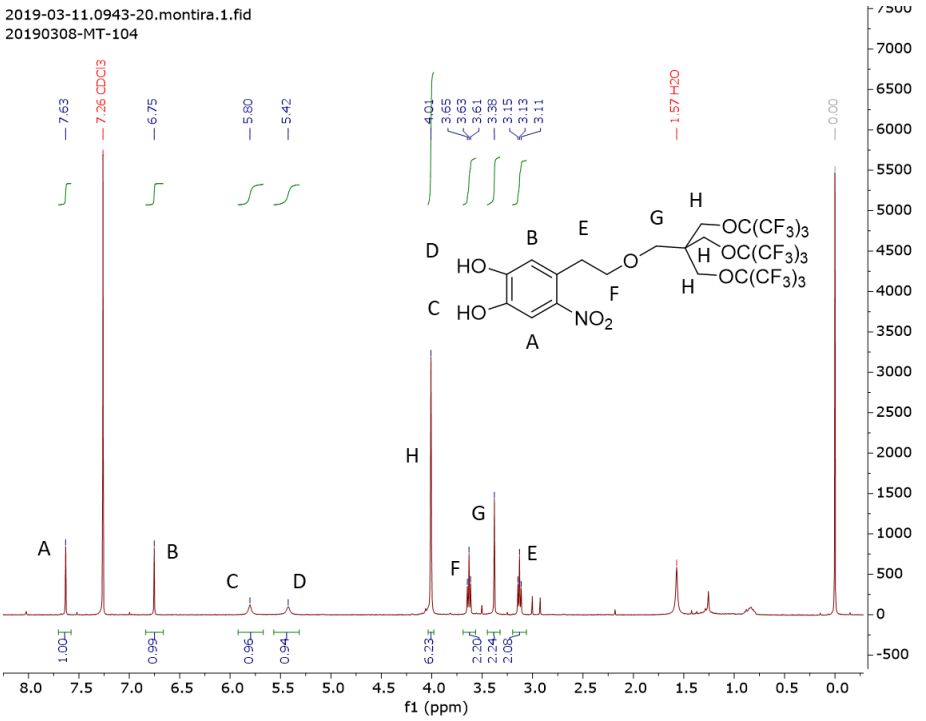

^{19}F NMR

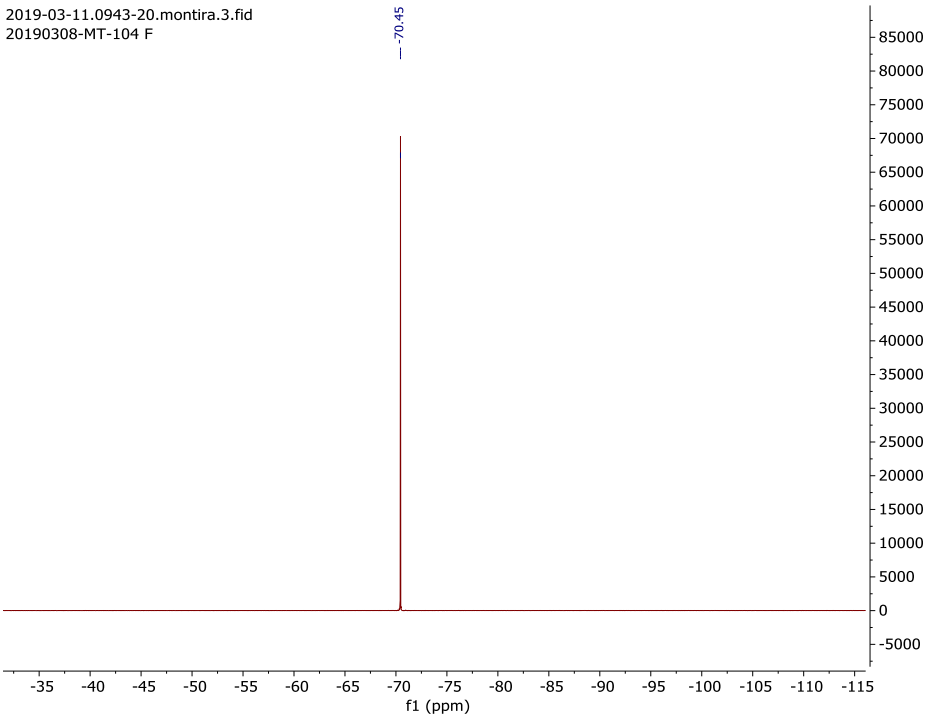

2-phenyl-1,3-dioxan-5-ol (**4-8**)

^{1}H NMR

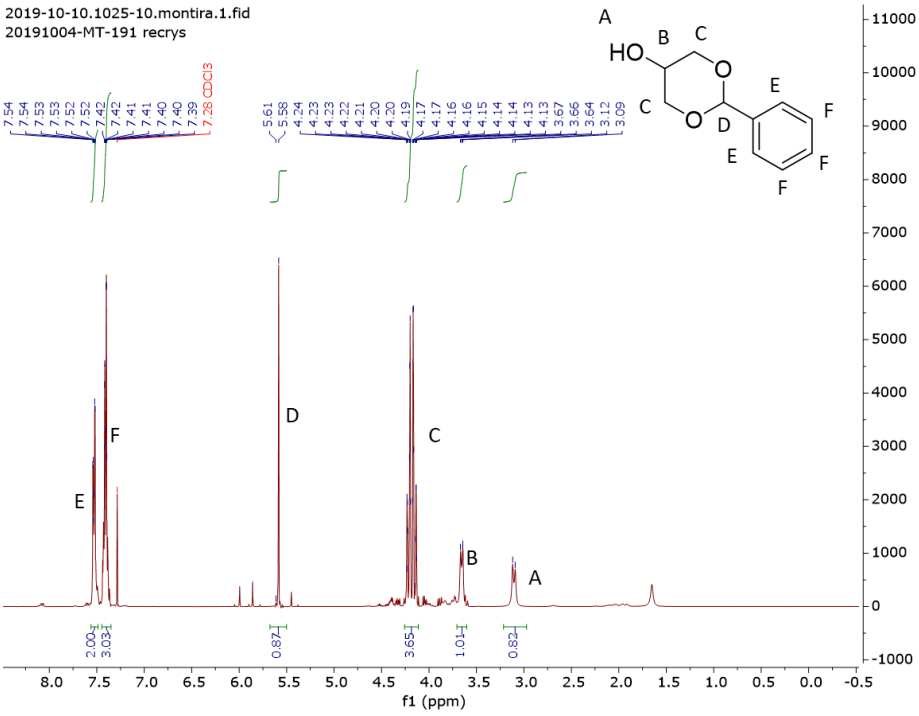

^{13}C NMR

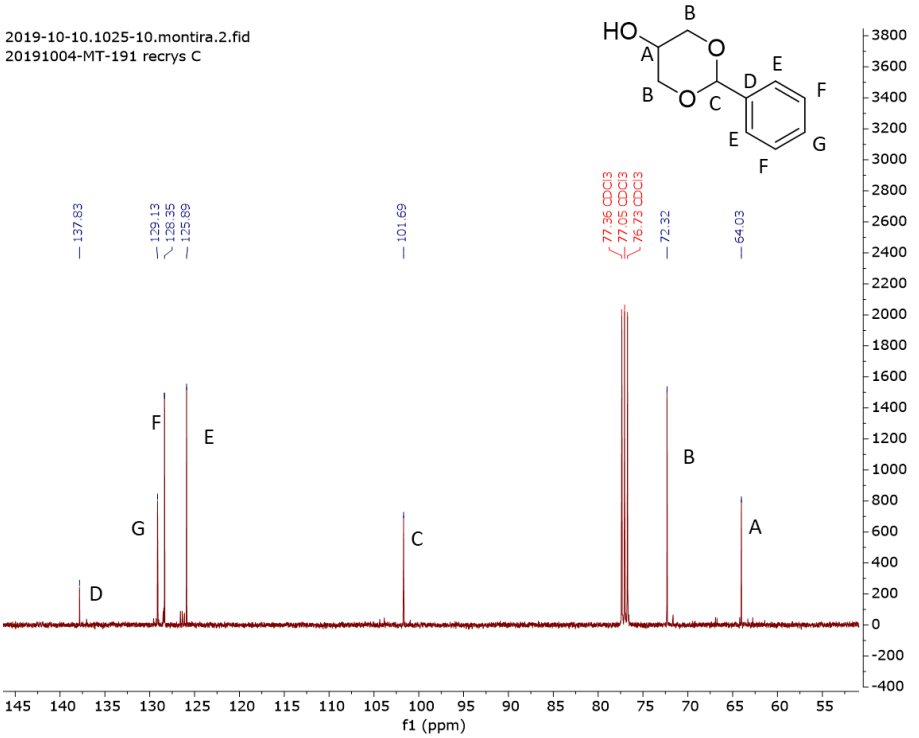

M2-OMs

^{1}H NMR

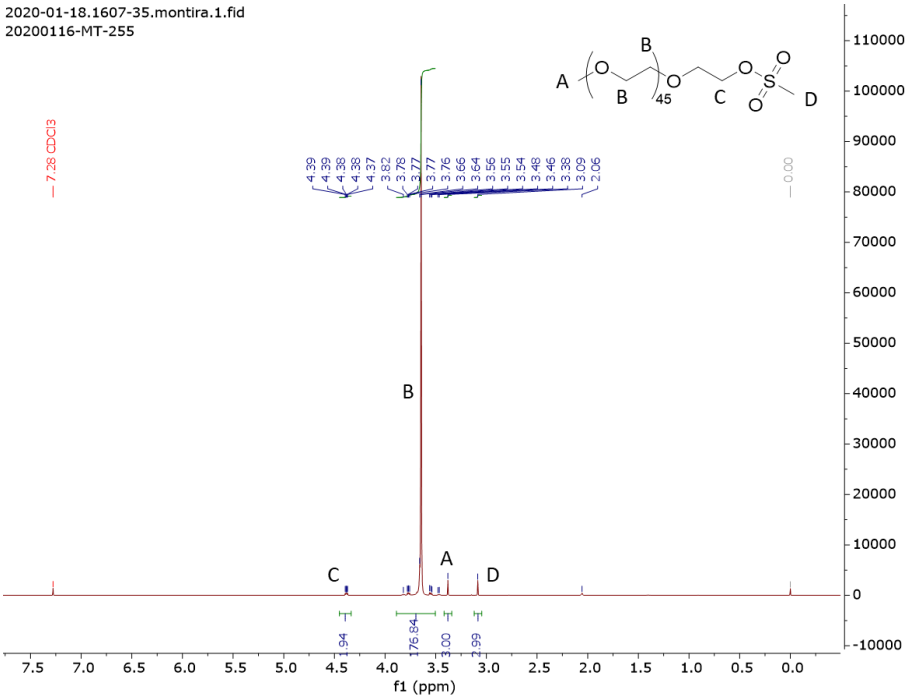

Benzylidene acetal-M2 (**4-9**)

^{1}H NMR

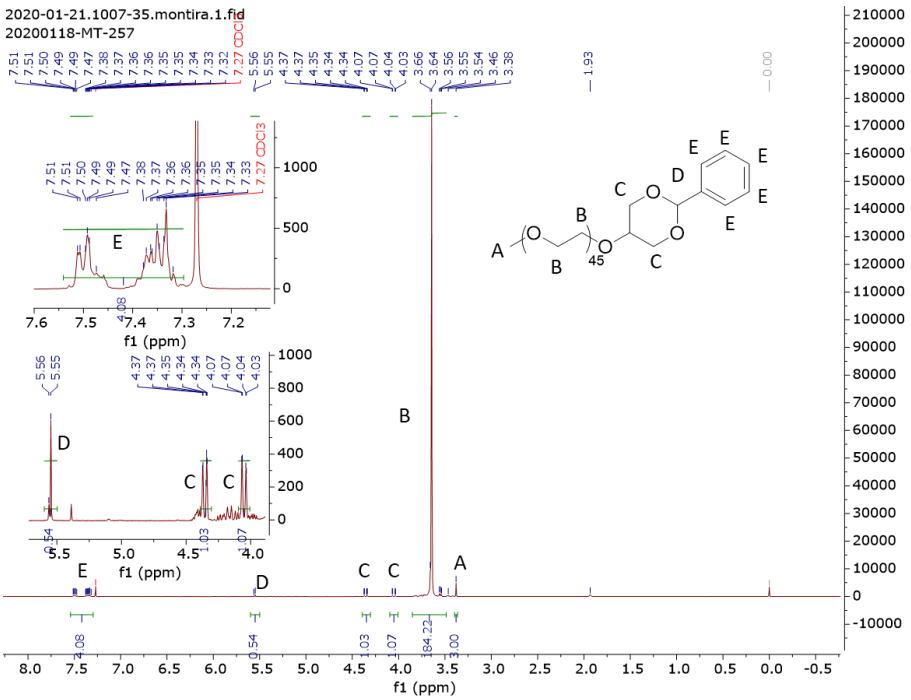

M2diOBn/OH (**4-10**), contains free M2-OH

^{1}H NMR

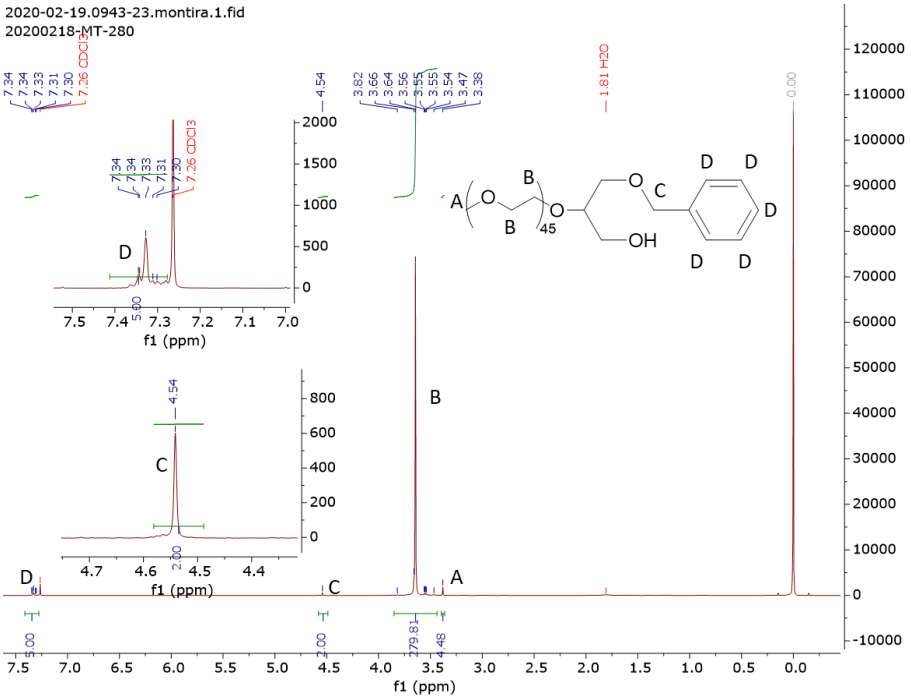

M2diOBn/OMs (**4-11**), contains free M2-OMs

^{1}H NMR

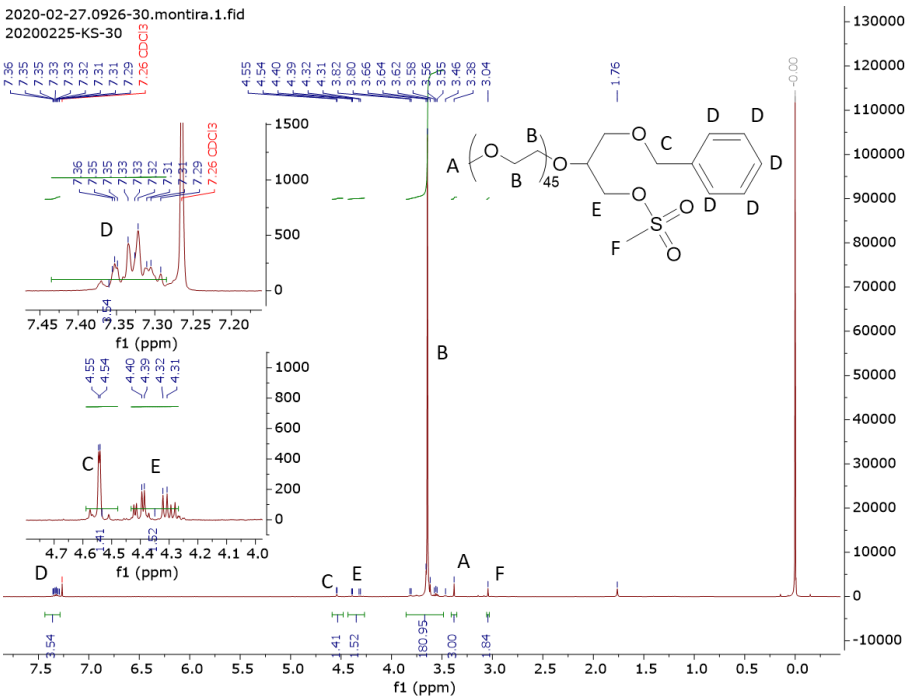

M2diDOPET(acetonide)/OBn (**4-12**)

^{1}H NMR

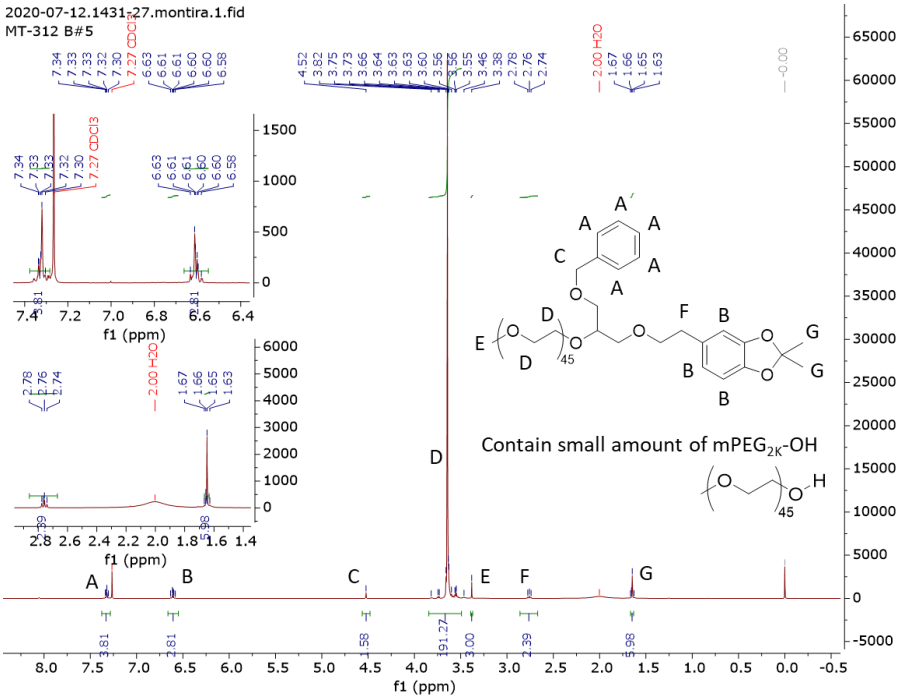

M2diDOPET(acetonide)/OH" (**4-13**)

^{1}H NMR

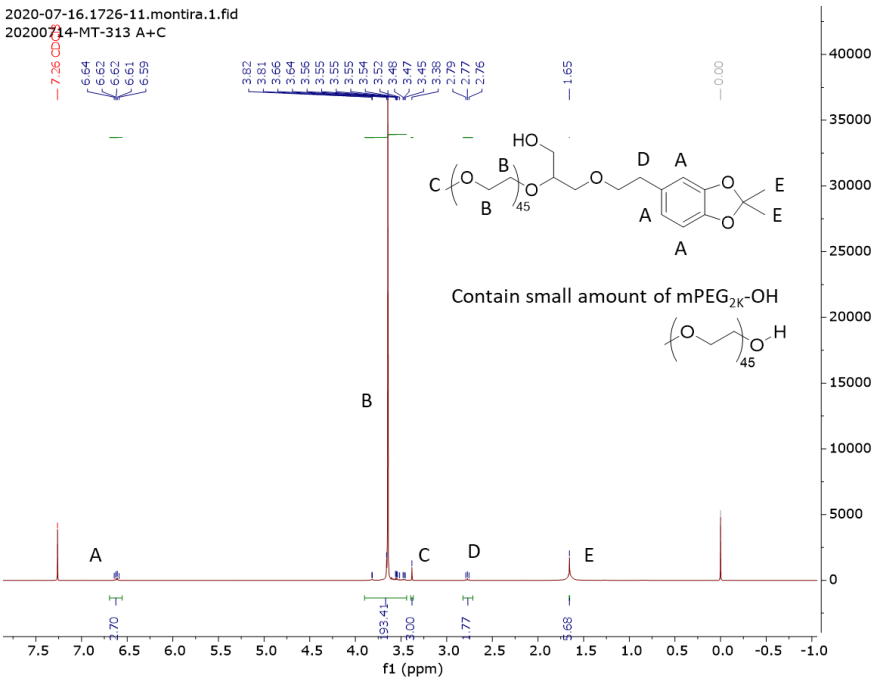

M2diDOPET(acetonide)/OMs (Intermediate of **4-14**)

^{1}H NMR

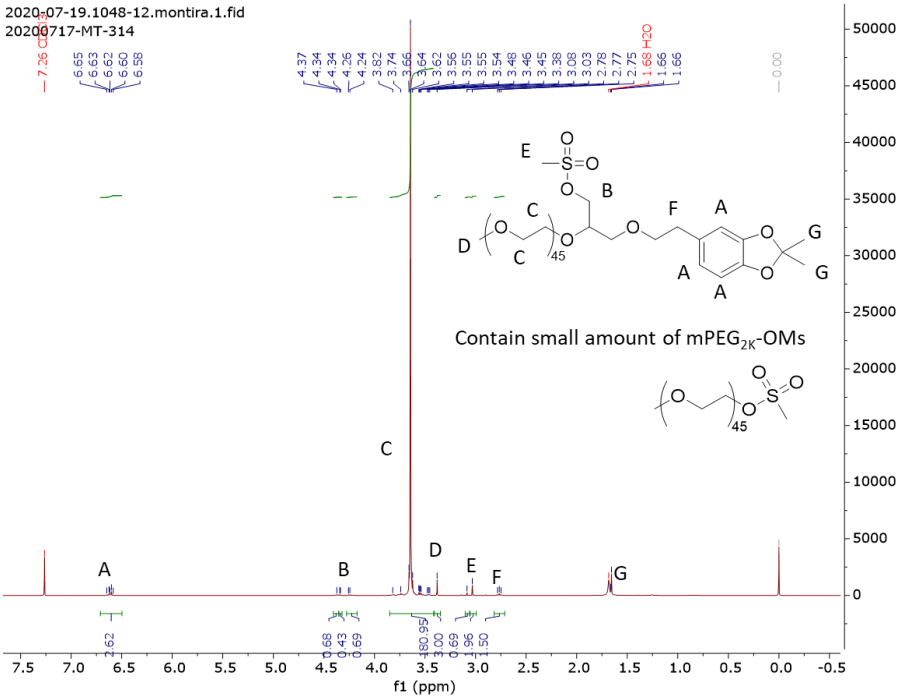

M2diDOPET(acetonide)/PFtB$_{TRI}$ (**4-14**)

^{1}H NMR

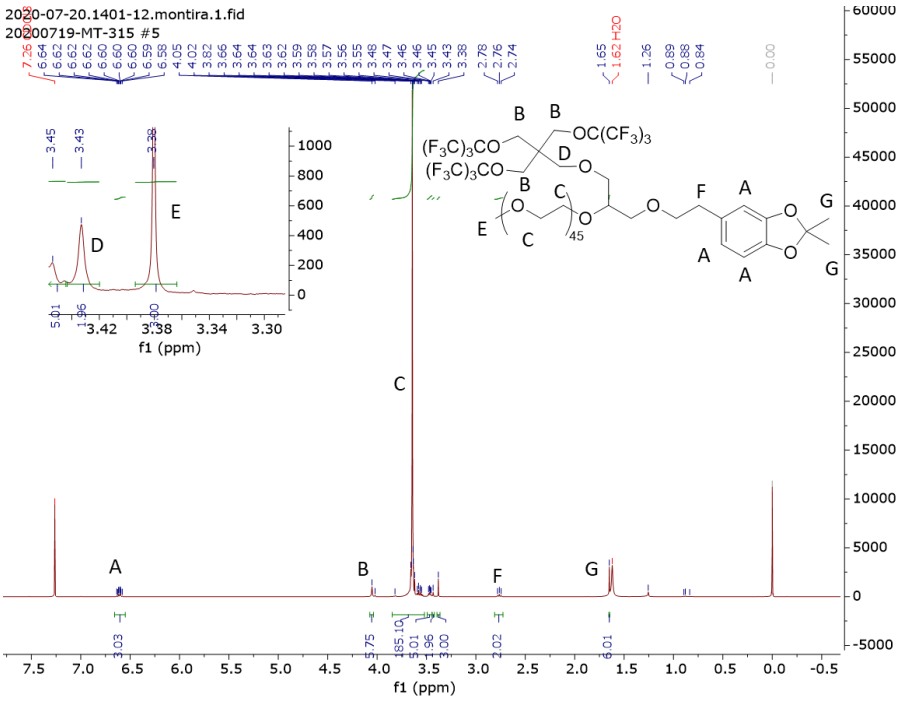

^{19}F NMR

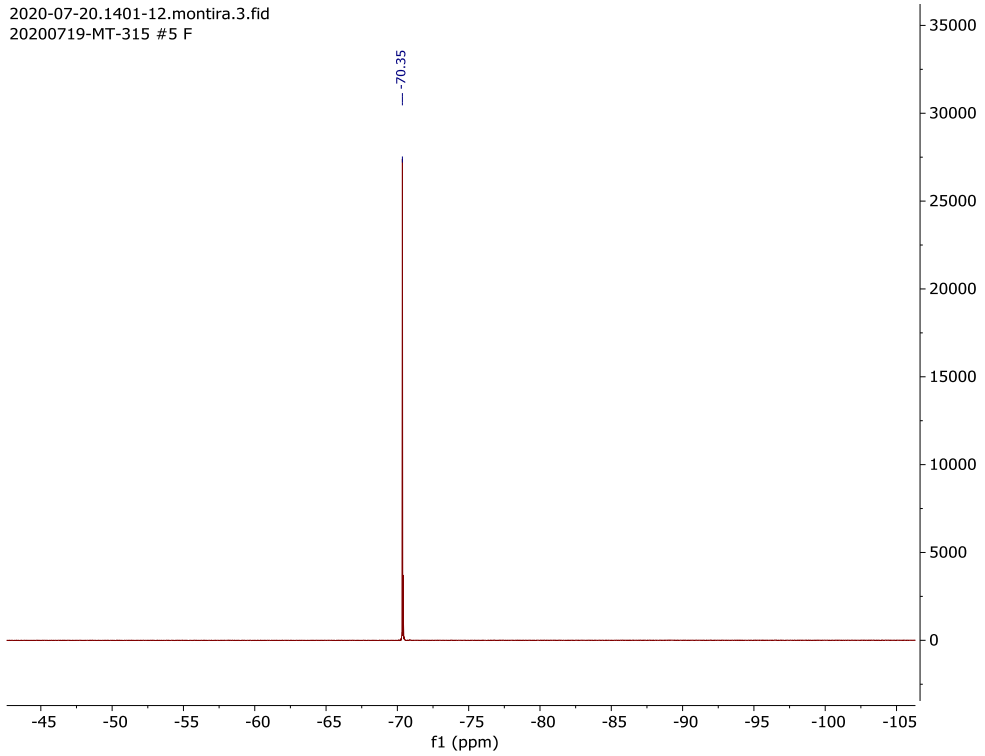
2020-07-20.1401-12.montira.3.fid
20200719-MT-315 #5 F
-70.35
35000
30000
25000
20000
15000
10000
5000
0
-45
-50
-55
-60
-65
-70
-75
-80
-85
-90
-95
-100
-105
f1 (ppm)

A3.1.4 Appendix 1: ^{1}H NMRs, ^{19}F NMRs, and ^{31}P NMRs

mPEG-PO_3H_2 (**A1-1**)

^{1}H NMR

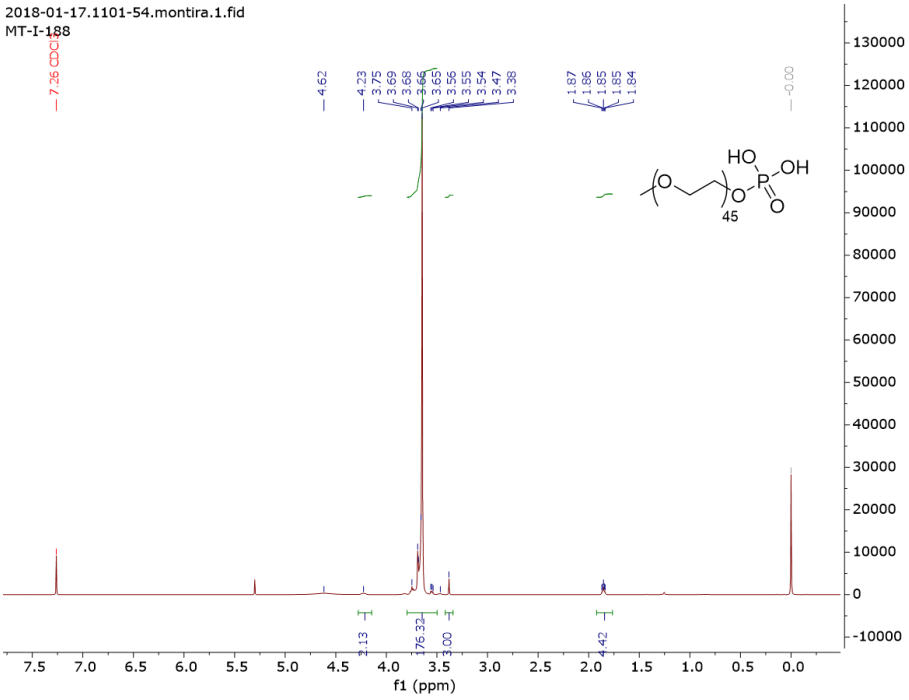

^{31}P NMR

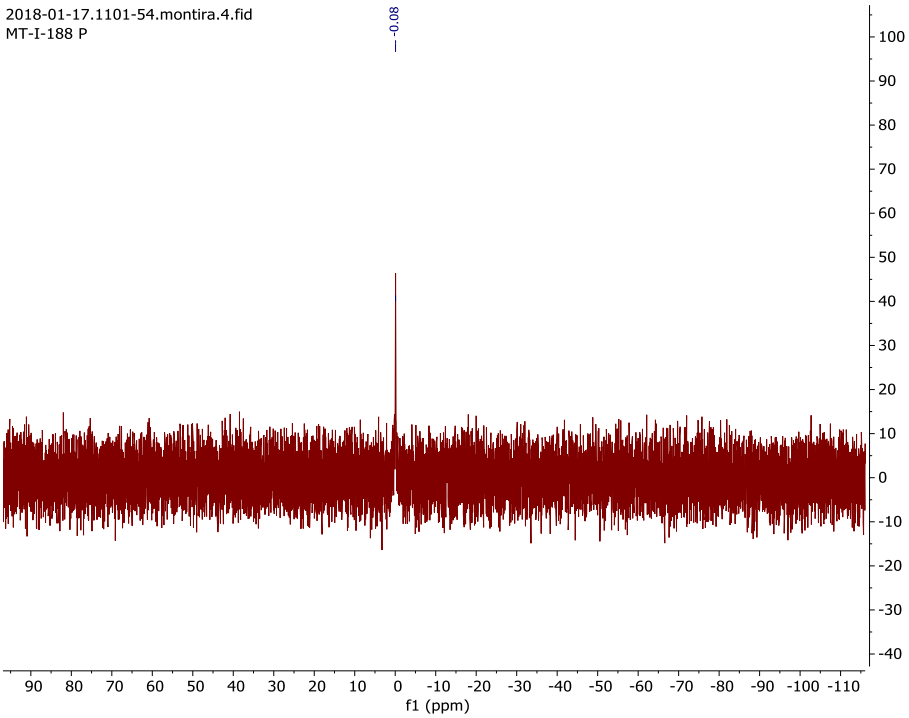

PFtB$_{TRI}$-diphenyl phosphate (**A1-2**)

^{1}H NMR

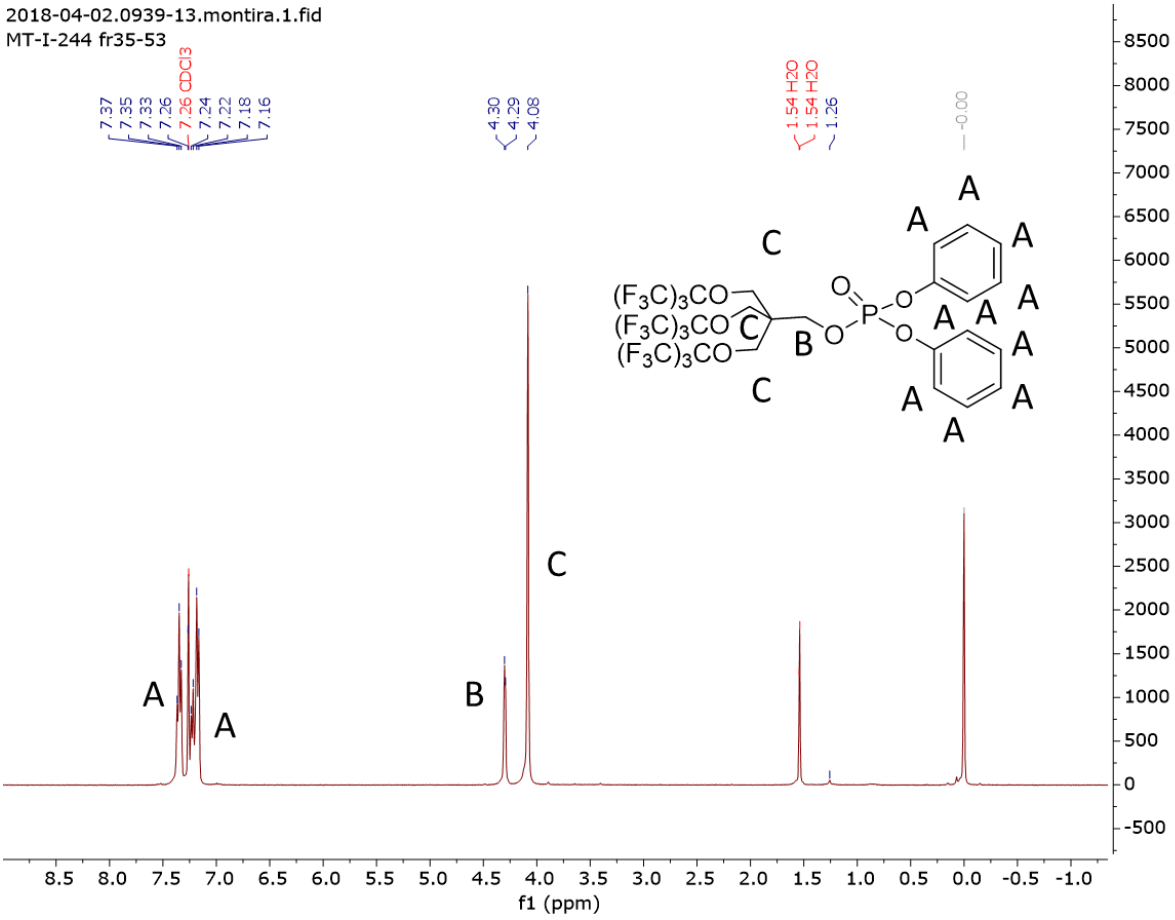

^{19}F NMR and ^{31}P NMR

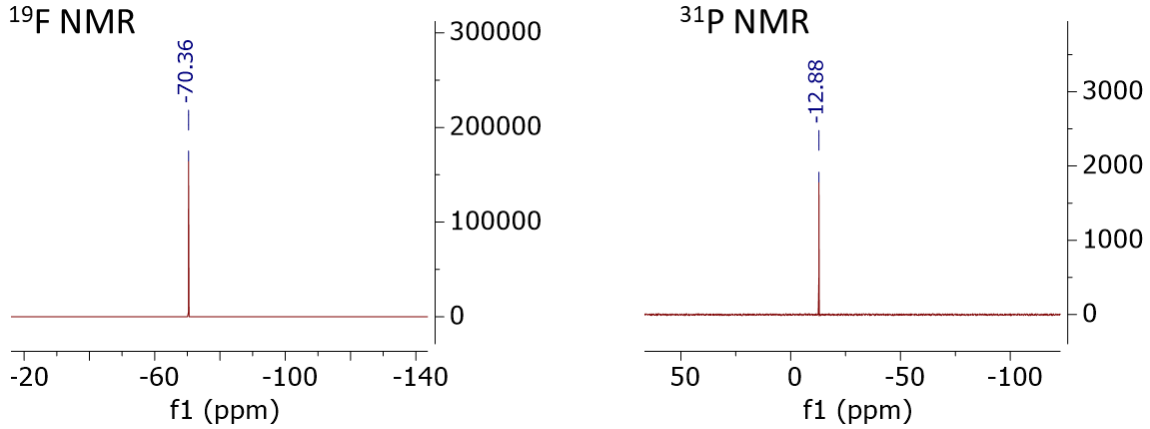

PFtB$_{TRI}$-diphenyl phosphate (**A1-3**)

^{1}H NMR

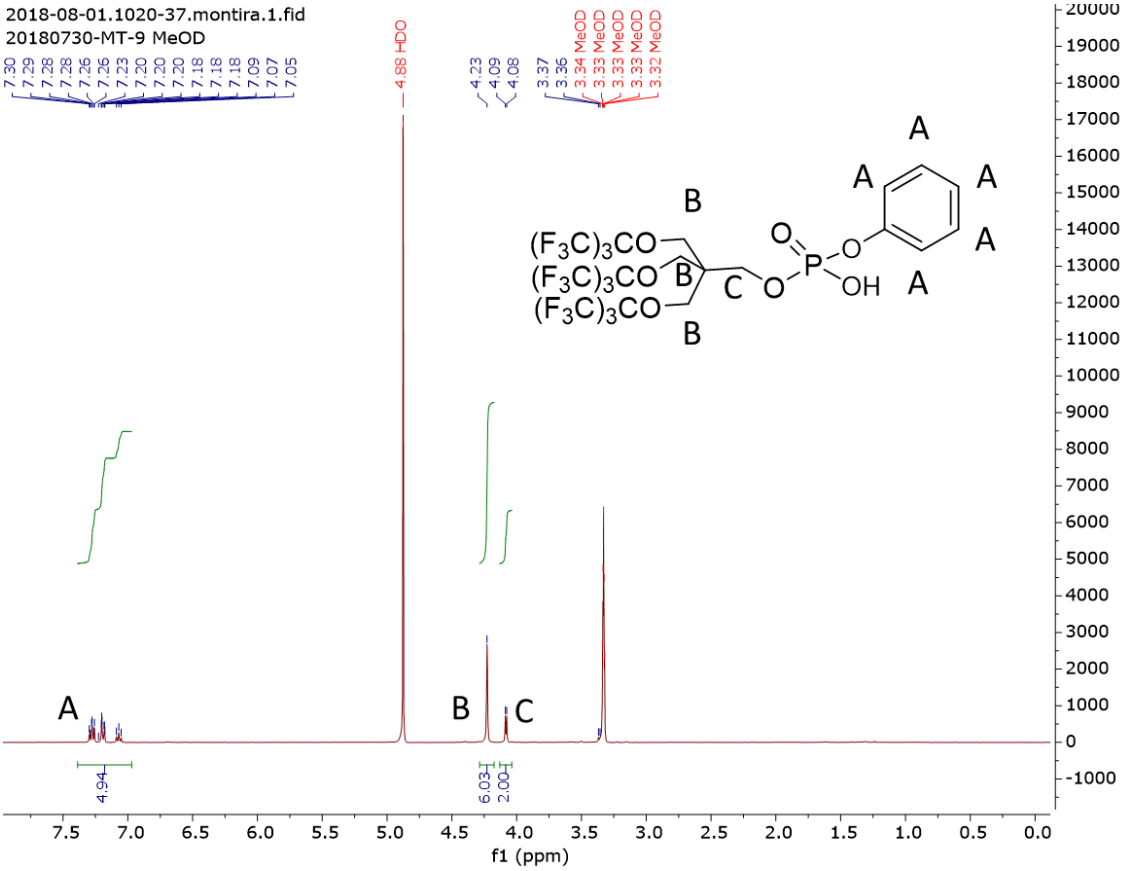

^{19}F NMR and ^{31}P NMR

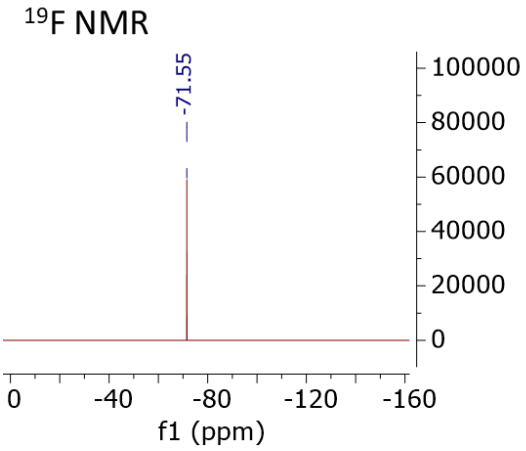

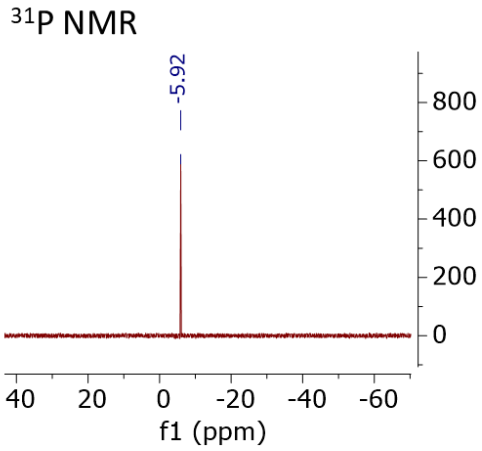

A3.2 Matrix Assisted Laser Desorption/Ionization (MALDI) Mass Spectra

A3.2.1 Chapter 2

M2H10PFtB$_{TRI}$ (**2-6**)

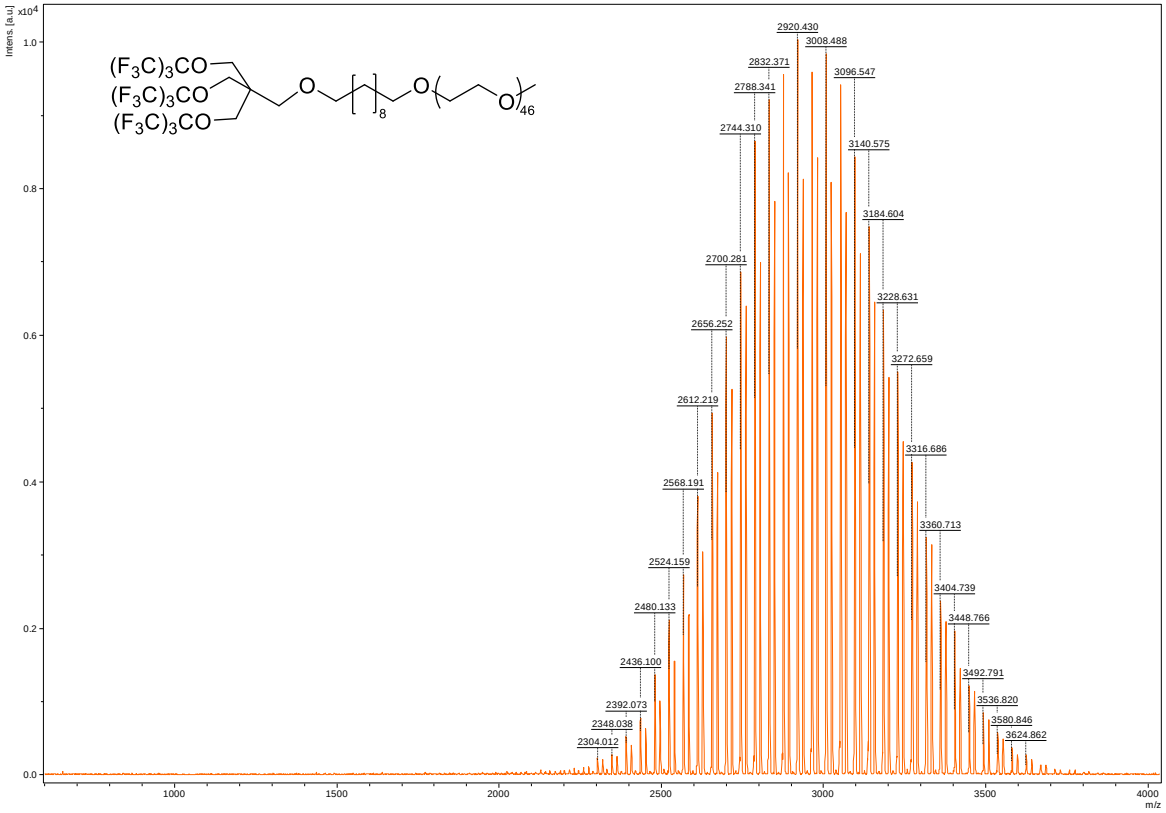

BnO-P2-OH (**2-7**)

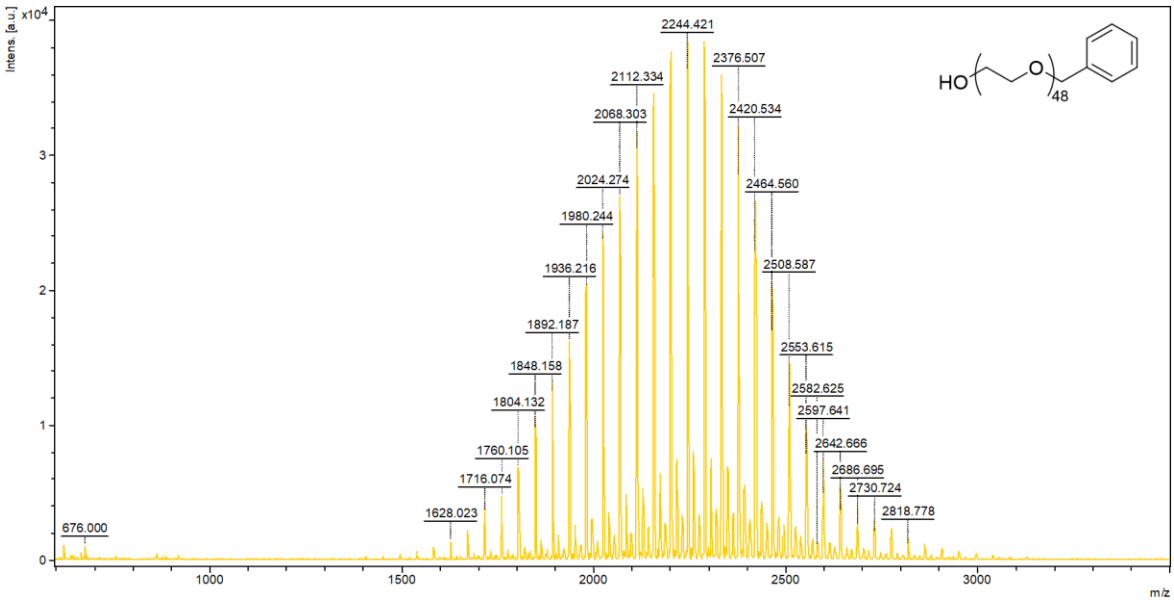

BnO-P2H10PFtB$_{TRI}$ (**2-9**)

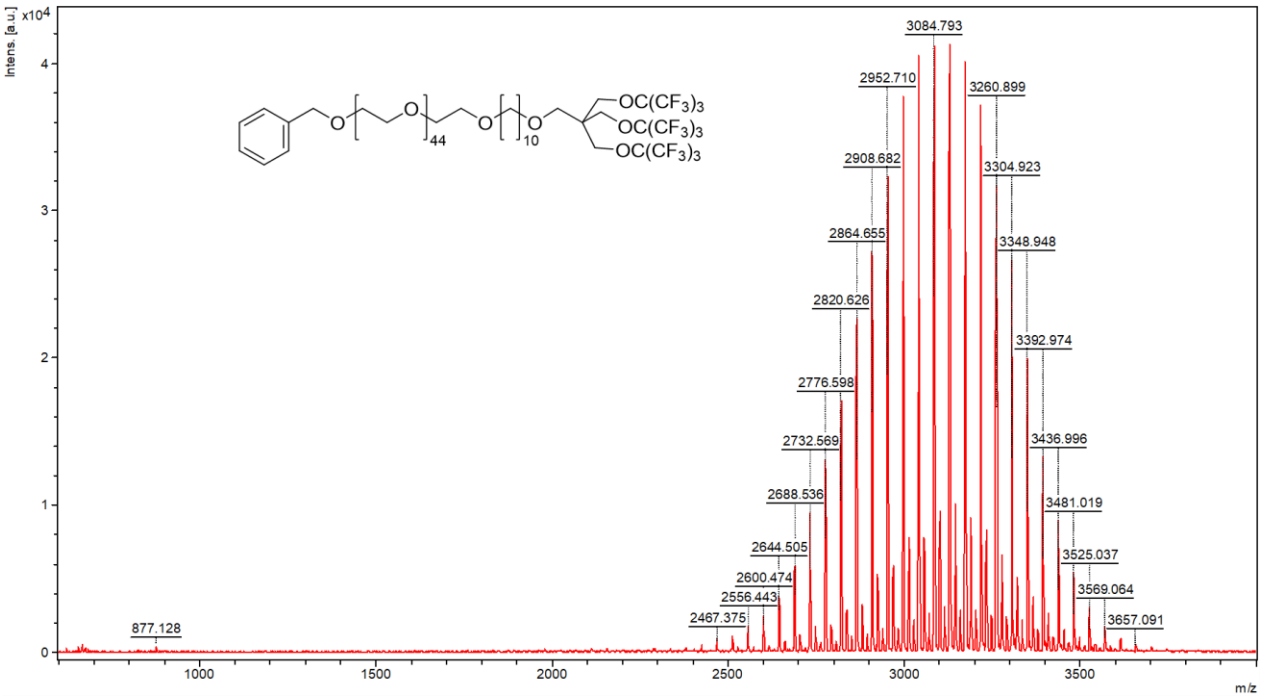

PMPI-P2H10PFtB$_{TRI}$ (**2-11**)

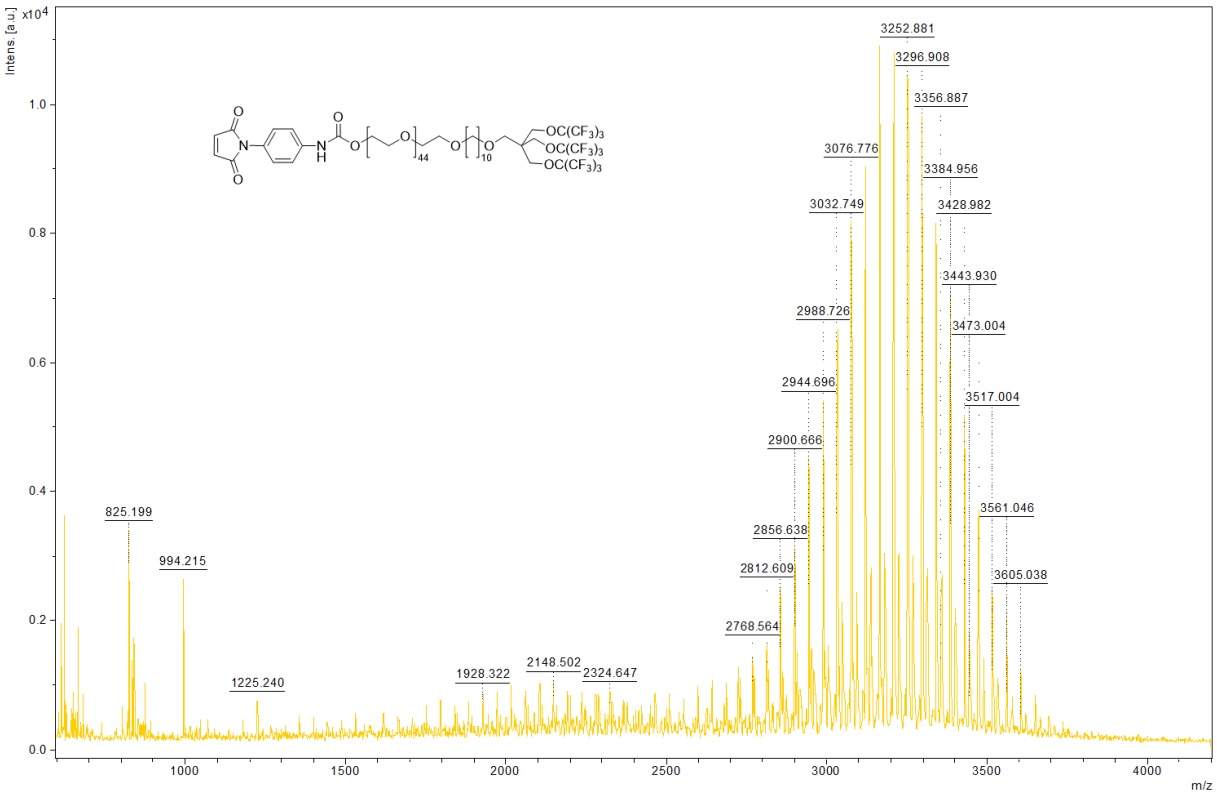

iRGD-PMPI-P2H10PFtB$_{TRI}$ (**2-12**)

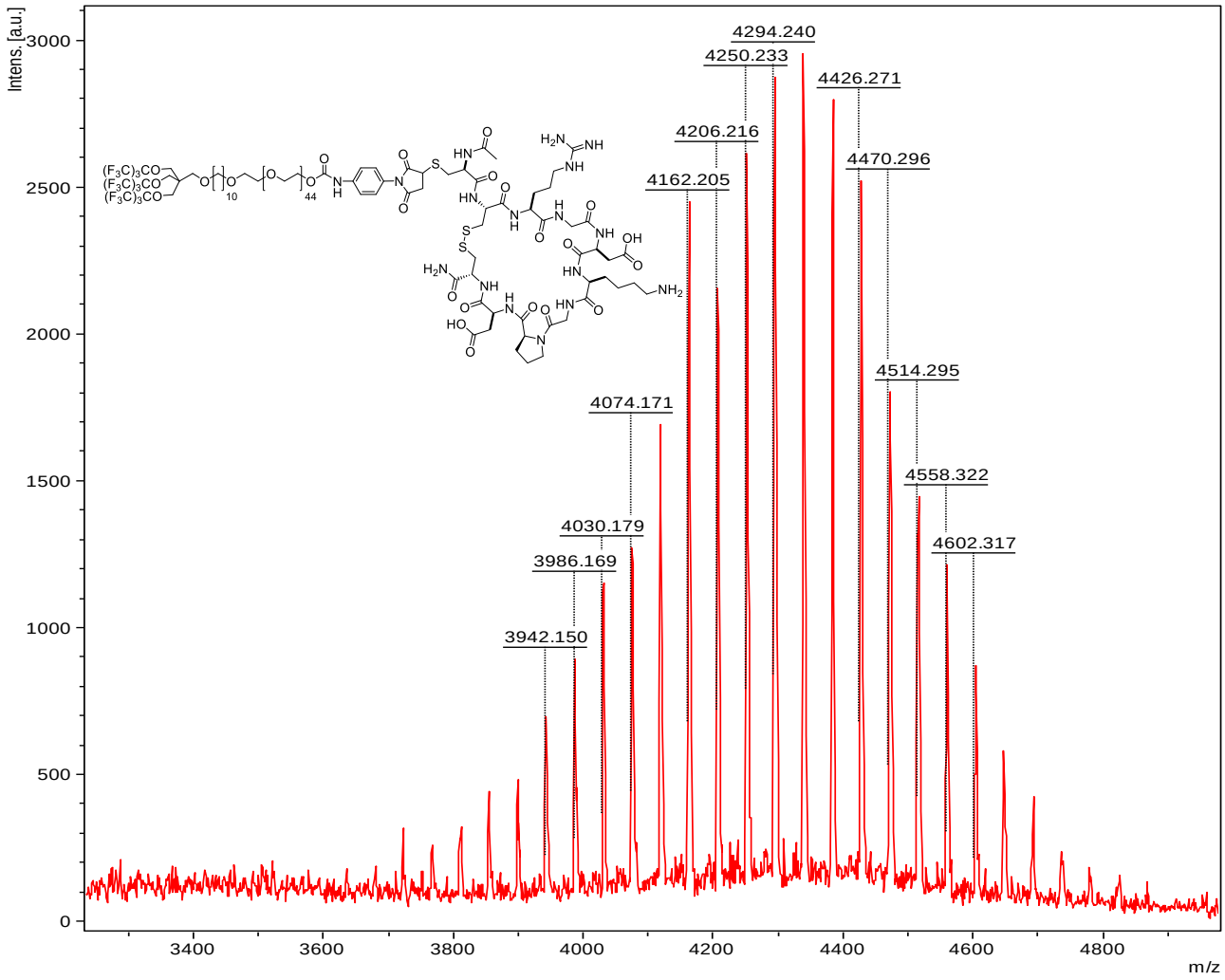

A3.2.2 Chapter 3

Benzylidene acetal-M2 (**3-3**)

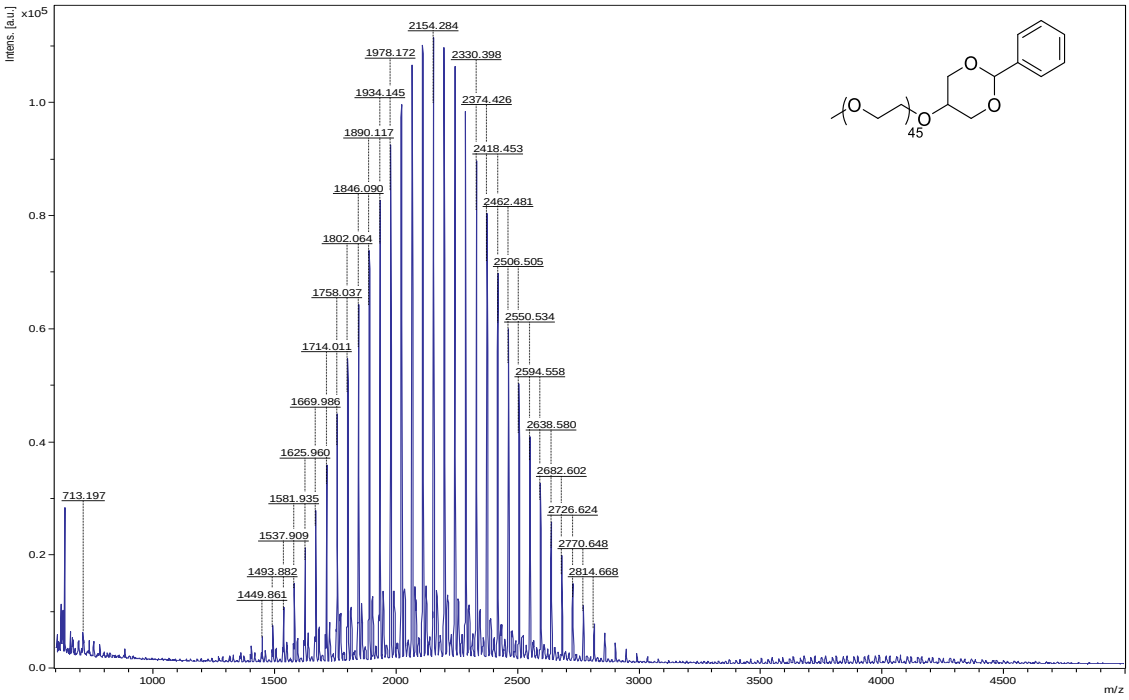

M2-diOH (**3-4**)

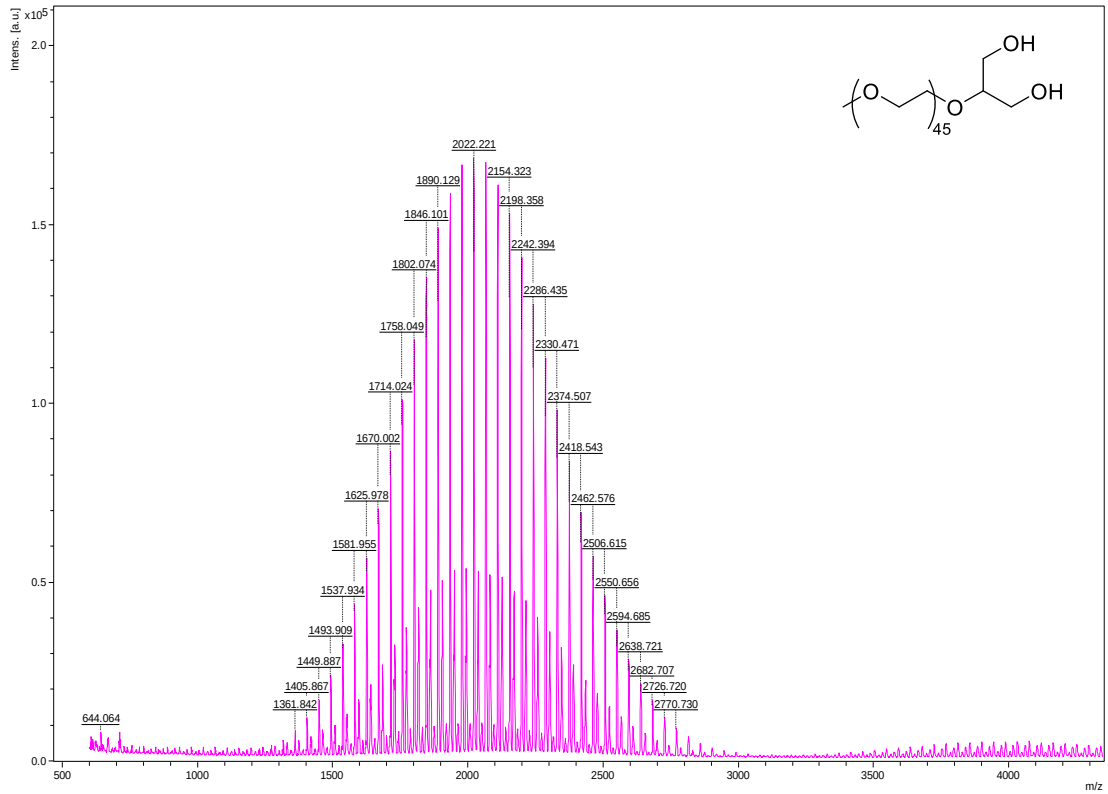

M2diF8H18 (**3-6**)

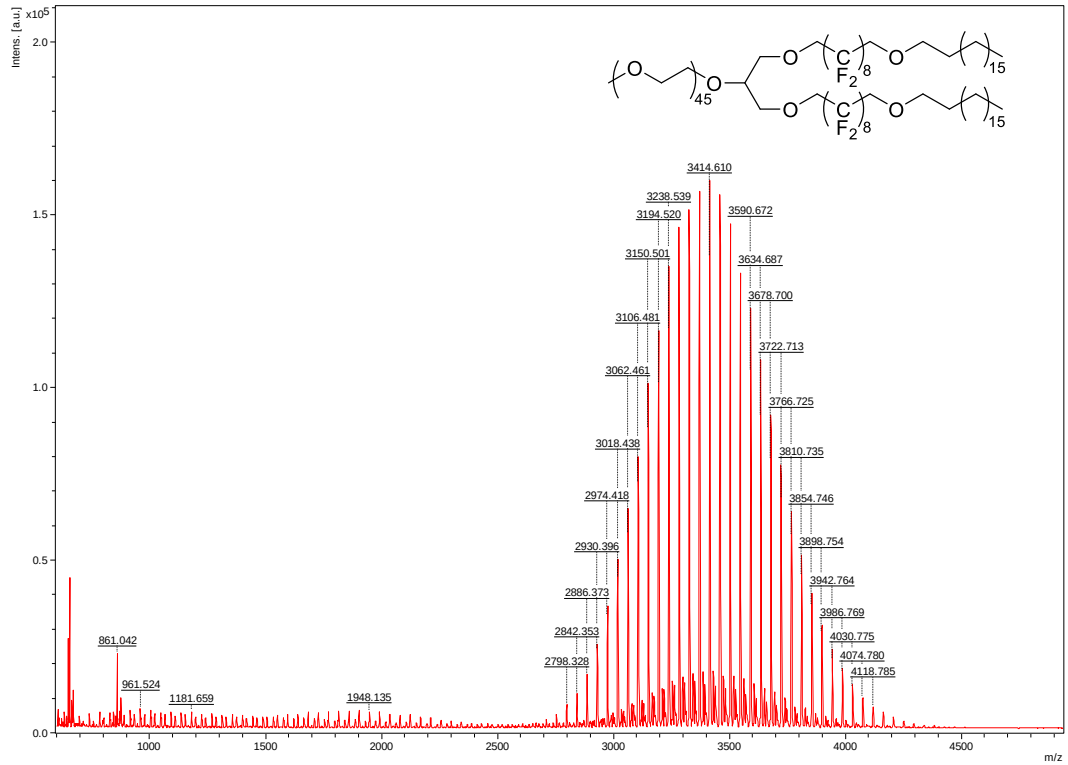

M2diOBn/F8 (**3-9**)

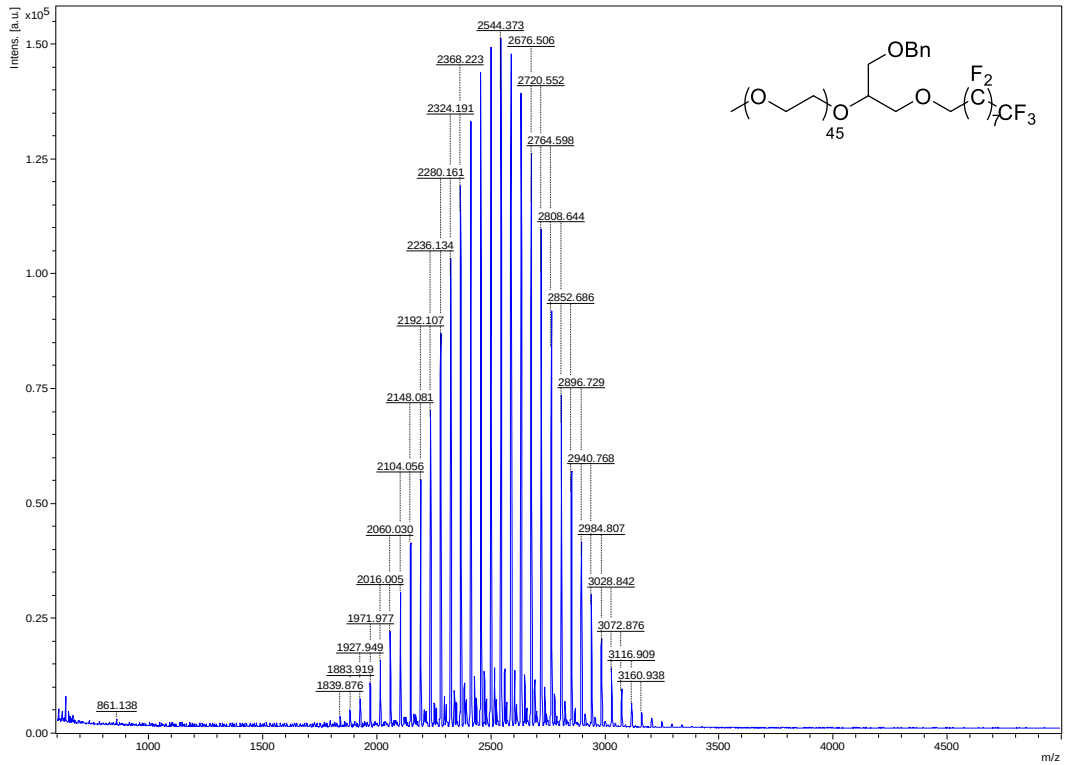

M2diOH/F8 (**3-10**)

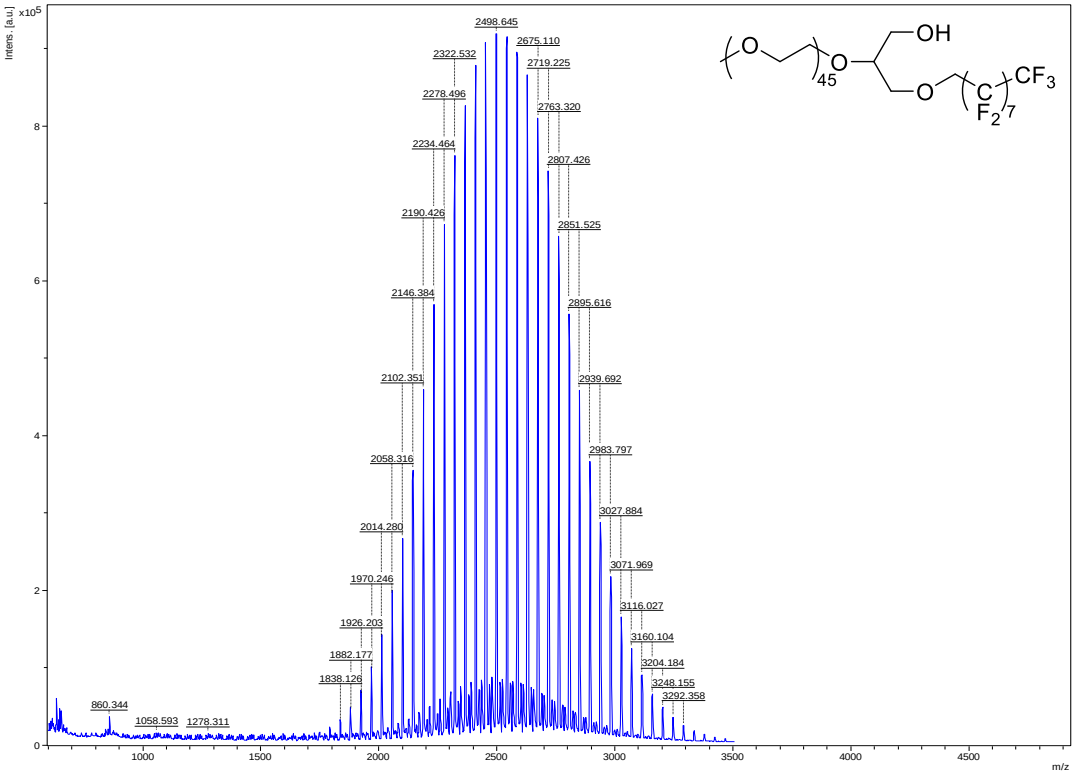

M2diF8H18/F8 (**3-12**)

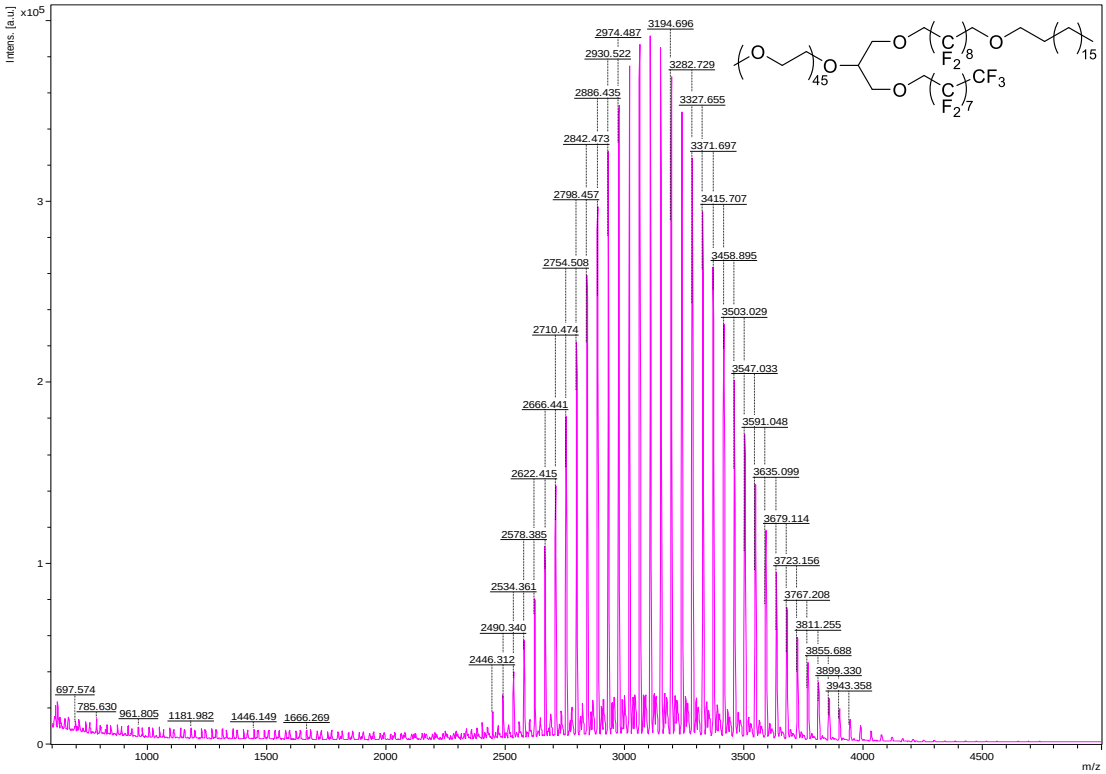

A3.2.3 Chapter 4

M2diDOPET(acetonide)/OBn (**4-12**)

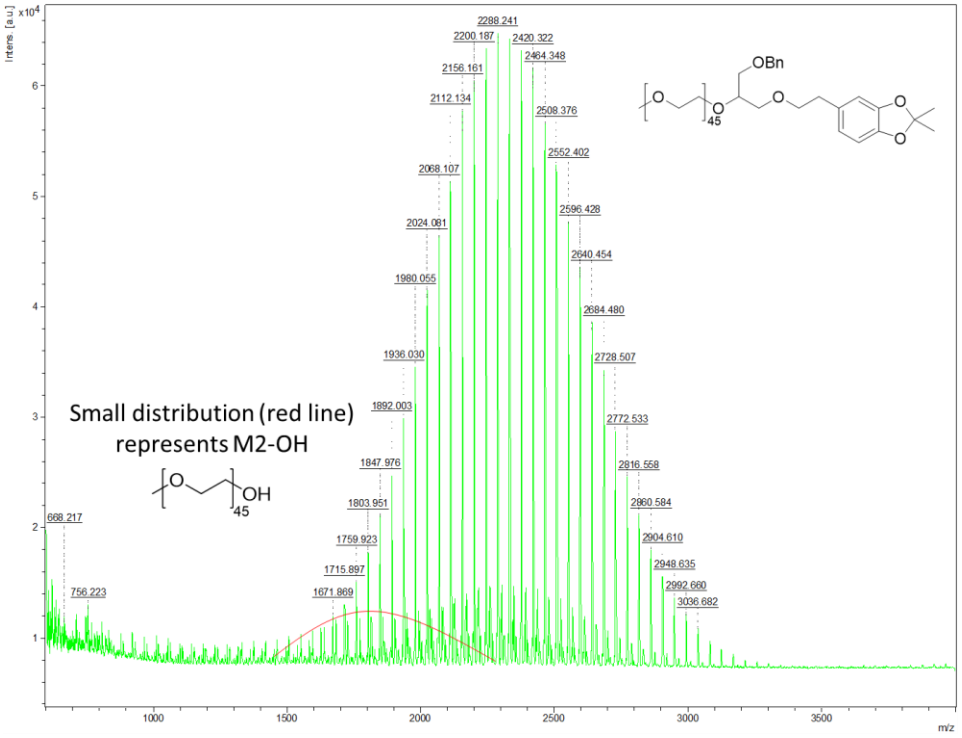

"M2diDOPET(acetonide)/PFtB$_{TRI}$" (**4-14**)

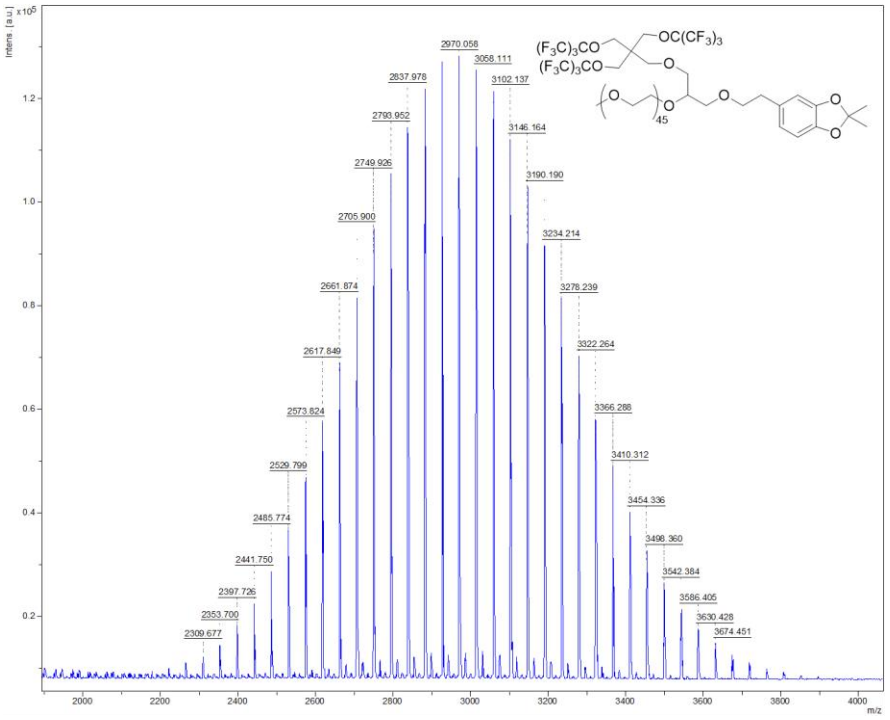

A3.3 HPLC

BnO-P2-OH (**2-4**)

	Inj. Number	Peak Name	R. Time	Area	Sample Descrip.
1	1.00	1	11.49	1099740.00	IT-I-37 Fr 158

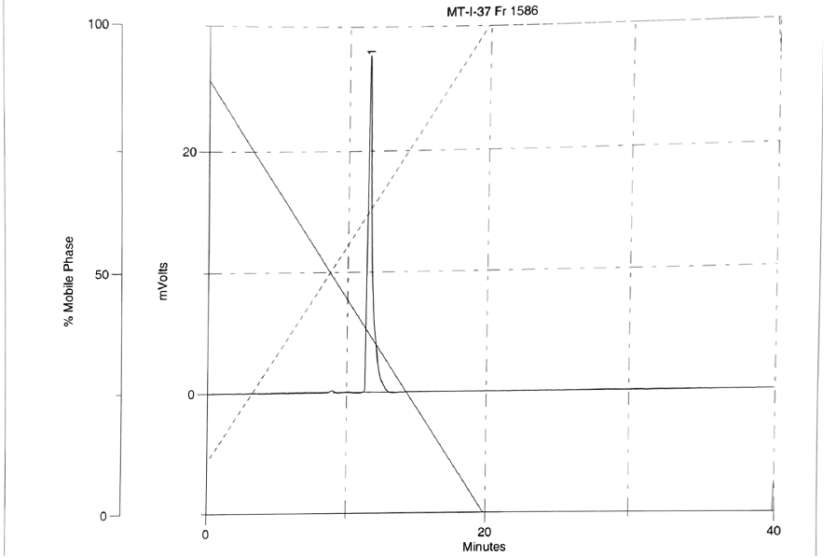

iRGD-PMPI-P2H10PFtB$_{TRI}$ (**2-9**)

	Inj. Number	Peak Name	R. Time	Area	Sample Descrip.
1	1.00	1	14.71	366888.31	MT-I-134

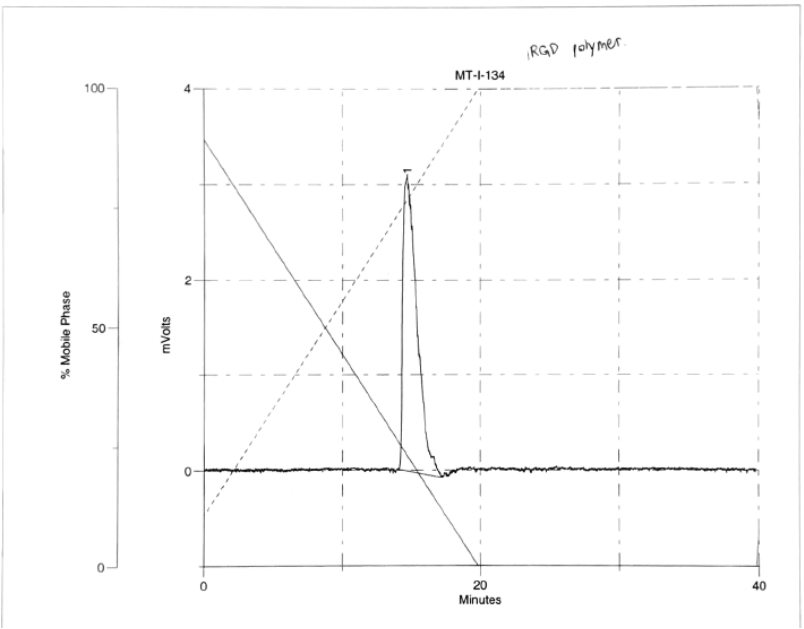

A3.4 CMC data measured by Pyrene 1:3 ratio method

A3.4.1 CMC of M2H10PFtB$_{TRI}$

Sample No.	Sample Conc. (mM)	I_1 (374 nm)	I_3 (384 nm)	I_1/I_3	Log(M)
P0	0	2.37793	1.51459	1.570016	-
P1	0.000418487	2.31415	1.49384	1.549128	-6.37832
P2	0.000836974	2.07581	1.30157	1.594851	-6.07729
P3	0.001673948	2.21893	1.43311	1.548332	-5.77626
P4	0.003347897	2.02881	1.33728	1.517117	-5.47523
P5	0.006695793	2.37915	1.633	1.45692	-5.1742
P6	0.016739483	2.96448	2.12738	1.393489	-4.77626
P7	0.033478967	3.85437	2.86285	1.34634	-4.47523
P8	0.066957934	4.4986	3.40424	1.32147	-4.1742
P9	0.167394834	7.17682	5.50537	1.303604	-3.77626
P10	0.334789668	7.34985	5.67474	1.295187	-3.47523
P11	0.502184503	8.69629	6.70563	1.296864	-3.29914
P12	0.669579337	8.29193	6.39954	1.295707	-3.1742

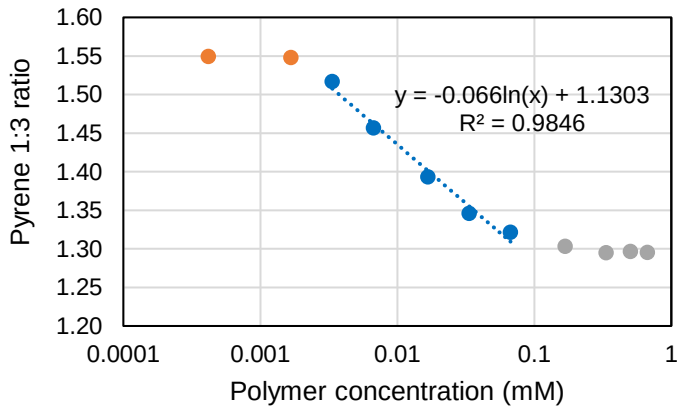

A1	1.55	
A2	1.3	
(A1+A2)/2	1.425	

Finding x0 by sub the above value in the equation y=-0.066ln(x) +1.1303

x_0	0.01150295	mM
CMC (=x_0)	11.5029528	µM
log(M)	-4.9391907	± 0.01

A3.4.2 CMC of M2F8H18

		1st run			2nd run			3rd run		
	Sample Conc. (mM)	I_1 (374)	I_3 (384)	I_1/I_3	I_1 (374)	I_3 (385)	I_1/I_3	I_1 (374)	I_3 (385)	I_1/I_3
P1	0.000461	2.062	1.789	1.153	2.042	1.358	1.504	1.937	1.301	1.489
P2	0.000922	1.772	1.232	1.439	1.970	1.330	1.481	2.192	1.490	1.471
P3	0.001844	1.749	1.235	1.417	1.967	1.330	1.479	2.194	1.662	1.320
P4	0.003689	1.449	1.116	1.298	2.045	1.419	1.442	2.234	1.562	1.430
P5	0.007377	1.498	1.147	1.306	2.160	1.586	1.362	1.535	1.156	1.328
P6	0.018443	1.510	1.242	1.216	2.765	2.235	1.237	1.945	1.646	1.182
P7	0.036886	3.382	2.840	1.191	3.075	2.650	1.161	3.475	3.097	1.122
P8	0.073773	4.536	3.984	1.139	4.605	4.085	1.127	4.411	4.024	1.096
P9	0.184432	6.165	5.353	1.152	6.473	5.828	1.111	6.222	5.733	1.085
P10	0.368863	7.285	6.262	1.163	7.791	7.013	1.111	7.220	6.638	1.088
P11	0.553295	8.266	7.134	1.159	8.530	7.662	1.113	6.376	5.968	1.068
P12	0.737727	5.994	5.264	1.139	8.201	7.446	1.101	8.193	7.507	1.091

1st run

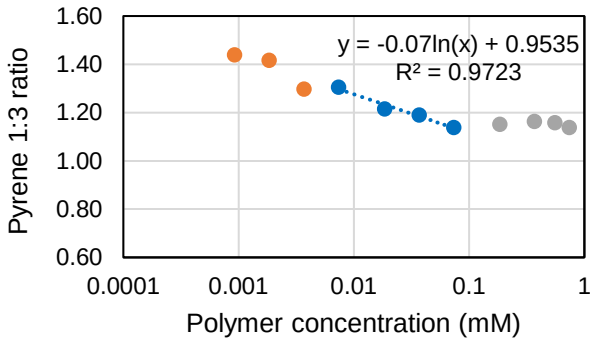

2nd run

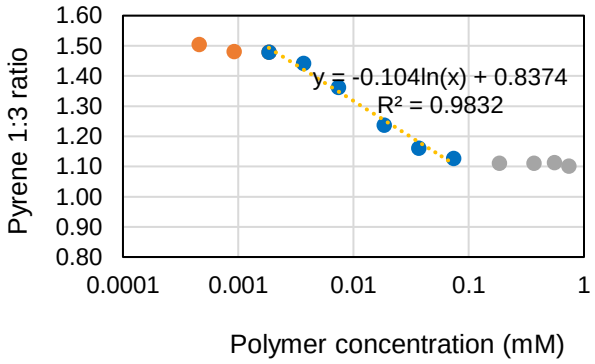

3rd run

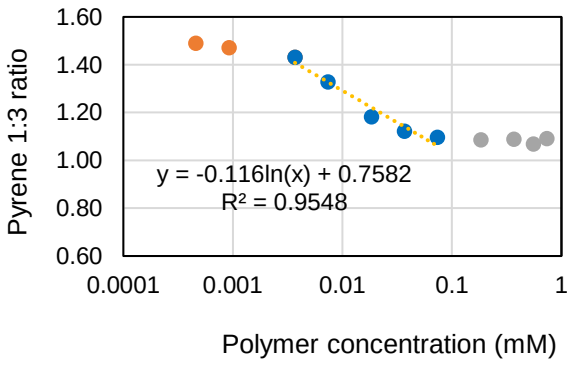

CMC average from 3 different runs

	CMC (μM)
Rep 1	8.106
Rep 2	11.868
Rep 3	11.785
average	11.826
SD	0.059

A3.4.3 CMC of M2diF8H18

		1st run			2nd run			3rd run		
	Sample Conc. (mM)	I_1 (374)	I_3 (385)	I_1/I_3	I_1 (373)	I_3 (384)	I_1/I_3	I_1 (373)	I_3 (385)	I_1/I_3
P1	7.18E-05	2.5580	1.6095	1.5893	2.4899	1.6617	1.4984	-	-	-
P2	0.000359	2.1423	1.6428	1.3041	2.4701	1.8704	1.3206	1.8576	1.3443	1.3818
P3	0.000718	2.2965	1.4926	1.5385	2.3004	1.5723	1.4631	2.0047	1.3113	1.5287
P4	0.001436	1.3190	0.8588	1.5359	2.7020	1.8240	1.4813	2.0889	1.4044	1.4874
P5	0.002872	2.1072	1.3895	1.5166	1.7712	1.2338	1.4356	1.8686	1.2927	1.4455
P6	0.005744	1.6122	1.1408	1.4133	2.7432	1.9797	1.3857	0.9287	0.7208	1.2883
P7	0.014361	0.3333	0.2802	1.1895	3.4390	2.7921	1.2317	2.5577	2.0718	1.2345
P8	0.028722	2.1320	1.7496	1.2186	3.3850	3.0115	1.1240	2.9855	2.6865	1.1113
P9	0.057443	2.3047	2.0035	1.1503	-	-	-	3.5483	3.3984	1.0441
P10	0.143608	2.5812	2.2885	1.1279	5.2853	5.0644	1.0436	4.9765	4.9780	0.9997
P11	0.287215	4.3594	3.8644	1.1281	5.1212	4.8734	1.0508	4.3298	4.3710	0.9906
P12	0.430823	4.5490	4.0421	1.1254	4.2609	4.1299	1.0317	4.7467	4.7769	0.9937

1st run

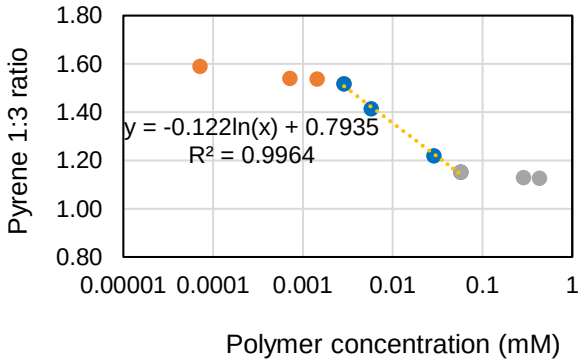

2nd run

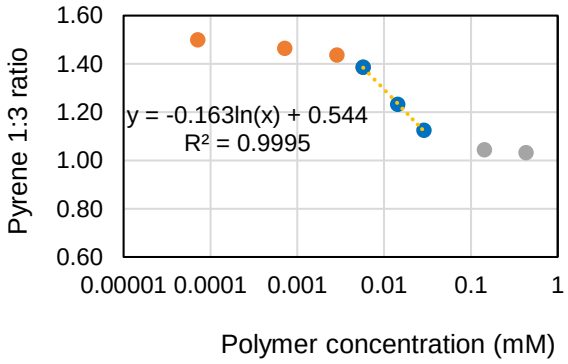

3rd run

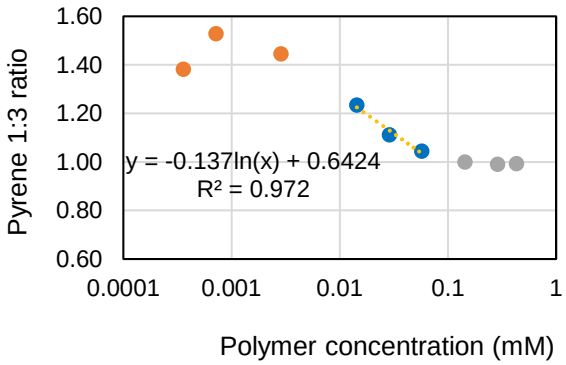

CMC average from 3 different runs

	CMC (μM)
Rep 1	12.436
Rep 2	14.410
Rep 3	14.402
average	13.749
SD	1.137

A3.4.4 CMC of M2diF8H18/F8

		1st run			2nd run			3rd run		
	Sample Conc. (mM)	I_1 (374)	I_3 (385)	I_1/I_3	I_1 (373)	I_3 (384)	I_1/I_3	I_1 (373)	I_3 (385)	I_1/I_3
P1	7.77076E-05	-	-	-	3.8226	2.5354	1.5077	1.9830	1.3616	1.4563
P2	0.000388538	3.7393	2.6077	1.4339	4.2218	3.2885	1.2837	1.9302	1.3101	1.4733
P3	0.000777076	5.4385	3.903	1.3933	4.1091	2.9605	1.3880	2.0797	1.3702	1.5178
P4	0.001554151	1.9815	1.450	1.3663	1.5240	1.0723	1.4211	2.0776	1.4553	1.4275
P5	0.003108303	2.9751	2.529	1.1761	-	-	-	2.1792	1.4990	1.4537
P6	0.006216605	4.5852	3.3770	1.3577	2.8625	2.0681	1.3840	-	-	-
P7	0.015541513	5.3805	4.3170	1.2463	3.7579	2.8411	1.3226	3.3123	2.5817	1.2829
P8	0.031083026	5.1998	4.3432	1.1972	3.1997	2.7218	1.1755	3.6453	3.1024	1.1749
P9	0.062166052	6.3217	5.589	1.1309	2.7533	2.8610	0.9623	3.1411	2.8515	1.1015
P10	0.155415129	5.9484	5.4388	1.0937	3.6364	3.4927	1.0411	5.7141	5.4971	1.0394
P11	0.310830259	9.1955	8.4463	1.0887	5.2862	5.2093	1.0147	4.6017	4.3991	1.0460
P12	0.466245388	7.4499	7.0504	1.0566	4.8123	4.7320	1.0169	6.3797	6.0516	1.0542

1st run

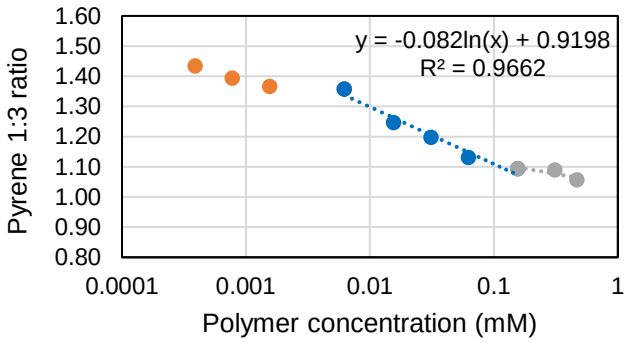

2nd run

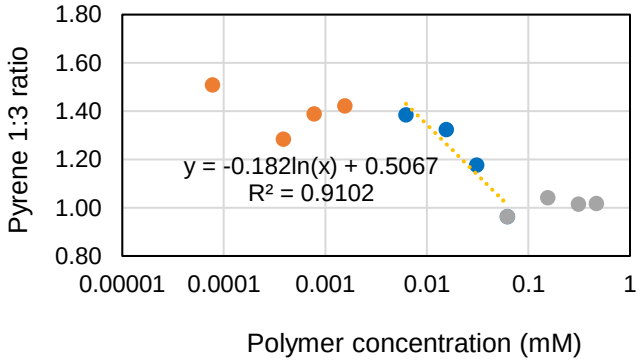

3rd run

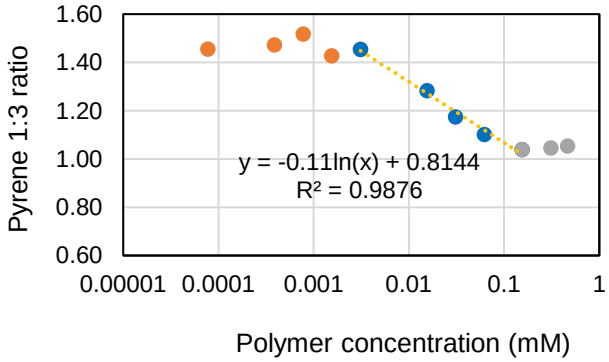

CMC average from 3 different runs

	CMC (μM)
Rep 1	21.732
Rep 2	21.623
Rep 3	18.023
average	20.459
SD	2.111

A3.4.5 CMC of $mPEG_{2K}$-DSG

		1st run			2nd run			3rd run		
	Sample Conc. (mM)	I_1 (374)	I_3 (385)	I_1/I_3	I_1 (373)	I_3 (384)	I_1/I_3	I_1 (373)	I_3 (385)	I_1/I_3
P1	9.53685E-05	2.3281	1.6183	1.4386	1.3925	1.2167	1.1444	1.5191	1.0604	1.4325
P2	0.000476843	3.2174	2.2506	1.4295	1.4895	1.0342	1.4402	1.3806	1.0510	1.3135
P3	0.000953685	4.1882	2.9785	1.4061	1.2710	0.8770	1.4492	1.3684	1.0040	1.3629
P4	0.00190737	4.7564	3.6679	1.2967	1.0522	0.7333	1.4348	1.2091	0.8398	1.4396
P5	0.003814741	4.8382	3.5122	1.3775	1.3244	0.9426	1.4049	1.0934	0.8016	1.3639
P6	0.007629482	4.2269	3.5797	1.1808	0.6954	0.5538	1.2556	0.7116	0.6280	1.1331
P7	0.019073705	7.6297	6.2915	1.2127	1.1596	1.1547	1.0042	1.3348	1.2893	1.0352
P8	0.038147409	7.4966	7.0153	1.0686	2.0816	1.9903	1.0458	1.8048	1.9061	0.9468
P9	0.076294818	6.6995	5.7309	1.1690	2.9834	2.8015	1.0649	2.0544	2.1948	0.9360
P10	0.190737046	8.6331	7.3342	1.1770	4.1564	3.8778	1.0718	2.836	3.0484	0.9303
P11	0.381474092	4.5248	3.8501	1.1752	4.7793	4.4357	1.0774	4.1189	4.4299	0.9298
P12	0.572211138	2.3281	1.6183	1.4386	4.8477	4.5684	1.0611	3.0184	3.2638	0.9248

1st run

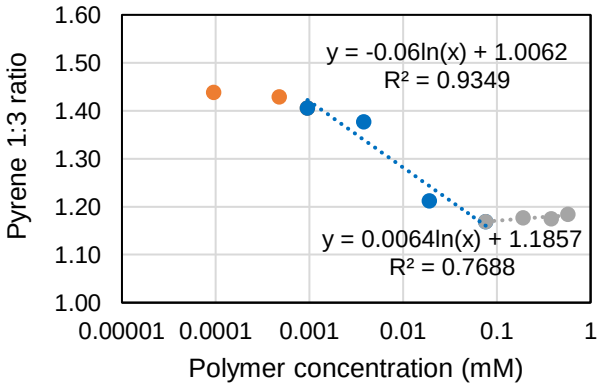

2nd run

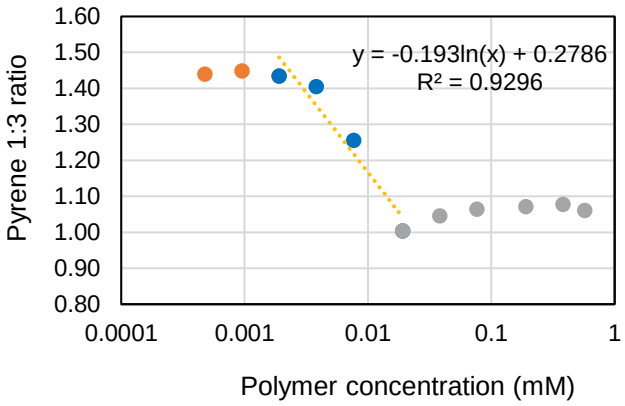

3rd run

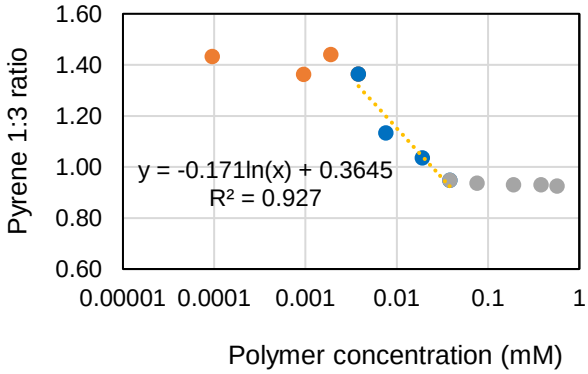

CMC average from 3 different runs

	CMC (μM)
Rep 1	7.391
Rep 2	6.591
Rep 3	9.225
average	7.736
SD	1.350

A3.4.6 CMC of M2H18

		1st run			2nd run			3rd run		
	Sample Conc. (mM)	I_1 (374)	I_3 (385)	I_1/I_3	I_1 (374)	I_3 (386)	I_1/I_3	I_1 (373)	I_3 (385)	I_1/I_3
P1	0.000110282	3.4723	2.2100	1.5711	2.1246	1.2863	1.6517	1.2045	0.8096	1.4878
P2	0.000551411	3.1369	1.9840	1.5811	2.0120	1.2354	1.6287	1.1545	0.7828	1.4749
P3	0.001102823	3.0924	1.9721	1.5681	1.3193	0.9021	1.4624	0.9421	0.6747	1.3962
P4	0.002205646	3.0032	1.9748	1.5208	2.0712	1.3220	1.5667	1.0089	0.7016	1.4380
P5	0.004411291	3.4152	2.3496	1.4536	2.1542	1.4559	1.4796	0.7532	0.5975	1.2605
P6	0.008822582	3.3920	2.5125	1.3501	1.6159	1.2991	1.2438	1.1752	0.9149	1.2845
P7	0.022056456	3.3041	2.8839	1.1457	2.0813	1.9891	1.0463	1.1792	1.0724	1.0996
P8	0.044112911	4.0216	3.8940	1.0328	2.0163	2.1564	0.9350	1.7877	1.7309	1.0328
P9	0.088225823	5.7636	5.7987	0.9939	3.6459	4.0679	0.8963	2.8461	2.7243	1.0447
P10	0.220564557	6.7087	7.0770	0.9479	4.5404	5.0247	0.9036	1.4511	1.6226	0.8943
P11	0.441129114	5.9839	6.1444	0.9739	3.2062	3.8464	0.8335	4.1589	4.0429	1.0287
P12	0.661693671	6.6336	6.5881	1.0069	5.3037	5.8148	0.9121	4.1898	4.0949	1.0232

1st run

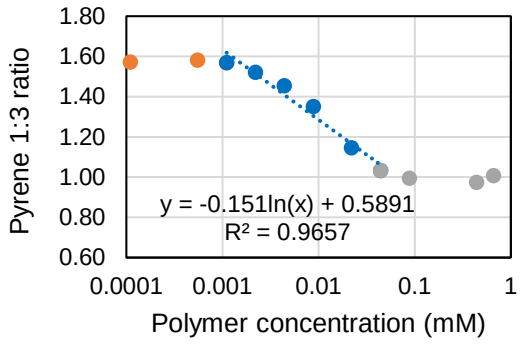

2nd run

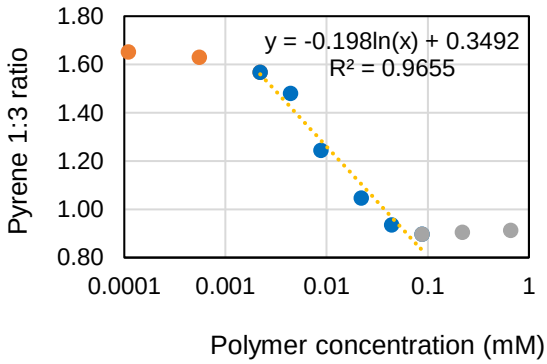

3rd run

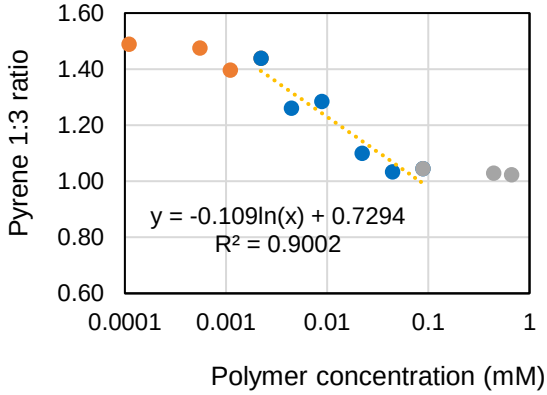

CMC average from 3 different runs

	CMC (μM)
Rep 1	9.792
Rep 2	10.060
Rep 3	9.179
average	9.677
SD	0.622

A3.5 Aggregation number data

A3.5.1 Aggregation number of M2H10PFtB$_{TRI}$

		Polymer concentration								
		1.084 mM (3mg/mL)			1.807 mM (5mg/mL)			2.53 mM (7mg/mL)		
	C153 (μM)	I	I_0/I	$\ln(I_0/I)$	I	I_0/I	$\ln(I_0/I)$	I	I_0/I	$\ln(I_0/I)$
P0	0.000	2.221	1.000	0.000	2.508	1.000	0.000	2.718	1.000	0.000
P1	3.319	1.851	1.200	0.182	2.252	1.114	0.108	2.605	1.043	0.042
P2	6.626	1.558	1.426	0.355	2.061	1.217	0.196	2.357	1.153	0.143
P3	9.901	1.197	1.855	0.618	1.991	1.260	0.231	2.204	1.233	0.210
P4	11.858	1.170	1.898	0.641	1.715	1.463	0.380	2.141	1.269	0.238
P5	13.155	1.057	2.102	0.743	1.660	1.511	0.413	2.099	1.295	0.259
P6	16.397	0.964	2.305	0.835	1.457	1.721	0.543	1.854	1.466	0.383
P7	19.608	0.782	2.839	1.043	1.336	1.878	0.630	1.772	1.534	0.428

Polymer conc.	Aggregation No.	Avg aggregation No.	Std
3 mg/mL	58.02225	56.1829	1.944657
5 mg/mL	56.3787		
7 mg/mL	54.14775		

A3.5.2 Aggregation number of M2H10PFtB$_{MONO}$

		Polymer concentration											
		1.189mM (3 mg/mL)			1.586mM (4 mg/mL)			1.783mM (4.5 mg/mL)			1.982mM (5 mg/mL)		
	C153 (μM)	I	I_0/I	$\ln(I_0/I)$	I	I_0/I	$\ln(I_0/I)$	I	I_0/I	$\ln(I_0/I)$	I	I_0/I	$\ln(I_0/I)$
P0	0.000	4.524	1.000	0.000	4.937	1.000	0.000	4.504	1.000	0.000	4.588	1.000	0.000
P1	3.319	3.683	1.228	0.206	4.178	1.181	0.167	3.792	1.188	0.172	4.086	1.123	0.116
P2	6.626	3.217	1.406	0.341	3.649	1.353	0.302	3.394	1.327	0.283	3.667	1.251	0.224
P3	9.901	2.639	1.714	0.539	3.369	1.466	0.382	2.926	1.539	0.431	3.188	1.439	0.364
P4	11.858	2.356	1.920	0.652	3.122	1.581	0.458	2.886	1.561	0.445	2.973	1.543	0.434
P5	13.155	1.943	2.328	0.845	3.085	1.600	0.470	2.725	1.653	0.503	2.917	1.573	0.453
P6	16.397	1.925	2.350	0.855	2.549	1.937	0.661	2.325	1.937	0.661	2.683	1.710	0.537
P7	19.608	1.751	2.584	0.949	2.270	2.175	0.777	2.174	2.072	0.728	2.254	2.035	0.711

Polymer conc.	Aggregation No.	Avg aggregation No.	Std
3 mg/mL	62.6916	65.6064	3.934341
4 mg/mL	61.7403		
4.5 mg/mL	68.952		
5 mg/mL	69.0417		

A3.5.3 Aggregation number of M2H10F13

		Polymer Concentration								
		1.068mM (3 mg/mL)			1.424mM (4 mg/mL)			1.78mM (5 mg/mL)		
	C153 (μM)	I	I_0/I	$\ln(I_0/I)$	I	I_0/I	$\ln(I_0/I)$	I	I_0/I	$\ln(I_0/I)$
P0	0.000	4.994	1.000	0.000	5.149	1.000	0.000	1.929	1.000	0.000
P1	3.319	3.700	1.350	0.300	4.042	1.274	0.242	1.711	1.128	0.120
P2	6.626	2.746	1.819	0.598	3.239	1.590	0.464	1.411	1.367	0.313
P3	9.901	2.337	2.136	0.759	2.971	1.733	0.550	1.247	1.547	0.436
P4	11.858	1.875	2.663	0.980	2.685	1.918	0.651	1.122	1.719	0.542
P5	13.155	1.773	2.816	1.035	2.350	2.191	0.784	1.061	1.818	0.598
P6	16.397	1.433	3.485	1.249	2.096	2.456	0.899	0.929	2.076	0.731
P7	19.608	1.134	4.402	1.482	1.646	3.127	1.140	0.779	2.478	0.908

Polymer conc.	Aggregation No.	Avg aggregation No.	Std
3 mg/mL	80.68804	80.02188	0.669208
4 mg/mL	80.02793		
5 mg/mL	79.34967		

A3.5.4 Aggregation number of M2F8H18

		Polymer Concentration								
		1.475mM (4 mg/mL)			1.66mM (4.5 mg/mL)			1.844mM (5 mg/mL)		
	C153 (μM)	I	I_0/I	$\ln(I_0/I)$	I	I_0/I	$\ln(I_0/I)$	I	I_0/I	$\ln(I_0/I)$
P0	0.000	6.722	1.000	0.000	7.373	1.000	0.000	5.422	1.000	0.000
P1	3.319	5.569	1.206	0.188	5.908	1.248	0.221	4.714	1.150	0.139
P2	6.626	4.478	1.500	0.406	4.963	1.485	0.395	4.255	1.274	0.242
P3	9.901	3.416	1.967	0.676	4.449	1.657	0.505	3.376	1.606	0.473
P4	11.858	3.254	2.065	0.725	3.899	1.891	0.637	3.259	1.663	0.509
P5	13.155	2.779	2.418	0.883	3.711	1.986	0.686	2.843	1.906	0.645
P6	16.397	2.633	2.552	0.937	3.286	2.243	0.808	2.655	2.042	0.714
P7	19.608	2.260	2.974	1.0	2.995	2.461	0.900	2.260	2.399	0.875

Polymer conc.	Aggregation No.	Avg aggregation No.	Std
4 mg/mL	87.498	83.941	3.081
4.5 mg/mL	82.082		
5 mg/mL	82.244		

A3.5.5 Aggregation number of M2diF8H18

		Polymer Concentration								
		0.574mM (2 mg/mL)			0.862mM (3 mg/mL)			1.292mM (4.5 mg/mL)		
	C153 (μM)	I	I_0/I	$\ln(I_0/I)$	I	I_0/I	$\ln(I_0/I)$	I	I_0/I	$\ln(I_0/I)$
P0	0.000	7.090	1.000	0.000	8.073	1.000	0.000	6.454	1.000	0.000
P1	3.319	4.871	1.456	0.375	5.993	1.347	0.298	5.390	1.197	0.180
P2	6.626	3.922	1.808	0.592	4.992	1.617	0.481	4.708	1.371	0.315
P3	9.901	2.766	2.563	0.941	3.787	2.132	0.757	4.428	1.457	0.377
P4	11.858	2.186	3.243	1.176	3.426	2.357	0.857	3.846	1.678	0.518
P5	13.155	1.881	3.768	1.327	3.155	2.559	0.940	3.925	1.644	0.497
P6	16.397	1.487	4.769	1.562	2.637	3.061	1.119	3.327	1.940	0.663
P7	19.608	1.409	5.032	1.616	2.062	3.915	1.365	2.935	2.199	0.788

Polymer conc.	Aggregation No.	Avg aggregation No.	Std
2 mg/mL	54.456	55.427	4.228
3 mg/mL	60.056		
4.5 mg/mL	51.769		

A3.5.6 Aggregation number of M2diF8H18/F8

		Polymer Concentration								
		0.932mM (3 mg/mL)			1.243mM (4 mg/mL)			1.399mM (4.5 mg/mL)		
	C153 (μM)	I	I_0/I	$\ln(I_0/I)$	I	I_0/I	$\ln(I_0/I)$	I	I_0/I	$\ln(I_0/I)$
P0	0.000	4.647	1.000	0.000	4.312	1.000	0.000	4.885	1.000	0.000
P1	3.319	3.190	1.457	0.376	3.413	1.263	0.234	3.861	1.265	0.235
P2	6.626	2.669	1.741	0.555	2.728	1.581	0.458	3.513	1.391	0.330
P3	9.901	2.163	2.148	0.765	2.329	1.851	0.616	2.853	1.712	0.538
P4	11.858	1.843	2.522	0.925	2.091	2.062	0.724	2.521	1.938	0.662
P5	13.155	1.716	2.708	0.996	2.061	2.092	0.738	2.318	2.107	0.745
P6	16.397	1.483	3.134	1.142	1.814	2.377	0.866	2.015	2.424	0.886
P7	19.608	1.213	3.831	1.343	1.546	2.788	1.025	1.804	2.708	0.996

Polymer conc.	Aggregation No.	Avg aggregation No.	Std
3 mg/mL	68.551	70.216	3.174
4 mg/mL	68.220		
4.5 mg/mL	73.876		

A3.5.7 Aggregation number of $mPEG_{2K}$-DSG

		Polymer Concentration								
		1.144mM (3 mg/mL)			1.526mM (4 mg/mL)			1.907mM (5 mg/mL)		
	C153 (μM)	I	I_0/I	$\ln(I_0/I)$	I	I_0/I	$\ln(I_0/I)$	I	I_0/I	$\ln(I_0/I)$
P0	0.000	6.385	1.000	0.000	6.025	1.000	0.000	5.914	1.000	0.000
P1	3.319	5.240	1.218	0.198	5.152	1.169	0.157	5.110	1.157	0.146
P2	6.626	4.425	1.443	0.367	4.267	1.412	0.345	4.603	1.285	0.251
P3	9.901	3.611	1.768	0.570	3.691	1.632	0.490	4.136	1.430	0.358
P4	11.858	3.192	2.000	0.693	3.395	1.774	0.573	3.817	1.549	0.438
P5	13.155	2.931	2.178	0.779	3.279	1.838	0.608	3.507	1.686	0.523
P6	16.397	2.547	2.507	0.919	2.838	2.123	0.753	3.140	1.884	0.633
P7	19.608	2.133	2.993	1.096	2.357	2.556	0.938	2.884	2.051	0.718

Polymer conc.	Aggregation No.	Avg aggregation No.	Std
3 mg/mL	65.335	69.685	3.776
4 mg/mL	72.117		
5 mg/mL	71.602		

A3.5.8 Aggregation number of M2H18

		Polymer Concentration								
		1.765mM (4 mg/mL)			2.206mM (5 mg/mL)			2.647mM (6 mg/mL)		
	C153 (μM)	I	I_0/I	$\ln(I_0/I)$	I	I_0/I	$\ln(I_0/I)$	I	I_0/I	$\ln(I_0/I)$
P0	0.000	5.276	1	0	3.449	1	0	3.014	1	0
P1	3.319	4.505	1.1713	0.158	3.205	1.0769	0.074	2.736	1.102	0.097
P2	6.626	4.059	1.299	0.262	2.837	1.2168	0.1957	2.409	1.251	0.224
P3	9.901	3.369	1.566	0.448	2.609	1.322	0.279	2.271	1.328	0.283
P4	11.858	3.157	1.671	0.514	2.428	1.421	0.351	2.158	1.397	0.334
P5	13.155	3.110	1.696	0.529	2.403	1.435	0.361	2.097	1.437	0.363
P6	16.397	2.653	1.989	0.687	2.141	1.611	0.477	1.846	1.633	0.490
P7	19.608	2.318	2.277	0.823	1.889	1.825	0.602	1.687	1.787	0.581

Polymer conc.	Aggregation No.	Avg aggregation No.	Std
4 mg/mL	73.899	71.842	6.702
5 mg/mL	64.352		
6 mg/mL	77.274		

A3.6 Microviscosity data

A3.6.1 Microviscosity of M2F8H18

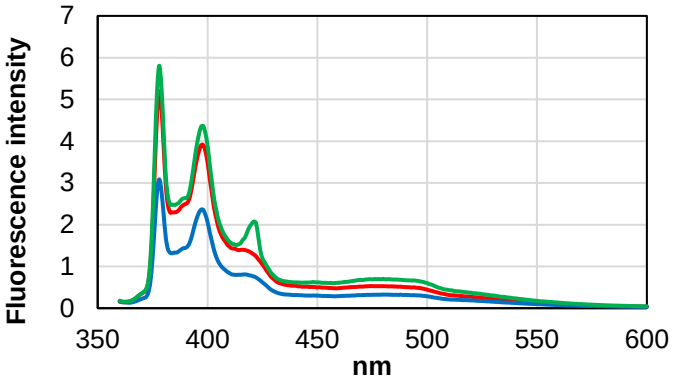

378 nm (I_M)	480 nm (I_E)	I_M/I_E
5.19379	0.527344	9.8489601
3.08563	0.326233	9.4583626
5.80505	0.701294	8.2776268
	Average	9.1949831
	SD	0.8181067

A3.6.2 Microviscosity of M2diF8H18

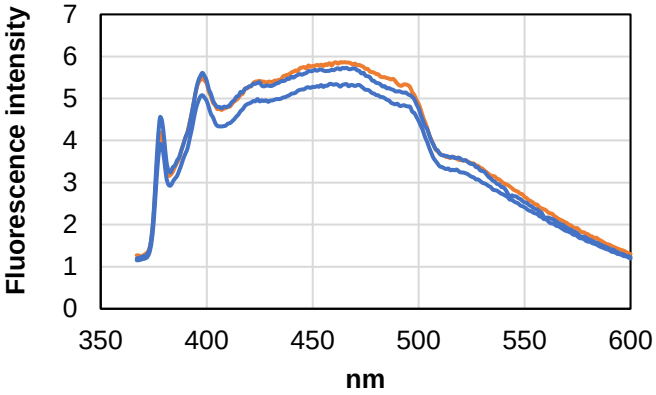

378 nm (I_M)	480 nm (I_E)	I_M/I_E
4.18762	5.58319	0.750041
4.55139	5.37079	0.847434
3.91022	5.08026	0.769689
	Average	0.789055
	SD	0.051504

A3.6.3Microviscosity of M2diF8H18/F8

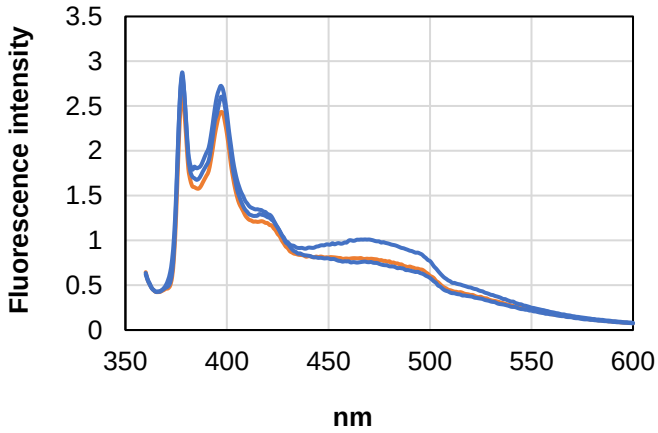

378 nm (I_M)	480 nm (I_E)	I_M/I_E
2.63702	0.767517	3.435781
2.83936	0.711365	3.991425
2.87628	0.961914	2.990163
	Average	3.472456
	SD	0.501637

A3.6.4 Microviscosity of $mPEG_{2K}$-DSG

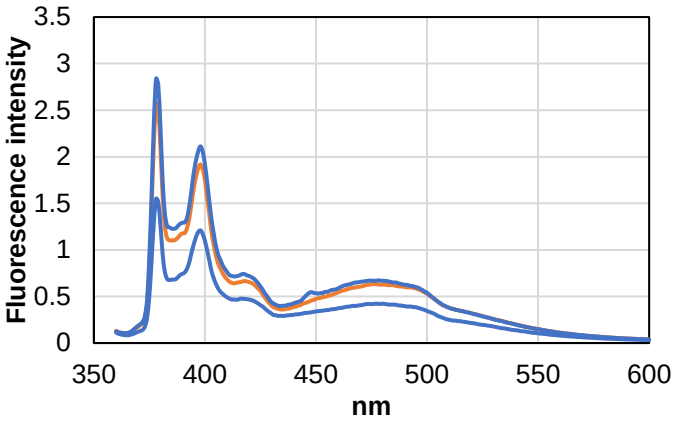

378 nm (I_M)	480 nm (I_E)	I_M/I_E
2.56866	0.627747	4.091871
2.836	0.668945	4.239511
1.54846	0.423279	3.658249
	Average	3.996544
	SD	0.302129

A3.6.5 Microviscosity of M2H18

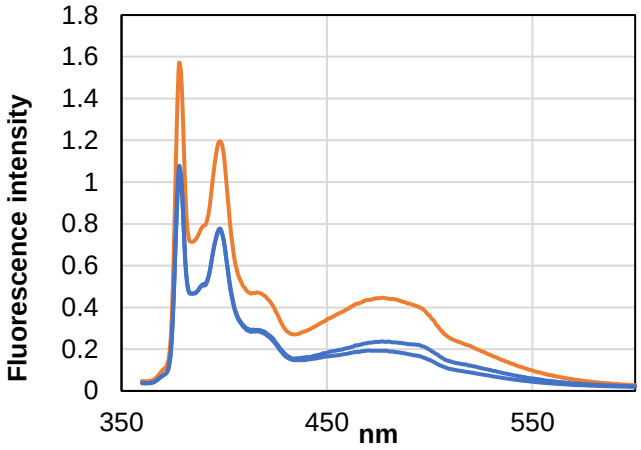

378 nm (I_M)	480 nm (I_E)	I_M/I_E
1.04858	0.236816	4.427826
1.763	0.320435	5.50189
1.07605	0.189819	5.668821
	Average	5.199514
	SD	0.673493